Computational investigation of skimming flow on stepped spillways using the smoothed particle hydrodynamics method.

Husain, Sarhang Mustafa

by

Sarhang Mustafa Husain

Submitted to Swansea University in Fulfilment of the

Requirements for the Degree of

Doctor of Philosophy

in

Dam Engineering

Department of Civil Engineering

Swansea University

2013

In The Name of God

Abstract

Stepped channels and spillways have been used for centuries as an effective and efficient means of dissipating the energy of overflowing water, since steps along the downstream slope increase the roughness of the spillway surface and generate high turbulence levels. Three main flow regimes, depending on step size and water discharge, have been recognized, namely nappe, transition and skimming flow. With the skimming flow regime, two regions, with respect to the air content, can be clearly identified along the chute slope, namely the non-aerated and aerated flow regions.
Numerous studies have investigated the hydraulics of skimming flow conditions in the aerated flow region, whereas such conditions in the non-aerated flow region have received much less attention, especially over inclined steps. Understanding the flow properties in the non-aerated flow region over the horizontal and upward inclined steps is therefore important to improve hydraulic structure design.
This study is a numerical investigation, applying the 2D SPHysics code, as an implementation of the SPH particle-based method, to characterize skimming flow conditions over stepped spillways having bottom slopes typical of embankment dams. The code is initially validated against two laboratory experimental results for free surface models over hydraulic structures. Agreement between both results is good, demonstrating that the code is robust in predicting flow field variables over stepped spillways. The validated code is then applied to twenty-six numerical stepped spillway cases, to explore the behaviour of the skimming flow with various step heights, chute slopes and step shapes. The current work provides new insight into the hydraulics of skimming flow conditions in the non-aerated flow region. The computational results obtained have important implications for designing embankment stepped chutes, such as determining the position of free surface aeration, optimum step configuration and maximum design discharge, which ensures the safety of steps against cavitation.

Declaration/ Statements

Declaration

This work has not previously been accepted in substance for any degree and is not being concurrently submitted in candidature for any degree.

13/08/2013

Statement 1

This thesis is the result of my own investigations, except where otherwise stated. Where correction services have been used, the extent and nature of the correction is clearly marked in a footnote(s).

Other sources are acknowledged by footnotes giving explicit references. A bibliography is appended

13/08/2013

Statement 2

I hereby give consent for my thesis, if accepted, to be available for photocopying and for inter-library loan, and for the title and summary to be made available to outside organizations.

13/08/2013

Contents

List of Figures

List of Tables

Notation

a	Refers to an interpolation point inside the computational domain
A	Value of the flow field function
--	Wetted cross sectional area of the channel (m^2)
A_1	Coefficient depends on the speed of sound
A_b	Value of the flow field function at position r_a
$A(r)$	Value of the flow field function of any point located at position r
$A(r_a)$	Value of the flow field function at the position r_a
$A(r')$	Value of the flow field function at the position r'
b	Refers to all the particles located inside the influence area of a certain interpolation point
B	Bulk modulus elasticity of the fluid (N/m^2)
c	Speed of sound (m/s)
c_a	Speed of sound at particle a (m/s)
c_b	Speed of sound at particle b (m/s)
c_i	Speed of sound of particle i (m/s)
c_o	Speed of sound at the reference density (m/s)
C_i	Mean air concentration at the inception point
C_s	Smagorinsky constant =0.12
C_1	Constant =0.0066
d	Flow depth along the chute slope (m)
d_i	Flow depth at the inception point (m)
d_w	Clear water depth at the inception point (m)
dx	Distance between particles in the X-direction (m)
dy	Distance between particles in the Y-direction (m)
dz	Distance between particles in the Z-direction (m)
D/Dt	Total material derivative

D_a	Total mass rate of particle a
e	Thermal energy per unit mass ($Kg.m^2/s^2/Kg$)
e_a	Thermal energy per unit mass of particle a ($Kg.m^2/s^2/Kg$)
E_a	Total energy rate of particle a ($Kg.m^2/s^2/s$)
E_o	Total head of the flow (m)
E_L	Energy loss of the flow (m)
$\vec{f}$	Force on fluid particles normal to the wall (N)
$\overrightarrow{F_a}$	Total force acting on particle a per unit mass (N/Kg)
F_s	Step Froude number
F_*	Froude number in terms of the roughness height
$F_{*\theta}$	Modified roughness Froude number in terms of the chute slope
$\mathbf{g}$	Body force per unit mass of the fluid (N/Kg)
g	Gravitational acceleration = 9.81(m/s^2)
h	Kernel smoothing characteristic length (m)
h_c	Critical flow depth (m)
h_o	Local still water depth (m)
--	Initial flow depth upstream of broad crested weir (m)
h_s	Step height (m)
H_o	Total head upstream of broad crested weir (m)
H_{res}	Residual energy (m)
$\vec{i}$	Unit vector in the X-direction
$\vec{j}$	Unit vector in the Y-direction
$\vec{k}$	Unit vector in the Z-direction
k	Factor used to scale the kernel smoothing characteristic length, h
k_l	Sub particle scale turbulent kinetic energy

K_s	Roughness height measured perpendicular to the flow direction (m)
l	Integer corresponding to the unit vector, $\vec{i}$
l_s	Step length (m)
L	Distance measured from the upstream corner of the weir along the chute slope (m)
$\mathbf{L}_a$	Matrix used to correct the kernel gradient at particle a
L_i	Length measured from the upstream end of the spillway crest to the inception point (m).
M	Mach number
m	Characteristic height (m)
--	Dimensionless parameter defines the proportion of the micro-roughness elements on the steps which equals to the ratio of the number of micro-roughness elements to the number of steps
m_a	Mass of particle a (kg/m^3)
m_b	Mass of all the particles located inside the compact support radius of a certain particle (kg/m^3).
n	Integer corresponds to the unit vector, $\vec{k}$
$\vec{n}$	Normal of the solid wall
np	Total number of particles including both fluid and boundary
N	Exponent of the velocity distribution over stepped spillways
--	Total number of particles surrounding a given particle
P	Pressure (N/m^2)
--	Wetted perimeter of the channel (m)
P_a	Pressure of particle a (N/m^2)

P_b	Pressure of all the particles located inside the compact support radius of a certain particle (N/m^2)
P^*_{ab}	Corrected pressure in the star region (N/m^2)
P_o	Reference fluid pressure which represents the pressure at a given point or section (N/m^2)
P_v	Vapour water pressure (N/m^2)
q	Water flow discharge per unit channel width (m^2/s^2)
--	Normalized distance between the particles = r/h
r	Distance between two particles (m)
r_a	Vectorial position of particle a
r_b	Vectorial position of particles located within the radius of the compact support of a certain particle
R	Hydraulic radius of the channel (m)
$\boldsymbol{R}$	Initial vectorial position of a fluid particle in the domain
S_{ij}	Strain tensor of an SPS element
$\vec{S}$	Tangent to the boundary particles in the Y direction
$\vec{t}$	Tangent to the boundary particles in the X direction
u	Horizontal velocity at different distances measured normal to the weir crest (m/s)
$\boldsymbol{u}$	Velocity vector in x, y and z directions (m/s)
$\boldsymbol{u_a}$	Velocity vector in x, y and z directions of particle a (m/s)
$\boldsymbol{u_b}$	Velocity vector in x, y and z directions of particle b (m/s)
$\boldsymbol{u_{ba}}$	Difference in velocity vector between particles a and b in x, y and z directions (m/s)
$u_\perp$	Velocity of the fluid particle projected on the normal (m/s)

U_a^R	Flow velocity at particle a in the right of the star region (m/s)
U_b^R	Flow velocity at particle b in the right of the star region (m/s)
U_{ab}^*	Flow velocity in the star region (m/s)
v_o	Mean approach flow velocity (m/s)
$\overrightarrow{v_{WP}}$	Velocity of water particles (m/s)
$\overrightarrow{v_{BP}}$	Velocity of boundary particles (m/s)
V	Maximum expected/ mean flow velocity (m/s)
--	Velocity parallel to the flow direction at different distances measured perpendicular to the pseudo bottom (m/s)
V_1	Flow velocity in a section before the hydraulic jump
$\overrightarrow{V_a}$	Flow velocity at particle a (m/s)
V_b	Volume of particle b (m^3)
V_{max}	Maximum flow velocity over stepped spillways (m/s)
$W(r-r',h)$	Smoothing or weighting kernel function
$\widetilde{W}_{ab}$	Corrected kernel function with respect to Shepard filter
W_{ab}^{MLS}	Corrected kernel function with respect to the moving least squares
ωa	Volume of particle a (m^3)
x	Distance measured horizontally from the upstream corner of broad crested weir (m)
x_a	Position of particle a in the X- direction
x_b	Position of particle b in the X- direction
y	Distance measured perpendicular to the pseudo bottom formed by the outer edges of the steps (m)

z_a	Position of particle a in the Z- direction
z_b	Position of particle b in the Z- direction

List of Symbols

α	Coefficient of the kinetic energy
α_D	Parameter depends on the number of dimensions involving the computational domain.
β_o	Coefficient used in the linear correction of kernel function
β_{1x}	Coefficient used in the linear correction of kernel function in the X-direction
β_{1z}	Coefficient used in the linear correction of kernel function in the Z-direction.
θ	Chute slope (degree)
ϑ	Upward inclination of the step with horizontal (degree)
η_m	Correction coefficient
σ	Cavitation index number
Ω	Space domain
δ	Dirac delta function
--	Thickness of the boundary layer (m)
$\delta\rho$	Variation of the fluid mass density (Kg/m^3)
ρ	Fluid mass density (Kg/m^3)
ρ_a	Mass density of particle *a* (Kg/m^3)
ρ_a^{new}	Updated mass density of particle *a* (Kg/m^3)
ρ_b	Mass density of all the particles located within the radius of of a certain particle (Kg/m^3).
ρ_{ab}	Mean value of the mass density of particle *a* and all of the particles located within the radius of compact support of

	particle a (Kg/m^3)
ρ_o	Reference fluid mass density (kg/m^3)
∇	Gradient
∇W_x	Kernel gradient in the X-direction
∇W_z	Kernel gradient in the Z-direction
$\widetilde{\nabla} W_{ab}$	Corrected kernel gradient
$\boldsymbol{\Theta}$	Refers to all the diffusion terms in the momentum equation
ψ	Perpendicular distance from the fluid particle to the wall (m)
ξ	Projection of the interpolated location onto the chord that joins two boundary particles.
Δb	Distance between any two neighbouring boundary particles
Δl	Particle-particle spacing (m)
Δt	Time step (sec)
Δt_{cv}	Time step based on the combination of both the viscous terms and the CFL number (sec)
Δt_f	Forcing time step (sec)
Δx	Spacing between particles in the X direction (m)
Δz	Spacing between particles in the Z direction (m)
Θ	Parameter representing all of the diffusion terms due to the viscosity.
μ	Dynamic viscosity = $1*10^{-3}$ (N.s/m^2) for water at 20° C
υ_o	Kinematic fluid viscosity (m^2/s)
ν_t	Turbulent eddy viscosity
$\boldsymbol{\tau}$	Shear stress (N/m^2)
$\boldsymbol{\tau}_{ij}$	Sub particle scale stress tensor of an element (N/m^2)

Π_{ab}	Stress tensor term
γ	Polytrophic constant its value ranges from 1 to 7.
ϵ	Constant; its value ranges from zero to unity

Abbreviations

BCC	Centred cubic grid
BP	Boundary particle
CFD	Computational fluid dynamics
CFL	Courant number
ICOLD	International commission on large dams
MLS	Moving least squares
LES	Large eddy simulation
SC	Simple grid
SPH	Smoothed particle hydrodynamics
SGS	Sub grid scale stress tensor
SPS	Sub particle scale stress tensor
VOF	Volume of fluid
WP	Water particle
2D	Two dimensional flow condition
3D	Three dimensional flow condition

Acknowledgments

The author would like to express his heartfelt thanks and appreciation to many individuals who have offered support, encouragement and inspiration throughout this research effort.

In the first place I wish to express my sincere gratitude to my supervisor, Professor Dominic Reeve for his generous guidance, continuous support, great instructions and invaluable kindness. Without his knowledge and exceptional encouragement this research would never have been conceived. I highly appreciate his ability to help me keep things in perspective. I would like also to acknowledge the continuous and unconditional assistance provided by my home supervisor, Professor Jowhar Muhammed at the different stages of this work. I am greatly indebted with him and I would like to acknowledge his wealth of knowledge on this particular subject. Appreciation is extended to my third supervisor Dr. Harshinie Karunarathna for her invaluable advice and helpful discussions on this investigation. I further wish to express my gratitude to the academic and administrative staff of the College of Engineering at Swansea University who shared with me their valuable expert advice and supported me in managing various issues throughout the course of this research.

The scholarship provided by the Ministry of higher education and scientific research of the Iraqi government is gratefully acknowledged. Additionally, sincere appreciation is expressed to the staff members of the Iraqi Cultural Attaché in London who provided continuous co-operation, support and advice through difficult times, and assistance whenever it was needed during our stay in the United Kingdom; their counsel and help were invaluable. A special thanks goes to the staff members of the Presidency of Salahaddin university in Erbil-Iraqi Kurdistan for their support and encouragement.

The author wishes to thank his parents, sisters and brothers for their continuous support and encouragement. A special thanks goes to my youngest brother, Farhang for his efforts in managing my financial and administrative issues at home during my stay in the United Kingdom. I wish I could write a chapter to express my deepest gratitude and appreciation to my wife, Shilan; without her continuous love, overwhelming support, unlimited patience and motivational talks this study would not have been possible. I deeply thank my children Govand, Govar, Muhammad and Alaa for their love, support and understanding. I hope one day I can offer them at least a small fraction of what they have offered me throughout all stages of this study.

Lastly, I would like to thank all my relatives and friends who provided me with help and encouragement. Without the support and love of all the above mentioned people, none of my dreams for the completion of a doctoral degree would have ever come true.

Summary

Dam spillways are designed to release excess water during times of peak flow. Water can overtop the dam crest, mainly because of insufficient dam storage and/or spillway capacity. In the absence of efficient protective measures, the high energy of the overtopping water may damage the downstream slope of the spillway and the surrounding area, which in turn might lead to entire dam failure. Statistical data on global dam accidents has reported that embankment dams account for a large portion of dam failures. The downstream slope of such kinds of dams is often run over moderate slopes and covered by compacted local site aggregates. A number of protection systems have recently been developed to ensure safe embankment dams during overtopping, such as riprap, gabions and stepped spillways.

The use of stepped spillways can be traced back for more than 3500 years. Nowadays, a stepped spillway is one of the most popular protection systems, for several reasons. The most obvious reasons are the ease of construction, simplicity of design, and recent advances in both the construction materials and the design technology of these materials, such as roller compacted concrete. The main concept of stepped spillways is to fit the downstream slope with steps of different shapes, dimensions and arrangements, in such a way so as to provide a staircase shape to its profile from top to bottom. These steps play a dual role: 1) generate high levels of turbulence, which increases the energy dissipation rate of the overflowing water, thereby reducing the need for a large basin at the end of the spillway; 2) increase the surface roughness, which on the one hand, contributes in decelerating the rapid velocity of the overflowing water, and on the other hand enhances the natural aeration mechanism taking place on the steps.

Depending on the discharge and step geometry, flow over stepped spillways has been classified into three regimes: nappe flow which occurs with low flow rates; skimming flow dealing with relatively high discharges; and transition flow with moderate discharges. Although stepped spillways can be found in various hydraulic engineering fields, most are designed to run under the skimming flow conditions. In fact, air plays a vital role in protecting the surface of such structures against cavitation damage. However, air may be entirely absent over the upstream reach of

the chute, especially when water flows with high rates, typical of skimming flow conditions, over low dams. This reach of stepped spillways is often known as the non-aerated flow region. It starts at some distance from the spillway crest and extends to where the turbulent boundary layer intersects the free surface at a point on the free surface known as the inception point of air entrainment.

Despite its importance, up to now no accurate approach is available in the literature to determine the distance between the weir crest and the free surface aeration on moderate slope stepped spillways. In addition, detailed information regarding the skimming flow conditions on upward inclined steps is completely lacking. Moreover, the maximum unit discharges in terms of the step height and chute slope at which cavitation can occur on moderate slope stepped spillways are not clearly defined. This study is a numerical investigation conducted to characterize the skimming flow regime on the horizontal and upward inclined steps in the non-aerated flow region over moderate slope stepped spillways typical of embankment dams. The main purpose is to evaluate the effect of various factors such as the step height, chute slope and step shape on the characteristics of the skimming flow regime. These properties include the position of the free surface, location of the inception point of self-aeration, velocity profile, growth of the boundary layer, energy dissipation rate and pressure distribution on both faces of the steps.

The present research uses the numerical 2D SPHysics model as an implementation of the computational smoothed particle hydrodynamics method. Twenty-six numerical stepped spillway models are examined using horizontal and upward inclined steps of different step sizes over moderate slopes typical of embankment dams. These numerical stepped spillway models are divided into two groups: the first group includes eighteen models, while the second group is represented by eight models. Three bottom slopes of 1V:2H, 1V:2.5H and 1V:3H are used for the models of the first group. Also, with each slope three step heights of 0.06m, 0.09 and 0.12m are tested. For the stepped spillway models of the second group the bottom slope is set to 1V:2H and 1V:3H, with two step heights of 0.05m and 0.075m for each slope. In addition, all these models are examined with a range of unit discharges typical of the skimming flow regime over stepped spillways. The numerical stepped spillway models of the first group are used to investigate the properties of the skimming flow conditions over moderate slopes. The main purpose of running the models of the

second group is to predict the maximum unit discharge above which cavitation could occur over moderate slope stepped spillways.

The 2D SPHysics code applied in this study is validated against the experimental results of two laboratory models conducted on: 1) broad crested weirs by Hager and Schwalt (1994); and 2) stepped spillways by Meireles et al. (2009). To do so, the convergence analysis is performed to: 1) select the most efficient numerical SPH techniques provided by the SPHysics code; and 2) to optimize the particle size. The aim of the convergence analysis is to obtain accurate results with less computational effort. The validation consists of comparing the computed and corresponding measured results in terms of the position of free surface, velocity profiles at different sections, and the pressure at different points along the broad crested weir. Despite the occurrence of some minor discrepancies between the computed and measured results, the overall comparison is good and demonstrates the ability of the numerical SPHysics code to predict the flow field variables on hydraulic structures.

The validated code is then applied on the numerical stepped spillway models of both groups prepared in the present work. This study provides new insights into the hydraulics of stepped spillways having bottom slopes typical of embankment dams. The effects of the step height, chute slope and step shape on the characteristics of the skimming flow condition in the non-aerated flow region are presented and explained. The computational results obtained in this study highlight that along with the unit discharge, the step height, chute slope and step shape are also important factors needing to be considered in determining the position of the inception point of air entrainment on moderate slope stepped spillways. Two separate relationships are presented which can be used to determine the location of the free surface aeration along the chute slope for the horizontal and upward inclined steps. In addition, the computational results of this investigation indicate that the upward inclined steps are more efficient than the conventional flat steps, not only in improving the energy dissipation rate, but also in decreasing both the length of the non-aerated flow region, which is prone to cavitation damage, and the mean flow velocity of the overflowing water. Finally, the current work presents the maximum unit discharges which assure the safety of steps against cavitation damage for various step heights and embankment chute slopes.

CHAPTER ONE

INTRODUCTION

Chapter One: Introduction

1.1. Embankment dams and potential for cavitation damage

Water is one of our most important natural resources, and has substantially contributed in the cultural development of mankind throughout the ages. Over the past few decades the rate of water consumption has considerably increased due to the abrupt changes in climate and rapid growth in global population. From the hydraulic perspective one possible way in which to meet this demand is to store runoff water from the seasonal rains, through building ponds and dams, and using it during drought seasons. This has motivated hydraulic engineers to design new dams and improve the performance of existing dams. ICOLD (1997) reported that as of 1995, there were about 145,000 dams of different sizes around the world, of which 93% were small sized dams. The dam size here refers to both its height and the volume of the reservoir. Accordingly, ICOLD has classified dams of heights lower than 15m and reservoir storage of less than 1 million m^3 as small dams. Globally, there is a preference for small sized dams, which might be due to the cost effectiveness and the time of construction needed for building such kind of dams.

The spillway is the major part of the dam, designed mainly to ensure the safe release of excess water from the dam reservoir to the downstream area, usually the river on which the dam has been constructed, during times of peak flow. Flow over spillways possesses relatively high kinetic energy and is generally characterized by high velocity (Chow, 1959). This is because the spillway conveys water from the dam reservoir through the spillway crest, the highest part of the spillway, to the toe, the lowest part situated at the end of the spillway, along the downstream slope. This high flow velocity usually results in a pressure drop to nearly the vapour pressure of water, in many cases to sub-atmospheric pressure, especially in the vicinity of the spillway surface. The combined high velocity and low pressure of the flow may cause cavitation and consequently serious damage to the spillway's downstream face and/or scour to the spillway base (André, 2004), which often leads to entire dam failure especially in the absence of efficient protection measures (Chanson, 2002).

Dams can also be classified into two main types depending on the material used in the construction:

1. Embankment or fill-type dams: in which the main body of the dam is usually built with natural materials such as earth and rock, which are possibly available in the dam site. The crest of this dam is often straight and long, typical of the broad crested weir type.

Figure 1.1. The dam at Bewl water in Kent, UK is an example of an embankment dam.

2. Gravity concrete dams: concrete has recently been used as a main construction material of this type of dams. However, masonry was also used in the construction of this kind of dam before the development of cementitious material. The crest of its spillway is usually designed to form an ogee shape (Chanson, 2007).

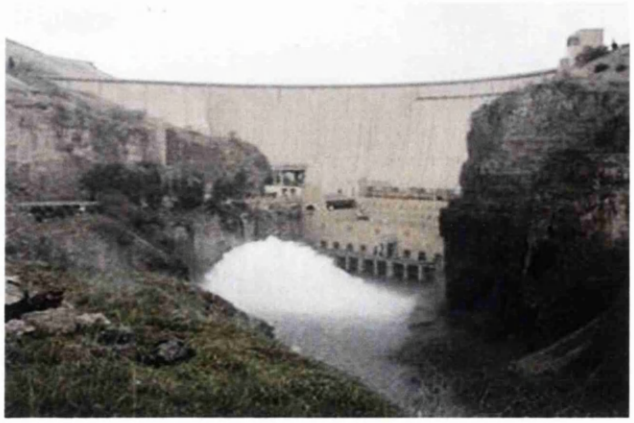

Figure 1.2. Dokan dam in Kurdistan region of Iraq is an example of the gravity dam type.

Although there are many factors that influence the selection of the dam type (Khatsuria, 2005), embankment dams lower than 30m are the most common type for constructing small dams due to the low cost and the ease of design and construction (André, 2004). However, the records of global dam failures have demonstrated that embankment dams are more likely to fail than concrete dams. Up to 1925, in Great Britain 13 of the 14 dam failure disasters were of the embankment dam type. In addition internationally, 12 embankment dams from a total of 16 dams have failed since 1925.

Needless to say spillways are usually equipped with mechanical devices, such as gates, and known as controlled or gated spillways. Controlled spillways are possibly safer than uncontrolled spillways as the gate could regulate both the flow rate over the spillway and the water depth in the dam reservoir. Indeed, water can overtop the dam and flow over its downstream face during severe flood events when:

1- the storage capacity of the dam reservoir is not sufficient to impound surplus water;
2- the spillway itself does not have sufficient capacity to pass the water;
3- there is a fault in the spillway gates so that water cannot be released.

Embankment dams are more prone to damage than gravity dams during an overtopping event because of the nature of the material covering the face of the downstream slope, especially when it is poorly compacted. In fact, 40% of embankment dam, having heights lower than 30m, failures around the world were due to overtopping (André, 2004). The re-evaluation of the storage of most existing dams has shown that a great number of embankment dams were designed with capacities lower than the actual design capacity required to pass the flooding water. This has been attributed to the fact that these dams were built in a period when the recent advanced technological instruments for measuring and recording the required hydrological data were lacking (Chanson, 2002; André, 2004; Gonzalez, 2005).

1.2. Stepped spillways as energy dissipators and protection measures

Stilling basins have been frequently constructed at the downstream of smooth spillways to dissipate the residual energy of the overflowing water and to protect the

toe base against damage caused by scouring. Despite the fact that constructing such a basin significantly increases the total cost of the whole structure, cavitation or erosion damage depending on the material covering the spillway surface may still occur. This is possibly because the spillway surface along the downstream slope is not rough enough to decelerate the high flow velocity and hence the flow still possesses high kinetic energy. A number of protection techniques have been recently developed to armour the downstream slope of spillways and embankment dams against potential damage caused by the high energy of overtopping water (Chanson, 2007). The most widely used techniques are:

a- Riprap: in which two or more layers of filters and rocks of relatively large sizes are placed on the downstream face of the spillway slope, as shown in Figure 1.3. The size and distribution of the rocks depend on the discharge and spillway slope. This kind of protection system is often designed with cofferdams and small dams (André, 2004). The main advantage of this technique is the ease of repairing the system by just replacing the rocks on site. However, the need for large size rocks may limit the use of this kind of protection system everywhere.

Figure 1.3. Riprap protection over a downstream slope

b- Pre-cast concrete blocks: As shown in Figure 1.4, concrete solid blocks of large sizes and various shapes are introduced into the downstream slope. The stability of the downstream slope depends on the weight of these blocks (Baker, 1997). Although this kind of protection is efficient in terms of the energy dissipation, it is not cost effective as the design requires blocks of large sizes.

Figure 1.4. Overflow embankment spillway of Zaraysk dam in Russia made of precast concrete blocks (from Chanson, 2000b)

c- Gabions: Figure 1.5 is an example of this type of protection system, which consists of a number of rectangular baskets of connected edges. These baskets are filled with angular rocks of small sizes. This technique is characterized by its simplicity of construction and cost effectiveness. However, the maintenance of this type of protection system is expensive, as repairing and replacing the damaged baskets after overtopping events would not be an easy task.

Figure 1.5. Downstream slope protection by gabion

d- Stepped spillways: This consists of a series of steps fitting into the spillway profile from the crest to the toe, as shown in Figure 1.6. These steps are able to slow down the velocity of the overflowing water. The following section provides more detail of this kind of protection system.

Figure 1.6. Melton dam stepped spillway in Australia (from Chanson, 2000b)

Stepped spillways have become the most efficient technique due to their simplicity in design and ease of construction (Chanson,1994). Additionally, the recent advances in the design technology of construction materials such as roller compacted concrete (Boes et al. 2002) have popularized this technique over the past few decades. In fact, this type of concrete is a mixture of cement and the local aggregates available at the dam site. Moreover, the equipment traditionally used in earthworks can be utilized to spread and compact this kind of concrete. Furthermore, its compatibility with the construction of stepped spillways may be another positive point of the roller compacted concrete as it can be placed in such a way to provide the staircase shape to the downstream slope (André, 2004; Gonzalez, 2005).

The use of stepped spillways goes back more than 3500 years, when the oldest structure of this type was built in Akarnania, Greece (Chanson, 1995). Typically, steps of different dimensions, configurations and arrangements are introduced into the surface of the conventional smooth spillway and arranged in such a way to provide a staircase shape profile from top to bottom. These steps play a dual role by:

1. Generating high levels of turbulence, which increases the energy dissipation rate of the overflowing water. This decreases the need for a large stilling basin at the end of the spillway.
2. Increasing the surface roughness, which accelerates the growth of the turbulent boundary layer and hence the process of self-aeration. This may effectively protect the spillway surface from cavitation damage.

In addition, stepped spillways can also be applied over the top of existing embankment dams to increase their capacities, thanks for the steps which could provide additional stability to the downstream slope (Boes, 2000; Chanson, 2002). This technique might be practically and economically the most feasible alternative solution for increasing the capacity of existing spillways or embankment dams (Frizzell & Mefford, 1997; Hunt et al. 2008). Over the past three decades, stepped spillways have been implemented in the design of a number of embankment dam spillways (Chanson, 2002). Moreover, stepped spillways were designed to act as a secondary spillway for nearly two-thirds of the dams constructed in the USA during the 1990s (Ditchey & Campbell, 2000).

Depending on the discharge and step geometry, flow over stepped spillways has been classified into three main regimes: nappe flow which occurs with low flow rates, skimming flow dealing with relatively high discharges and transition flow with moderate discharges. The flow at each regime behaves differently, and is described in more detail in Section 1.3.1. However, modern stepped spillways are often designed to operate under a skimming flow regime (Chanson, 2002; Meireles et al. 2009).

Finally, it is also worth noting that although horizontal steps have been commonly used to fit the downstream slope of spillways, the performance of upward inclined steps (Essery & Horner, 1969; Peyras, 1992; Chinnarasri et al. 2004; Barani et al. 2005; Chinnarasri et al. 2006) end sills and blocks (André, 2004) and longitudinal vanes (Gonzalez, 2005) have also been examined to enhance the energy dissipation mechanism and accelerate the self-aeration process. Figure 1.7 shows various step shapes and arrangements which have been used so far in the design of stepped spillways.

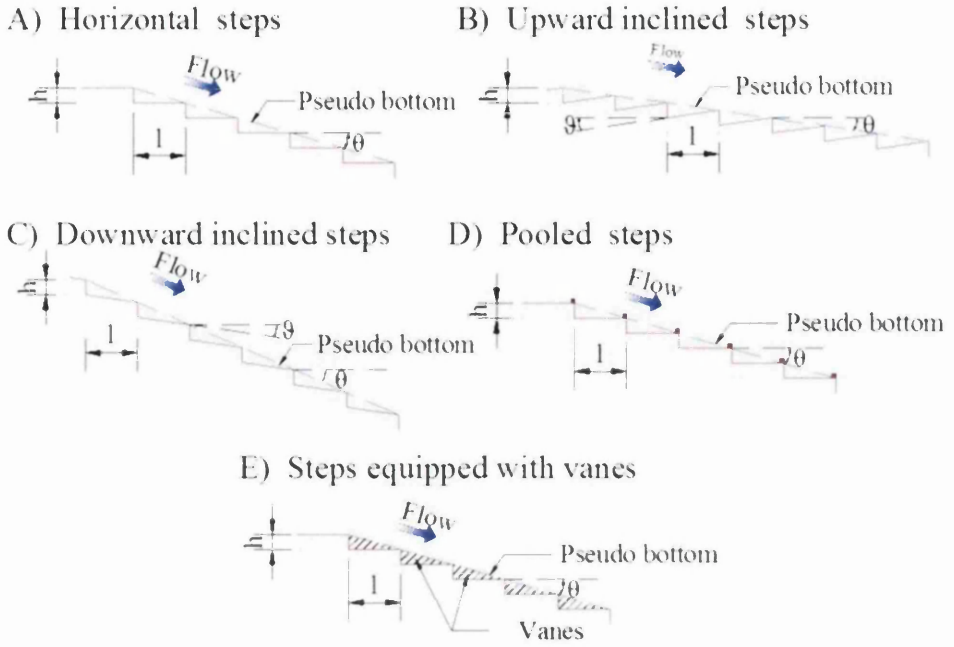

Figure 1.7. Stepped spillways with different step shapes and configurations.

1.3. Hydraulics of stepped spillways

The present study focuses on the characteristics of the skimming flow regime in the non-aerated flow region over stepped spillways having slopes typical of embankment dams. To make this issue more understandable it is essential to start with the features of flow over stepped spillways. The following subsections present the hydraulics of stepped spillways including the flow regimes, the onset of flow regimes, and the typical flow regions of skimming flow condition over stepped spillways.

1.3.1. Flow regimes over stepped spillways

Based on the discharge and step geometry, three different flow regimes have been recognized over a stepped spillway, namely nappe, transition and skimming flow regimes. Although the flow at each regime behaves differently, it is generally characterized by high levels of turbulence and intense air bubble entrainment (Chanson, 2007). Detailed characteristics of the flow regimes are individually described below.

1.3.1.1. Nappe flow regime

This regime often takes place with small flow rates and low/wide steps. As can be seen in Figure 1.8a, at this regime the flow along the chute is characterized by: a series of over-falls; a free falling nappe at the upstream end of each step; a pool of recirculating water with an air pocket above and a hydraulic jump (André, 2004; El-Kamash et al. 2005; Toombes & Chanson, 2008) downstream the impacting point of the jet on the tread of each step (Chamani & Rajaratnam, 1994; Chanson, 1996; Toombes, 2002). In nappe flow conditions air can enter the flow on each step due to the intersection of the free falling nappe with the recirculating pool on each step. The formation of the hydraulic jump on each step is mainly dependent on the discharge of the nappe flow condition. In addition, in this regime if the hydraulic jump forms, it could significantly increase the dissipation rate of the overflowing energy (Chanson, 1994).

Practically, the design of a stepped spillway to operate typically for this type of flow regime is appropriate for very low dams and flat spillway slopes such as those found in water treatment plants. This flow regime is outside of the scope of the present study.

1.3.1.2. Transition flow regime

This regime often occurs with moderate discharges. The flow in this regime has been investigated only rarely, therefore the detailed information about this regime is limited. Elviro and Mateos (1995) and Yasuda and Othsu (1997) were the first who revealed the existence of this flow condition on stepped spillways. Basically, the flow is chaotic due to the presence of spray and splash. The height of splashing water droplets is about 3 to 8 times the step height, especially downstream of the inception point (Chanson & Toombes, 2004). The increase of flow discharge gradually changes the flow condition from nappe to skimming regime (André, 2004). For this regime, the nappe flow condition features at some steps, while rotating vortices appear inside the other steps, which refer to the skimming flow regime (Gonzalez, 2005). Figure 1.8b illustrates the transition flow regime, which is not investigated in the present work, over a stepped chute.

1.3.1.3. Skimming flow regime

For relatively high discharges, the flow skims over the pseudo bottom as a coherent stream and is cushioned by re-circulating eddies underneath (Chanson, 2002). These eddies are trapped inside the steps and rotated in a rounded triangular shape (Diez-Cascon et al. 1991; Chanson 1994; Chamani & Rajaratnam 1999; Pegram et al. 1999). The term pseudo bottom refers to a hypothetical line parallel to the chute slope passing through the step outer edges (Chanson, 1994). Figure 1.8c presents a skimming flow regime over a stepped spillway. The free surface flow in this flow regime is smooth, wavy and glassy (Chanson, 2002). Air entrainment starts at a point on the free surface along the chute slope when the turbulent boundary layer fully develops and reaches the surface. Furthermore, the transmission of shear stress from the flowing fluid sustains the vortices that are considered to be the predominant factor of the energy dissipation mechanism in this flow regime (Chanson, 2002; Gonzalez, 2005). Indeed, modern stepped spillways are currently designed to operate under the skimming flow regime (Chanson, 2002; Gonzalez, 2005; Amador et al. 2006).

The present study looks at the properties of the skimming flow regime over stepped chutes having moderate slopes. This is mainly to provide the designers new knowledge on the performance of small embankment dams when water with high discharges corresponding to the skimming flow conditions which is typical to a flood flow event flows over the downstream slope.

1.3.2. Onset of skimming flow regime

Predicting the flow regime is the key element in the design of stepped spillways, as the flow pattern of each regime is completely different. Numerous experimental studies have been conducted to set the boundary between the flow conditions mentioned above. Since the current work focuses only on the characteristics of skimming flow, this section presents a number of published experimental works conducted previously to indicate the onset of this regime. However, it might be difficult to determine the limits of each flow regime analytically due to the complexity of the flow structure of each flow condition. Although dimensional analysis has demonstrated that the prediction of the flow regime is mainly dependent

on the discharge and the slope (Essery & Horner 1978; Peyras et al. 1992), most of the equations available in the literature are empirical. These equations have been developed based on the visual interpretation of the attainment of the features for each flow condition.

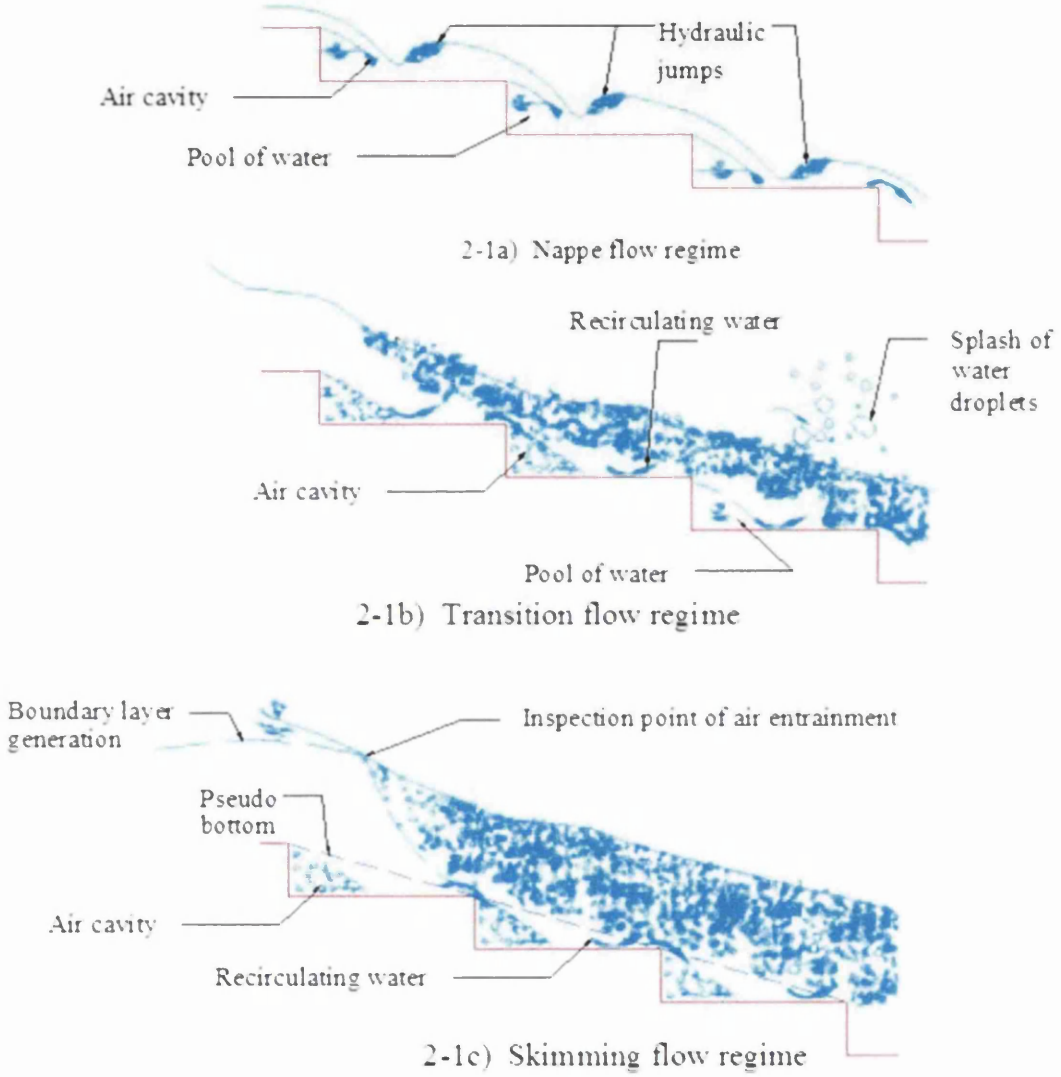

Figure 1.8. Typical flow regimes over stepped spillways (from Gonzalez, 2005).

Rajaratnam (1990) was the first to define the onset of skimming flow in terms of the dimensionless parameter h_c/h_s where h_c, is the critical flow depth on the weir crest and, h_s is the step height. From his experimental tests on stepped spillways of slopes, defined by h_s/l_s, where l_s is the step length, ranging between 0.4 and 0.9, he observed

that the skimming flow condition was achieved when the value of h_c/h_s was greater than 0.8.

Chanson (1994) suggested the following equation to predict the onset of skimming flow for $0.2 < h_s/l_s < 1.25$ based on fitting the experimental data:

$$\frac{h_c}{h_s} = 1.06 - 0.456\frac{h_s}{l_s} \tag{1.1}$$

In addition, the following two equations were proposed by Yasuda and Othsu (1999) to predict the upper limit of the nappe flow regime and the lower limit of the skimming flow regime, respectively, for stepped spillways of slopes lower than 55°:

$$\frac{h_c}{h_s} = \frac{\left(1.4 - \frac{h_s}{l_s}\right)^{0.26}}{1.4} \tag{1.2}$$

$$\frac{h_c}{h_s} = 0.826\left(\frac{h_s}{h_s}\right)^{-0.165} \tag{1.3}$$

Furthermore, Chamani and Rajaratnam (1999) developed the following equation to determine the onset of the skimming flow regime by assuming that the jet of the skimming flow is the same as the bed slope of the spillway:

$$\frac{h_s}{l_s} = \sqrt{0.89\left\{\left(\frac{h_c}{h_s}\right)^{-1} - \left(\frac{h_c}{h_s}\right)^{-0.34}\right\}} - 1 \tag{1.4}$$

Moreover, Chanson (2002) stated that the onset of the skimming flow regime can be predicted from the following equation:

$$\frac{h_c}{h_s} = 1.20 - 0.325\frac{h_s}{l_s} \tag{1.5}$$

The derivation of the above equation is based on the re-analysis of a large number of experimental observations regarding the change of flow conditions.

The experimental results of Boes and Hager (2003) on stepped spillways of slopes of 30°, 40°, and 50° showed that the following equation can be used to predict the onset of skimming condition:

$$\frac{h_c}{h_s} = 0.90 - 0.14\frac{h_s}{l_s} \tag{1.6}$$

The above equation agrees well with the experimental data of Rajaratnam (1990), Stephenson (1991), Chanson (1996), Tatewar and Ingle (1999), Yasuda and Ohtsu (1999) and Matos (2001) for slopes steeper than 25° and flatter than 55°.

Chinnarasri et al. (2004) studied the effect of the step inclination on the upper limit of nappe flow and the lower limit of skimming flow over three different slopes 30°, 40° and 50°. For this purpose three step heights and step inclinations were examined with a range of flow discharge ranging from 0.01 to 0.17m^2/s. They observed that the upper limit of nappe flow was independent of the step inclination, while the lower limit of skimming flow was slightly increased as the step inclination was increased. However, they presented the following equation to predict the minimum critical depth required for the onset of skimming flow on chutes with inclined steps for ($0.1 \leq l_s/h_s \leq 1.73$):

$$\frac{h_c}{h_s} = (0.844 + 0.003\vartheta)\left(\frac{h_s}{l_s}\right)^{(-0.153+0.004\vartheta)} \tag{1.7}$$

in which ϑ is the upward inclination of the step with the horizontal face.

André (2004) developed the following equations to define the upper limit of the nappe flow and the lower limit of the skimming flow regime respectively in the presence of micro-roughness elements such as endsills and blocks. The experiments were conducted on gated stepped spillways of two slopes of 30° and 18.6° and one step height of 6cm.

$$\frac{h_c}{h_s} = \left(\frac{0.743}{\eta_m}\right)\left(\frac{h_s}{l_s}\right)^{-0.244} \tag{1.8}$$

$$\frac{h_c}{h_s} = 0.939\eta_m\left(\frac{h_s}{l_s}\right)^{-0.364} \tag{1.9}$$

where η_m is the correction coefficient and depends on the arrangement of the roughness elements along the chute slope and across the chute width. The following equation was proposed to determine this parameter:

$$\eta_m = -\ln(m) + 1 \tag{1.10}$$

where m is a dimensionless parameter that determines the proportion of the macro-roughness elements on the steps. In other words it is the ratio between the number of the micro-roughness elements and the number of steps.

1.3.3. Typical flow regions over steeped spillways in the skimming flow regime

When the skimming flow condition occurs on a stepped spillway, distinct regions can be clearly observed as displayed in Figure 1.9. There may be three or four regions depending on the chute length. The flow properties in each flow region are described as follows:

1- As water flows down a stepped spillway, the flow accelerates and the boundary layer develops rapidly next to the crest, which slightly affects the free water surface. This reach is known as the developing or non-aerated flow region and the flow depth is known as the clear water depth. In this region the flow depth decreases and the flow velocity along the chute slope increases. The free surface flow appears as smooth, wavy and glassy in this region.

2- Natural air entrainment or self-aeration initiates at a point on the stepped spillway where the turbulent boundary layer is fully developed and its outer edge intersects the free surface; this point is termed the inception point of air entrainment. It is characterized by high turbulence and is the start of the apparition of "white water" on the chute (Chanson, 1994). In fact, the high level of turbulence is due to the vortices acting next to the free surface, which are responsible for controlling both the surface tension and buoyancy of the air bubbles (Chanson, 1997).

3- Downstream of this point a layer containing air and water extends the flowing fluid, which may cause a rapid increase of air concentration over a short reach, which is called the rapidly varied flow region. The flow depth

increases in this region as water mixes with air, which in turn reduces the flow velocity (Ohtsu & Yasuda, 1997).

4- A gradual change of the flow characteristics can be noticed along the rest of the chute length until the toe (Chanson, 2002). The main feature of this region is that it contains high amounts of air, which significantly contributes towards protecting the structure from the potential of cavitation damage. This region is termed as the gradually varied flow region.

5- The uniform flow region, which starts downstream of the gradually varied flow region and extends to the end of the structure. The uniformity of the flow condition has been justified on the ground that there will be a slight change in the flow properties on this reach (André, 2004). However, Chanson (2002) revealed that in order to attain the uniform flow condition on a steeped spillway, the length of its downstream slope needs to be long enough to allow the bed resistance force to counterbalance the gravitational force (Chow, 1959).

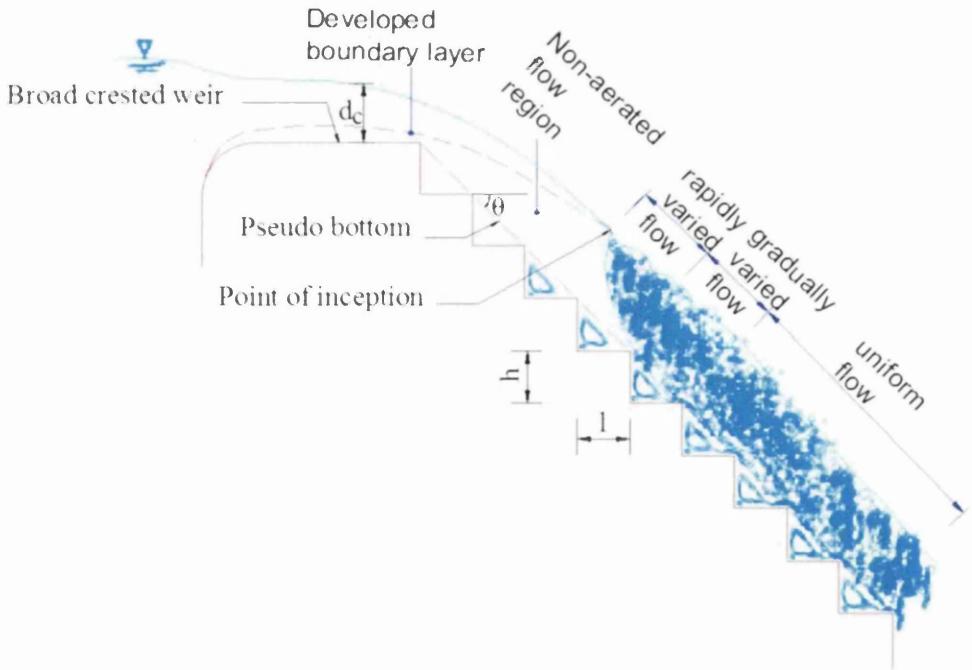

Figure 1.9. Flow regions of a skimming flow down a stepped spillway (from Gonzalez, 2005).

1.4. Stepped spillways in real applications

As mentioned earlier, stepped spillways are characterized by their ease of design and construction, time and cost effectiveness and compatibility with the construction techniques of RCC. These features have attracted the attention of engineers to design this kind of hydraulic structure in different engineering disciplines, such as:

1- Flood protection systems for dams, spillways and weirs.
2- Energy dissipators for spillways and steep channels.
3- Auxiliary spillways for existing embankment dams, such as Monksville dam in the USA (Chanson, 1994).
4- Water plant treatments, such as Murgon and Chinchilla weirs in Australia (Gonzalez, 2005).
6- Fountains in public places, such as in Brisbane, Hong Kong and Taipei (Chanson, 2002).

1.5. Problem statement

Although air plays a vital role in protecting the surface of this structure against cavitation damage, it might be entirely absent or insufficiently present along the upstream portion of the chute, especially when water flows with high rates, as is typical of skimming flow conditions. This portion is termed the non-aerated flow region; it starts at some distance from the spillway crest and extends to where the turbulent boundary layer intersects the free surface at a point on the free surface known as the inception point of air entrainment (Chanson, 2002). The remaining downstream portion of the spillway is called the aerated region. At the inception point of air entrainment the turbulence level is so high that air can enter and mix into the flow in a continuous process known as self- or natural aeration. This process provides white colouring to the flowing water, which can be clearly seen along the chute slope and across its width. The quantity of air bubbles in this region may be large enough to protect the spillway surface from cavitation damage.

Investigating the skimming flow properties in the non-aerated flow region is of major importance, especially in small embankment dams. This is because its length along the downstream slope may be not long enough to allow the self-aeration process to take place and hence sufficient amount of air required to resist cavitation

damage may not enter the flowing water. Therefore, a significant distance, if not the whole chute length, along the downstream slope might be vulnerable to such damage. To date, only a small number of studies have been conducted investigating the pressure behaviour, as a main parameter in predicting the cavitation tendency, in the non-aerated flow region on moderate slopes. Understanding the pressure pattern on the step faces under severe conditions is therefore an important aspect of improving the design of said structures. The current work is a numerical investigation which presents and describes the features of pressure flow field on the horizontal and vertical faces of steps situated in the non-aerated flow region for a wide range of slopes typical of moderate slopes.

In addition, to the best of the author's knowledge the flow properties in terms of the inception point, pressure and velocity flow fields and energy dissipation upstream of the inception point for embankment dams of slopes flatter than 27° have yet not been investigated. Therefore, the current work evaluates the effects step height and chute slope have on the behaviour of skimming flow in the non-aerated flow region over moderate slope stepped spillways.

Finally, the research on the hydraulics of stepped flow over upward inclined steps has so far been focused on the flow regimes and their contribution to energy dissipation over stepped spillways having slopes steeper than 30°. Hence, no detailed information has until now been available regarding the skimming flow properties in the non-aerated flow region over embankment dams using upward inclined steps. Therefore, this work looks at the characteristics of the inception point of self-aeration and the velocity and pressure flow fields on upward inclined steps under the skimming flow condition over moderate slope stepped spillways.

1.6. Motivation

The author is motivated to conduct the present investigation as he hypothesizes that the hydraulics of stepped spillways, especially on moderate slopes typical of embankment dams, in the non-aerated flow region have not yet been studied in terms of the pressure variation on steps. The pressure field is the key factor for predicting the part of the spillway subject to cavitation risk which is linked in the present work to the cavitation index and the sub-atmospheric pressure. Applying a new particle based method to this problem is another motivation point. This is because up to now

only grid-based numerical methods have been applied to simulate the flow properties over stepped spillways and the application of a particle-based numerical method is completely lacking. The reason behind applying the particle-based method in this investigation is that numerical simulations with grid-based methods based on the Lagrangian approach suffer from mesh distortion and therefore it is not easy to handle problems associated with large deformations. Moreover, it is difficult to 1) predict the elevation of free surface; 2) model irregular geometries and 3) record time history of flow field variables when an Eulerian approach method is used as the numerical simulation technique. The particle-based method is a purely mesh free Lagrangian method so that the mesh free particle property allows one to address the problem of large deformations, as no meshes or grids need to be predefined. In addition, the Lagrangian property allows recording the evolution of the flow properties over and inside the steps with respect to time. Also, the author is motivated to study the influence of upward inclined steps on the growth of the turbulent boundary layer and the process of self-aeration. Moreover, the upward inclined step may significantly increase the rate of energy dissipation and reduce the velocity of the overflowing water along the non-aerated flow region. This has motivated the author to investigate how this kind of step configuration could reduce the risk of cavitation on moderate slope stepped spillways.

1.7. Objectives of the present study

The present investigation is a numerical study conducted on stepped spillways having three different bottom slopes 1V:2H, 1V:2.5H, and 1V:3H typical of embankment dams using conventional horizontal and upward inclined steps. Furthermore, three step heights are used with horizontal steps, providing different numbers of steps for each slope, whereas one step height with three different step inclinations are examined with upward inclined steps. All these are tested in the non-aerated flow region under a range of discharge typical of the skimming flow condition.

The main objectives of the present work are:

1- To investigate the effect of the step height and chute slope on the behaviour of skimming flow over horizontal steps in terms of the position of free

surface and velocity profiles at different sections, and the energy dissipation rate.

2- To investigate the effect of step inclinations and chute slope on the behaviour of skimming flow over inclined steps including the position of free surface and velocity profiles at different sections, and the energy dissipation rate.
3- To study and compare aspects of the pressure flow field on horizontal and upward inclined steps to predict the maximum permissible discharge above which cavitation could occur on moderate slope stepped spillways.
4- To determine and compare the position of the inception point of free surface aeration on the horizontal and upward inclined steps.
5- To investigate the performance of the SPH model as a new technique of computational fluid dynamics method in predicting the properties of skimming flow upstream of the inception point of air entrainment.
6- To formulate the numerical results of the present investigation and compare with the available formulae and data of other investigators.

1.8. Thesis outline

The thesis of the present study is divided into eight chapters. The first Chapter introduces the concept of stepped spillways and states the main objectives of the present investigation. Chapter two reviews the published experimental and numerical works previously conducted for investigating the features of the skimming flow condition in the non-aerated flow regions. The mathematical model using the smoothed particle hydrodynamics is illustrated in Chapter three. It also explains the main features of the SPHysics numerical code and shows the various numerical techniques implemented in this work. The next Chapter describes the setup of the numerical models and shows the way by which the code is calibrated. Chapter five presents and discusses the main results obtained in the present study in terms of the position of the free surface elevation and the location of the inception point of free surface aeration. The computational velocity profiles and energy dissipation rates obtained in the current work are presented in Chapter six. Chapter seven deals with the pressure distribution on both step faces, and evaluates the potential of cavitation damage on moderate slope stepped spillways. Finally, the main conclusions and suggestions for further investigations are summarized in Chapter eight.

CHAPTER TWO

LITERATURE REVIEW

The current work is a numerical investigation which is conducted to characterize the skimming flow regime in the non-aerated flow region on stepped spillways having moderate slopes typical of embankment dams. It is mainly focused on predicting the maximum design discharge above which cavitation can occur in this kind of hydraulic structure. Also, it looks at the effects of various factors such as the step geometry, for instance step height, step shape, step inclination and the chute slope, on reducing the potential for cavitation formation. Moreover, it presents the properties of the inception point of self-aeration on horizontal and upward inclined steps over moderate slopes due to different flow rates typical of skimming flow conditions.

Flow over stepped spillways has been investigated extensively using both laboratory experiments and numerical simulations. For this reason, the review of most previously published works is divided herein into two parts: The first part begins with a comprehensive review of the experimental works for flow over stepped spillways having slopes typical of embankment dams. The second part presents a number of grid-based numerical models that have been applied to simulate the flow properties over stepped spillways. However, it should be noted that the particle-based methods, utilized in the present study, have not yet been applied to flow over stepped spillways.

2.1. Experimental investigations of flow over stepped spillways

Research into flow over stepped spillways has been active since the early eighties of the last century and more specifically since the recent development of new construction materials and design technology (Chanson, 2002). The flow over stepped spillways is free surface and it is characterized by high velocity and high turbulence levels, and contains high amounts of air in the aerated flow region (Chanson, 1997). Numerous laboratory studies have been conducted to study the characteristics of the flow over stepped spillways of different slopes, ranging from flat to very steep. In addition, horizontal steps have been widely used to investigate different flow properties on stepped spillways. However, the current work focuses on

the features of the skimming flow regime on horizontal and upward inclined steps in the non-aerated flow region over stepped spillways having slopes typical of embankment dams.

The following sections review the findings of laboratory studies investigating the properties of flow over stepped spillways on horizontal, upward inclined steps and blocks. It includes the location of the inception point of air entrainment and the characteristics of skimming flow condition such as the position of the free surface, velocity and pressure distributions on the steps and amount of energy dissipation in the non-aerated flow region.

2.1.1. Inception point of air entrainment

The location of this point is necessary for the designer of stepped spillways. This is because the upstream portion of this point is likely prone to cavitation risk, while the air entering the flow at the downstream part of the inception point bulks the flow depth and therefore the height of the chute wall changes accordingly. Chanson (2002) defined the point where the turbulent boundary layer, which is developed from the upstream face of the weir, intersects the water surface on the spillway chute as the inception point of air entrainment. Based on visual observation, it corresponds to the point of the appearance of so called "white water" (Chanson, 1994; Chamani, 2000; Matos, 2000). However, Boes (2003) defined this point as that point at which the air concentration is about 1%. Indeed, researchers have not only differed in defining the inception point of air entrainment, but also in the factors influencing its location from the crest. Chanson (2002) reported that the length of the inception point depends on the discharge and step height. Meanwhile, Matos (2000) stated that both the discharge and the chute slope are important factors that should be considered in estimating the length of the non-aerated flow region. Moreover, Chamani (2000) concluded that steps along the downstream slope increase the roughness of the spillway surface and hence accelerate the growth of the turbulent boundary layer to meet the free surface much earlier compared to the smooth surface. This is because steps allow the formation of various flow structures inside the steps, including the wake, vortices and internal jet, when the mainstream of the flow hits the step tread (André, 2004).

Different empirical equations have been proposed by investigators to estimate the length to, and flow depth of, this point. Wood (1983) developed the following equation to determine the location of the point where air entrainment may start on smooth spillways:

$$\frac{L_i}{K_s} = 13.6(\sin\theta)^{0.0796} F_*^{0.713} \quad (2.1)$$

Where L_i is the length to the inception point of air entrainment, θ is the chute slope, K_s is roughness height measured perpendicular to the flow direction given by: $K_s=h_s cos\theta$; h_s is the step height and, F_* is the Froude number based on the roughness height deduced from:

$$F_* = \frac{q}{\sqrt{g \sin\theta K_s^3}} \quad (2.2)$$

where q is unit discharge and g is the gravitational acceleration.

A wide range of the model-prototype experimental data of Sorenson (1985), Beitz & Lawless (1992), Frizzell & Mefford (1991), Bindo et al. (1993), and Tozzi (1994) was re-analysed by Chanson (1996) and the following two equations were proposed to predict the length to and the depth of flow at the point of inception for stepped spillways having slopes within the range of $27° < \theta < 59°$:

$$\frac{L_i}{K_s} = 9.719(\sin\theta)^{0.0796}(F_*)^{0.713} \quad (2.3)$$

$$\frac{d_i}{K_s} = \frac{0.4034}{(\sin\theta)^{0.04}}(F_*)^{0.592} \quad (2.4)$$

Combining Equation (2.3) and Equation (2.4) yields:

$$\frac{d_i}{L_i} = 0.0611(\sin\theta)^{0.133}.\left(\frac{L_i}{K_s}\right)^{-0.17} \quad (2.5)$$

In fact, Chanson (1994) reported that great care should be taken when applying these equations in the design of stepped spillways of slopes flatter than 27°. The experimental results of Hunt et al. (2010) showed that Equations (2.3) and (2.4) can

be applied on stepped spillways of slopes steeper than 1V:4H when F_* is larger than 10. However, the present study deals with a range of skimming flow discharge that posits F_* as smaller than 10. Therefore, these equations need to be modified to apply in the present study.

The experimental investigation of Boes and Hager (2003) on gated stepped flumes, with the results gathered on $26° < \theta < 55°$ crested stepped spillways, produced the following equations:

$$\frac{L_i}{K_s} = \frac{5.90\,(\cos\theta)^{1/5}}{\sin\theta}\,F_*^{4/5} \tag{2.6}$$

$$\frac{d_i}{h_s} = 0.40\;F_S^{0.60} \tag{2.7}$$

where F_s is the step Froude number calculated from:

$$F_S = \frac{q}{\sqrt{g\sin\theta h_S^3}} \tag{2.8}$$

It should be noted that the equations proposed by Boes and Hager (2003) were developed to define the location of the air inception point at a section close to the crest, based on the condition that the air concentration in water needs to be at least 1%. In addition, they neglected the effects of the turbulent boundary layer in this issue. Following Chanson (2002), in the present work the development of the turbulent boundary layer is considered as the main factor in predicting the location of the inception point.

André (2004) conducted experiments on horizontal steps over two chute slopes (30° and 18.6°) and one step height 0.06m, and proposed the following equation to determine the location of air entrainment:

$$\frac{L_i}{K_S} = \frac{8.0}{\tan\theta}F_{*,\theta}^{0.730} \tag{2.9}$$

where $F_{*,\theta}$ is the modified roughness Froude number in terms of the chute slope, as proposed by Chow (1959):

$$F_{*,\theta} = \frac{q}{\sqrt{g\cos\theta K_S^3}} \tag{2.10}$$

Also, the same author developed the following equation to introduce the effect of micro-roughness elements, such as endsills and blocks, on the growth of the turbulent boundary layer for $F_{*,\theta} > 4$:

$$\frac{L_i}{K_s} = 4.1(F_{*,\theta} - 0.58) \quad (2.11)$$

The author further observed that when the endsills were placed over every step and $m=4$, where m is the concentration of the blocks across the chute width, the inception point of air entrainment was displaced further upstream compared to other arrangements of the micro-roughness elements used in his experimental work. The experimental results of this work confirm that the shape and dimension of the steps have a significant effect on the coordinates of the inception point of air entrainment. This has encouraged us to conduct the current work in order to see how upward inclined steps with different inclinations deal with this issue.

Meireles et al. (2009) studied the skimming flow regime in the non-aerated flow region down a 26.6° stepped spillway. They obtained the following two equations, which agree well with the experimental data of other investigators:

$$\frac{L_i}{K_s} = 5.25F_*^{0.95} \quad (2.12)$$

$$\frac{d_i}{K_s} = 0.28F_*^{0.68} \quad (2.13)$$

It should be noted that the above two equations were obtained from experimental data gathered on a laboratory model in which only one step height and one chute slope were examined.

From the aforementioned literature one can conclude that although different empirical formulae have been proposed to predict the coordinates of the inception point, the dependable criteria for embankment dams is still lacking. Generally, Lane (1953) from his experimental data on small spillways concluded that the flow properties at this point depend on the discharge and step geometry, including the height, slope and shape. In the present study three chute slopes typical of embankment dams and three step heights for each slope are examined to investigate the influence of the spillway slope and step height on the inception point of air entrainment due to various discharges typical of skimming flow condition. Also, upward inclined steps of identical height but with three different slopes are used to

investigate the influence of this type of step configuration on the development of the boundary layer and the properties of the skimming flow condition.

2.1.2. Pressure flow field in the non-aerated flow region

As described earlier, the turbulent boundary layer grows as the flow attaches the spillway body at the upstream face of the weir crest. The thickness of this layer increases along the spillway slope until it meets the water surface at a certain point. At this point, which is known as the air entrainment inception point (Chanson, 2002), air continuously enters the flow naturally and this mechanism is termed self-aeration. In fact, this point divides the chute length into two main regions: The first is the non-aerated or black water region, as air has yet not entered the flow. This region is located between the upstream face of the weir crest and the inception point of air entrainment. The second is the aerated region where white water can be clearly seen across the chute width and extends along the chute slope until the toe.

Self-aeration plays a vital role in providing air to the spillway surface in the downstream region, which in turn eliminates or at least reduces the damage caused by cavitation. However, the upstream region is potentially more prone to cavitation than the downstream region, due to the lack of sufficient air content in the flow compared with that in the aerated region. Peterka (1953) documented that the presence of about 5 to 8% of air in the flow close to the spillway surface might be enough to prevent damage associated with cavitation. In fact, the increase of the flow velocity in the non-aerated flow region close to the inception point of air entrainment is so rapid that the pressure could drop to zero or/and negative pressure values close to the step's outer edge and thus cavitation may form. Despite the importance of this fact, little attention has been paid to this issue, especially for flow over stepped spillways of moderate slopes. This section reviews the most important previous experimental works conducted on stepped spillways investigating the pressure pattern on moderate slopes typical of embankment dams.

The main focus of the experimental work of Frizzell and Mefford (1991) was to predict whether cavitation can occur, due to the drop of pressure to sub-atmospheric values, in flows over stepped spillways. Experiments were performed on two stepped spillway models built on 1V:2H and 0.8V:1H sloping flumes, and examined for various heads. The main finding of this study was that the region close to the top of

the return eddy may be prone to cavitation damage if it occurs. However, the location of potential cavitation in relation to the inception point of air entrainment was not specified.

Ohtsu and Yasuda (1997) conducted a systematic series of experiments on a wide range of sloping stepped spillways. Their study focused mainly on the characterization of the flow conditions, including nappe, transition and skimming flow, based on the pressure measurements at the step corners. The skimming flow was described as the condition of eddy formation inside the step cavity upstream of the impinging point of the jet. It should be noted that in their study no observations were made regarding pressure variation on the vertical face of the steps located in the non-aerated flow region.

An experimental investigation was carried out by Frizzell and Renna (2011) to study the potential of cavitation damage on stepped spillways of two different slopes; one was typical of embankment dams 1V:2.48H and the other corresponded to the gravity dams 2.48V:1H. The roughness height in both cases was 0.05m. In their study, the authors used the cavitation index number to characterize the potential of cavitation along the chute slope. The cavitation index may be defined by the following equation:

$$\sigma = \frac{2(P_o - P_v)}{\rho V_o^2} \tag{2.14}$$

where σ is the cavitation index, P_o and P_v are respectively the reference pressure and the vapour pressure of water at a given temperature, ρ is the density of water and V_o is the reference velocity.

The experimental results of the moderate slope collected in the low ambient pressure chamber revealed that: cavitation is likely to form in the absence of aeration; with a cavitation index of 0.6-0.7 cavitation bubbles could occur along the pseudo bottom; the number of cavitated bubbles significantly increased and appeared close to the step tips as the cavitation index decreased. From their research one can conclude that 0.6 can be considered as the inception cavitation index underneath which cavitation damage can take place on stepped spillways of moderate slopes. However, Frizzell and Renna (2011) in their study didn't specify the value of the flow velocity that caused cavitation to form.

From the above it is clear that the investigation of cavitation formation, especially in the non-aerated flow region under skimming flow conditions over stepped spillways of moderate slopes, is a key issue for improving the design of these structures. The current study focuses on the pressure variation on both the horizontal and vertical step faces under a range of discharges typical of skimming flow, down three different slopes typical of embankment dams. This allows us to determine the maximum discharge above which cavitation can form based on the critical cavitation index on different moderate slopes and step heights. Also, this work looks at whether upward inclined steps could increase the permissible velocity/ discharge responsible of the cavitation damage on horizontal steps.

2.1.3. Flow over stepped spillways with upward inclined steps

As mentioned earlier, steps have the ability to reduce the energy dissipation mechanism and accelerate the self-aeration process when they are introduced into the face of the downstream slope of the structure. Although horizontal steps have been commonly and widely used in the design of stepped spillways, different step shapes, such as inclined steps, blocks, endsills and vanes, have also been examined. Essery and Horner (1978) reported that with the same chute slope, step size and discharge, the design of stepped spillways with inclined steps might be more economical than that with horizontal steps. This is because the inclined steps lessen the total number of steps needed to fit the downstream slope compared to the conventional horizontal steps. The following presents a number of experimental published works previously conducted on various step configurations.

According to Horner (1969) the flow over inclined steps was classified to three main conditions, namely; subcritical, transition and supercritical. The occurrence of each flow condition depends largely on the discharge, which varies from small, via intermediate to high flow rates respectively. However, Chinnarasri and Wongwises (2004) classified the flow over the inclined steps into three flow regimes similar to those observed on horizontal steps. They found that the step inclination with the horizontal has a great influence on each flow condition. Despite the fact that the upward inclined steps is believed to perform better than the other step configurations, such as horizontal, blocks and endsill, in terms of the energy dissipation rate, Chinnarasri and Wongwises (2006) revealed that the energy

dissipation rates obtained with the endsill were higher compared to the upward inclined steps. In contrast, Barani et al. (2005) observed that the upward inclined steps produced higher energy dissipation rates compared to the endsills and horizontal steps.

It can be observed that only a small number of experiments have been performed to deal with the hydraulics of flow over stepped spillways with inclined steps. Also, it is obvious that these studies were focused on two points: 1) to identify the flow condition or 2) to examine their efficiency to reduce the energy of the flow. In addition, these findings were obtained from experimental studies conducted on slopes steeper than those typical of embankment dams. Therefore, to the best of the author's knowledge, investigation of the flow properties on upward inclined steps in the non-aerated region over embankment dams is essential not only to increase their efficiency in terms of the energy dissipation, but also to optimize their ability in terms of surface protection measures. The present work looks at the effect of this kind of step configuration on the flow properties, mainly the location of the inception point of self-aeration, pressure and velocity flow fields in the non-aerated flow region due to various skimming flow discharges.

2.2. Numerical simulation of flow over stepped spillways

In this section the role of numerical simulation in solving complex engineering problems is discussed. Also, the concept of numerical simulation is described and the most common numerical methods are summarized. Moreover, the numerical models that have been applied up to now to simulate the flow characteristics over stepped spillways are reviewed.

It is worth mentioning that various grid-based numerical models have been applied to simulate the flow over stepped spillways, whereas the particle-based method, used in the present investigation, has yet not been applied.

2.2.1. Concept of numerical simulation and its role in solving engineering problems

Recent advances in computers, hardware technology and the development of robust computational fluid dynamic (CFD) software have led to numerical simulation being used widely for solving practical scientific problems. In addition to the cost and time of laboratory experiments, the direct measurement of some flow field properties needed in many of these experiments is often problematic, even when precise and developed instruments are used.

Numerical simulation expresses most of the parameters describing a certain physical phenomenon as a set of partial differential equations, describing fluid flow in space and in time. These equations are generally known as the governing equations. The key issue behind developing the numerical simulation is to convert this set of equations into not necessarily differential equations. The domain is represented by a discrete set of points and this process is known as the discretisation. The governing equations apply to continuously varying quantities. Numerical simulation represents quantities on a discrete set of points and performs an approximate solution to the continuous equations. Fluid flow problems are mostly subject to the hydrodynamic equations, which are based on the mass, momentum and energy conservation laws.

Two fundamental methods have been employed to simulate fluid flow problems numerically: grid-based methods and particle-based methods. A set of mesh or grid must be predefined in order to represent the computational domain of the problem under consideration when grid-based methods are applied. Particle-based methods by contrast represent the domain with randomly distributed particles. Each method has its own characteristics which are described in detail in the following sections. Further, the governing equations are expressed via two main approaches: the Eulerian and Lagrangian approaches. The finite element method is the typical representation of the Lagrangian approach (Liu & Quek, 2003), while the finite difference method and finite volume method, which comprise most CFD problems, are the typical representations of the Eulerian approach (Leveque, 2002). In both approaches, the Eulerian and the Lagrangian, the flow field variables are evaluated as a function of space and time. The main difference is that, in the Eulerian method fixed points are selected in the domain and the flow field variables are computed accordingly, whilst in the Lagrangian method the grids are fixed on the material and

therefore the spatial changes of the flow field variables can be evaluated (Liu et al. 2003).

Various numerical models have been applied by hydraulic researchers and engineers to investigate the hydraulic characteristics of flow over stepped spillways using grid-based methods. In the present study this problem is investigated using a particle-based method for the first time.

2.2.2. Grid-based numerical methods for simulating flow over stepped spillways

The key feature of the Lagrangian approach is the grid attachment on the material. This allows a straightforward treatment of many challenges of the computational simulation, with which the Eulerian approach might not deal effectively, such as recording time history data, tracking the interface and moving boundaries and modelling irregular and complex geometries. On the other hand, large deformations can be easily handled with the Eulerian approach, which is considered a difficult task with the Lagrangian approach (Liu et al. 2003).

The discretisation of the problem domain in this method is based on the pre-defined mesh or grid procedure in which a frame of connective points is utilized to describe the whole domain. The complexity of the hydraulic behaviour of the flow over stepped spillways, as described in the literature, might cause the numerical modelling of such types of flows be somewhat difficult. A few numerical simulations of flow over stepped spillways have been conducted using various techniques, including the finite difference method, finite volume method and the finite element method. This section presents some important studies performed in this field of hydraulic engineering.

Mehdi (1997) applied a 2D numerical model based on the finite element method to predict the position of free surface flow over the downstream slope of an ogee crest stepped spillway, by solving Bernoulli's equation. It was observed that the model provided accurate results only in the uniform flow region, which is located at the downstream portion of the structure. This was attributed to the use of the well-known U.S. Army Corps of Engineering formula for introducing the effect of air entrainment on the flow. However, Chen et al. (2002) claimed that the difference between the computed and measured data was increased at and downstream to the

section of free surface aeration. They reported that this could be due to the fact that the governing equations of the numerical model applied in their study, which was based on the finite volume method, were solved assuming that the flow is of single phase fluid. Moreover, despite the use of a transport equation to introduce the effect of air in the fluid flow, André (2004) observed that the numerical model produced inaccurate computational results when compared with the experimental data. This was attributed to the fact that the Boussinesq correction coefficient was not sufficient to simulate and describe the turbulent flow structures, such as internal jets and recirculating eddies developing inside the steps cavities. Furthermore, Tabbara et al. (2005) stated that the omission of the effects of the air entrainment in solving the governing equations of the numerical ADINA model, which is based on the finite element method, led to some discrepancies between the experimental and numerical results. Carvalho and Martins (2009) applied a 2D numerical model, which is based on the Reynolds averaged equations, to simulate the flow properties over a relatively large-scale stepped spillway model of 1V:2.75H bottom slope in order to characterize the pressure and hydrodynamic forces on the baffles and sills. For this purpose they used a finite difference staggered grid system of rectangular cells of variable width and height to descretize the governing equations. They concluded that the numerical model is capable of predicting the flow field variables over stepped spillways as the computational results were in close agreement with the corresponding experimental results. Tongkratoke et al (2009) carried out a numerical work for simulating the flow over stepped spillways with various step heights and slopes. They applied the finite volume method to descretize the governing. The main aim of their study was to assess the performance of various turbulence models including the LES with Smagorinsky-Lilly SGS, the linear RNG k-ε turbulence model, the non-linear k-ε turbulence model of craft et al (1996) and the modified non-linear k-ε turbulence model in predicting the flow field variables over stepped spillways. Comparison between the numerical results of these models and the experimental results showed that the computational results of the LES turbulence model were more accurate than those provided by the linear k-ε and non-linear turbulence models for the cases of stepped spillways with flatter slopes. However, they found that the computational time with the LES method is nearly four times higher compared to that required with the non-linear modified method. Fabian et al.

(2010) concluded that the high level of turbulence close to the inception point of air entrainment could be the major source of inaccuracy in the numerical results.

It is worth mentioning here that the numerical models presented above are categorized under the grid based method. In other words, complex mesh generation is needed to simulate the physical geometry of stepped spillways. In addition, these models solve the governing equations based on the Eulerian fluid flow scheme. Therefore, it is difficult to detect the flow behaviour with respect to time, especially inside the step cavity. The numerical particle based method applied in this study provides a straightforward way to reproduce the computational domain. Also, the mathematical model is based on the Lagrangian approach which allows one to record the evolution of flow with time.

2.2.3. Particle-based numerical methods for simulating free surface flows

Grid-based methods have been used widely in simulating hydrodynamic problems, in particular free water surface flow problems, as described in the previous section. Although the grid-based method has been successfully applied in various engineering and scientific disciplines, many limitations are marked with this method, even when both the Lagrangian and Eulerian approaches are combined such as ALE, due to the existence of some inherent difficulties such as mesh distortion, particularly in case of high velocity impact problems (Liu et al. 2003). Nowadays, the trajectory of the computational methods tends toward the second generation, which are known as mesh free particle-based methods. Problems associated with complex geometries, tracking moving boundaries, and interfaces can be successfully treated by this method without any mesh refinement or grid transformations, which are essential tasks when grid-based methods are applied. This method is characterized by a pure mesh free, adaptive and Lagrangian approach, in which the grids are replaced by arbitrarily distributed particles carrying the fluid properties (Monaghan, 1989).

Smoothed Particle Hydrodynamics method is the oldest of the mesh free particle techniques. It was originally invented by Lucy (1977) and Gingold and Monaghan (1977) to solve three-dimensional astrophysical problems. Recent improvements and modifications to its stability, accuracy and adaptability have led to this approach

being extensively used to deal with other physical and engineering applications, such as coastal hydrodynamics, fluid structure interaction and free surface flows. However, up to now this method has not been applied to simulate the flow behaviour over stepped spillways.

Initially, Monaghan (1994) studied free surface flow by representing the continuum via a finite set of randomly distributed particles. Each particle carries the physical fluid properties, including density, pressure and velocity, which might change with time, and moves according to the governing equations (Gómez-Gesteira et al. 2012).

Ferrari (2010) developed a new SPH scheme to simulate the flow over a sharp-crested weir. The mathematical model of her study was developed on the basis of the Navier-Stokes equations and the equation of state proposed by Tait (1887), considering the fluid as weakly compressible. The model was solved by using the 3D parallel SPH scheme, to track the free surface profile and compute the pressure field, proposed by Ferrari (2008) for free surface flows. The numerical results were quantitatively and qualitatively in good agreement with the experimental data of Scimemi (1930).

From the previously published numerical modelling investigations of the flow over stepped spillway it can be concluded that numerical modelling of stepped spillways has been extensively carried out using grid-based methods such as finite element and finite volume methods, whereas particle-based methods, such as SPH method, have not been applied yet. Hence, SPHysics code as an implementation of the SPH method is used in the present work to simulate the properties of the skimming flow down stepped spillways of moderate slopes, typical of embankment dams, in the non-aerated flow region.

CHAPTER THREE

NUMERICAL SMOOTHED PARTICLE HYDRODYNAMICS METHOD

Chapter Three: Numerical Smoothed Particle Hydrodynamics Method

This chapter describes the features of both the computational SPH numerical method and the numerical SPHysics model applied in the current work. It begins with the concept of the numerical simulation of the SPH mesh free particle-based method covering: the theoretical background, the standard SPH formulations and the governing equations based on the conservation laws in the discretised form. Then the numerical SPHysics code, as an implementation of the SPH method, which is applied in the present study, is described including: boundary conditions, time step algorithm, computational efficiency of the code and most of the recent numerical techniques developed to modify the SPH method in an attempt to improve the accuracy of the numerical results.

3.1. Numerical smoothed particle hydrodynamics method

SPH is a particle based method initially developed by Lucy (1977) and Gingold and Monaghan (1977) in the field of astrophysics. Since its first application to the simulation of free surface flows by Monaghan (1992), numerous efforts have been made to increase the stability and accuracy of SPH computational results. Over the past two decades this method has been applied with promising outcomes in various free surface flow problems, such as flow in open channels (Lopez & Marivela, 2009a; Federico et al. 2010; Lopez et al, 2010) and flow over hydraulic structures (Gatti et al. 2007; Lopez et al. 2009b; Ferrari, 2010). In addition, this method has gained considerable interest from industry see Violeau et al. (2007); Violeau (2008) and Lee et al. (2010) for solving a range of difficult problems where the gird-based methods have great difficulty, such as mesh generation for complex geometries and non-linear large deformations (Liu & Liu, 2003).

Indeed, simulation time and system size are the two main numerical issues which may limit the application of this method in cases, such as flooding hydro-science, where detailed information is required to understand the flow characteristics under real conditions (Lee et al. 2010). However, the development of modern supercomputers and parallel computing systems (Rogers et al. 2007; Moulinec et al.

2009; Ferrari, 2010) have significantly contributed to accelerating existing numerical SPH models.

As stated earlier, SPH method is a purely mesh free, Lagrangian and adaptive particle method, in which a set of particles is used to represent the state of a system. Conservation equations can be applied on these particles, which carry fluid properties, and they move accordingly (Liu et al. 2003).

Theoretically, the SPH method takes advantage from the integral interpolants theory and kernel functions. The SPH formulation is mainly dependent on two tasks: integral representation (kernel approximation) and particle representation/approximation. The former is performed through the use of an interpolating function to transfer the partial differential equations, appearing in the governing equations of a certain fluid flow problem, into integral equations and therefore the flow field variables at any point within the computational domain can be estimated. The latter is then applied to achieve the numerical computation of the integrals by summing the values of the flow field variable under consideration that are carried only by the neighbouring particles. The procedure of the above two tasks is presented in the following section.

To begin with the first task, it should be noted that the integral form of any function $A(r)$ can be expressed over all the space Ω using the Dirac delta function as:

$$A(r) = \int_{\Omega} A(r')\delta(r - r')dr' \tag{3.1}$$

where r is the vectorial position of any point in the space Ω and δ is the Dirac delta function defined by:

$$\delta(r - r') = \begin{cases} 1 & r = r' \\ 0 & r \neq r' \end{cases} \tag{3.2}$$

The integral interpolant of Equation (3.1) can be approximately obtained when the delta function is replaced by a smoothing function W of a characteristic length h:

$$A(r) \approx \int_{\Omega} A(r')W(r - r', h)dr' \tag{3.3}$$

$W(r - r', h)$ is also called the smoothing or weighting kernel function. The characteristic length, h plays an indispensable role in smoothing the kernel function because it determines the influence domain area of the smoothing function.

The second task, particle approximation, transforms Equation (3.3) into the discrete form of a given interpolation point, a by the following summation equation that is carried out over all of the neighbouring particles located within its influence domain:

$$A(r_a) = \sum_b A_b \, V_b W(r_a - r_b, h) \tag{3.4}$$

where the subscript, b refers to all of the particles located inside an influence area of circular shape, in 2D fluid flow simulations, having a radius characterized by the smoothing length times a scaling factor kh, known as the compact support of the kernel function, V_b is the volume of that particle and A_b is the value of the function at the position r_b. Figure 3.1 illustrates the influence area of a given particle and the neighbouring particles within this area.

The volume, $V_b$can be expressed as the relationship between the mass m_b and mass density ρ_b as follows:

$$V_b = \frac{m_b}{\rho_b} \tag{3.5}$$

Substituting Equation (3.5) into Equation (3.4) yields:

$$A(r_a) = \sum_b A_b \frac{m_b}{\rho_b} W(r_a - r_b, h) \tag{3.6}$$

The above equation can be considered as the basic expression of the SPH method, which can be used to approximate a continuous vectorial or scalar field function.

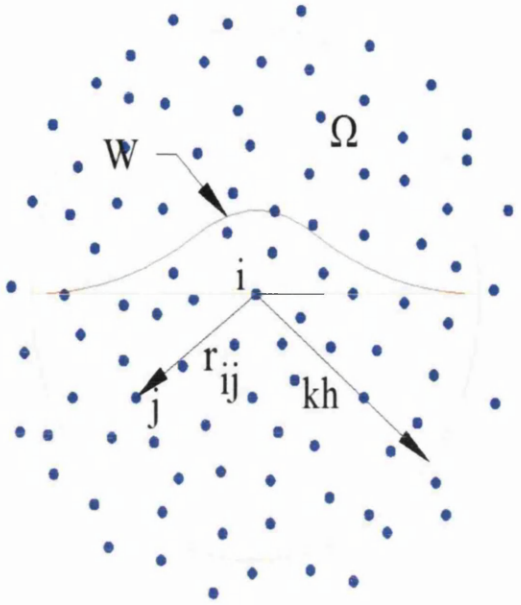

Figure 3.1. The influence area of a given particle of radius *kh* and the neighbouring particles located in this area (from Gómez-Gesteira et al. 2012).

Similar to other numerical simulation methods, the derivatives of the flow field functions appearing in the governing equations, which are typically of the first and second orders in most fluid flow problems, are also needed. In the SPH method, based on both the values of the function carried by a number of particles, situated within its compact support, and the analytical form of the smoothing function, which should be of continuous differentiable type, the spatial derivative of the field function may be evaluated. Thus, differentiating Equation (3.6) with respect to x produces:

$$\frac{d}{dx}A(r_a) = \frac{d}{dx}\left\{A_b \frac{m_b}{\rho_b} W(r_a - r_b, h)\right\} \tag{3.7}$$

$$= \frac{d}{dx}\left(A_b \frac{m_b}{\rho_b}\right) W(r_a - r_b, h) + A_b \frac{m_b}{\rho_b} \frac{d}{dx} W(r_a - r_b, h) \tag{3.8}$$

Since the value of $A_b \frac{m_b}{\rho_b}$ at a given point is independent of the space components x, y *and* z, therefore;

$$\frac{d}{dx}A(r_a) = A_b \frac{m_b}{\rho_b} \frac{d}{dx} W(r_a - r_b, h) \tag{3.9}$$

Thus,

$$\nabla A(r_a) = \sum_b A_b \frac{m_b}{\rho_b} \nabla W(r_a - r_b, h) \tag{3.10}$$

Based on the second golden rule of the SPH method, which states that the formulae can be represented in a better manner when the density is placed inside the operator (Monaghan, 1989):

$$\nabla(\rho A) = \rho \nabla(A) + A \nabla \rho \tag{3.11}$$

$$\rho \nabla(A) = \nabla(\rho A) - A \nabla \rho \tag{3.12}$$

$$\nabla(A) = \frac{1}{\rho}(\nabla(\rho A) - A \nabla \rho) \tag{3.13}$$

Applying this rule to Equations (3.6) and (3.10) and taking into consideration that only the smoothing kernel is affected when the derivative of a summation interpolant is carried out:

$$\nabla A(r_a) = \frac{1}{\rho}\left\{\sum_b \rho_b A_b \frac{m_b}{\rho_b} \nabla W(r_a - r_b, h) - \sum_b A \rho_b \frac{m_b}{\rho_b} \nabla W(r_a - r_b, h)\right\} \tag{3.14}$$

$$\nabla A(r_a) = \frac{1}{\rho}\{\sum_b A_b \, m_b \nabla W(r_a - r_b, h) - \sum_b A \, m_b \nabla W(r_a - r_b, h)\} \tag{3.15}$$

$$\nabla A(r_a) = \frac{1}{\rho}\sum_b (A_b - A) \, m_b \nabla W(r_a - r_b, h) \tag{3.16}$$

In fact, the second golden rule of the SPH method can be symmetrised in the following form:

$$\frac{\nabla(A)}{\rho} = \nabla\left(\frac{A}{\rho}\right) + \frac{A}{\rho^2} \nabla \rho \tag{3.17}$$

$$\nabla(A) = \rho\left\{\nabla\left(\frac{A}{\rho}\right) + \frac{A}{\rho^2} \nabla \rho\right\} \tag{3.18}$$

Hence, Equation (3.16) can be rewritten as:

$$\nabla A(r_a) = \rho\left\{\sum_b \frac{A_b}{\rho_b} \frac{m_b}{\rho_b} \nabla W(r_a - r_b, h) + \sum_b \frac{A}{\rho^2} \rho_b \frac{m_b}{\rho_b} \nabla W(r_a - r_b, h)\right\} \tag{3.19}$$

$$\nabla A(r_a) = \rho\left\{\sum_b \frac{A_b}{{\rho_b}^2} m_b \nabla W(r_a - r_b, h) + \sum_b \frac{A}{\rho^2} m_b \nabla W(r_a - r_b, h)\right\} \tag{3.20}$$

$$\nabla A(r_a) = \rho \sum_b \left\{\frac{A_b}{{\rho_b}^2} + \frac{A}{\rho^2}\right\} m_b \nabla W(r_a - r_b, h) \tag{3.21}$$

Thus, the symmetrised forms for the pressure gradient and the velocity divergence of particle, a can be respectively expressed by the following two equations:

$$(\nabla P)_a = \rho \sum_b \left\{ \frac{P_b}{{\rho_b}^2} + \frac{P_a}{{\rho_a}^2} \right\} m_b \nabla W(r_a - r_b, h) \tag{3.22}$$

$$\nabla . \mathbf{u}_a = \rho \sum_b \left\{ \frac{\mathbf{u}_b}{{\rho_b}^2} + \frac{\mathbf{u}_a}{{\rho_a}^2} \right\} m_b . \nabla W(r_a - r_b, h) \tag{3.23}$$

Similarly, using the same procedure shown above starting from the original formula represented by Equation (3.6), the second order derivative of the smoothed field quantity function can be obtained as follows:

$$\nabla^2 A(r_a) = \sum_b A_b \frac{m_b}{\rho_b} \nabla^2 W(r_a - r_b, h) \tag{3.24}$$

3.2. The weighting function

The performance of an SPH method in terms of accuracy and computing time is strongly dependent on the kernel function (Liu et al. 2003). In analogue to the finite difference method, where various schemes are used, various kernel functions have been proposed since the invention of the SPH method, in an attempt to increase its stability and accuracy. The following section highlights the properties that kernel functions should have and presents the most widely used functions in the SPH method.

Liu et al. (2003) reported that a kernel function in an SPH method should possess the following properties:

1- Normalization: this can be satisfied when the integral of the kernel function is unity:

$$\int_\Omega W(r, h) dr = 1 \tag{3.25}$$

2- Positivity: this will ensure the averaging function of the kernel:

$$W(r, h) \geq 0 \tag{3.26}$$

3- Dirac delta function's behaviour: this should be satisfied by the delta function as the smoothing functions approaches zero (Benz, 1990; Monaghan, 1992):

$$\lim_{h \to 0} W(r, h) = \delta(r) \tag{3.27}$$

4- Compact support: this limits the contribution only to the particles located inside the compact support of radius h of a certain particle inside the computational domain while computing is performed to evaluate any field function at that particle.

$$W(r,h) = 0, \quad as \ \|r\| > h \tag{3.28}$$

5- The monotonic decrease of the function as the distance from the particle under consideration is increased (Liu et al. 2003).

6- Even function: this property may ensure the achievement of symmetry.

Based on the order of the kernel function, various functions have been proposed in the SPH method. The higher the order of the kernel function the higher the accuracy of the results will be, but the computational time will be greater. The following kernels are considered as the most widely used functions in the SPH method.

1- Gaussian: this kernel was originally proposed by Gingold and Monaghan (1977). It takes the following form:

$$W(r,h) = \alpha_D e^{-q^2} \tag{3.29}$$

where α_D is a parameter that depends on the number of dimensions involving the computational domain and defined as:

$$\alpha_D = \begin{cases} \frac{1}{(\pi h^2)}, & in\ 2D \\ \frac{1}{\left(\pi^{3/2} h^3\right)}, & in\ 3D \end{cases} \tag{3.30}$$

where h is the smoothing length. This defines the area of influence called the influence domain. q is the dimensionless distance between the particles defined by:

$$q = \frac{r}{h} \tag{3.31}$$

where r is the distance between the two particles being considered.

This function is characterized by its smoothness, even for higher order of derivatives, stability and accuracy, particularly for disordered particles (Liu et al. 2003). One of the drawbacks of this function is that all the particles have to be used in the computation procedure because it theoretically never falls to zero, unless, q

approaches to infinity. It is therefore computationally more expensive than other types.

2- Quadratic: This type was used by Johnson et al. (1996) to treat problems associated with compressive instability, due to the impact of high velocity. This kind of kernel function can be expressed by:

$$W(r,h) = \alpha_D \left[\frac{3}{16}q^2 - \frac{3}{4}q + \frac{3}{4}\right] \tag{3.32}$$

with,

$$\alpha_D = \begin{cases} \frac{2}{(\pi h^2)}, & in\ 2D \\ \frac{5}{(4\pi h^3)}, & in\ 3D \end{cases} \tag{3.33}$$

3- Cubic spline: This kind of kernel function, which is one of the most popular and widely used functions, was proposed by Monaghan and Lattanzio (1985). The general expression of this function is as follows:

$$W(r,h) = \alpha_D \begin{cases} 1 - \frac{3}{2}q^2 + \frac{3}{4}q^3, & 0 \le q \le 1 \\ \frac{1}{4}(2-q)^3, & 1 \le q \le 2 \\ 0, & q \ge 2 \end{cases} \tag{3.34}$$

where,

$$\alpha_D = \begin{cases} \frac{10}{(7\pi h^2)}, & in\ 2D \\ \frac{1}{(\pi h^3)}, & in\ 3D \end{cases} \tag{3.35}$$

The shape of this kernel type is similar to the Gaussian type but with a narrower compact support, especially when q is equal to or greater than 2, and hence it needs lesser computational time.

4- Quintic (Wendland, 1995): This can be defined by the following expression:

$$W(r,h) = \alpha_D \left(1 - \frac{q}{2}\right)^4 (2q+1), \qquad 0 \le q \le 2 \tag{3.36}$$

in which,

$$\alpha_D = \begin{cases} \frac{7}{(4\pi h^2)} & , \ in\ 2D \\ \frac{21}{(16\pi h^3)} & , \ in\ 3D \end{cases} \tag{3.37}$$

This type of kernel function is also close to the Gaussian type and is stable (Liu et al, 2003) but is computationally more expensive than the cubic spline function.

It is worth mentioning that the choice of the kernel function has a significant role in improving the accuracy of the computational results and optimizing the computational time. In the above equations it can be noted that, h and q are the dominant factors affecting the smoothing kernel functions. In the present investigation the cubic spline kernel function is used to obtain results that are as accurate as possible, while taking into account the need to minimize computing time. However, the spline kernel function has been widely used to simulate free surface flow problems, for example: in Lopez et al. (2009a) for simulating fish-ways; Lopez et al. (2009b) for calibrating the SPH model using prototype spillway data; Ferrari (2010) to simulate the flow over sharp crested weirs; and Crespo (2010) to model the 2D and 3D dam break problem. This is because this kind of function has provided numerical results close to those obtained from the experiments in a relatively short computing time. Thus, in the present investigation the spline kernel function is used as an interpolation scheme to estimate the flow field variables over stepped spillways.

3.3. Governing equations

In this section the differential equations governing fluid flow motion and the numerical schemes developed for solving them in the SPH method are presented. Since the fluid inside the domain is completely defined by particles which follow the fluid motion, it is therefore worthwhile to formulate the equations on the basis of the Lagrangian form. As with the grid-based methods, the conservation laws of mass and momentum are applied in the SPH method to express the fluid motions. Indeed, in an SPH method this motion has been traditionally simulated based on considering the fluid as compressible. Thus, an equation of state can be directly applied to calculate the pressure instead of solving a pressure differential equation of the Poisson-type

(Monaghan, 1989). However, the concept of a weakly compressible fluid has also been widely used to address the issue of fluid incompressibility in the SPH method (Monaghan, 1994). In addition, Dalrymple et al. (2006) stated that it is reasonable to consider the fluid as compressible to a certain degree when a relatively large variation of pressure exists.

3.3.1. Conservation of mass

Basically, in particle-based methods, mass conservation can be achieved when: 1) the number of particles used in the simulation is kept constant and 2) the same mass is initially assigned to each particle (Monaghan, 1994).
In the Lagrangian form, the mass conservation law can be expressed as:

$$\frac{1}{\rho}\frac{D\rho}{Dt} = -\nabla.\mathbf{u} \tag{3.38}$$

where ρ and $\mathbf{u}$ are respectively the density and velocity of the particle, t is the time and $\frac{D}{Dt}$ is the total material derivative. The discrete form of the above equation would be:

$$\left(\frac{d\rho}{dt}\right)_a = \sum_b m_b\,(\mathbf{u}_a - \mathbf{u}_b)\nabla_a W_{ab} \tag{3.39}$$

where $\nabla_a W_{ab}$ is the gradient of the kernel function at particle a, $\mathbf{u}_a$ and $\mathbf{u}_b$ are the velocity of particles, a and b respectively.

3.3.2. Conservation of momentum

Basically, the following equation might be used to describe the fluid motion on the basis of the Lagrangian form in which its derivation is based on Newton's second law of motion:

$$\frac{D\mathbf{u}}{Dt} = -\frac{1}{\rho}\nabla P + \Theta + \mathbf{g} \tag{3.40}$$

where $\mathbf{u}$ is the spatial velocity of the particle, P is the pressure and $\mathbf{g}$ accounts for the body force per unit mass due to the effect of gravitational acceleration. In this equation, all diffusion terms, caused mainly by the effects of the fluid viscosity, are

parameterised by Θ. Different approaches have been proposed to model the diffusivity in the SPH method. It can be observed that the convection term in the SPH momentum equation is dropped. This can be attributed to the fact that the Lagrangian form is based on the material coordinates, not on spatial coordinates like the Eulerian form, by which the motion of the particles facilitates the automatic calculation of the time independent acceleration terms. This can be counted as another advantage of using the Lagrangian form which helps in solving such complex equations in a more straightforward manner.

The total force acting on a particle, including the internal and external forces, is represented by the right hand side of Equation (3.40), whereas the left hand side represents its acceleration. Indeed, it should be noted that the direct application of the gradient form expressed by Equation (3.40) on the pressure, the first term of the right hand side, could not guarantee momentum conservation (Monaghan, 1989). This is because all particles would not necessarily be symmetrically subjected to the same pressure value and hence the fundamentals of the action-reaction law might not be entirely accomplished. However, in applying the SPH formulations, the following symmetrised form of the SPH discretised notation may be used to express the pressure gradient:

$$\left(-\frac{1}{\rho}\nabla P\right)_a = -\sum_b m_b \left(\frac{P_b}{\rho_b^2}+\frac{P_a}{\rho_a^2}\right)\nabla_a W_{ab} \tag{3.41}$$

where P_b, ρ_b, P_a and ρ_a are the pressures and the densities corresponding to particles a and b respectively.

As pointed out above, different approaches have been proposed to model the diffusivity term, Θ in the Lagrangian momentum equation, which is highly affected by the fluid viscosity, especially in free surface flows. In the SPHysics code three approaches have been employed to introduce the effect of the fluid viscosity, namely;

1- Artificial viscosity
2- Laminar viscosity
3- Laminar viscosity and sub-particle scale (SPS) turbulence.

Since the flow over stepped spillways is characterized by fully turbulent flow, the third approach is used is the present investigation.

The laminar viscosity and SPS turbulence approach was initially developed by Gotoh et al. (2004). The diffusion term, Θ is split into two parts; the laminar stress, $\mu\nabla^2$ part and the sub-particle scale stress tensor, $\nabla.\boldsymbol{\tau}$ part. Thus, the momentum equation can be expressed as:

$$\frac{D\mathbf{u}}{Dt} = -\frac{1}{\rho}\nabla P + v_o\nabla^2\mathbf{u} + \frac{1}{\rho}\nabla\boldsymbol{\tau} + \mathbf{g} \tag{3.42}$$

where $v_o = \mu/\rho$ is the kinematic viscosity of water, μ the dynamic viscosity of water, ρ is the mass-density of water and $\boldsymbol{\tau}$ is the sub-particle scale stress tensor. Lo and Shao (2002) modified the laminar stress term for particle, a on the basis of the interactive neighbouring particles b located inside its compact support, and the following equation was presented:

$$(v_o\nabla^2\mathbf{u})_a = \sum_b m_b \left\{\frac{4v_o r_{ab}\nabla_a W_{ab}}{(\rho_a+\rho_b)|r_{ab}|^2}\right\}\mathbf{u}_{ab} \tag{3.43}$$

The symmetrised form of the stress tensor of particle, a based on the SPH formulations and notations can be given by:

$$\left(\frac{1}{\rho}\boldsymbol{\tau}\right)_a = \sum_b m_b\left(\frac{\boldsymbol{\tau}_b}{\rho_b^2} + \frac{\boldsymbol{\tau}_a}{\rho_a^2}\right)\nabla_a W_{ab} \tag{3.44}$$

where $\boldsymbol{\tau}_a$ and $\boldsymbol{\tau}_b$ are respectively the stress tensors at particles, a and b. The SPHysics code determines the stress tensors at each particle based on the LES type sub-particle scale SPS turbulence model proposed by Lo and Shao (2002). This model in mesh free particle methods is the same as the sub-grid scale SGS in the grid based methods. Various advanced SPS models have been proposed in the literature. For a compressible fluid, the SPS stress tensor is commonly modelled on the basis of the Boussinesq's hypothesis-eddy viscosity assumption using the Favre-averaging technique (Gómez-Gesteira et al. 2012), as follows:

$$\frac{\boldsymbol{\tau}_{ij}}{\rho} = \nu_t\left(2S_{ij} - \frac{2}{3}k_1\delta_{ij}\right) - \frac{2}{3}C_I\Delta^2 S_{ij}|S_{ij}|^2 \tag{3.45}$$

where $\boldsymbol{\tau}_{ij}$ is the sub-particle scale stress tensor, $\nu_t = [(C_s\Delta l)]^2|S|$ is the turbulent eddy viscosity, C_s=0.12 is the Smagorinsky constant, $|S| = \left(2S_{ij}S_{ij}\right)^{1/2}$, S_{ij} is the element of the SPS strain tensor, Δl is the particle-particle spacing, $C_I = 0.0066$, k_1 is the sub-particle scale turbulence kinetic energy and, δ_{ij} is the kronecker delta

function. Comprehensive details regarding the theory of the LES type SPS turbulence model can be found in Pope (1994).

Substituting Equations (3.41, 3.43, and 3.44) into the momentum Equation (3.42) yields the discretised Lagrangian form of the momentum equation in the SPH notations:

$$\left(\frac{du}{dt}\right)_a = -\sum_b m_b \left(\frac{P_b}{\rho_b^2} + \frac{P_a}{\rho_a^2}\right) \nabla_a W_{ab} + \sum_b m_b \left\{\frac{4v_o r_{ab} \nabla_a W_{ab}}{(\rho_a + \rho_b)|r_{ab}|^2}\right\} \mathbf{u}_{ab} + \sum_b m_b \left(\frac{\tau_b}{\rho_b^2} + \frac{\tau_a}{\rho_a^2}\right) \nabla_a W_{ab} \quad (3.46)$$

The above equation conserves both the linear and angular momentums of all of the particles involving the computational domain.

3.4. Equation of State

As mentioned earlier, the standard SPH formulation is based on considering the fluid as compressible. However, the concept of weakly compressible fluid has also been widely used by applying a stiff equation of state, modified by Monaghan (1994), in which the pressure of each particle can be explicitly calculated as a function of its density (Batchelor, 1974) as:

$$P = B\left[\left(\frac{\rho}{\rho_o}\right)^{\gamma} - 1\right] \quad (3.47)$$

where P is the pressure, and ρ_o is the reference fluid density. The density of the fluid at the free surface, which is subject to atmospheric pressure, is usually taken as the reference fluid density; for water ρ_o= 1000 kg/m^3, γ is the polytrophic constant, with values ranging from 1, for low Reynolds flow problems as recommended by Morris et al. (1997), to 7 which fits the oceanic data, and B is the bulk modulus elasticity of the fluid, defined by:

$$B = \frac{c_o^2 \rho_o}{\gamma} \quad (3.48)$$

where c_o is the speed of sound defined in terms of the reference density. The speed of sound can be determined when the first derivative is performed on Equation (3.47) with respect to the density as follows:

$$c_o^2 = c^2(\rho) = \frac{\partial P}{\partial \rho}\Big|\rho_o = \frac{B\gamma}{\rho_o}\left(\frac{\rho}{\rho_o}\right)^{\gamma-1}\Big|\rho_o \tag{3.49}$$

$$c_o^2 = \frac{B\gamma}{\rho_o} \tag{3.50}$$

The main advantage of using the concept of weak compressibility is the explicit calculation of the pressure instead of solving a partial differential equation, which considerably lessens the computation time. Equation (3.50) illustrates that an appropriate value should be given to the speed of sound so that the Mach number M, defined as the ratio between the flow speed and the speed of sound, could be significantly reduced in such a way that the maximum density variation should be kept less than 1%.

$$\frac{|\delta\rho|}{\rho_o} \sim \frac{V^2}{c_o^2} = M^2 \tag{3.51}$$

where $\delta\rho$ is the difference in density and V the maximum expected flow speed. However, Monaghan (1994) suggested the Mach number should not exceed 0.1, which requires the minimum value for the speed of sound be 10 times greater than the maximum expected flow velocity. This is to keep variation of the relative density, (ρ/ρ_o), which appears inside the state Equation (3.47), by less than 1%. Consequently the effect of compressibility can be reasonably neglected. Moreover, it is obvious from Equation (3.47) that the relative density is raised to the power γ and therefore any small increase of its value may cause the pressure flow field to fluctuate greatly. Indeed, according to the Courant-Friedrich-Levy condition, this approach increases the time step, Δt required for the computation by 10 times, since it is based on the speed of sound $\Delta t \approx \Delta x/c_o$ rather than the maximum expected flow speeds $\Delta t \approx \Delta x/V$, in which Δx is a resolution length.

3.5. Movement of particles

Particles used in the simulation with an SPH method are moved according to the following expression, known as the XSPH variant (Monaghan, 1989):

$$\frac{dr_a}{dt} = \mathbf{u}_a + \epsilon \sum_b \frac{m_b}{\rho_{ab}} \mathbf{u}_{ba} W_{ab} \tag{3.52}$$

where ϵ is a constant the value of which varies from zero to one with a frequently used value as 0.5 and $\rho_{ab} = (\rho_a + \rho_b)/2$. Crespo (2008) defined this expression as the correction for the velocity of a particle with respect to the neighbouring particles inside the compact support of that particle. Thus, the velocity of particle a is approximately equal to the average velocity of the neighbouring particles. Furthermore, Crespo (2008) stated that particle penetration might be considerably controlled when this equation is used to simulate high velocity fluid flow problems.

3.6. Numerical SPHysics code

Since the invention of the smoothed particle hydrodynamics method, many codes have been developed to simulate fluid flow problems. The numerical part of the present work is conducted using the SPHysics code, as an implementation of the SPH mesh free particle method, to simulate the characteristics of skimming flow over moderate slope stepped spillways. This code was developed via the collaboration of four international institutions: Johns Hopkins University (USA), Universidade de Vigo (Spain), University of Manchester (UK) and University of Rome, La Sapienza (Italy). The first version of this code was released in 2007 and is still under development. It is based on the standard formulations proposed by Monaghan (1989) for free surface flows and includes most of the corrections and modifications which have recently been made to improve its stability and efficiency. In this section the boundary conditions, the numerical schemes used to solve the SPH governing equations and most of the corrections employed by the SPHysics code will be presented. Furthermore, the initial particle configuration required for both the boundary and fluid particles are also described.

3.6.1. Code description

In SPHysics code, the main source code programme is based on FORTRAN language, while MATLAB software is used to visualize the flow. 2D and 3D fluid flow problems can be simulated with this code. Also, the serial and parallel versions are provided to run the problem. The main source code is split into two parts: 1) SPHysics.gen and 2) SPHysics. All the subroutines necessary for setting up the geometry and the initial fluid particle configuration are included in the first part, while all the subroutines required for solving the differential equations governing the problem under consideration are contained in the second part.

In the present work the source code is compiled with the SILVERFROST compiler package as one of the compiling options provided by the SPHysics code, while licensed MATLAB 2012b software is used for the flow visualization. The SONY PCG-71613M PC model is used to run all the models proposed in the present work, using the 2D serial version.

3.6.2. Boundary conditions

In this section the boundary conditions employed by the SPHysics numerical model and applied in the current study are presented. It explains the way whereby both types of particles the boundary and fluid particles constituting the computational domain are reproduced.

3.6.2.1. Boundary particles

In an SPH method, the solid boundaries composing the boundary walls of the geometry under consideration are also represented by discrete particles carrying the flow properties of mass, density, pressure and velocity, in the same way as a fluid particle. Fluid particles moving close to the boundary particles are subject to a repulsive force from the boundary particles in the normal direction (Monaghan, 1992). This force could prevent fluid particles from penetrating the boundary particles. Despite their disappearance in the SPH formalism, these boundary particles

may cause unrealistic results if they are not properly treated (Gómez-Gesteira et al. 2012). This is because on the one hand, the compact support of the fluid particles is truncated and therefore the number of neighbouring particles located inside the compact support is reduced, as there are no fluid particles outside the wall, and consequently the radius of the compact support is restricted to only one side. On the other hand, some of the flow field variables carried by the fluid particles close to the boundary particles might be affected, such as velocities where their values are reduced to zero. In an SPH method various kinds of boundary conditions have been proposed. Indeed, the SPHysics code applied in the current study uses three kinds of boundary conditions, namely 1) Dynamic boundary conditions, 2) Repulsive boundary conditions and 3) Periodic boundary conditions. In the present work the first two kinds are applied, see Chapter 4, to choose the method that produces more accurate numerical results. Therefore, the explanation that follows in this section is focused on the dynamic and repulsive boundary conditions.

In dynamic boundary condition the boundary particles are treated as the same as the fluid particles such that to verify the conservation laws and the equation of state. The only difference is that these particles are fixed in their positions or moved when some external functions, such as gates, moving objects and wave makers are imposed.

This type of boundary condition was initially proposed by Dalrymple and Kino (2000) and then extensively used by others. In this type two successive rows/columns of boundary particles are set up in a zigzag manner, as shown in Figure 3.2. The distance between these two rows is fixed to half of the initially imposed spacing between the particles: $(1/2\Delta x)$ for the horizontal boundaries and $(1/2\Delta z)$ for the vertical boundaries. The repulsion mechanism is based on the pressure exerted on the fluid particles as they approach the boundary particles. This can be obviously observed from Equation (3.39) in which the movement of fluid particles close to the boundary particle may lead to an increase in the density of the boundary particles and as a result, following Equation (3.46), the force exerted by the boundary particles is increased accordingly (Gómez-Gesteira et al. 2012). Although this force may protect the boundary particles from the penetration of fluid particles, the impermeability of this type of boundary conditions in an SPH method has not been guaranteed. Users should apply this method cautiously and the numerical results obtained with this technique need to be evaluated to see how they

are affected by the unrealistic physical phenomenon of penetration. This is marked as the main disadvantage of this type of boundary condition in an SPH numerical method, especially for high velocity flows. However, since the boundary particles are treated as the same as the fluid particles, the conservation laws and the equation of state can be applied to both of them with less programming effort. This is the main advantage of this type of boundary particles.

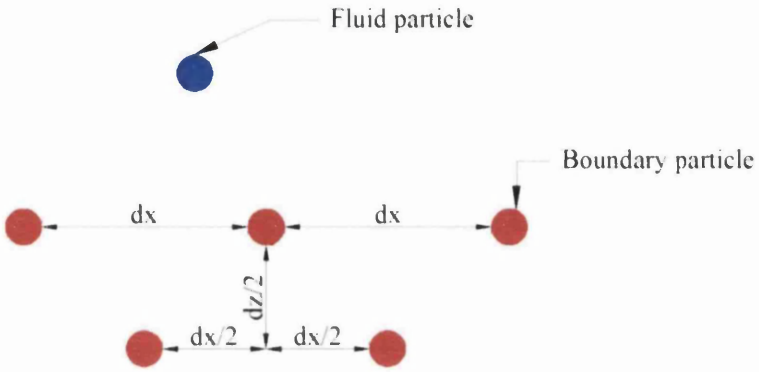

Figure 3.2. Schematic view of the dynamic boundary particles (red colour circles) (from Gómez-Gesteira et al. 2012).

The repulsive boundary condition technique was initially developed by Monaghan (1994) to represent the particles constituting the solid walls of the physical geometry. In this method the crossing of fluid particles through the boundary particles is prevented by a central force exerted on the fluid particles when they tend to approach them. This force per unit mass is defined by the Lennard-Jones equation, as a function of the distance, r between the fluid particles and the boundary particles. Monaghan and Kos (1999) later modified this equation to minimize the effect of the distance between the boundary particles on the repulsion force of the wall. In addition, the following equation was proposed by Rogers and Dalrymple (2008) to describe the force, $\vec{f}$ exerted on fluid particles:

$$\vec{f} = \vec{n}R(\psi)P(\xi)\varepsilon(z, u_{\perp}) \tag{3.53}$$

where $\vec{n}$ is the normal of the solid wall, ψ is the perpendicular distance of the particle from the wall, ξ is the projection of the interpolation location ξ_i onto the chord that connects two neighbouring boundary particles, and $u_{\perp}$ is the velocity of the fluid particle projected onto the normal.

The first function $R(\psi)$ appearing in Equation (3.53) is called the repulsion force, which can be evaluated based on the dimensionless distance, q and the sound speed of particle, i as follows:

$$R(\psi) = A\frac{1}{\sqrt{q}}(1-q) \tag{3.54}$$

in which, $q = \psi/2h$ and A is a coefficient defined by:

$$A = \frac{1}{h}0.01c_i^2 \tag{3.55}$$

where c_i is the speed of sound of particle i.

Meanwhile, the second function is selected in such a way as to ensure that all fluid particles need to be subject to a constant repulsive force when they are moving parallel to a solid wall. This function is usually expressed as the following:

$$P(\xi) = \frac{1}{2}\left\{1 + \cos\left(\frac{2\pi\xi}{\Delta b}\right)\right\} \tag{3.56}$$

where Δb is the distance between any two adjacent boundary particles.

Finally, the function that was originally suggested by Monaghan and Kos (1999) is modified to adjust the magnitude of the force. This function is expressed in terms of both the local water depth and the velocity of the fluid particle normal to the boundary wall as follows:

$$\varepsilon(z, u_\perp) = \varepsilon(z) + \varepsilon(u_\perp) \tag{3.57}$$

The function $\varepsilon(z)$ is defined as:

$$\varepsilon(z) = \begin{cases} 0.02 & z \geq 0 \\ |z/h_0| + 0.02 & 0 > z > -h_0 \\ 1 & |z/h_0| > 1 \end{cases} \tag{3.58}$$

The following equation is proposed to evaluate the function $\varepsilon(u_\perp)$:

$$\varepsilon(u_\perp) = \begin{cases} 0 & u_\perp > 0 \\ \dfrac{|20u_\perp|}{c_0} & |20u_\perp| < c_0 \\ 1 & |20u_\perp| > c_0 \end{cases} \tag{3.59}$$

In the above two equations, z is the elevation measured above the local still water level h_0, $u_\perp$ is the velocity of the fluid particle normal to the boundary, which can be estimated from: $u_\perp = (\overrightarrow{v_{WP}} - \overrightarrow{v_{BP}}).\vec{n}$

where, the subscripts WP and BP refer to the water and boundary particles respectively and, c_0 is the sound speed at the reference density.

To generate the system of normals in this kind of boundary condition, the coordinates of the adjacent neighbour particles to each individual boundary particle need to be defined. Figure 3.3 displays the boundary wall of a 2D case and shows how the boundary particles of the repulsive boundary condition method are reproduced. It can be seen from this figure that the boundary particles, *i-1*, *i+1*, *j-1* and *j+1* are adjacent neighbours to the boundary particle, *i* in which their positions are already known. This allows one to calculate the tangents, $\vec{t}$ and $\vec{S}$, and normal, $\vec{n}$ as follows:

$$\vec{t} = \frac{(\overrightarrow{r_{i+1}} - \overrightarrow{r_{i-1}})}{|\overrightarrow{r_{i+1}} - \overrightarrow{r_{i-1}}|} \tag{3.60}$$

$$\vec{s} = \frac{(\overrightarrow{r_{j+1}} - \overrightarrow{r_{j-1}})}{|\overrightarrow{r_{j+1}} - \overrightarrow{r_{j-1}}|} \tag{3.61}$$

and

$$\vec{n} = \vec{t} * \vec{s} \tag{3.62}$$

In these equations, $\vec{t}$ and $\vec{S}$ are the tangents to the boundary particles in the X and Y directions respectively, while $\vec{n}$ represents the normal of the solid wall to these tangents.

It is worth mentioning here that this kind of boundary condition is more popular than the dynamic boundary condition, as it is impermeable and only one layer of equally spaced boundary particles is needed to simulate the boundary walls of the physical geometry. This considerably reduces the computing time compared to the dynamic boundary condition, especially for complex geometries and when small size particles are needed. Despite the fact that an empirical equation is used to determine the repulsion force, which is considered as the main disadvantage of this kind of

boundary condition, it has been widely used to simulate different fluid flow problems and produced reasonable results.

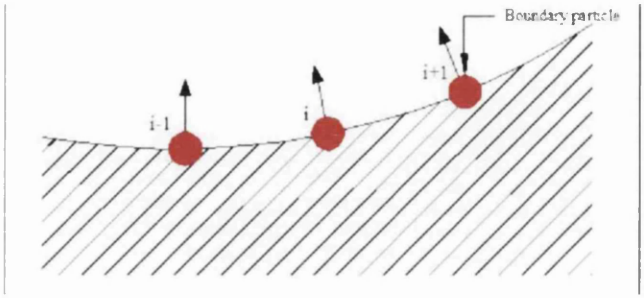

Figure 3.3. Reproducing boundary particles in the repulsive boundary condition approach.

3.6.2.2. Fluid particles

Two approaches are employed by the SPHysics code to initially place each fluid particle in a fixed location in the computational domain, namely 1) Cartesian grid and 2) staggered grid methods. The following section sheds light on the main features of each approach individually.

In the Cartesian grid type, which was initially proposed by Monaghan and Koss (1999), nodes of a square grid are used to hold particles in 2D problems. In 3D fluid flow cases, nodes of a simple cubic (SC) grid hold particles based on the fundamentals of vectors such as:

$$\boldsymbol{R} = ldx\boldsymbol{i} + mdy\boldsymbol{j} + ndz\boldsymbol{k} \tag{3.63}$$

where $\boldsymbol{R}$ is the initial vectorial position of a given fluid particle in the computational domain, dx, dy, and dz are the distance between particles in X, Y and Z directions respectively, $\boldsymbol{i}$, $\boldsymbol{j}$and $\boldsymbol{k}$ being the unit vectors in each direction and l, m and n the integers corresponding to each unit vector. Figure 3.4 illustrates the way whereby both boundary and fluid particles are initially placed in a 2D domain using this approach.

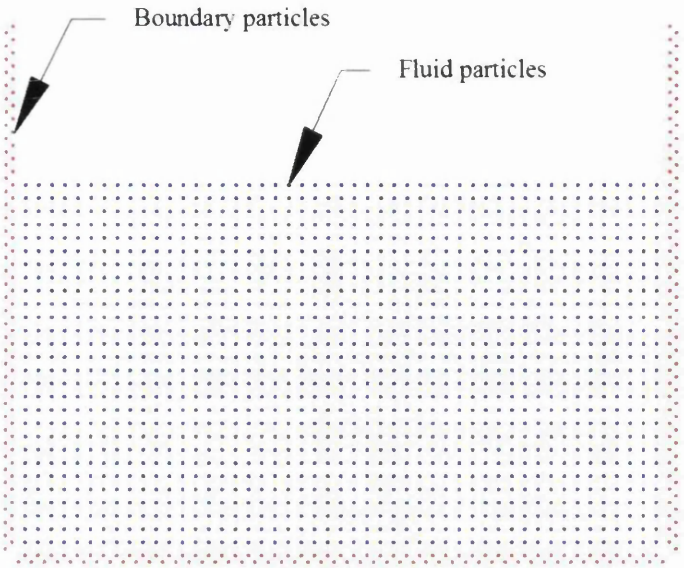

Figure 3.4. 2D initial configuration of boundary (red colour) and fluid particles (blue colour) in a 2D domain using the Cartesian grid approach (from Gómez-Gesteira et al. 2012).

The staggered grid method was used by Monaghan and Lattanzio (1991) to locate the initial position of the fluid particles. As can be seen in Figure 3.5, both the boundary and the fluid particles are placed in the same manner as the first method. The only difference is that in the staggered method an extra particle is placed in the centre of the square grid.

The staggered grid method is believed to have the potential of increasing the accuracy of the numerical SPH results, as more neighbouring particles are occupied within the smoothing length of particles inside the domain (Crespo, 2008). However, this technique is computationally more expensive than the Cartesian grid as more time is needed to perform the interpolation for evaluating a flow variable. In the current study both approaches are applied to select the one which optimizes both the accuracy and computational time, see Section 4.3.2.1.

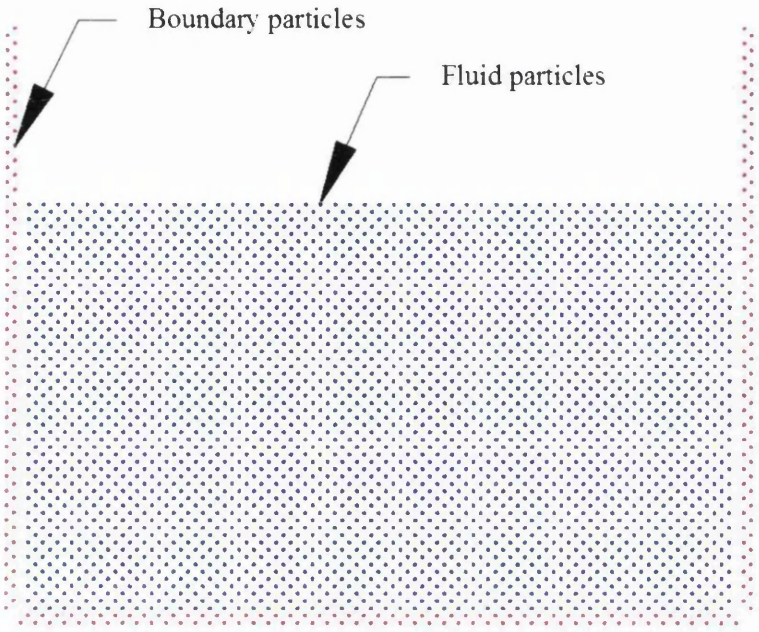

Figure 3.5. 2D initial configuration of boundary (red colour) and fluid (blue colour) particles using the staggered grid approach (from Gómez-Gesteira et al. 2012).

3.7. Time stepping

As mentioned earlier, the integration of the ordinary differential equations, obtained from the conversion of a set of partial differential equations, can be numerically achieved by applying an appropriate time step algorithm. However, in SPH method, the partial differential equations governing the physical domain are simplified to a set of ordinary differential equations, which facilities the application of any numerical time integration. However, Gómez-Gesteira et al. (2012) recommended that the accuracy of the time scheme used in particle methods should be no less than the second order as the particles are moving in space.

The governing equations represented in Section 3.3 and the particle movement equation expressed by Equation (3.54) can be summarized as follows:

$$\frac{d\overrightarrow{v_a}}{dt} = \overrightarrow{F_a} \tag{3.64}$$

$$\frac{d\rho_a}{dt} = D_a \tag{3.65}$$

$$\frac{de_a}{dt} = E_a \tag{3.66}$$

$$\frac{d\overrightarrow{r_a}}{dt} = \overrightarrow{V_a} \tag{3.67}$$

Indeed, four different numerical schemes of at least second order accuracy are used by the SPHysics code to integrate the SPH equations with respect to time, namely 1) predictor corrector algorithm, 2) Verlet time step algorithm, 3) Symplectic time step algorithm and 4) Beeman time step algorithm. The Verlet scheme is computationally one of the fastest and simplest time integrator algorithm in an SPH method and has been commonly used in many particle based numerical simulations. The Verlet time integrator scheme is therefore adopted in the current study and the following section describes this time stepping algorithm.

3.7.1 Verlet numerical scheme

This first use of this scheme in molecular dynamics is due to Verlet (1967), where it was applied to calculate trajectories of particles. It is characterized by its stability, simplicity and lower computational expensive (Gómez-Gesteira et al. 2012). The algorithm is divided into two stages; in the first stage the variables are calculated as follows:

$$\rho_a^{n+1} = \rho_a^{n-1} + 2\Delta t D_a^n \tag{3.68}$$

$$\vec{r}_a^{n+1} = \vec{r}_a^{n-1} + \Delta t \vec{v}_a^n + 0.5\Delta t^2 \vec{F}_a^n \tag{3.69}$$

$$\vec{v}_a^{n+1} = \vec{v}_a^{n-1} + 2\Delta t \vec{F}_a^n \tag{3.70}$$

$$e_a^{n+1} = e_a^{n-1} + 2\Delta t E_a^n \tag{3.71}$$

Then in the second stage, which performs at a pre-defined time step, these variables are re-calculated using the following expressions:

$$\rho_a^{n+1} = \rho_a^n + \Delta t D_a^n \tag{3.72}$$

$$\vec{r}_a^{n+1} = \vec{r}_a^n + \Delta t \vec{v}_a^n + 0.5\Delta t^2 \vec{F}_a^n \tag{3.73}$$

$$\vec{v}_a^{n+1} = \vec{v}_a^n + \Delta t \vec{F}_a^n \tag{3.74}$$

$$e_a^{n+1} = e_a^n + \Delta t E_a^n \tag{3.75}$$

3.8. Variable time step

In the SPH method the time step can be updated periodically before the next time is started. Therefore, the time step is variable and its value depends on three main factors: the CFL number, the forcing terms and the viscous diffusion term. Monaghan and Kos (1999) proposed the following formula to calculate the time step:

$$\Delta t = 0.3.\min(\Delta t_f , \Delta t_{cv}) \tag{3.76}$$

where Δt_f is the forcing time step defined by:

$$\Delta t_f = min_a\left(\sqrt{h/|f_a|}\right) \tag{3.77}$$

$|f_a|$is the force per unit mass.

Δt_{cv} is the time step based on the combination of both the viscous terms and the CFL number given by:

$$\Delta t_{cv} = min_a \frac{h}{c_s + max_a\left|\frac{h\vec{v}_{ab}\vec{r}_{ab}}{\vec{r}_{ab}^2}\right|} \tag{3.78}$$

The iteration is performed over all particles in the domain to find the flow field variables based on the minimum time step value evaluated by Equation (3.76).

3.9. Computational efficiency

It was explained in previous sections that each particle should verify the differential equations governing the fluid flow. When the interaction of all the particles involving the domain is considered in calculating a flow field variable at a certain particle, the process is computationally too expensive, especially when the number of particles is large. Many techniques have been proposed in an attempt to improve computational efficiency. The key idea of these techniques is to introduce the physical quantities only carried by a number of particles located near to a certain particle, on which the computation is performed, in the interpolation procedure,

taking into consideration accuracy as well. This could result in a significant reduction of the computation time, as the process of searching for particles for each particle and at each time step needs an excessive time. Therefore, the influence length, on which the selection of the neighbouring particles is based, of each particle, should be pre-scribed in advance.

A linked list method is one of the most powerful techniques that has been developed to improve the computational efficiency (Gómez-Gesteira et al. 2012). It uses the compactness of the kernel function having an influence length of radius *2h*. The details of this technique are explained in the following section.

3.9.1. Linked list

Following Monaghan and Lattanzio (1985), this technique, which is implemented by the numerical SPHysics code, divides the computational domain into squares having dimensions exactly the same as the radius of the kernel function *2h* (Gómez-Gesteira et al. 2012), as shown in Figure 3.6. Thus, the number of particles surrounding the particle under consideration is reduced because the contribution of the particles located outside this area is neglected. Then, for each Z level in a 2D domain the grids are swept along the X direction so that repetition of the particle interactions could be minimised to a great extent. This can be conducted by searching for particles placed in the E, N, NW and NE cells surrounding each cell. The mechanism of sweeping and searching for particles using the linked list technique is shown in Figure 3.7. The procedure is that: cells (N), (E), (NE) and (NW) are checked while searching for neighbouring cells which contain interacting particles with a particle inside the cell (*ik*). Whereas, the cells (S), (W), (SE) and (SW) were already checked while interacted particles searched in the reverse interaction.

Since all the fluid particles are continuously moving, their position should be updated each time step. Meanwhile, some of the boundary particles, such as gates, moving objects and wavemakers, are also moved with respect to time, and the rest are fixed. Therefore, their position needs to be updated as well.

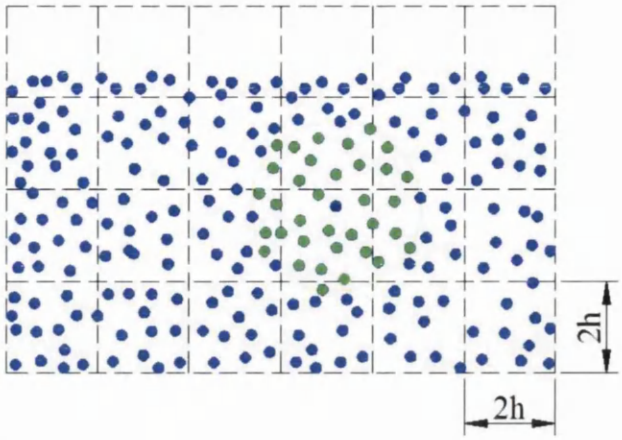

Figure 3.6. 2D Computational domain is divided into squares having the same dimensions as the compact support radius (from Gómez-Gesteira et al. 2012).

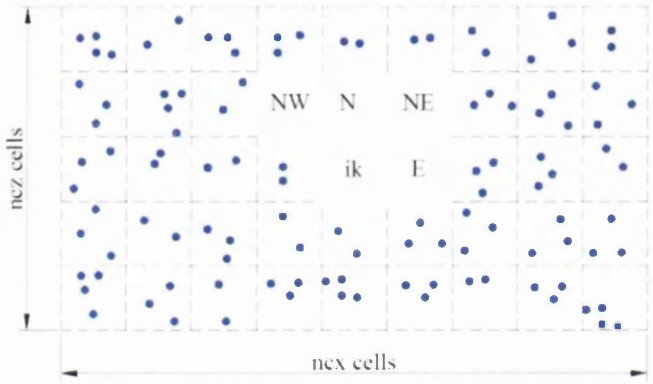

Figure 3.7. Mechanism of searching for particles and sweeping the grids of the link list scheme (from Gómez-Gesteira et al. 2012).

3.10. Modifications to the standard SPH method

The direct use of the classical SPH formulations may cause instability and uncertainty in the numerical results. This is because there are two main issues in an SPH method that were not addressed in the original form. The first one is the truncation of the compact support of the particles located close to the boundaries, such as the solid walls of the geometry and the free surface. The second is that the SPH method treats the fluid as weakly compressible, which may cause fluctuations in both the velocity and pressure flow fields.

Many efforts have been made since the invention of the numerical SPH method to modify the standard equations for the sake of enhancing the numerical results. The

following sections present the main techniques that have been developed recently and provided by the SPHysics code to sort out these numerical SPH problems.

3.10.1. Normalization of kernel function

As shown in Section 3.2., one of the main conditions that a kernel function should possess is normalization. This condition may not be exactly fulfilled for particles situated close to both the solid wall boundaries of the geometry and the free surface. This is because the kernel function truncates in these regions, due to the absence of particles outside of these boundaries. Two different approaches have been developed and employed by the numerical SPHysics code to overcome this problem; this first one corrects the kernel function, while the kernel gradient is corrected in the second approach. Both these techniques are described in the following sections:

3.10.1.1. Kernel correction

Liu et al. (1997) first proposed this approach to modify the kernel function in such a way that achieves the exact interpolation to a certain degree. They introduced a linear function to correct the kernel function. Then, Bonet and Lock (1999) proposed a constant function instead of the linear function, and improvements in the physical quantities, especially carried by particles located close to the domain boundaries, were observed. The following expression is proposed to estimate the value of a vectorial variable, $\overrightarrow{f_a}$:

$$\overrightarrow{f_a} = \frac{\Sigma_b \frac{m_b}{\rho_b} \overrightarrow{f_b} W_{ab}}{\Sigma_b \frac{m_b}{\rho_b} W_{ab}} \tag{3.79}$$

3.10.1.2. Kernel gradient correction

This method modifies the kernel gradient instead of the kernel function. The normal kernel gradient, ∇W_{ab} will be replaced by the corrected kernel gradient, $\tilde{\nabla} W_{ab}$ to

calculate the forces in the equation of motion. For this purpose a correction matrix, **L** is usually used as follows:

$$\tilde{\nabla} W_{ab} = \boldsymbol{L}_a \nabla W_{ab} \tag{3.80}$$

$$\boldsymbol{L}_a = M_a^{-1} \tag{3.81}$$

The matrix, $\boldsymbol{L}_a$ may be evaluated explicitly from the following expression:

$$M_a = \sum_{b=1}^{N} \frac{m_b}{\rho_b} \nabla W_{ab} \otimes (x_b - x_a) \tag{3.82}$$

where N refers to all particles interacting with the particle under consideration a.

3.10.2. Density reinitialization

As mentioned in Section 3.4., the fluid in the numerical SPHysics code is considered to be weakly compressible, which allows the explicit determination of the pressure using the equation of state, significantly reducing the computational time. However, this issue may cause fluctuations in the pressure and velocity flow fields even when the fluid density is varied slightly. In fact, three main approaches have been developed to solve this problem in an SPH method, namely: 1) Shepard density filter, 2) Moving least squares and 3) Riemann solver. Although the concept of incompressible fluid is also incorporated in the SPH method to remove such oscillations, the results are improved slightly and computing time is increased significantly (Gómez-Gesteira et al. 2012). Following Monaghan (1994), in the present study the fluid is treated as weakly compressible. The following section presents the three techniques mentioned above that have been implemented by the SPHysics code to smooth both the velocity and pressure flow fields.

3.10.2.1. Shepard filter

This is also called the first order correction of the density flow field. It is the simplest and quickest technique, in which a filter is performed over the density of the

particles, assigning a new density to each particle. The numerical SPHysics code repeats this procedure every at least 30 time steps using the following equation:

$$\rho_a^{new} = \sum_b m_b \widetilde{W}_{ab} \tag{3.83}$$

where $\widetilde{W}_{ab}$ is the zeroth order corrected kernel function, the same as that described in Section 3.10.1.1.

3.10.2.2. Moving least squares MLS

This approach was proposed by Dilts (1999) and applied successfully by Colagrossi and Landrini (2003) and Panizzo (2004). This is the first order correction as a linear function is used to reproduce the linear variation of the density flow field. Similar to the zeroth order correction, the following expression is repeated every 30 time steps:

$$\rho_a^{new} = \sum_b m_b W_{ab}^{MLS} \tag{3.84}$$

The corrected kernel, W_{ab}^{MLS} here can be evaluated from the following equation:

$$W_{ab}^{MLS} = [\beta_0(\vec{r_a}) + \beta_{1x}(\vec{r_a})(x_a - x_b) + \beta_{1z}(\vec{r_a})(z_a - z_b)]W_{ab} \tag{3.85}$$

where β_0, β_{1x} and β_{1z} are the coefficients of the linear correction function.

3.10.2.3. Riemann solver

This technique in the numerical simulation has been developed mainly to solve the issue of discontinuity in the flow field variable at a location in space. This issue is typical of the variation of density in the numerical SPH method, especially when the weakly compressible version is used. The Riemann solver concerns the region where the variation is high, known as the star region, which separates the shock wave from the rarefaction wave. The solution takes into account the variables located within the star region and the speeds of the shock and rarefaction waves. The numerical SPHysics code implements the non-conservative form of the Riemann solver method

which was firstly introduced into the SPH method by Parshikov et al. (1999 and 2001). This approach modifies the pressure gradient appearing in the momentum equation of the SPH method as follows:

$$\left(\frac{du}{dt}\right)_a = -\sum_b m_b 2P^*_{ab}\left(\frac{1}{\rho_a^2}+\frac{1}{\rho_b^2}\right)\nabla_a W_{ab} \tag{3.86}$$

Also, Villa (1999) proposed the following expression as an alternative modification to the pressure gradient:

$$\left(\frac{du}{dt}\right)_a = -\sum_b m_b \left(\frac{2P^*_{ab}}{\rho_a\rho_b}\right)\nabla_a W_{ab} \tag{3.87}$$

In the above two equations, the corrected pressure $2P^*_{ab}$ can evaluated from:

$$2P^*_{ab} = P_a + P_b \tag{3.88}$$

Similarly, the velocity at the centre of the line that joins two particles can be estimated from:

$$2U^*_{ab} = U^R_a + U^R_b \tag{3.89}$$

where, $U^R = \boldsymbol{u}.\left\{\frac{\vec{r}_a-\vec{r}_b}{r_{ba}}\right\}$ (3.90)

Hence, the continuity equation may change from:

$$\left(\frac{d\rho}{dt}\right)_a = \sum_b m_b(\mathbf{u}_a - \mathbf{u}_b)\nabla_a W_{ab} \tag{3.91}$$

to

$$\left(\frac{d\rho}{dt}\right)_a = -2\sum_b m_b(\boldsymbol{u}^*_{ab} - \mathbf{u}_a)\nabla_a W_{ab} \tag{3.92}$$

Now, considering the values carried by the particles, a and b as the left and right states respectively, the intermediate values of the velocity and pressure in the star region can be evaluated as:

$$U_{ab}^{*} = \frac{\rho_a c_a U_b^R + \rho_b c_b U_a^R + P_a - P_b}{\rho_a c_a + \rho_b c_b} \tag{3.93}$$

$$P_{ab}^{*} = \frac{\rho_a c_a P_b + \rho_b c_b P_a - \rho_a c_a \rho_b c_b (U_b^R - U_a^R)}{\rho_a c_a + \rho_b c_b} \tag{3.94}$$

To optimize both the numerical results and computational time, all of the techniques, including the kernel and density corrections mentioned above, are examined in two stages: first all these techniques are applied individually; second, each technique of the kernel correction is used, along with the density correction techniques separately. These are described in more detail in Section 4.3.2.1.

CHAPTER FOUR

CODE VALIDATION

Chapter Four: Code Validation

The SPHysics code has so far been applied to investigate various fluid flow problems, including wave breaking (Dalrymple & Rogers, 2006), dam-break (Crespo et al. 2008), interaction with coastal structures (Gómez-Gesteira & Dalrymple, 2004), and moving breakwaters (Rogers et al. 2010). Researchers have compared their numerical results with either the experimental observations and/or analytical results to examine the performance of the numerical SPHysics code in predicting the physical quantities of their studies. In the present investigation the code is applied to simulate the characteristics of the skimming flow over stepped spillways having slopes typical of the embankment dams in the non-aerated flow region. In order to have confidence in the numerical SPHysics model it is important to validate it against the existing published data. This chapter concentrates on the procedure of validating the numerical SPHysics model in the current investigation. To accomplish this, the results of two previously published experimental models are considered to evaluate the computational results obtained in this study. Also, it sheds light on the effects of various numerical SPH techniques implemented by numerical SPHysics code on the computational results, in terms of accuracy and computational time. Moreover, it presents the numerical results obtained in this study and compares them with the corresponding experimental results.

4.1. Experimental models considered in this study

Since the current work concerns features of the skimming flow over stepped spillways, which is characterized by free surface, turbulent and gravitational flow, the experimental results of two laboratory models featuring nearly the same flow characteristics are considered to validate the numerical SPHysics code. The first one is the experimental work of Hager and Schwalt (1994) for flow over a broad crested weir, while the second experimental work is the flow over stepped spillways on a moderate slope carried out by Meireles and Matos (2009). To characterize the flow in a more accurate way the SPS turbulent model, see Section 3.2.3.1 for more information, is applied in both test cases to introduce the effect of turbulence in the numerical simulation. In addition, as mentioned earlier, in both validation test cases

the cubic spline kernel function, see Section 3.3, is used to interpolate the flow field variables. The Verlet numerical scheme, see Section 3.5, is also incorporated to numerically integrate the differential equations. These can be justified on the grounds that these techniques have been commonly used to simulate various free surface problems that provide relatively accurate computational results without excessive computational time.

4.2. Estimation of the flow field variables

In the present work the numerical and experimental results are compared qualitatively, to see how well the numerical model captures the conditions of the flow while overtopping broad crested weirs and stepped spillways, and quantitatively to ensure that the numerical results provided by the numerical model are reliable. The quantitative comparison includes the position of the free surface, velocity profiles at various sections, and the bottom pressure on the crest of the broad crested weir due to various discharges.

The discharge value of the numerical model for both validation test cases is obtained from the flow depth and velocity profile at the critical section perpendicular to the flow direction. The critical section designates the section of the weir crest where the Froude number is equal to one. The reference discharge is calculated at the critical section from the following equation (Chow, 1959):

$$q = \sqrt{h_c^3 g} \tag{4.1}$$

where q is the discharge per unit channel width, h_c is the flow depth at the critical section on the weir crest known as the critical flow depth and g is the gravitational acceleration. In the current work the critical section for all discharges is found between half to two thirds of the crest length measured from the upstream corner, which agrees well with the range reported in Chow (1959) and André (2004). Furthermore, in this study the highest particle existing at any section perpendicular to the flow direction, taking into account the splashed particles, is considered as a free surface particle. This is marked as another advantage of the numerical SPH method, as there is no need to define the pressure of the free flow particles, as a gird

based method does (Monaghan, 1992). Moreover, velocity profile in this study is taken at various sections perpendicular to the flow direction. Each section includes a number of fluid particles, a and the velocity of each particle, v_a is estimated from the following equation proposed by Gómez -Gesteira et al. (2005):

$$v_a = \frac{\sum_b v_b W_{ab}}{W_{ab}} \tag{4.2}$$

where b denotes all fluid particles located within the influence area of the particle being considered, v_b is the velocity of neighbouring particles and W_{ab} is the kernel function.

As mentioned earlier, the repulsive boundary condition, which is used in the current work, assigns zero pressure to the boundary particles during the whole simulation time. Therefore, the pressure value at boundary particles needs to be estimated as well. In this study the pressure value of each boundary particle is estimated using the method proposed by Oger et al. (2006). In this method, the average pressure at each boundary particle is estimated from the pressure carried by the neighbouring fluid particles situated in a square region of a width equal to the diameter of the pressure instrument used in the experiments and a height of $5h$, where h is the smoothing length.

It is also worth mentioning that the Lagrangian property of the SPH numerical method applied in the present study allows us to estimate the mean velocity and pressure values at desired points from a number of successive output files, for instance 3-5 output files.

Finally, as mentioned above, two experimental works are considered in the present study to validate the numerical SPHysics code. Hence, this chapter is divided into two main sections to describe how the numerical SPHysics code is validated in the present study. Each section initially describes the physical model of the experimental work and the numerical models set up procedure, then focuses on the sensitivity analysis that is conducted in the current work to improve the numerical results, taking into account computational time; finally, the numerical results obtained in this study are presented and compared with the corresponding experimental results.

4.3. Case 1: Flow over broad crested weirs (Hager and Schwalt, 1994)

Broad crested weirs are usually used in hydraulic applications as a discharge measuring device. The crest is horizontal and the length is much larger than the flow depth, which allows the streamlines to be straight and parallel to the crest (Chow, 1959; Handerson, 1966). The flow over broad crested weirs is free surface and is driven by gravity. Also, the flow upstream of the weir is subcritical, Froude number <1, and is supercritical, Froude number >1, downstream. In between, somewhere on the weir crest, lies the critical section where the Froude number is equal to one. Froude number, F_r in the hydraulics of open channel flow can be defined as.

$$F_r = \frac{V}{\sqrt{gR}} \tag{4.3}$$

where V is the mean flow velocity in the channel, g is the gravitational acceleration and R is the characteristic depth, usually referred to the hydraulic radius. The hydraulic radius R is defined as the ratio between the wetted area, A and the wetted perimeter, P as $R= A/P$. In 2D fluid flow test cases the parameter R can be approximately represented by the flow depth (Chow, 1959; Handerson, 1966). Hence, in the current work the flow depth is applied in Equation (4.3) to determine the Froude number.

In fact, the location of the critical section depends on the discharge and the upstream weir configuration (Chanson, 2004). However, experimental results have demonstrated that the critical section usually occurs between one third and half of the crest length from the downstream corner of the weir (Chow, 1959; André, 2004). The computed discharge value on the weir crest at the critical section for various values of the total upstream head H_o are evaluated and compared with the corresponding experimental value. In the present work the value of the upstream total head H_o is estimated from:

$$H_o = h_o + \frac{V_o^2}{2g} \tag{4.4}$$

where h_o is the initial flow depth upstream of the weir and V_o is the mean approach velocity. The value of the initial depth is taken, as reported in Hager and Schwalt (1994), at a distance upstream to the weir where the flow depth does not change. Also, the mean approach velocity is deduced from the velocity profile at that section. Then, this value of the upstream total head is used to determine the numerical discharge based on the flow depth and velocity profile at the critical section on the weir crest.

Finally, it is worth mentioning that numerous experimental works have been carried out to investigate the flow properties on broad crested weirs. In the current investigation the experimental results presented by Hager and Schwalt (1994) on the flow properties over a broad crested weir of a square edge are considered in the present study to validate the SPHysics code. The validation includes comparing the computed results with the measured data in terms of the position of the water surface level, velocity profile at different sections along the crest, as well as the pressure bottom head at different boundary points along the crest for a range of discharges.

4.3.1. Description of the experimental and numerical models

Hager and Schwalt (1994) conducted their experiments to characterize the flow properties on broad crested weirs. The experimental work was performed in a horizontal and rectangular laboratory flume of 7m length, 0.499m width and 0.7m height. The weir was placed at a distance of 4.82m from the flume inlet. The broad crested weir had a sharp upstream edge, length = 0.5m, height = 0.401m and width matching the entire flume width. The discharge was varied within a range producing the total upstream head H_o, with respect to the weir crest, to be varied between 0.0509 and 0.2047m. A miniature propeller meter was used to measure the streamwise velocity profile at various sections along the weir crest, while a number of pressure taps were inserted at different points along the weir crest to measure the bottom pressure. Figure 4.1 plots the physical model tested by Hager and Schwalt (1994) in their experimental work.

Following Ferrari (2010) and Lopez e al. (2010), the upstream tank approach is used in the present work to set up the numerical computational domain. However, in this case study the length of the upstream tank and the dimensions of the weir are identical to that of the physical model of Hager and Schwalt (1994).

Figure 4.1. 2D schematic view of the physical laboratory model used by Hager and Schwalt (1994) for flow over broad crested weir.

For this purpose a number of equally spaced boundary particles were used to fix a solid wall at 4.82m to the left of the upstream corner of the weir. This wall was placed to prevent the fluid particles from leaving the solution domain at the left hand side. However, no wall was placed to the right hand side of the weir to allow the fluid particles to leave the end of the solution domain freely.

The tank between upstream of the weir and the fixed wall of the solution domain was filled with fluid particles, with an initial upstream water head of 0.375m as a maximum flow depth above the weir crest. The position of each particle was defined based on the initial distance between them, while their horizontal and vertical velocities were initially set to zero. The flow depth at the left hand side of the weir decreased gradually with time evolution, without feedback. This allowed us to obtain different total heads upstream of the weir and various unit discharges, velocity profiles and pressure distribution along the weir crest. The total simulation time was 12s and the initial time step was set to 10^{-5}s to achieve the requirements of the CFL condition.

For now in each figure the distances in both directions are metres, velocities are in metres per second, pressures are in pascals (N/m^2) and densities are in kilograms per cubic metre. Also, the colour of each particle appearing in the snapshots represents the instantaneous value of the flow variable under scope carried by that particle.

4.3.2. Sensitivity analysis

The key idea of the sensitivity analysis is to improve the computational results, while taking into consideration the computational time. In this study a sensitivity analysis is performed to: 1) identify the most efficient numerical SPH techniques, provided by the SPHysics code, used for free surface computations, and 2) optimize the initial distance between the particles. This allows the author to find out the numerical SPH techniques and particle size that provide accurate computational results with less computational cost. The following two sections demonstrate the effect of each factor individually on improving the computational results of flow over the broad crested weir.

4.3.2.1. Identifying the most efficient numerical SPH techniques

It is the purpose of this section to examine the performance of various numerical SPH techniques provided by the SPHysics code in improving the numerical results. In fact, the numerical SPH techniques examined in this section are: A) staggered and Cartesian grid methods, B) dynamic and repulsive boundary conditions, C) kernel and kernel gradient correction methods, D) Shepard and Moving least square density filters and the non-conservative Riemann solver approach. To simulate the models proposed in the present investigation in a more accurate way, the most efficient techniques, among the aforementioned numerical SPH techniques, need to be found. For this purpose, in the first stage these techniques are applied separately, then the most efficient technique of the kernel modification method and the density filter approaches are applied together. The numerical results obtained in this study using these techniques are presented in the following sections. Following Ferrari (2010) the initial distance between the particles, for both the fluid and boundary particles is fixed to 0.0075m in both directions to examine the performance of these numerical SPH techniques.

A- Staggered and Cartesian grid methods

As mentioned, staggered and Cartesian grid techniques are commonly used in numerical SPH methods to reproduce the initial condition of the computational

domain. The properties of each technique are individually presented in Section 3.6.2.2. However, in this section the performance of the staggered grid approach is compared with the Cartesian grid method to see which technique is more efficient to represent the fluid particles in the computational domain. The staggered and Cartesian grid methods produce a total number of 136924 and 69409 particles respectively. Hence, the staggered method is computationally more expensive than the Cartesian grid method. It should be noted that the repulsive boundary condition method is used herein to generate the boundary particles of the physical walls. Figures 4.2a and 4.2b show the initial condition of the numerical SPHysics code for the flow over the broad crested weir for a number of fluid particles located close to the upstream weir crest using the staggered and Cartesian grid methods respectively. These figures show that with the Cartesian grid method a smaller number of fluid particles need to be generated compared to the staggered grid method.

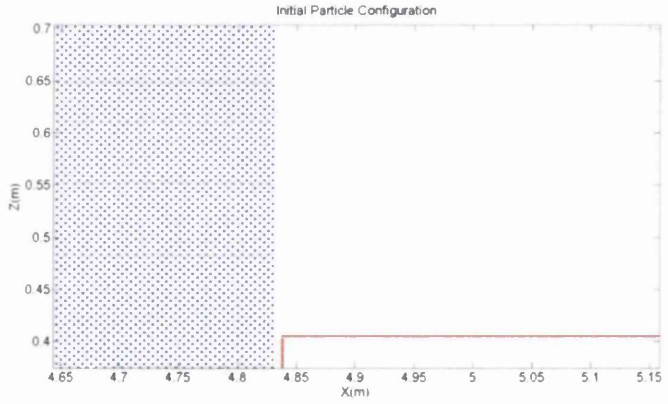

a

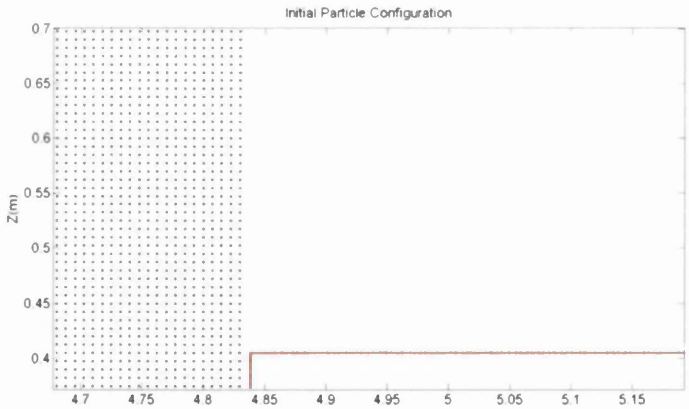

b

Figure 4.2. The initial condition of the numerical SPHysics model at t=0 for:
a) staggered gird method and b) Cartesian grid method

Table 4.1 presents the discharge values predicted by the SPHysics code $q_{SPHysics}$ with the Cartesian and staggered grid methods for different values of the total upstream head H_0 and compares them with the experimental $q_{experimental}$ values. Also, it presents the percentage of the relative error for each total upstream head value due to the difference between the computed and measured discharge. The percentage of the relative error, Relative Error %, is calculated from the following expression:

$$Relative\ Error\% = \frac{q_{SPHysics} - q_{experimental}}{q_{experimental}} \tag{4.5}$$

As can be seen from this table the differences between the computed and measured discharge are relatively high, reaching 34% as a maximum percentage relative error. The most obvious reason of these differences is that no numerical SPH technique, except the SPS turbulence model, is used for solving the governing equations and hence the numerical results are due to the standard SPH formulations. In addition, the particle size of 0.0075 may not be sufficient to produce accurate results.
Moreover, despite the fact that the staggered grid method considerably increases the computational time compared to the Cartesian grid method, no major improvements can be observed in Table 4.1 regarding the numerical results provided by the staggered grid method. Therefore, in the present study the Cartesian grid method is used to achieve satisfactory results and save execution time.

H_o (m)	$q_{experimental}$ (m^2/s)	$q_{SPHysics}$ (m^2/s) Staggered	Relative Error%	$q_{SPHysics}$ (m^2/s) Cartesian	Relative Error%
0.2047	0.13614	0.09706	-28.71	0.09430	-30.73
0.178	0.10966	0.07828	-28.62	0.07616	-30.55
0.1392	0.07518	0.05457	-27.41	0.05314	-29.32
0.1084	0.05196	0.03787	-27.12	0.03677	-29.23
0.0844	0.03562	0.02601	-26.98	0.02530	-28.97
0.0607	0.02180	0.01595	-26.84	0.01554	-28.72

Table 4.1. Comparison between the experimental and computed discharge predicted by the SPHysics code by using the staggered and Cartesian grid methods.

B- Dynamic and repulsive boundary conditions

This section presents the computed discharge values of this study produced by both the dynamic and repulsive boundary condition methods, with the corresponding experimental ones presented by Hager and Schwalt (1994) for different total upstream heads. This allows one to examine their performance in simulating the boundary walls of the physical geometry. The initial condition of the numerical SPHysics code for the flow over the broad crested weir is depicted in Figures 4.3 and 4.4, using the dynamic and repulsive boundary condition methods respectively. These figures illustrate that with the dynamic boundary condition each particular wall is represented by two layers of zig-zag particles, whereas the wall is modelled by one layer of particles with the repulsive boundary condition method.

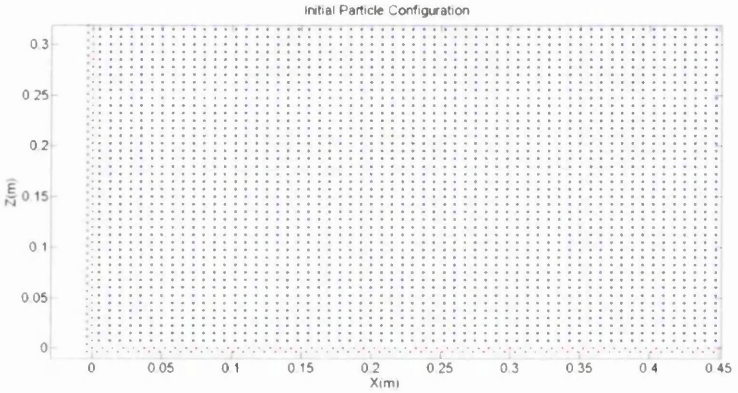

a

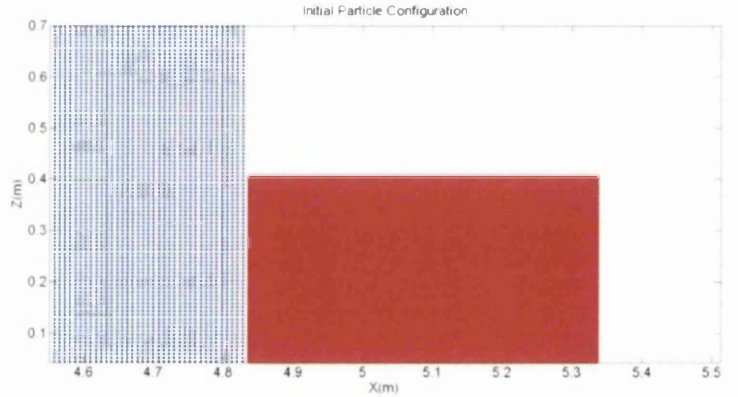

b

Figure 4.3. Initial condition of the numerical SPHysics model for the flow over the broad crested weir. The blue particles represent the fluid particles and red particles represent the dynamic boundary particles: a) near the corner and b) near the weir crest.

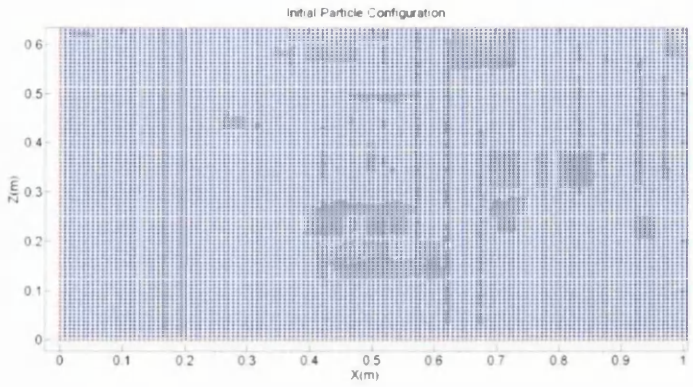

a

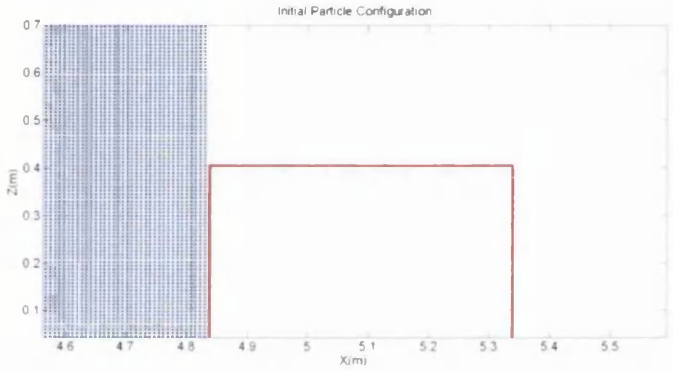

b

Figure 4.4. Initial condition of the numerical SPHysics model for the flow over the broad crested weir. The blue particles represent the fluid particles and red particles represent the repulsive boundary particles: a) near the corner and b) near the weir crest.

Figures 4.5 and 4.6 display the evolution of flow with time over the broad crested weir with the dynamic and repulsive boundary condition methods respectively at different time instants of the numerical simulation.

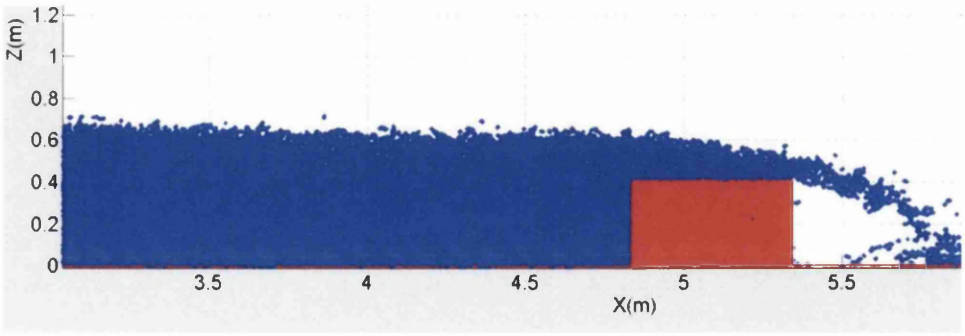

a

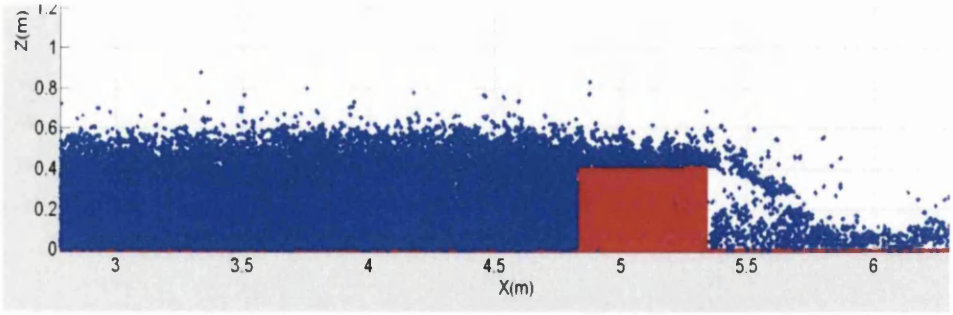

b

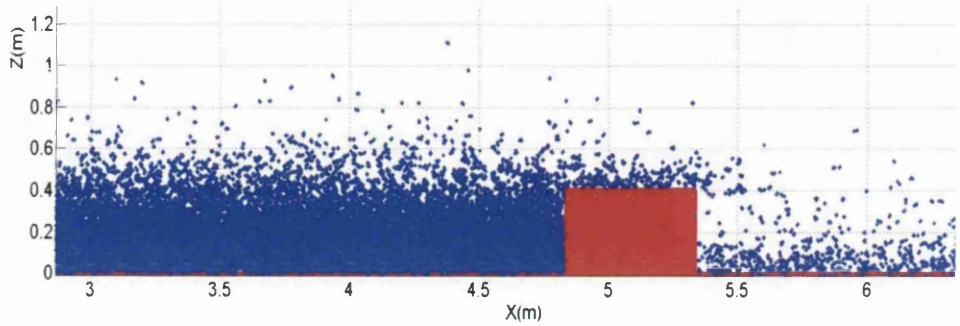

c

Figure 4.5. Evolution of flow over the broad crested weir with the dynamic boundary condition at: a) t=1s, b) t=2s and c) t=3s.

It is obvious from Figure 4.5 that despite the use of a large number of boundary particles with the dynamic boundary condition method to represent the 2D geometry of the weir, a number of fluid particles are able to penetrate the boundary walls. Meanwhile, Figure 4.6 shows that the repulsive boundary condition technique is more efficient than the dynamic boundary condition method in terms of preventing fluid particles from crossing the boundary walls. In fact, Gómez-Gesteira et al. (2012) stated that the dynamic boundary condition may not be fully impermeable and recommended using this kind of boundary condition with great care, especially in high velocity flow problems.

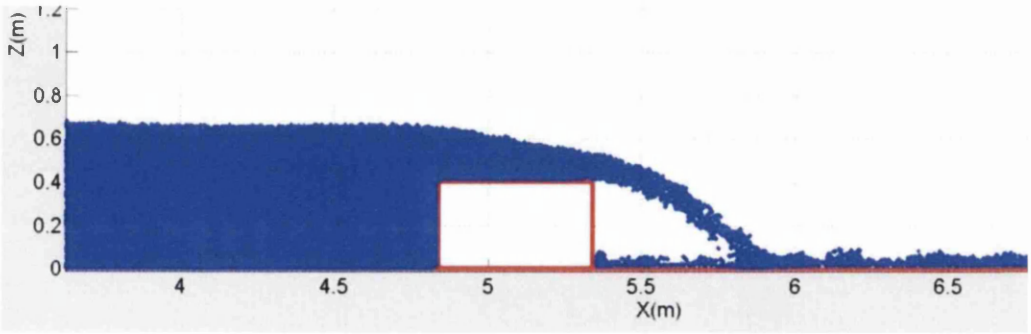

a

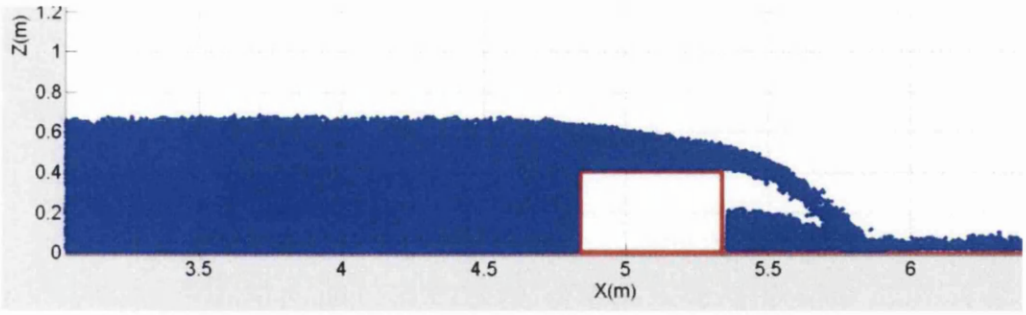

b

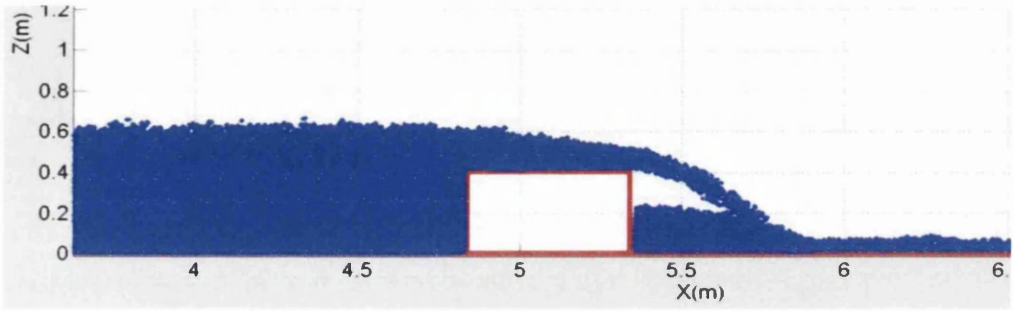

c

Figure 4.6. Evolution of flow over the broad crested weir with the repulsive boundary condition at: a) t=1s, b) t=2s and c) t=3s.

In addition, as can be observed from Figure 4.5, there are quite a few particles in the air, which may be due to the repulsion force exerted by the boundary particles on the fluid particles. To compare the numerical results of both methods, Table 4.2 shows the percentage of the relative error due to the differences between the experimental and computed discharge values provided by both the dynamic and repulsive boundary conditions. This table clearly demonstrates that for all of the total upstream head values the numerical results in terms of the discharge obtained with the repulsive boundary condition are much better than those predicted with the dynamic boundary condition. This can be attributed to the effect of the penetration phenomenon that occurred with the dynamic boundary condition. Thus, in the current work the repulsive boundary condition is used to avoid the issue of penetration and to optimize time as well.

It can be also observed that the computed discharges with the repulsive boundary condition are still far from those presented by Hager and Schwalt (1994) from their experimental work. The differences between the measured and computed discharge values can be also explained by: 1) the use of only the classical SPH formulations to solve the governing equations without the use of the recent developed numerical

particle-based techniques and 2) the use of the particle size of 0.0075, which in terms of the particle size may be relatively coarse for this particular test case.

H_o (m)	$q_{experimental}$ (m^2/s)	$q_{SPHysics}$ (m^2/s)	Relative Error%	$q_{SPHysics}$ (m^2/s)	Relative Error%
		Dynamic		Repulsive	
0.2047	0.13614	0.08306	-39.00	0.09430	-30.73
0.178	0.10966	0.06610	-39.72	0.07616	-30.55
0.1392	0.07518	0.04476	-40.46	0.05314	-29.32
0.1084	0.05196	0.03122	-39.92	0.03677	-29.23
0.0844	0.03562	0.02142	-39.89	0.02530	-28.97
0.0607	0.02180	0.01310	-39.91	0.01544	-28.72

Table 4.2. Comparison between the experimental and computed discharge predicted by the SPHysics code by using the dynamic and repulsive boundary conditions.

C- Kernel and kernel gradient correction approaches

These two numerical SPH techniques have been employed by the SPHysics code to handle numerical instabilities caused by fluid particles located close to the domain boundaries, such as the wall boundaries and free surface, due to the truncation of the kernel function. These methods are applied herein individually to: 1) see whether these techniques could improve the accuracy of the computed values and 2) find out the technique that provides numerical discharge values which are closest to the experimental results.

Table 4.3 presents the computational results provided by the SPhysics code from both techniques and compares them with the corresponding experimental results. As can be seen from this table, both techniques improve the numerical results and considerably reduce the relative errors compared to those presented in Table 4.2. These improvements in the numerical results can be attributed to the fact that the modified kernel function and modified kernel gradients play an effective role in summing up the flow field variables carried by the fluid particles, especially those located near the domain boundaries. Also, minor differences can be observed between the computational results of these two approaches, demonstrating that both perform nearly the same in terms of improving the computational results. Moreover, the execution time required for calculating the numerical results of both these

techniques is almost identical. However, in the present study the modified kernel function is used to simulate the numerical models of flow over stepped spillways.

H_o (m)	$q_{experimental}$ (m^2/s)	$q_{SPHysics}$ (m^2/s) Modified kernel function	Relative Error%	$q_{SPHysics}$ (m^2/s) Modified kernel gradients	Relative Error%
0.2047	0.13614	0.1005	-26.18	0.10046	-26.25
0.178	0.10966	0.8144	-25.73	0.08132	-25.85
0.1392	0.07518	0.05592	-25.62	0.05604	-25.46
0.1084	0.05196	0.03876	-25.41	0.03880	-25.33
0.0844	0.03562	0.02664	-25.21	0.02660	-25.32
0.0607	0.02180	0.01636	-24.95	0.01632	-25.14

Table 4.3. Comparison between the experimental and computed discharge predicted by the SPHysics code by using the modified kernel function and modified kernel gradients.

Further, it can be observed that the computational results are still away from the experimental data, as the maximum absolute relative error is approximately 26%. This may because the modifications of the kernel function and its gradients have just fixed the numerical instabilities caused by a number of particles located near the domain boundaries, and the issue of pressure oscillations still exists. Figures 4.7a to 4.7c depict the pressure flow field predicted by the SPHysics code with the modified kernel function and modified kernel gradients at time instants of t=4.5s, 5.5s and 6.5s respectively. These figures clearly show that although the kernel function and its gradients are modified in such a way as to handle the truncation of kernel function close to the boundaries of the computational domain, fluctuations with high amounts still appear in the pressure flow field. The explicit determination of the pressure on the fluid particles using the equation of state could be the main source of these fluctuations.

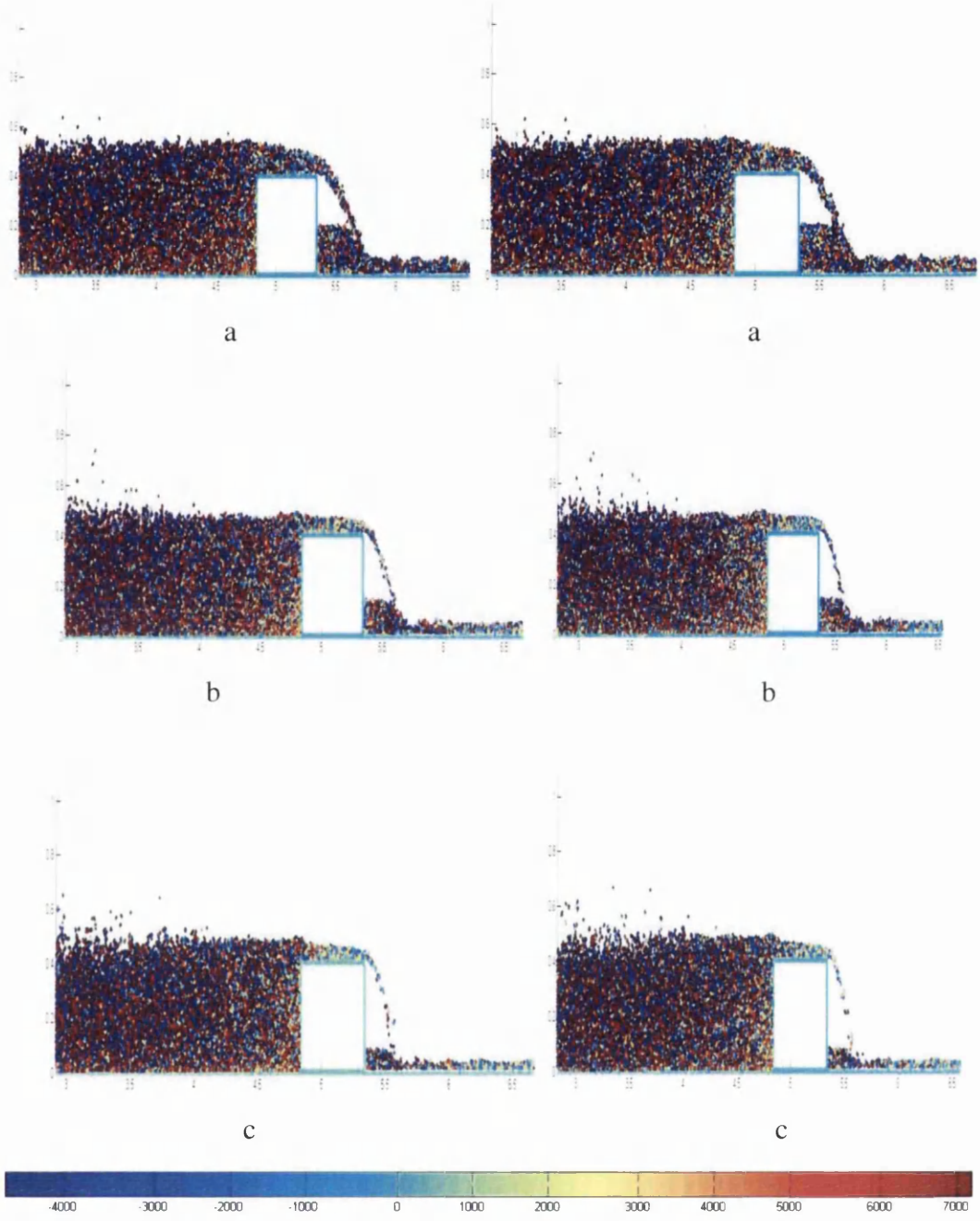

Figure 4.7. Pressure flow field with colour-coded pressures predicted by the numerical SPHysics code with the modified kernel function (left) and modified kernel gradients (right) at: a) t=4.5s, b) t=5.5s and c) t=6.5s.

D- Numerical SPH density filter approach

To smooth out the fluctuations in the density flow field remaining from the previous numerical simulations it is necessary to apply density filters. The SPHysics code applied in this study implements three different methods, namely; Shepard, MLS and non-conservative Riemann solver. The features of each technique are described in detail in Sections 3.7.5, 3.7.6 and 3.7.7 respectively. However, in this section these three approaches are applied separately to evaluate their capability in removing oscillations in the flow fields. Table 4.4 shows the discharge values produced by each of the density filter techniques mentioned above for various values of the total upstream heads. Also, the percentages of the relative error due to the differences with the corresponding experimental data are presented.

This table shows that with the Riemann solver the maximum percentage absolute relative error is minimum compared to the Shepard and MLS techniques. This demonstrates that the Riemann solver performs significantly better than the Shepard and MLS density filters in removing the fluctuations in the density field.

H_o (m)	$q_{experimental}$ (m^2/s)	$q_{SPHysics}$ (m^2/s) Shepard	Relative Error%	$q_{SPHysics}$ (m^2/s) MLS	Relative Error%	$q_{SPHysics}$ (m^2/s) Riemann Solver	Relative Error%
0.2047	0.13614	0.11104	-18.45	0.11120	-18.32	0.11828	-13.11
0.178	0.10966	0.09006	-17.87	0.09076	-17.24	0.09572	-12.71
0.1392	0.07518	0.06184	-17.74	0.06244	-16.95	0.06578	-12.50
0.1084	0.05196	0.04290	-17.44	0.04342	-16.45	0.04560	-12.24
0.0844	0.03562	0.02948	-17.25	0.02990	-16.06	0.03132	-12.07
0.0607	0.02180	0.01806	-17.06	0.01834	-15..87	0.01920	-11.93

Table 4.4. Comparison between the experimental and computed discharge predicted by the SPHysics code by using the Shepard, MLS and Riemann solver density filters.

Figures 4.8 to 4.10 display the pressure evolution at four different time instants during the numerical simulation, as predicted by the SPHysics code obtained with the Shepard, MLS and Riemann solver techniques respectively. These figures show that the Riemann solver is more efficient than the Shepard and MLS techniques in

removing the oscillations in the pressure flow field. This could be due to the mechanisms by which the Riemann solver performs the removal of such oscillations. In addition, the Riemann solver updates the density and pressure flow fields every time step, while the Shepard and MLS density filters need to be applied occasionally, for instance every 30 time steps, to avoid excessive execution time. It can also be observed that the performance of both the Shepard and MLS techniques is approximately the same. However, it is worth mentioning that the Riemann solver increases the computational time by 15% compared to the other two density filter approaches. Although the calculation time of the non-conservative Riemann solver is more than the Shepard and MLS method, the Riemann solver technique is used in this study in order to keep the flow field variables as smooth as possible and to simulate the characteristics of the flow over broad crested weirs and stepped spillways in a more accurate way.

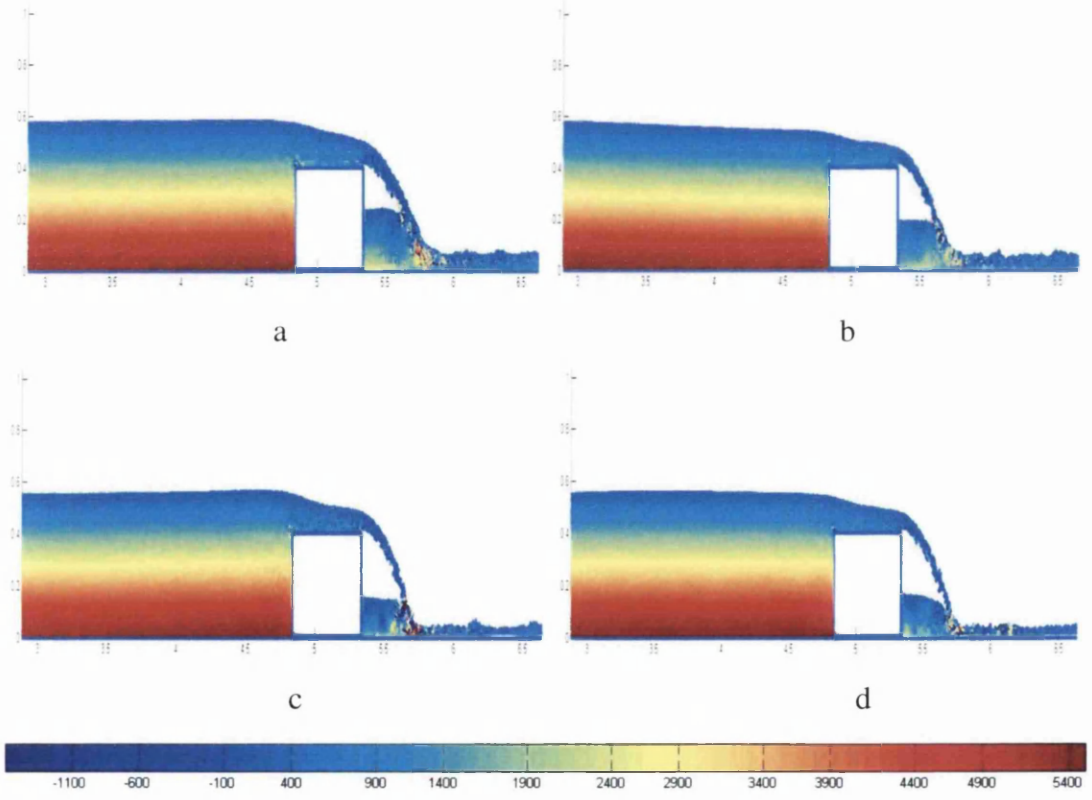

Figure 4.8. Pressure flow field with colour-coded pressure values predicted by the numerical SPHysics code with the Shepard density filter at: a) t=4.5s, b) t=5.5s, c) t=6.5s and d) t=7.25s.

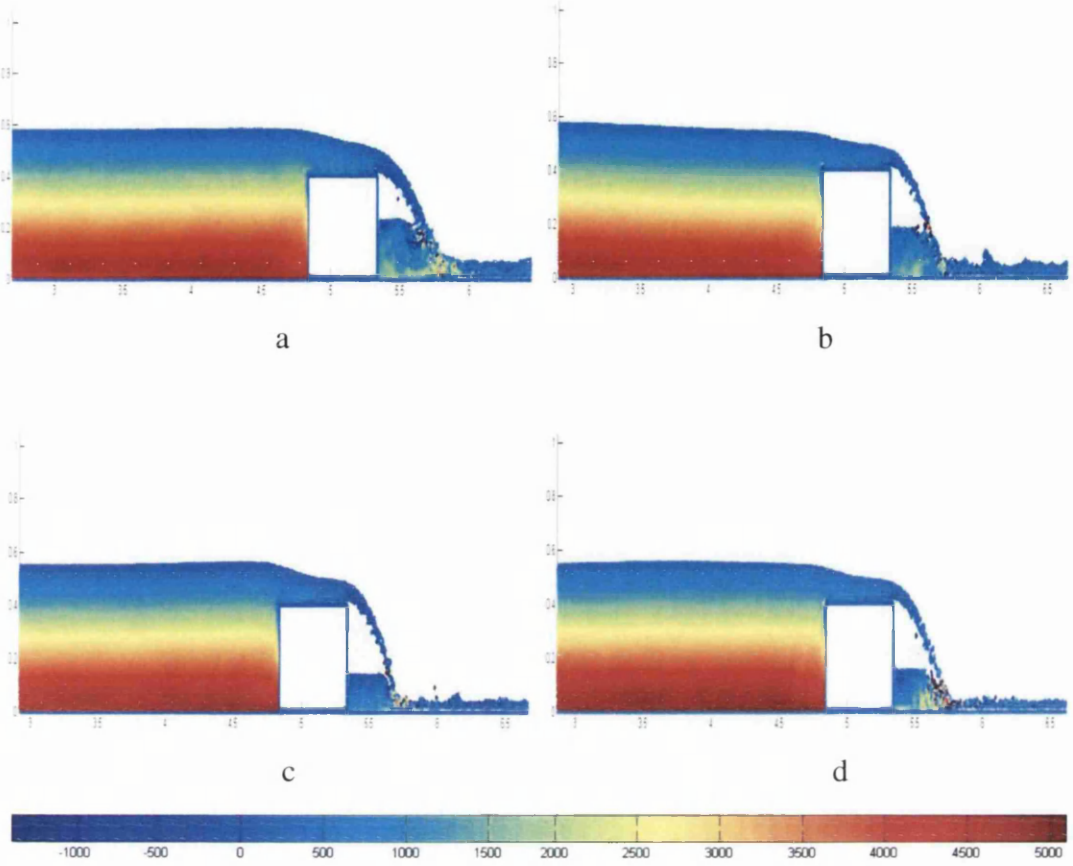

Figure 4.9. Pressure flow field with colour-coded pressure values predicted by the numerical SPHysics code with the MLS density filter at: a) t=4.5s, b) t=5.5s, c) t=6.5s and d) t=7.25s.

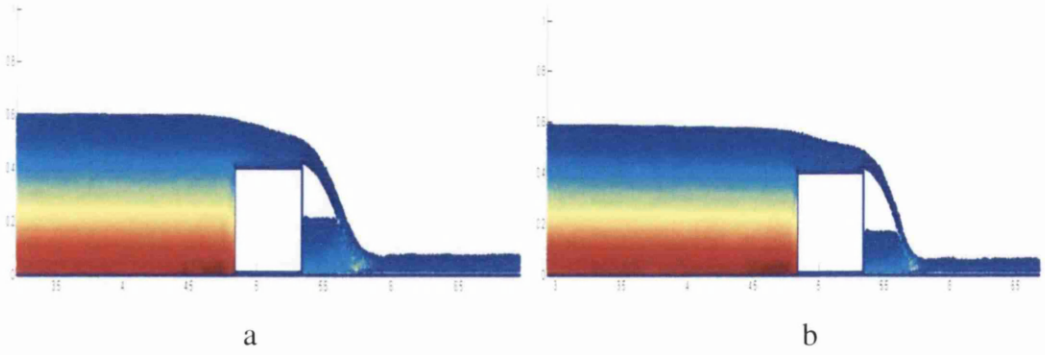

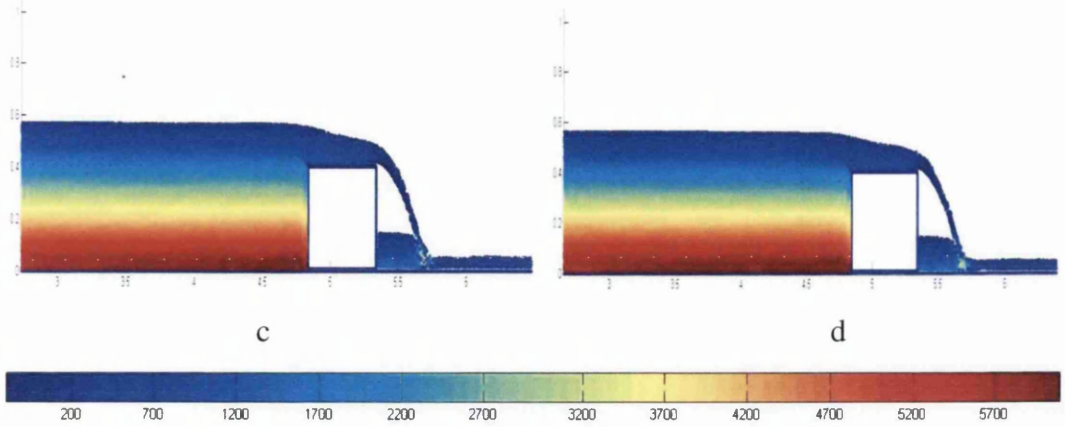

Figure 4.10. Pressure flow field with colour-coded pressure values predicted by the numerical SPHysics code with the Riemann solver density filter at: a) t=4.5s, b) t=5.5s, c) t=6.5s and d) t=7.25s.

E- Modified kernel function approach combined with the non-conservative Riemann solver approach.

Sections D and E confirm that the modified kernel function and Riemann solver effectively contribute in improving the computational results of the SPHysics code when they are applied separately. In this section both of them are applied together in an attempt to increase the accuracy of the numerical results. The computational results of this case are presented in Table 4.5 and compared with the results gathered from the experimental work. It is obvious that the accuracy of the computational results is considerably improved when these two numerical methods are both used. This is because the modified kernel function may solve the compactness issue of the kernel function, while the non-conservative Riemann solver could reduce the considerable amount of the fluctuations occurring in the flow field.

Figures 4.11a to 4.11d show the pressure flow field over the broad crested weir predicted by the numerical SPHysics model obtained with the modified kernel function and Riemann solver technique, at time instants of t= 4.5s, 5.5s, 6.5s and 7.25s respectively. From these figures it can be concluded that the accuracy of the computed discharges is increased when the modified kernel function and the Riemann solver density filter techniques are applied together. Hence, both these

numerical SPH approaches are utilized together in the current investigation to accurately simulate the subsequent numerical models.

H_o (m)	$q_{experimental}$ (m^2/s)	$q_{SPHysics}$ (m^2/s) Riemann Solver& modified kernel function	Relative Error%
0.2047	0.13614	0.12132	-10.89
0.178	0.10966	0.09922	-9.52
0.1392	0.07518	0.06794	-9.63
0.1084	0.05196	0.04750	-8.58
0.0844	0.03562	0.03268	-8.27
0.0607	0.02180	0.01994	-8.52

Table 4.5. Comparison between the experimental and computed discharge predicted by the SPHysics code by using the modified kernel function and the Riemann solver density filters.

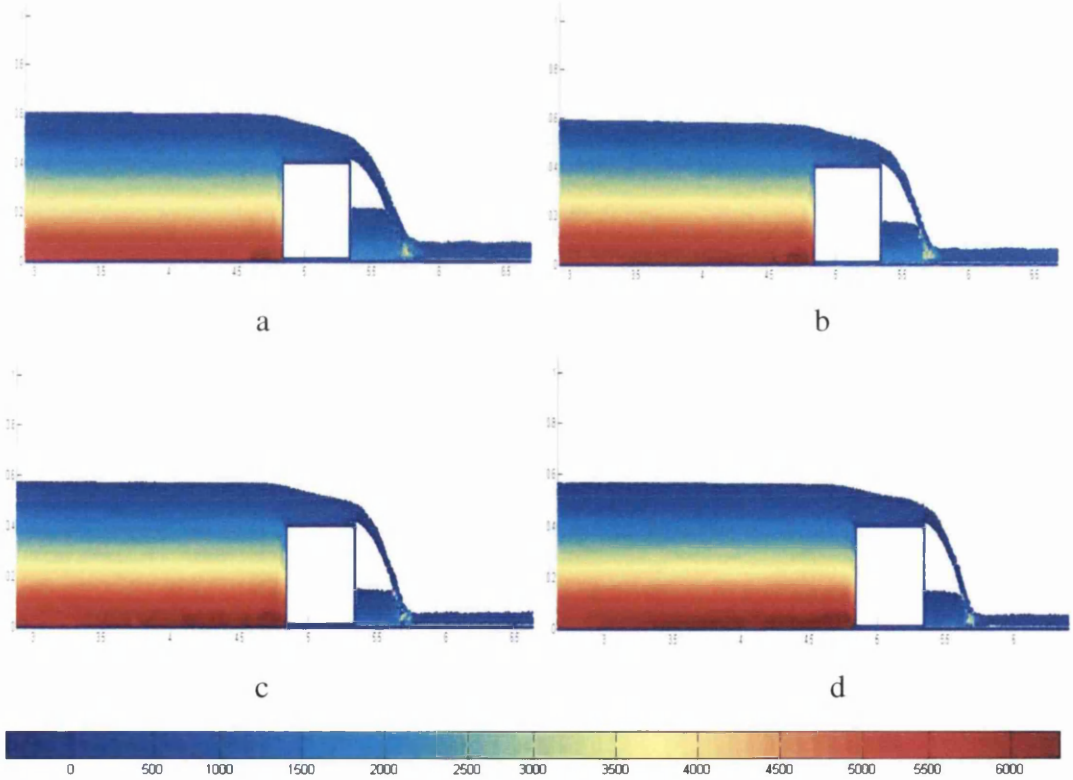

Figure 4.11. Pressure flow field with colour-coded pressure values predicted by the numerical SPHysics code with the modified kernel function and Riemann solver density filter at: a) t=4.5s, b) t=5.5s, c) t=6.5s and d) t=7.25s.

4.3.2.2. Optimizing the initial distance between the particles

The above section presents the most efficient numerical SPH techniques required to accurately simulate free surface flow over the hydraulic structures that are the concern of the current work. As has been observed, the numerical results provided by the SPHysics code in terms of the discharge above the weir crest are still far from those documented by Hager and Schwalt (1994) in their experimental work. However, the computed discharges presented in the above section are obtained with only one particle size, of 0.0075m. It is therefore essential to examine different particle sizes in order to increase the accuracy of the computational results. This section aims to find the particle spacing which best improves the numerical results and optimizes the computational time. Four different resolutions, of 0.01, 0.0075, 0.005 and 0.003 are used herein to perform the convergence study in terms of the initial distance between both the fluid and boundary particles. These resolutions produce a total number of particles of 45345, 67985,123456 and 234567 respectively.

Table 4.6 shows the percentages of the relative error produced by each particle size examined in the present study for various values of the total upstream head. The error is due to the difference between the computed and measured discharge values. As can be observed from this table, the error is increased when the distance between the particles is increased. This can be attributed to the fact that as the particles are placed far away from each other a smaller number of them will be included in the interpolation procedure to estimate the velocity at the points located along the critical section. In addition, it is observed that for all values of the total upstream, when the initial distance between particles is smaller than 0.005m the discharge value is slightly improved and the computational time is considerably increased.

H_o (m)	Relative error%				
	Particle size (m)	**0.003**	**0.005**	**0.0075**	**0.01**
0.2047		-5.20	-5.50	-10.89	-12.81
0.178		-4.05	-4.50	-9.52	-11.78
0.1392		-4.12	-4.58	-9.63	-10.91
0. 1084		-4.07	-4.46	-8.56	-9.04
0.0844		-4.55	-4.95	-8.27	-9.94
0.0607		-3.12	-3.67	-8.52	-9.83

Table 4.6. Convergence study for optimizing the initial distance between the particles by using four different resolutions to compare between experimental and numerical values of discharge.

Moreover, it is worth mentioning that for all values of the total upstream head, the SPHysics code under-predicts the discharge of the experimental work, even when the smallest particle spacing, 0.003m, is used. This may be due to the fact that Equation (4.1), which is used to calculate the reference discharge in the present study, is basically derived on the basis that: 1) the pressure distribution on the weir crest is hydrostatic and 2) the energy loss between the upstream corner of the weir and the critical section is so small that it can be considered to be negligible. Nevertheless, from Table 4.6 one can consider that 0.005m is probably the most appropriate value of the particle spacings among the other values examined in this study, in terms of the accuracy and the time required for computing the numerical results. Therefore, the initial distance between the boundary and fluid particles in both directions is fixed to 0.005m to run the subsequent numerical models of flow over the broad crested weir.

4.3.3. Comparison of the computational results with the experimental data

In this section the results obtained from the experimental work of Hager and Schwalt (1994) are compared with the numerical results provided by the SPHysics code. As mentioned earlier, the comparison is divided into two the parts: qualitative and quantitative comparisons.

Before beginning with the qualitative comparison, it is worth explaining the flow conditions of overtopping broad crested weirs. The flow over a broad crested weir is

a free surface problem. Along with the internal force, the flow is also influenced by the gravitational force to overtop the weir crest, and in form it looks like a jet. As time evolves the flow hits the bottom floor of the right tank with large deformations at some distance downstream of the weir, depending on the total head of water upstream to the weir, forming a nappe at the end of the crest. At this instant a portion of the flow continuously returns towards the weir body, which gradually increases the flow depth in the region under the jet. Then this region gradually empties as both the head and the velocity of the jet decrease. As shown in Figures 4.12a to 4.12f, these flow conditions are depicted from the snapshots of the numerical simulation for the flow over the broad crested weir at different time instants. These snapshots demonstrate that the computational results provided by the SPHysics code are qualitatively in good agreement with the experimental data, demonstrating that the numerical SPHysics code captures the physical behaviour of the flow over broad crest weirs well.

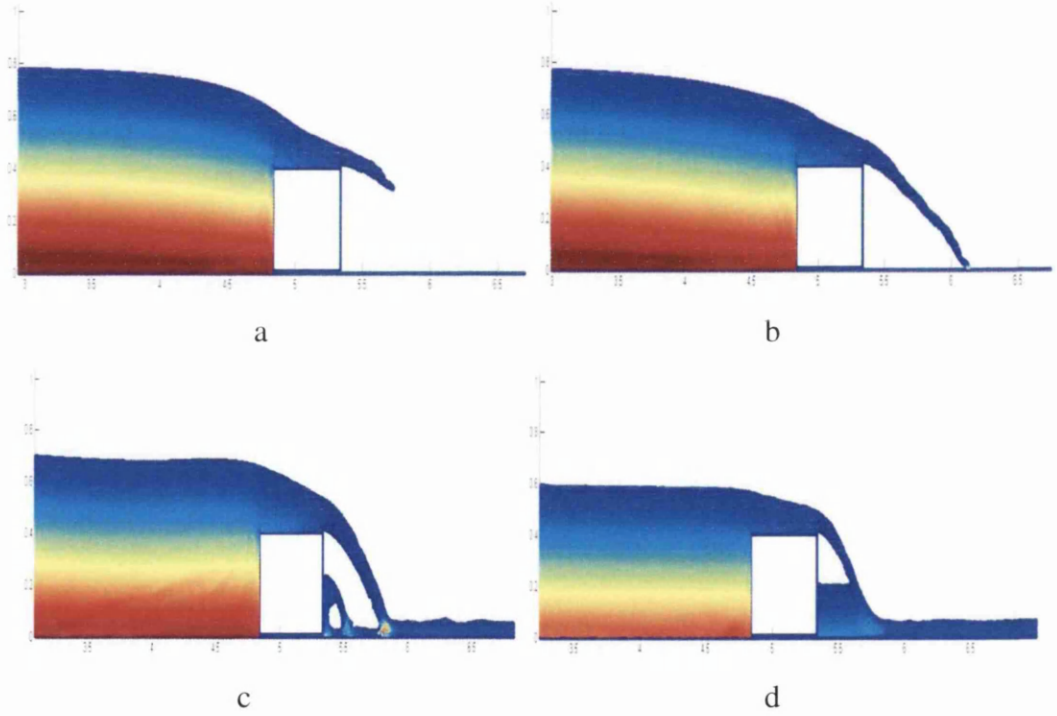

a b

c d

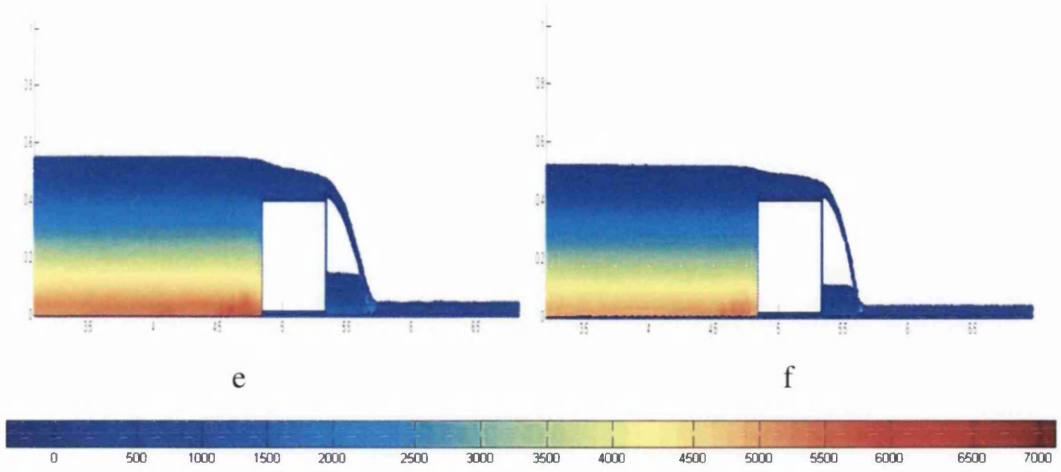

Figure 4.12. Snapshots of free surface profile at: (a) t=0.4s, (b) t=0.55s, (c) t=1.35s, (d) t=4.9s, (e) t=8.0s and (f) t=11.5s of flow over the broad crested weir predicted by the SPHysics code with colour-coded pressures.

Now the quantities of the flow field variables predicted by the numerical SPHysics code will be presented and compared with the experimental data. This includes the position of the free surface, velocity profiles at different sections along the weir crest and the pressure head at different points along the top of the weir.

Hager and Schwalt (1994) presented different free surface profiles due to various discharge rates. Figure 4.13 displays the experimental and computed free surface profiles, in which x represents the horizontal distance originating at the upstream edge of the weir and y is the position of the free water surface relative to the weir crest. The maximum absolute relative error due to the difference between the experimental and numerical values is found to be less than 8.0%. This error may be due to the difference in discharge value produced by both the experimental and numerical results. However, it can be concluded that although the numerical results tend to slightly under-predict the measured results, especially for high discharges, the numerical model predicts the position of free surface well for all discharges.

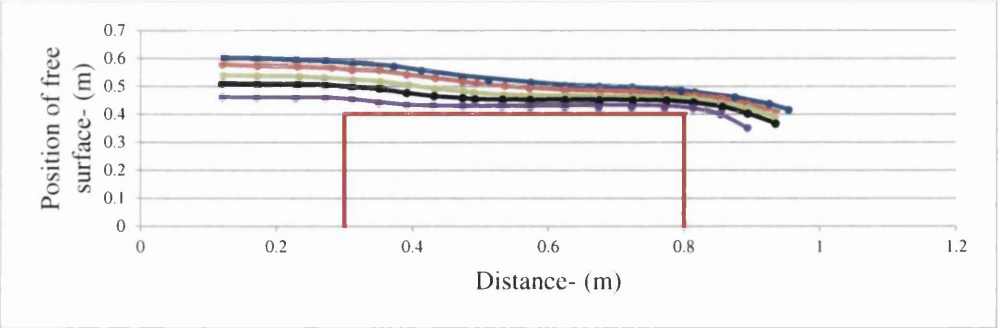

Figure 4.13. Comparison between experimental (continuous curves) and numerical SPHysics (circles) free surface positions for some test runs: Run11 (——) Run10 (——) Run9 (——) Run8 (——) and Run6 (——).

Velocity profiles measured by Hager and Schwalt (1994) at different sections along the crest of the weir for the maximum discharge are compared with those predicted by the SPHysics code. The horizontal component of the flow velocity u was measured at different points in the direction perpendicular to the flow and at different distances from the upstream weir corner. Figures 4.14a to 4.14d show these velocity profiles in terms of the normalized velocity $u/(2gH_o)^{1/2}$, and normalized vertical distance y/H_o at sections $x/H_o = 0, 0.5, 1$ and 2 respectively, where g is the gravitational acceleration and H_o is the total upstream head. The horizontal velocity of flow at the upstream edge of the weir at $x/H_o=0$ is rapidly varied over a short distance in the vertical direction on the weir crest. This is the region where water attaches to the body of the weir and hence the thickness of the boundary layer is small. Negative velocities were measured by Hager and Schwalt (1994) and well predicted by the SPHysics numerical model at $x/H_o=0.5$. The negative velocity is due to the presence of some eddies moving in a recirculation region next to the upstream corner of the weir. The formation of this region may be due to the square edge configuration of the weir used in the experimental work. Further downstream from the upstream edge and specifically at $x/H_o=1$ and $x/H_o=2$ the flow velocity has reached its peak value at relatively higher distances from the weir crest. This reveals that the thickness of boundary layer increases along the weir length.

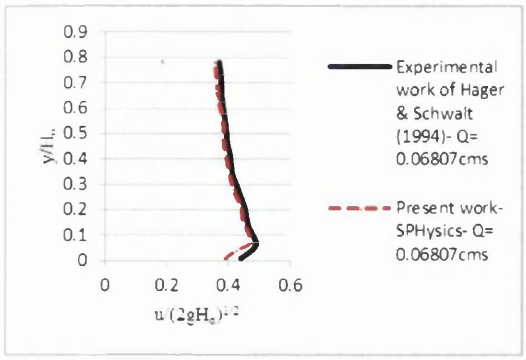

a

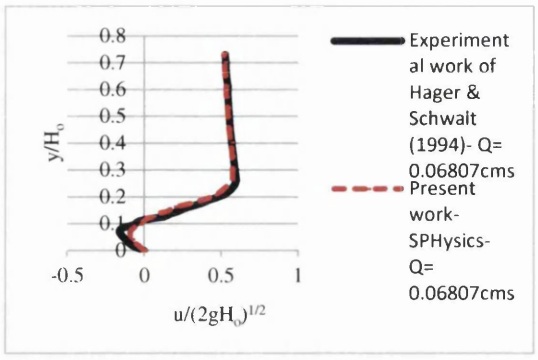

b

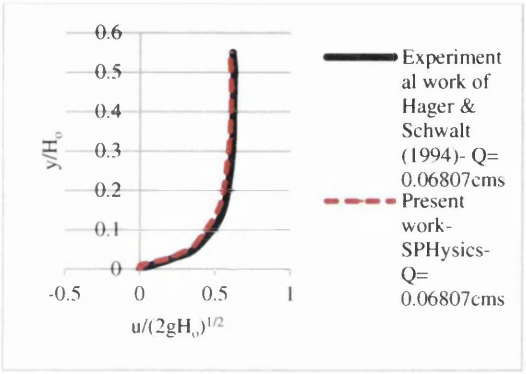

c

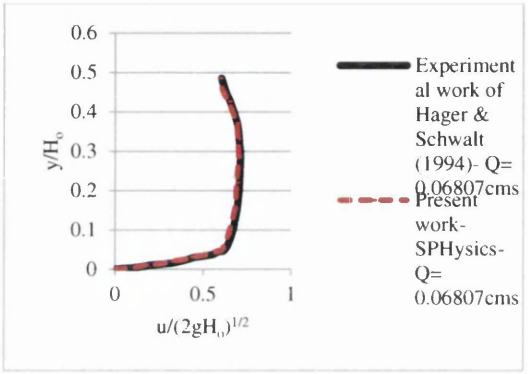

d

Figure 4.14. Comparison between the experimental and SPHysics numerical velocity profiles at sections: (a) $x/H_o=0$, (b) $x/H_o=0.5$, (c) $x/H_o=1$ and (d) $x/H_o=2$.

Figures 4.15a to 4.15d present variations of the horizontal flow velocity along the weir crest obtained from the numerical SPHysics code applied in the current work. Overall, one can observe that both the value and shape of the velocity profiles predicted by the SPHysics code are in close agreement with the corresponding experimental results.

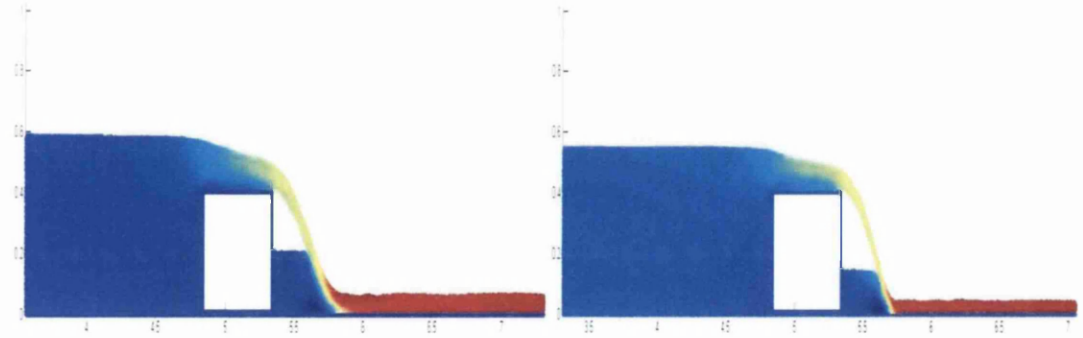

a

b

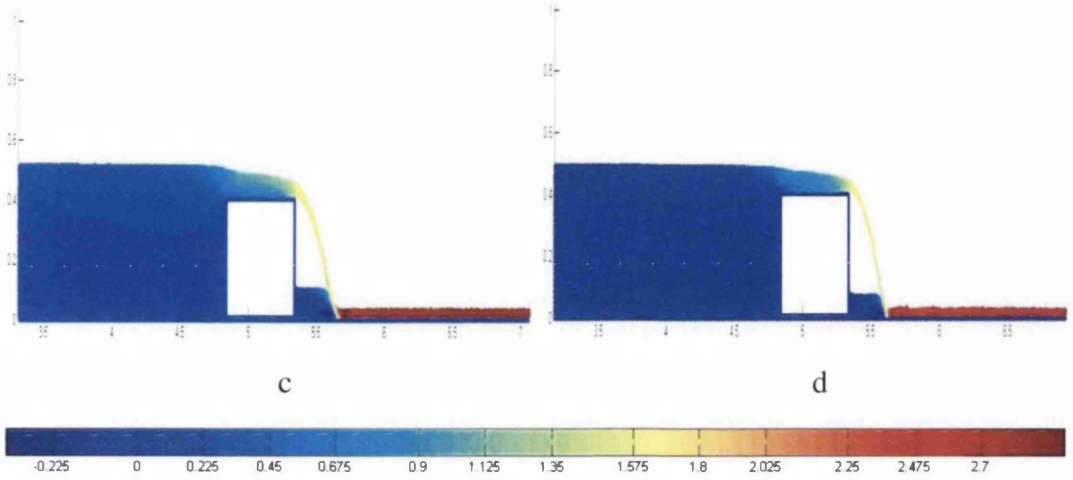

Figure 4.15. Variation of the horizontal velocity of flow along the weir crest with colour-coded velocities: (a) H_o=0.204m, (b) H_o=0.178m, (c) H_o=0.1392m and (d) H_o=0.1084m.

Finally, Hager and Schwalt (1994) characterized the bottom pressure head along the weir crest using pressure taps. Figure 4.16 illustrates both the normalized pressure heads $(P/\rho gH_o)$ measured at different points along the weir crest and those predicted by the SPHysics code for one set of experimental discharge values. In fact, the highest relative error, due to the difference in the experimental and computational results, is about 9%. This indicates that the numerical values are in reasonably good agreement with the corresponding experimental values, especially in predicting the value and position of both the minimum and maximum pressures.

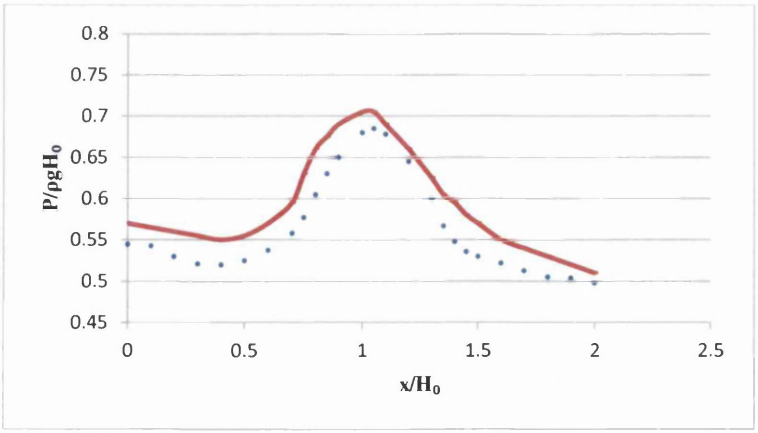

Figure 4.16. Comparison between the experimental (continuous curve) and SPHysics (circles) numerical values of pressure head above the weir crest - Run11.

4.4. Case 2: Characteristics of skimming flow region in the non-aerated flow region on moderate slopes (Meireles and Matos, 2009)

The aim of this section is to verify the numerical SPHysics code based on the experimental results gathered by Meireles and Matos (2009). They conducted their experiments on a laboratory model to investigate the features of skimming flow condition in the non-aerated flow region over a moderate slope stepped spillway. This section starts with a description of both the experimental and numerical models, then the experimental results are compared with the computational results in terms of the flow depth and velocity profile at different sections along the non-aerated flow region for a range of discharges typical of skimming flow conditions.

4.4.1. Description of the experimental and numerical models

Experimental work was conducted by Meireles and Matos (2009) to investigate the properties of skimming flow in the non-aerated region on a stepped spillway of 1V:2H bottom slope. The model consisted of a broad crested weir of a semi-circular shape upstream corner. The height and length of the weir were 0.5m, and ten identical steps of 0.05m height were used to fit the downstream slope. Figure 4.17 is the 2D plot of the laboratory stepped spillway model tested with all parameters required to define the skimming flow conditions in the non-aerated flow region. In addition, Meireles and Matos (2009) used point gauges to measure the flow depth, in order to locate the position of the free surface along the non-aerated flow region. Also, a pitot tube was used to measure the streamwise velocity at different sections perpendicular to the pseudo bottom originating at the outer edge of steps, located in the non-aerated flow region.

The main objective of their study was to determine the coordinates of the inception point of air entrainment for a range of flow rates, represented by the normalized critical depth above the weir crest h_c/h_s, where h_c is the critical flow depth and h_s is the step height, $1.27<h_c/h_s<1.74$, typical of the skimming flow conditions. The authors in their investigation defined the inception point as where white water starts to appear along the slope and across the entire width of the chute.

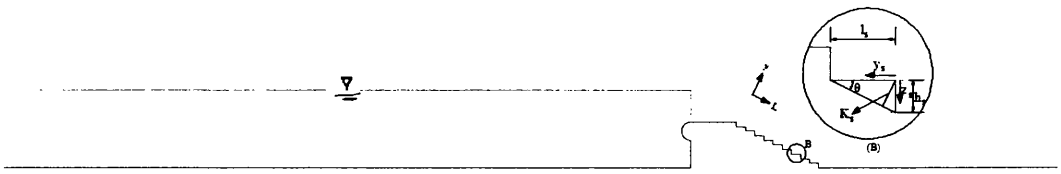

Figure 4.17. 2D schematic representation of the laboratory model used in the experimental work of Meireles and Matos (2009) for flow over a stepped spillway.

In the present work the repulsive boundary particle is used to represent the solid walls of physical geometry. In addition, fluid particles are initially placed to the left hand side of the stepped spillway using the Cartesian grid approach. The initial distance between each pair of particles, both fluid and boundary, is 0.005m, determined by a convergence study in Chapter 4. In fact, in the computations different lengths are initially assigned to the length of the tank upstream of the broad crested weir in an attempt to diminish the wavy free surface observed by the author in the upstream tank during the simulation tests. The occurrence of this phenomenon can be partly attributed to the fact that the boundary particles along the left wall of the domain produce a repulsive force, forcing fluid particles to move forward and flow over the weir. In contrast, the repulsive force from the boundary particles of the upstream wall of the weir acts in the opposite direction and hence the nearby water particles move towards the left wall of the domain. Both of these movements of water particles cause the free surface to be unstable and wavy. It was found that a tank length of 7.5m is sufficient to achieve an almost stationary condition of the free surface on the upstream tank. Ferrari (2010) also used this length to study the characteristics of flow over sharp crested weirs. Therefore, in this case a solid wall is placed 7.5m upstream of the broad crested weir and the distance between them is filled with fluid particles with an initial upstream head of 0.175m as a maximum flow depth with respect to the crest level.

In this case study the whole simulation time is 15s and the time step is initially set to 10^{-4}s to fulfil the CFL condition. Following Meireles and Matos (2009), Equation (1.1) proposed by Chanson (1994), see Chapter 1, is used in this test case to ensure the establishment of the skimming flow condition, while Equation (4.1) is used to determine the discharge overflowing the stepped spillway.

Finally, it should be noted the numerical SPH techniques which have been found from the sensitivity analysis of the present work, see Section 4.3.2.1A to section 4.3.2.1E, are also applied herein to simulate the properties of the skimming flow conditions above the stepped spillway studied in this case study.

4.4.2. Comparison between the experimental and computational results

The flow over stepped spillways is free surface and it is driven by gravitational acceleration. When water flows over stepped spillways with rates typical of the skimming flow condition, it flows over the weir crest like a jet and hits the horizontal face of nearly all the steps downstream of the weir. The flow can be divided into two parts: the first part is the main flow represented by the stream, which coherently skims over the pseudo bottom formed by the step outer edges (Chanson, 2002). The second part is the secondary flow which often forms under the main flow and is the flow entrapped in the recirculation zone located inside the step cavity, delimited by both the horizontal and vertical faces. In this zone some water particles continuously return towards the vertical face of the steps and rotate in a triangular area, then eject back to the main flow. The height of the triangular area is nearly the same as the step height, whereas the base is about two thirds of the step tread (André, 2004). In the current work after 4.5s, almost all the aforementioned flow features are achieved, which reveal that the conditions of the skimming flow regime have been attained. In Figures 4.18a to 4.18d, four snapshots are shown from the simulation predicted by the numerical SPHysics code at different time instants. These figures show the capability of the numerical model to capture the physical behaviour of the skimming flow condition over moderate stepped spillways.

The following section presents the computational results obtained in the current work and compares them with the corresponding experimental results gathered by Meireles and Matos (2009). Convergence analysis in terms of the particle size is also performed in this test case using four particle sizes: 0.003, 0.005; 0.0075 and 0.01m,

providing four different total number of particles: 621332, 233691, 100820 and 56768 respectively.

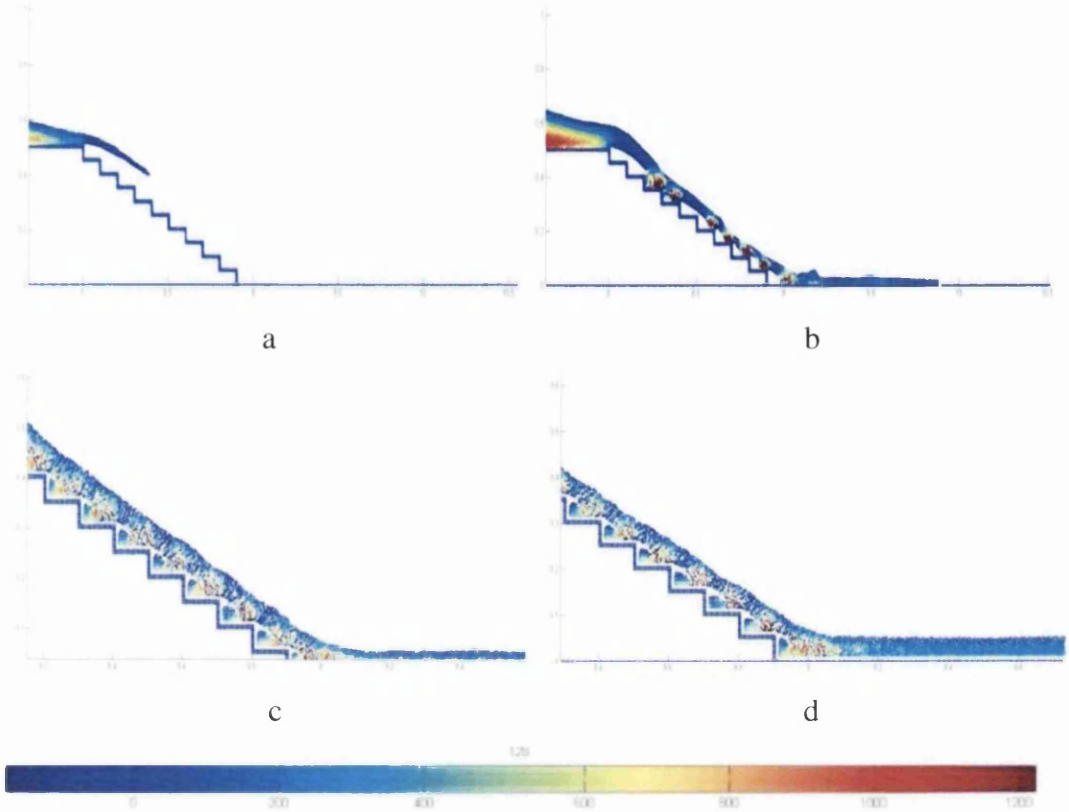

Figure 4.18. Snapshots of flow over stepped spillways predicted by the SPHysics numerical code applied in this study at (a) 0.45s, (b) 1s, (c) 5s and (d) 6.4s with pressure colour-coded.

The percentages of the relative error due to the difference between the experimental and computed discharge for different critical flow depths h_c, initial distance between particles dx and total number of particles np are presented in Table 4.7. As can be observed in this table, using the particle size 0.005m produces good optimization in terms of computational time and accuracy.

h_c (m)	Relative error%				
	dx (m)	**0.003**	**0.005**	**0.0075**	**0.01**
	np	**621332**	**233691**	**100820**	**57678**
0.087		-5.35	-5.63	-11.8	-14.7
0.07935		-4.25	-4.71	-9.94	-12.35
0.0716		-3.52	-4.00	-8.32	-10.12
0.0635		-4.07	-4.45	-7.25	-9.27

Table 4.7. Convergence analysis in terms of particle size and percentage of the relative error as a result of the differences between experimental and SPHysics numerical values of discharge for different values of the critical depths.

Table 4.8 presents the experimental and SPHysics numerical values of discharge per unit width q for different critical flow depths over the weir crest h_c examined in the experimental work. Apparently, for all values of h_c the numerical model under-predicts the experimental results with an absolute maximum error of 5.63%. This indicates that the numerical values in terms of the discharge agree reasonably well with the experimental results.

h_c (m)	$q_{experiment}$ (m^2/s)	$q_{SPHysics}$ (m^2/s)	Relative error%
0.087	0.0804	0.0755	-5.63
0.07935	0.070	0.0667	-4.71
0.0716	0.060	0.0576	-4.00
0.0635	0.050	0.0478	-4.45

Table 4.8. Comparison between the experimental and SPHysics numerical values of discharge per unit width, for particle spacing of 0.005m.

Also, based on their experimental data for free surface positions along the chute slope in the non-aerated flow region for various discharges, Meireles and Matos (2009) developed the following two equations to define the coordinates of the inception point:

$$\frac{L_i}{K_s} = 5.25(F_*)^{0.95} \quad (4.6)$$

$$\frac{d_i}{K_s} = 0.28(F_*)^{0.68} \quad (4.7)$$

where L_i is the length to the inception point, d_i is the flow depth at the inception point, K_s is the roughness height perpendicular to the pseudo bottom which can be determined from $K_s = h_s \cos\theta$ and F_* is the roughness Froude number defined by $F_* = q_w/\sqrt{g \sin\theta K_s^3}$ where q_w is the discharge per unit channel width, g is the gravitational acceleration and θ is the bottom slope of the stepped spillway.

The experimental values of the flow depth along the chute slope d, normalized by the flow depth at the inception point d/d_i, were correlated with L/L_i, where L is the length measured from the upstream end of the spillway, as below:

$$\frac{d}{d_i} = 0.971 + 0.891e^{-3.41(L/L_i)} \tag{4.8}$$

The numerical flow depths along the chute slope predicted by the SPHysics code obtained in this study for the range of discharges tested in the experimental work, $1.27 \leq h_c/h_s \leq 1.74$, are compared with the corresponding experimental values. In practice, Equations (4.6), (4.7) and (4.8) are used to perform this comparison as not all experimental data gathered by Meireles and Matos (2009) is available. Figure 4.19 plots the computed and measured free surface profile d along the chute slope L in the non-aerated flow region for a range of flow rates, represented by h_c/h_s. The comparisons demonstrate a very good agreement between the experimental and SPHysics numerical results with a maximum relative error between measured and simulated flow depth of less than 10%. In addition, it is clear that the rapid flow without aeration in the non-aerated flow region decreases the flow depth along the chute slope towards the inception point of air entrainment. This has been clearly observed by most of researchers (e.g. Ohtsu & Yasuda, 1997; Chanson, 2002; Meireles and Matos, 2009) who investigated the skimming flow conditions in the non-aerated flow region on stepped spillways of moderate slopes.

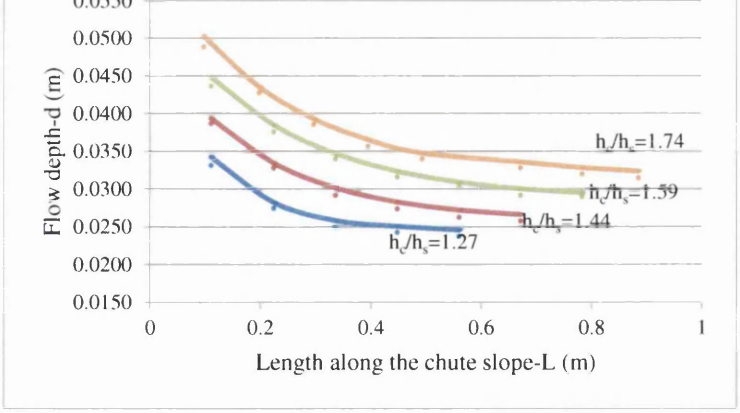

Figure 4.19. Comparisons between the experimental (curves) and numerical (circles) free surface profiles along the chute slope for different discharges represented by h_c/h_s.

It is worth mentioning that the current work estimates the start point of air entrainment based on the hypothesis of Chanson (2002), stating that it corresponds to the point downstream of the weir crest where the turbulent boundary layer intersects the free surface. To do so, the thickness of the turbulent boundary layer δ along the chute slope is determined from the velocity profiles along the chute slope for different discharges. The thickness of the turbulent boundary layer refers to that point of the velocity profile above which the velocity is 0.99 of the maximum flow velocity. Figure 4.20 shows the determination of the inception point of air entrainment for $q= 0.05\ m^2/s$ and $2.2 \leq L/K_s \leq 5$.

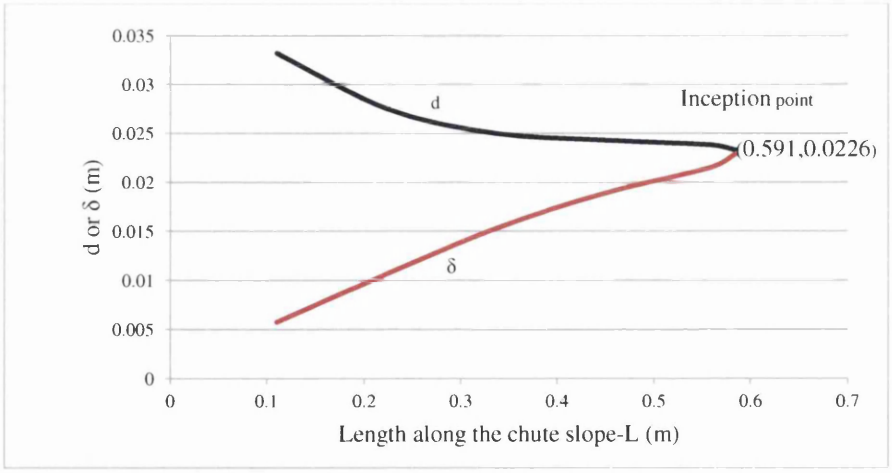

Figure 4.20. The inception point of air entrainment determined by the SPHysics code from the intersection point of numerical free surface with the developed turbulent boundary layer for $q=0.05m^2/s$ and $2.2 \leq L/K_s \leq 5$.

Table 4.9 shows a comparison between the experimental results of Meireles and Matos (2009) and the SPHysics numerical predictions, in terms of the coordinates of the inception point for the range of discharges tested in the experimental work. The experimental results are deduced from Equations (4.6) and (4.7), while the numerical results are estimated based on the definition of the inception point defined above. From Table 4.9 it can be noticed that the maximum percentage relative error among the experimental and numerical results is about 6.15%, demonstrating a reasonable agreement between them.

h_c/h_s	$d_{i\text{-}exp.}$ (m)	$d_{i\text{-}SPHysics}$ (m)	Relative error%	$L_{i\text{-}exp.}$ (m)	$L_{i\text{-}SPHysics}$ (m)	Relative error%
1.27	0.0235	0.0226	-3.83	0.566	0.591	4.42
1.44	0.0266	0.0255	-4.14	0.673	0.708	5.20
1.59	0.0295	0.0280	-5.08	0.779	0.821	5.40
1.74	0.0325	0.0305	-6.15	0.884	0.934	5.66

Table 4.9. Comparison between the experimental and SPHysics numerical results in terms of the coordinates of the inception point of air entrainment for different normalized discharge h_c/h_s values.

In the current work the velocity flow field along the chute slope predicted by the SPHysics for h_c/h_s= *1.74* and 1.59 are plotted in Figures 4.21a and 4.21b respectively. Apparently, different velocity distributions on the steps can be observed along the flow direction. The flow velocity at steps close to the weir crest is relatively low and is almost constant over the entire flow depth. This indicates that the thickness of the boundary layer is small. Then the velocity increases towards the downstream and reaches its peak value at a section called the inception point of air entrainment. At this section the flow velocity varies across the whole flow depth, revealing that the boundary layer has fully developed.

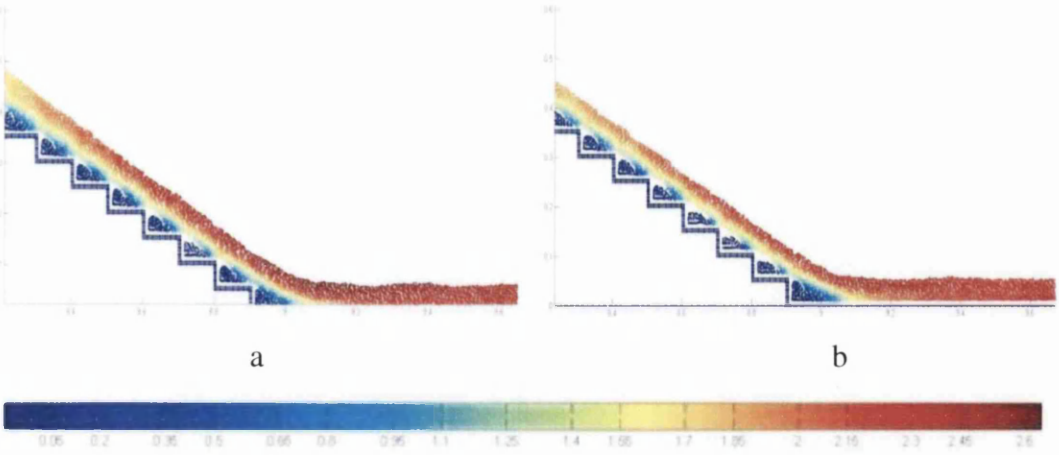

Figure 4.21. Variation of flow velocity over a stepped spillway, predicted by the SPHysics code applied in this study, with colour-coded velocities: (a) h_c/h_s= *1.74* and (b) h_c/h_s= *1.59*.

Furthermore, Meireles and Matos (2009) measured the flow velocity *V* parallel to the flow direction along the chute slope *L* with an origin at the downstream corner of the weir in different sections due to various discharges. Figures 4.22 and 4.23 show the velocity profiles provided by the experimental and numerical models within the non-aerated flow region in *L=0.11*m, and the inception point respectively. In these profiles *y* refers to the distance of the point at which the flow velocity was measured from the step outer edge, taken at any section perpendicular to the pseudo bottom. As can be seen from these figures there is a slight difference between the numerical and experimental velocity values with a maximum relative error of 4.5%, the shapes of the velocity profiles are very similar.

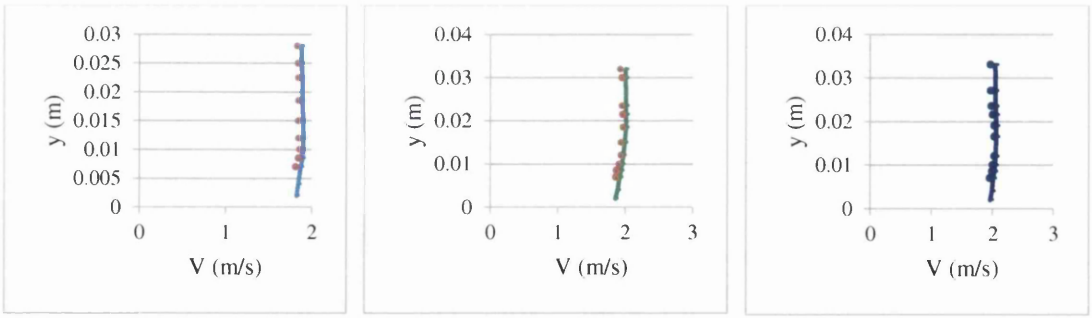

a b c

Figure 4.22 Comparison between the experimental (continuous lines) and SPHysics numerical (circles) velocity profiles at L= 0.11m. (a) h_c/h_s=1.27, (b) h_c/h_s=1.44 and (c) h_c/h_s=1.59.

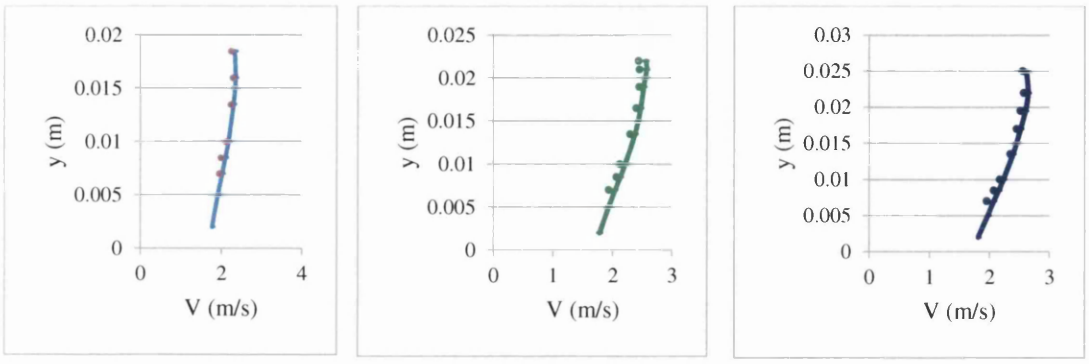

a b c

Figure 4.23 Comparison between the experimental (continuous lines) and SPHysics numerical (circles) velocity profiles at the inception point. (a) h_c/h_s=1.27, (b) h_c/h_s=1.44 and (c) h_c/h_s=1.59.

From the above two case studies it can be observed that the numerical SPHysics code, as an implementation of the computational smoothed particle hydrodynamics method, is capable of simulating the properties of skimming flow condition over stepped spillways. Therefore, this numerical code is applied to simulate all the computational models proposed in this investigation. It is worth mentioning here that in this study the values of C_s and ϵ are taken as 0.12 and 0.5 respectively for calculating the turbulent eddy viscosity in Equation (3.45) and the velocity of fluid particles in Equation (3.52). This is justified on the ground that these values are the default values of the SPHysics code applied in the present work. However, it would be interesting to conduct a sensitivity analysis by using different values for both parameters in order to investigate their impact on the accuracy of the computational results.

The next chapter presents and discusses the computational results obtained in this study in terms of the position of the free water surface and inception point of self-aeration over the horizontal and upward inclined steps.

CHAPTER FIVE

RESULTS AND DISCUSSION:

Free surface profile and inception point of air entrainment

Chapter Five: Results and Discussion: Free Surface Profile and Inception Point of Air Entrainment

5.1. Introduction

This chapter concentrates on the computational results provided by the numerical SPHysics code applied in the present work. Initially, the parameters needed to generate the computational domain of numerical models tested in the current work will be described. Then the numerical results obtained in this study in terms of the position of the water surface level and the location of the inception point of air entrainment will be presented and discussed.

5.2. Numerical models of the present study

As mentioned earlier, the current study is conducted to characterize the skimming flow conditions in the non-aerated flow region over moderate slope stepped spillways using horizontal and upward inclined steps. For this purpose twenty six numerical cases are prepared and examined in the present work. The following sections present details of the physical parameters required to create the geometry of the numerical models.

5.2.1. Chute slope

Chanson (2002) stated that when the bottom slope of a stepped spillway is flatter than 27^{o} and steeper than 16^{o}, the structure is usually known as a moderate slope stepped spillway. Also, this slope is commonly used in the design of the downstream face of embankment dams. In addition, McLean and Hansen (2000) and Matos (2002) revealed that bottom inclinations of 26.6^{o} and 18.4^{o} are the most common slopes used in the design of the downstream face of embankment dams. However,

Gonzalez (2005) used chute slopes of 16° and 21.8° for conducting his laboratory experiments to investigate the properties of skimming and transition flow conditions on embankment dams. Moreover, two different stepped spillways slopes of 30° and 18.4°, were examined by André (2004) to investigate the flow conditions over moderate slope stepped spillways. In the current investigation three slopes (18.4°, 21.8° and 26.6°) are examined to cover the range of moderate slope stepped spillways. For simplicity, from now these three slopes will be represented by 1V:3H, 1V:2.5H and 1V:2H respectively.

5.2.2. Step height

To explore what effect the step height has on the flow properties of the skimming flow condition, three different step heights 0.06, 0.09 and 0.12m are considered with the horizontal steps. For the upward inclined steps the step height is fixed to 0.09m and three step inclinations of 1V:6H, 1V:4H and 1V:3H are examined with each chute slope. The step heights are selected in such a way as to scale and to satisfy the requirements of Froude similitude in stepped spillways. However, the step height in practice could be either 0.30m, 0.60m or 0.90m, based on the construction techniques available for placing roller compacted concrete (Boes and Matos, 2000). However, Chanson (2000a), Gonzalez & Chanson (2004) and Chanson & Gonzalez (2005) reported that to apply the Froude similitude satisfactorily in stepped spillways it is necessary to use the step height $h_s > 0.02m$ and keep the Reynolds number $Re > 10^5$. Also, Matos (2001) observed in his experimental work that the results in terms of the location of air entrainment were identical with model scales of 1:6 and 1:25. Finally, Boes (2003) and Boes & Hager (2003) reported that in order to achieve the Froude model similitude in stepped spillways, the scale ratio, which can be defined as the ratio between the prototype and model dimensions, needs to be no greater than 15. Accordingly, the step heights of 0.06, 0.09 and 0.12m that are tested in the present study produce scale ratios of 10, 6.67 and 5 respectively, when 0.60m is considered as the step height in the prototype structure. In addition, all the discharge values tested in the numerical models of the current work provide Reynolds number higher than that recommended above, i.e. $Re > 10^5$. Hence, the computational results obtained in this project can be used in the design of moderate slope stepped spillways of heights 0.30, 0.60 and 0.90m.

5.2.3. The crest and discharge

Broad crested weirs are usually used in the design of embankment dams and/or steeped spillways of moderate slopes (Chanson, 2002). In addition, as mentioned in Section 4.3.2.1, broad crested weirs are also used to measure the discharge based on the critical flow depth on the weir crest. The main parameters that need to be considered in the design of a broad crested weir are the length and height of the weir. The crest needs to be long enough to allow the streamlines to flow parallel above the crest. Also, in order to establish the critical flow condition on broad crested weirs, it is essential to keep the ratio between the crest length and the total upstream head with respect to the weir crest greater than 1.5 (Chow, 1959). The total upstream head in the approach section, which is located at a distance from the upstream corner of the weir where the flow is considered to be uniform, can be approximately estimated by applying the Bernoulli equation between that section and the critical section on the weir crest, and by neglecting the head losses between them.

The critical flow depth h_c has been widely used in steeped spillways, not only to determine the discharge over stepped spillways, but to predict the type of the flow regime, such as nappe, transition and skimming, as well. Since the present study focuses on the characteristics of the skimming flow regime, the critical flow depth is important to estimate, to:

1- satisfy the attainment of skimming flow conditions.
2- determine the length of the weir crest.

As mentioned earlier in Section 1.3.2, various equations have been proposed to define the onset of the skimming flow regime over stepped spillways. However, the following equation, which was derived by Chanson (2002) based on laboratory and prototype data, is used in the present study to identify the skimming flow regime on horizontal steps:

$$\frac{h_c}{h_s} > 1.20 - 0.325\frac{h_s}{l_s} \quad (5.1)$$

where h_s and l_s respectively refer to the height and length of the steps.

The reason behind using Equation (5.1) in this study can be justified on the ground that it provides higher values of the critical depth compared to the other equations available in the literature. Hence, it gives the author more confidence regarding the attainment of the skimming flow conditions, which often occur with relatively high discharges.

Further, Equation (5.2) shown below, is used to ensure that the skimming flow condition is established in the present work on upward inclined steps. This equation was proposed by Chinnarasri and Wongwises (2004), based on their experimental data, to determine the onset of the skimming flow regime on the upward inclined step:

$$\frac{d_c}{h_s} > (0844 + 0003\vartheta)(\frac{h_s}{l_s})^{-0.513+0.004\vartheta} \quad (5.2)$$

where ϑ is the angle of the upward inclined step. They also reported that Equation (5.2) is valid on stepped spillways having slopes steeper than 1V:10H and flatter than 1V:1.75H. Since the three chute slopes tested in the present work, 1V:2H, 1V:2.5H and 1V:3H, are within the range recommended by Chinnarasri and Wongwises (2004), Equation (5.2) is used herein to predict the minimum discharge required to establish the skimming flow regime on upward inclined steps over moderate slope stepped spillways.

It is worth mentioning here that the range of the skimming flow regime examined in the present study is $1.10 \leq h_c/h_s \leq 2.90$. The minimum and maximum values of h_c/h_s appearing in this range are due to the horizontal step of heights 0.12m and 0.06m respectively. However, the maximum critical flow depth on the weir crest tested in this study is about 0.20m. Having determined the approximate value of the maximum total upstream head, based on the maximum critical flow depth, the crest length of 0.5m might be sufficient to fulfil the condition recommended by Chow (1959) for the occurrence of the critical flow depth on broad crested weirs. In fact, this value of crest length is used in the design of all the numerical stepped spillway

cases examined in the present study to investigate the inception point, position of water surface flow, velocity profiles, pressure distributions over both the horizontal and upward inclined steps.

Furthermore, the experimental data of the pressure variation on the vertical face of steps within the non-aerated flow region of steeply sloping stepped spillway presented by Amador et al. (2006) and Amador et al. (2009) showed that the pressure may drop to the sub-atmospheric value, which may cause cavitation to form close to the step outer edge for critical flow depths h_c greater than 0.15m. Accordingly, negative pressure values on moderate slope stepped spillways may attain at critical flow depths higher than on steep slopes, as the mean velocity on steep slopes is higher compared to the flatter slopes. Indeed, this encourages us to carry out an investigation to predict the maximum permissible discharge above which cavitation commences. To achieve this, the numerical stepped spillway models need to be tested for values of h_c/h_s higher than those examined for predicting the position of the free surface level, velocity profiles and pressure distributions. The crest length in such cases also needs to be increased in order to establish the condition of the critical flow above the weir crest. For this purpose, eight numerical models have been set up to investigate the cavitation formation based on the cavitation index number. Four of these models are for horizontal steps with two step heights of 0.05 and 0.075m and two chute slopes of 1V:2H and 1V:3H. Meanwhile, the other four models represent upward inclined steps having heights identical to those used with the horizontal steps. In addition, for these cases the step inclination with the horizontal face is set as the same as the chute slope. Moreover, the spillway height of these eight models is fixed to 1.2m and the range of the discharge in terms of the dimensionless critical flow depth tested is $4.0 < h_c/h_s < 9.0$. The maximum and minimum dimensionless critical flow depths of this range are respectively due to the step heights of 0.05 and 0.075m. Accordingly, based on the recommendation of Chow (1959) regarding the establishment of the critical depth on the weir, the crest length for these eight numerical models is set to 1.2m. Therefore, the computational results obtained on these two step heights can be applied on prototype stepped spillways of step heights 0.6 and 0.9m with the scale ratio of 1:12.

Overall, twenty-six numerical stepped spillways cases have been set up and divided into two main groups: the first group is represented by eighteen cases, which are designed to investigate the location of the inception point of air entrainment, position

of the water surface level, velocity distribution and energy dissipation rate. The second group consists of eight cases prepared to study the potential for cavitation damage. It should be noted that these stepped spillway models are equally divided between the horizontal and upward inclined steps. Tables 5.1 and 5.2 present the details of the first and second groups respectively for the numerical models prepared in the present investigation. In addition, Figures 5.1 and 5.2 demonstrate the 2D physical geometries of the numerical stepped spillways cases of the first and second groups respectively.

5.2.4. Run of the numerical models

In the present study the numerical 2D SPHysics serial version code, as an implementation of the computational smoothed particle hydrodynamics technique, is used to run the numerical stepped spillway models mentioned above. Since the present investigation concentrates on the properties of the skimming flow regime, the numerical results are obtained in each numerical model when:

1- almost all of the conditions of this flow regime, as laid out in Chapter 1, are achieved during the simulation time.
2- the flow properties, especially the flow depth and flow velocity, upstream of and above the weir crest, are almost constant for 3-4 consecutive time steps.

It is worth mentioning here that the initial flow depth upstream of the weir for stepped spillway cases is categorized under the first and second groups with respect to the weir crest being set to 0.45m and 1.00m respectively. The total simulation time for all cases is set to 12sec, with an initial time step of 10^{-4}sec to achieve the requirements of the CFL condition.

Stepped spillway				Steps				Range of skimming Flow condition
length (m)	height (m)	no. of steps	slope (degree)	shape	height (m)	length (m)	step inclination (degree)	h_c/h_s
0.5	1.08	18	1V:2H	Horizontal	0.06	0.12	0	2.0-2.80
			1V:2.5H			0.15		
			1V:3H			0.18		
		12	1V:2H		0.09	0.18		1.5-1.95
			1V:2.5H			0.225		
			1V:3H			0.27		
		9	1V:2H		0.12	0.24		1.15-1.45
			1V:2.5H			0.3		
			1V:3H			0.36		
		12	1V:2H	Upward inclined	0.09	0.18	1V:6H	1.50-2.0
							1V:4H	
							1V:3H	
			1V:2.5H			0.225	1V:6H	
							1V:4H	
							1V:3H	
			1V:3H			0.27	1V:6H	
							1V:4H	
							1V:3H	

Table 5.1. First group numerical stepped spillway cases.

Stepped spillway				Steps				Range of skimming flow condition
length (m)	height (m)	no. of steps	slope (degree)	shape	height (m)	length (m)	step inclination (degree)	h_c/h_s
1.2	1.2	24	1V:2H	Horizontal	0.05	0.1	0	5.0-6.5
		24	1V:3H			0.15		5.5-7.0
		16	1V:2H		0.075	0.15		5.5-6.5
		16	1V:3H			0.225		6.0-7.5
		24	1V:2H	Upward inclined	0.05	0.1	1V:2H	6.0-7.5
		24	1V:3H			0.15	1V:3H	6.5-8.5
		16	1V:2H		0.075	0.15	1V:2H	6.5-8.0
		16	1V:3H			0.225	1V:3H	7.0-9.0

Table 5.2. Second group numerical stepped spillway cases.

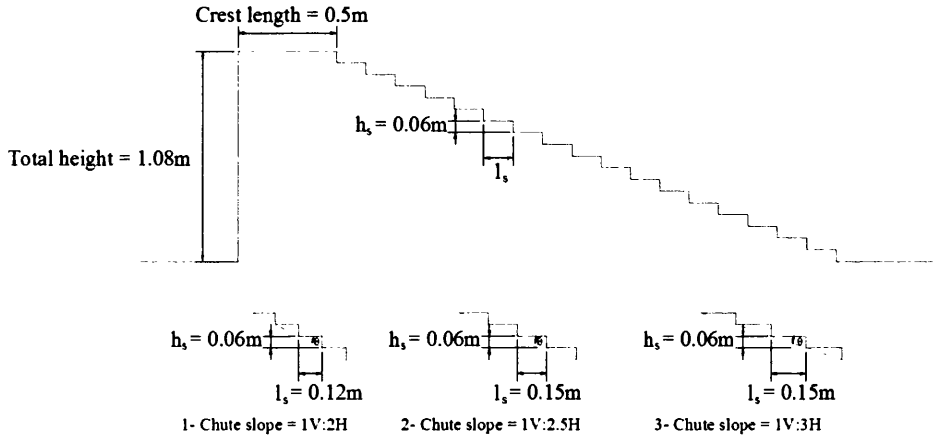

a) horizontal steps with height 0.06m.

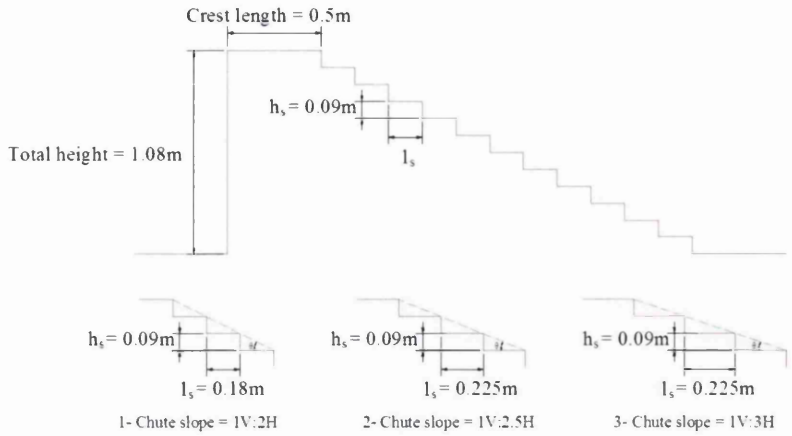

b) horizontal steps with height 0.09m.

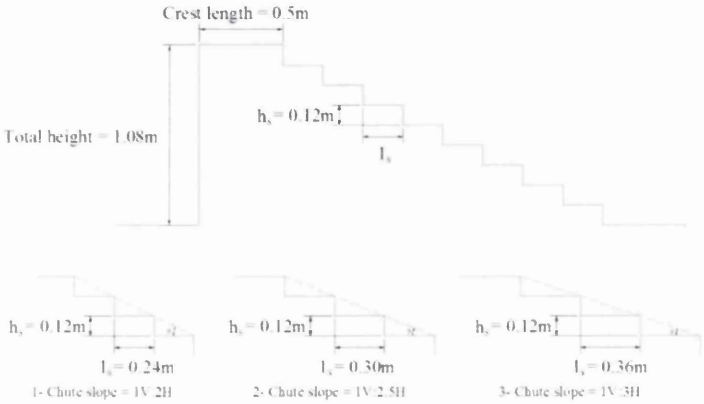

c) horizontal steps with height 0.12m.

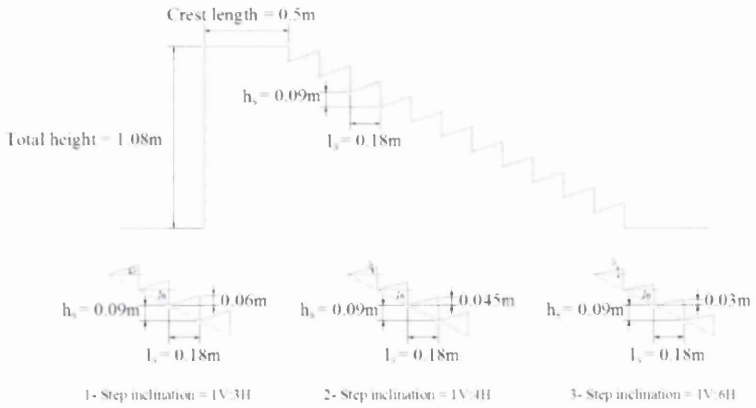

d) upward inclined steps with height 0.09m over the chute slope 1V:2H.

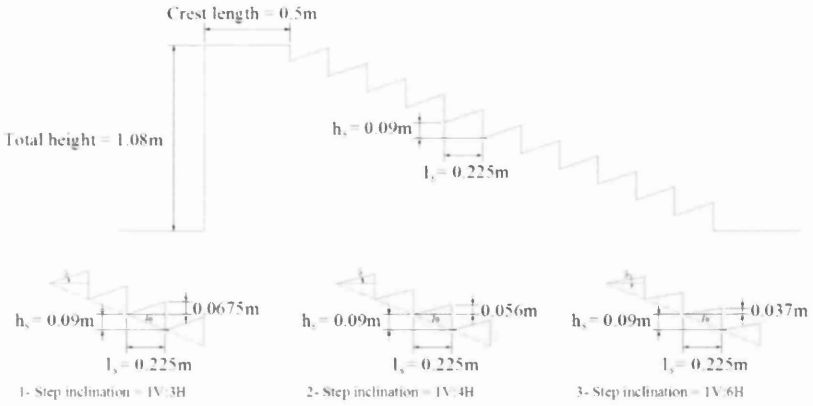

e) upward inclined steps with height 0.09m over the chute slope 1V:2.5H.

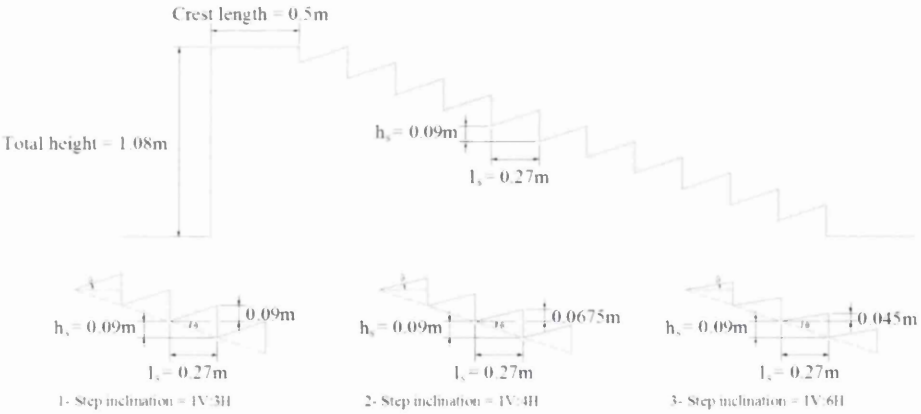

f) upward inclined steps with height 0.09m over the chute slope 1V:3H.

Figure 5.1. 2D schematic view of the physical geometry for the first group stepped spillway cases with different configurations.

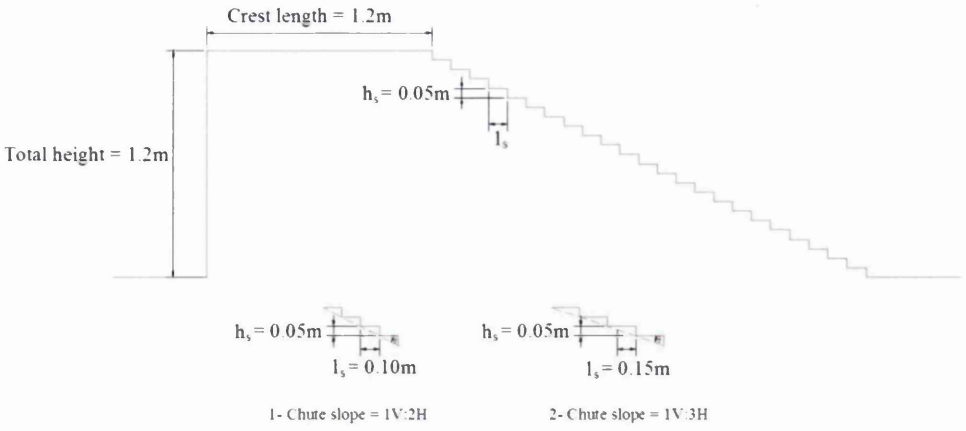

a) horizontal steps with step height 0.05m.

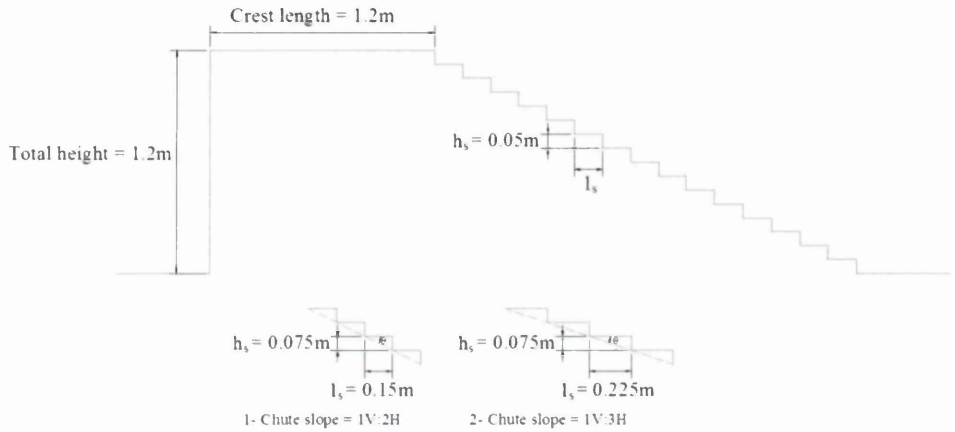

b) horizontal steps with step height 0.075m.

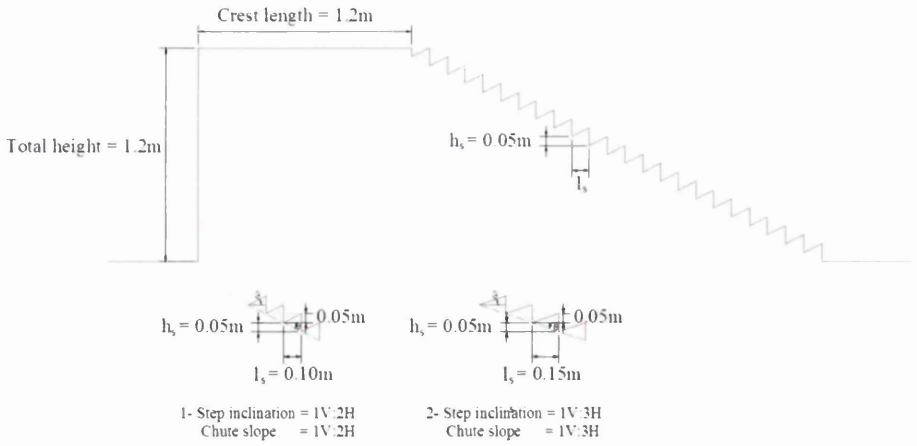

c) upward inclined steps with step height 0.05m and chute slopes 1V:2H and 1V:3H.

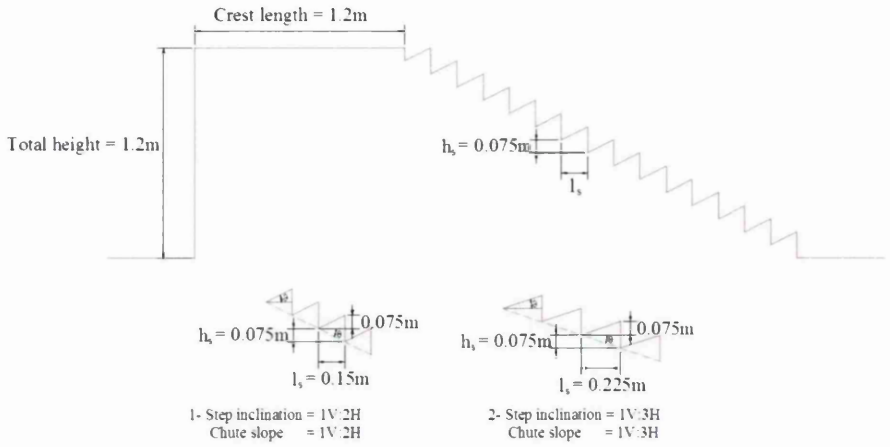

d) upward inclined steps with step height 0.075m and chute slopes 1V:2H and 1V:3H.

Figure 5.2. 2D schematic view of the physical geometry for the second group stepped spillway cases with different configurations.

5.3. Free surface profile and inception point of air entrainment

As mentioned earlier, the position of the inception point of air entrainment on stepped spillways is important for the designer of stepped spillways, as it indicates the length of the spillway part which may be prone to cavitation. In addition, the level of the free water surface is essential in the design of the chute wall.

This section presents the computational results obtained in the present investigation, including the positions of the free water surface in the non-aerated flow region and the distance from the downstream face of the weir crest to the inception point of air entrainment on stepped spillways having moderate slopes typical of the embankment dams. These results are obtained on a number of numerical stepped spillway models having three chutes slopes using: 1) horizontal steps of three different step heights and 2) upward inclined steps of one step height and three different step inclinations. These models are examined under a range of flow rates typical of the skimming flow conditions over stepped spillways. These all together allow us to evaluate the effect of step geometry, such as step height, step shape, and chute slope on the position of the free water surface and the inception point of air entrainment.

This part is divided into two sections: in the first section the computational results in terms of the free water surface will be presented, followed by the second part which focuses on the length to the inception point of air entrainment.

5.3.1. Position of free water surface

In order to clarify the effects of step geometry and chute slope on the free surface profile over moderate slope stepped spillways, it is important to look initially at how the numerical SPHysics code, which is applied in this study, predicts the flow conditions of the skimming flow regime. Figures 5.3 and 5.4 illustrate a number of snapshots of the flow evolution predicted by the numerical SPHysics code during the simulation of skimming flow, over horizontal and inclined steps respectively, at different numerical time instants.

As can be seen from these figures, a jet forms at the first stage as the water flows over the weir crest and then down the spillway slope. This is because the flow here is driven by both gravity and the upstream total head of water relative to the weir crest. Also, an impact of the lower mainstream jet on the horizontal face of the steps can be observed while the overtopping water flows down. This may cause vortices to continuously develop and flow backward against the step riser. These vortices rotate in a triangular area with a length of about two thirds of the step length, and height approximately the same as the step height, and are then ejected back into the main flow. In addition, these vortices fill the step cavities delimited by the horizontal and vertical step faces under the lower layer of the skimming flow. Finally, despite the wavy free surface, the water flow over the steps looks like a coherent stream. All these indicate the establishment of the skimming flow condition over the stepped spillways. These observations are consistent with those reported by Chanson (1994) and André (2004) during their experimental work on skimming flow conditions on moderate stepped spillways.

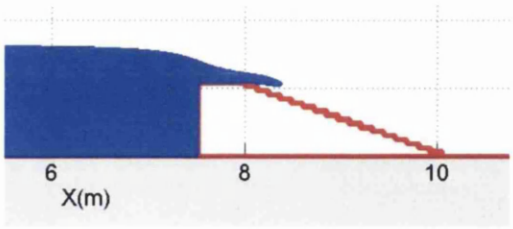

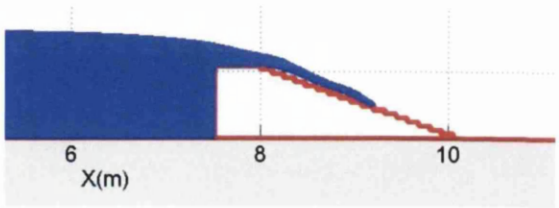

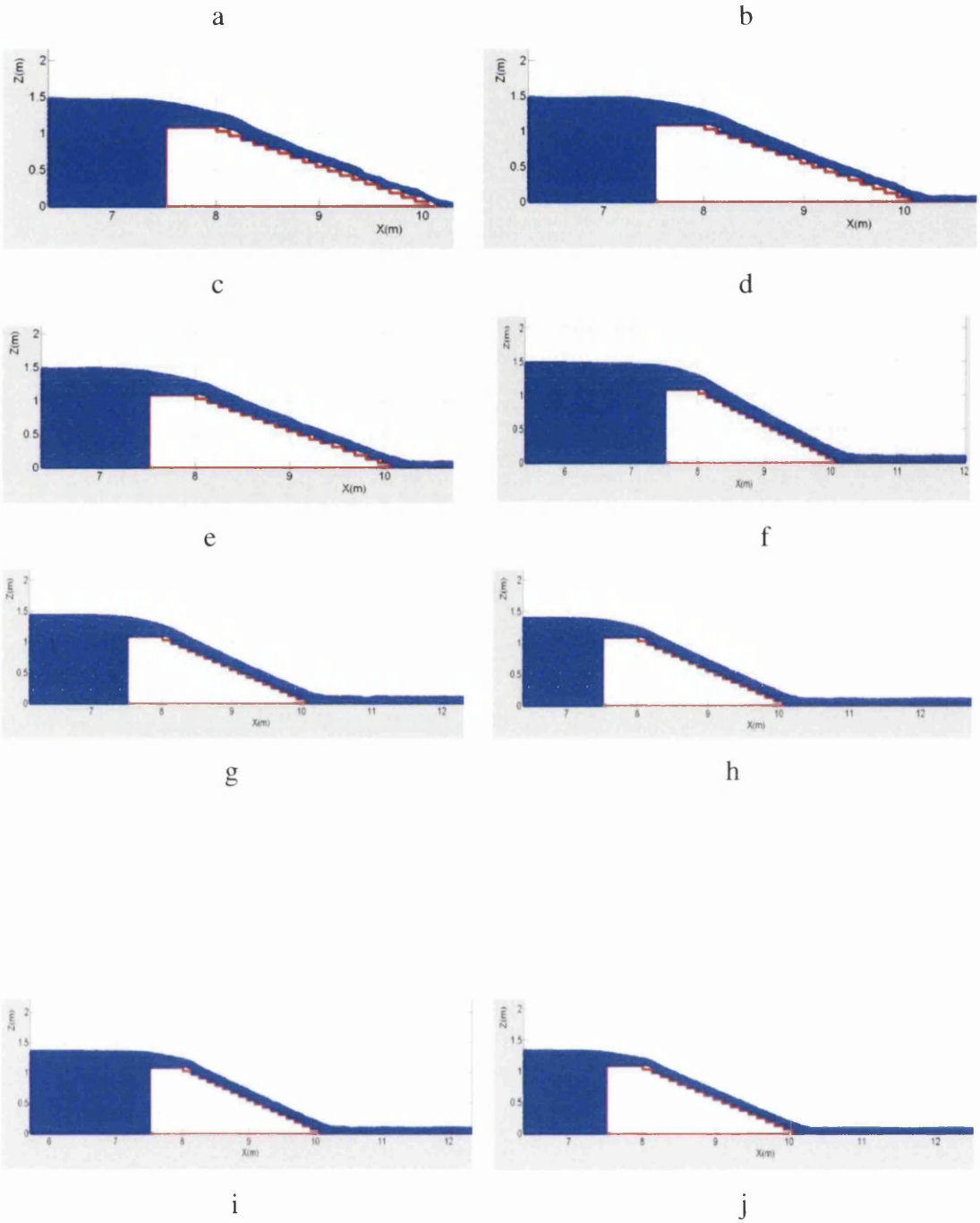

Figure 5.3. Snapshots of unsteady skimming flow condition attainment down a numerical stepped spillway model of bottom slope 1V:2H and step height of 0.06m, predicted by the SPHysics code at: a) t=0.05s, b) t=0.20s, c) t=0.40s, d) t=0.50s, e) t=0.85s, f) t=1.2s, g) t=1.75s, h) t=2.4s, i) t=3.3s and j) t=4.2s.

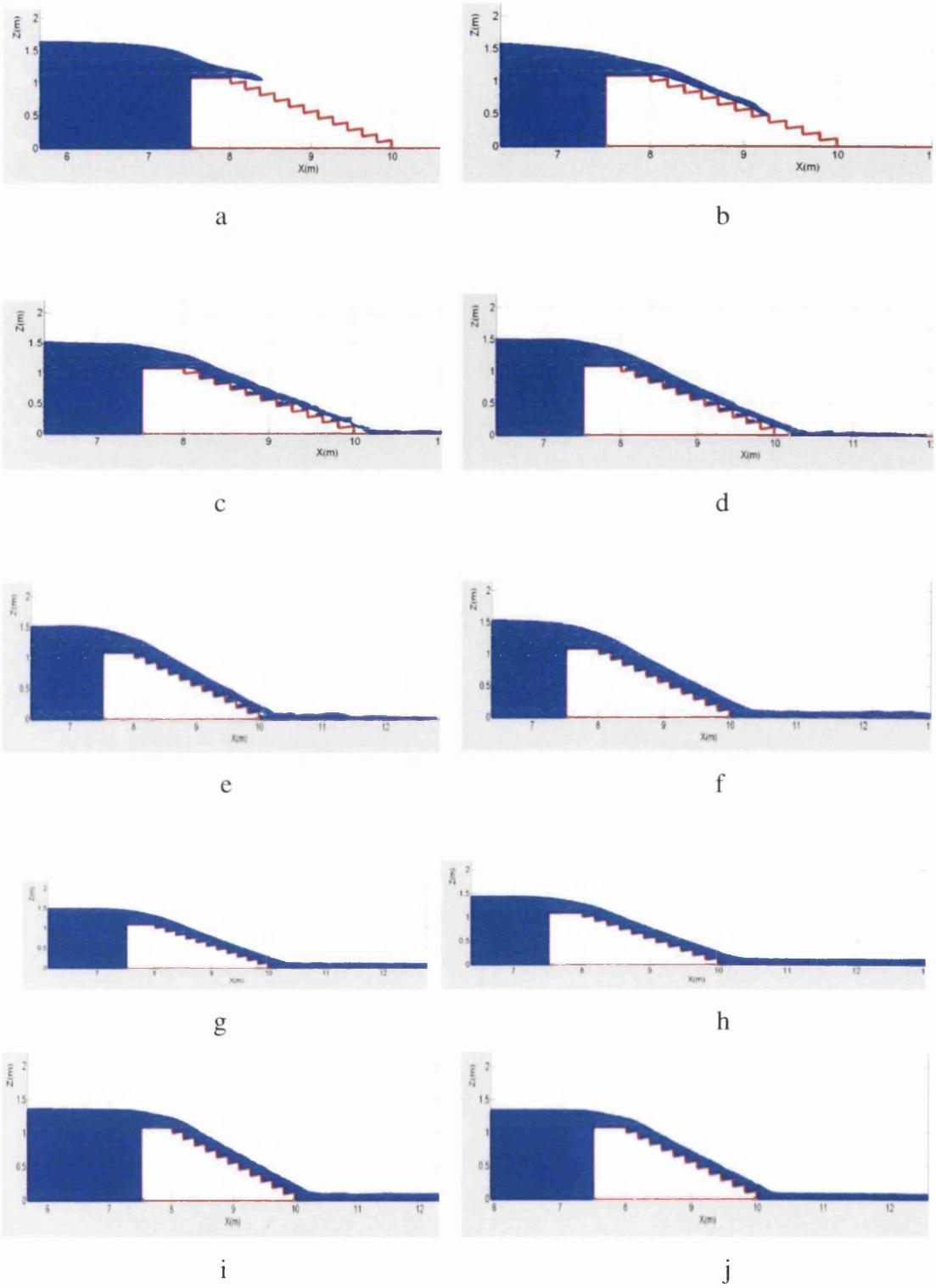

Figure 5.4. Snapshots of unsteady skimming flow condition establishment down a numerical stepped spillway model of bottom slope 1V:2H and step height of 0.09m, predicted by the SPHysics code at: a) t=0.05s, b) t=0.25s, c) t=0.40s, d) t=0.50s, e) t=0.80s, f) t=1.3s, g) t=1.85s, h) t=2.3s, i) t=3.2s and j) t=4.1s.

To see how the step height influences the water surface level over moderate stepped spillways, three step heights of 0.06m, 0.09m and 0.12m are examined in the present study, with horizontal steps. Figure 5.5 displays the position of the free water surface along the non-aerated flow region on horizontal steps, using three different step heights fitting the downstream face of a stepped spillway of bottom slope 1V:2H, due to three different unit discharges: q_w= *0.230, 0.190* and *0.155*m^2/s. In these figures d_s represents the highest point of the skimming layer and L represents the longitudinal distance along the chute slope to the point under consideration, measured from the downstream corner of the weir crest.

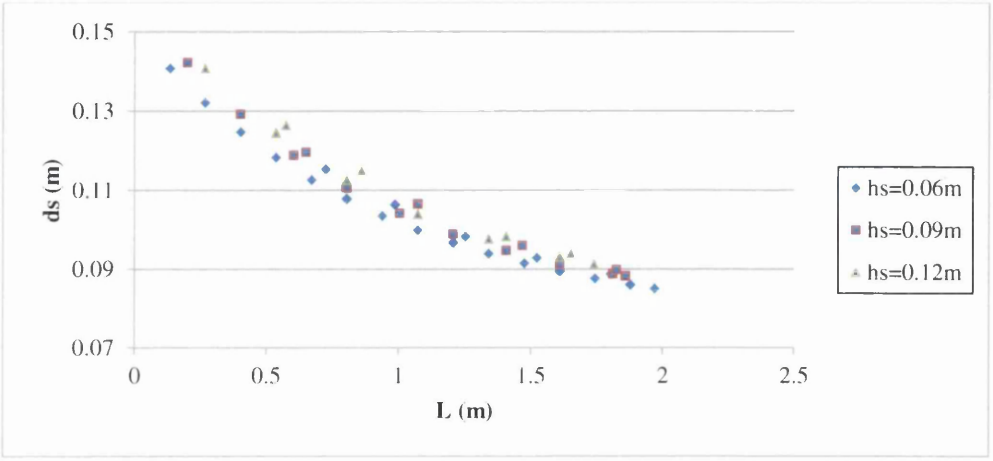

a

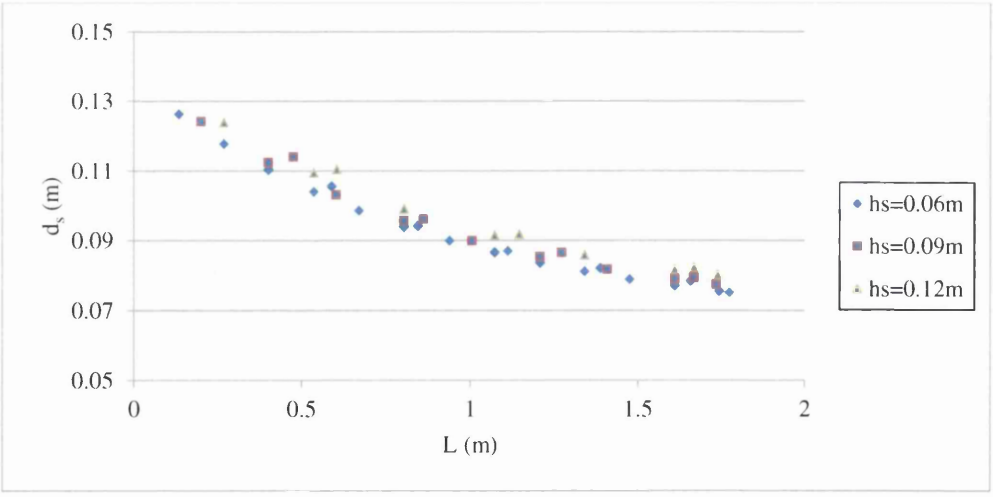

b

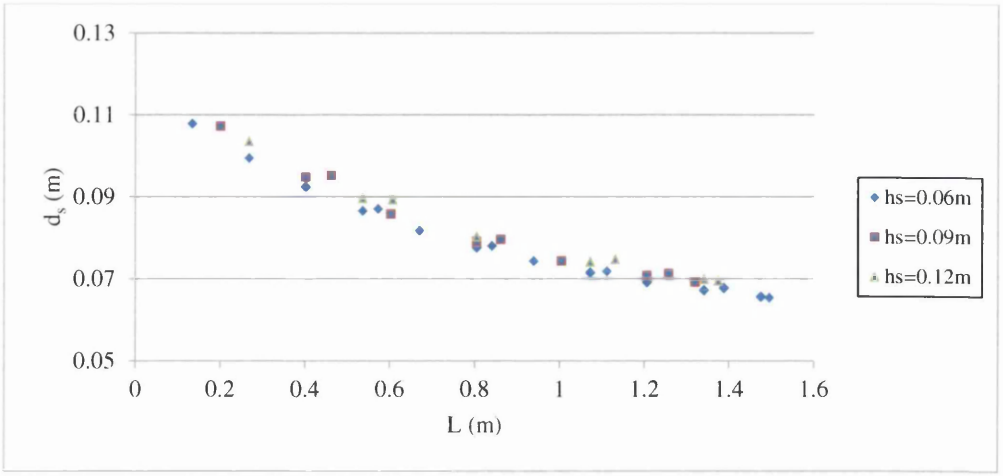

c

Figure 5.5. Free surface profile over along the stepped spillway of bottom slope 1V:2H over horizontal steps of heights 0.06m, 0.09m and 0.12m, for unit discharges of: a) q_w=0.230m^2/s, b) q_w=0.190m^2/s and c) q_w=0.155m^2/s.

As can be seen from these figures, the shape of the free surface profile over all step heights is almost the same, featuring a drop down curve and wave-like surface (Chanson, 1994; Boes & Matos, 2003, Meireles & Matos, 2009). In other words, the flow depth decreases along the chute slope in the non-aerated flow region. This may be due to the fact that in this region, as the water flows down its velocity increases due to gravity acceleration, until it reaches the peak value close to the inception point of air entrainment (Chanson, 2002). Consequently, there will be a decrease in the flow depth. The absence of air in this region is another reason, as the mixture of water with air often bulks up the flow depth (Boes and Hager, 2003).

These figures demonstrate further that for the same chute slope and unit discharge, the step height of 0.12m moves the position of the free water surface upward by about 7% compared to that obtained with the step height of 0.06m. This agrees well with the experimental data obtained by Hunt et al. (2009) in their work conducted on a stepped spillway of 1V:4.0H bottom slope to characterize the free surface and the inception point of air entrainment using three different step heights.

Moreover, as mentioned earlier, in the present investigation three different bottom slopes of 1V:2H, 1V:2.5H and 1V:3H are used to examine the effect of the chute slope on the position of the free water surface. Figure 5.6 illustrates the free surface profile along the non-aerated flow region over the slopes for unit discharges of q_w= *0.250, 0.210* and *0.182m^2/s*. These figures represent the computational free

surface levels over horizontal steps with the step height of 0.09m. It can be observed that the chute slope has an inverse effect on the position of the free water surface for the same value of the discharge and step height. In other words, the steeper the chute slope is, the lower the free water surface level will be. This can be linked to the flow velocity on steep slopes, which is relatively higher than that on flatter slopes (Chow, 1959; Handerson, 1966, Chanson, 2002), and hence the flow depth would be decreased.

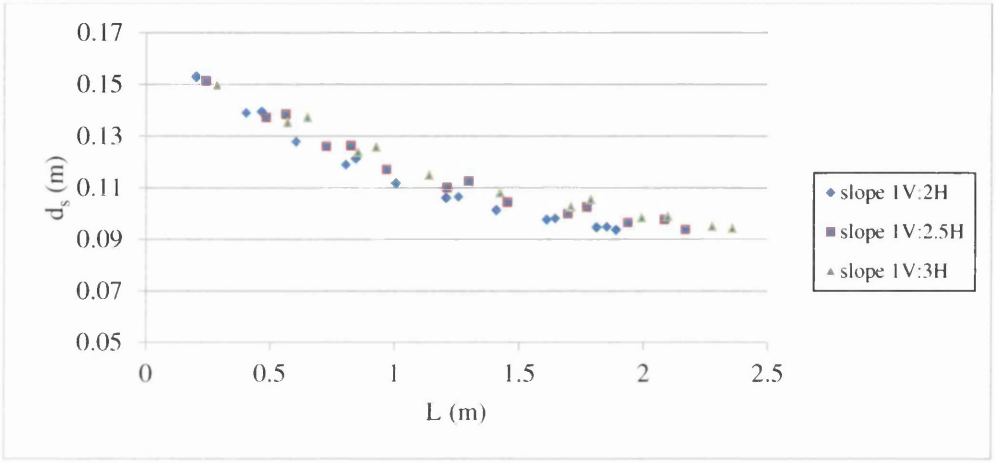

a

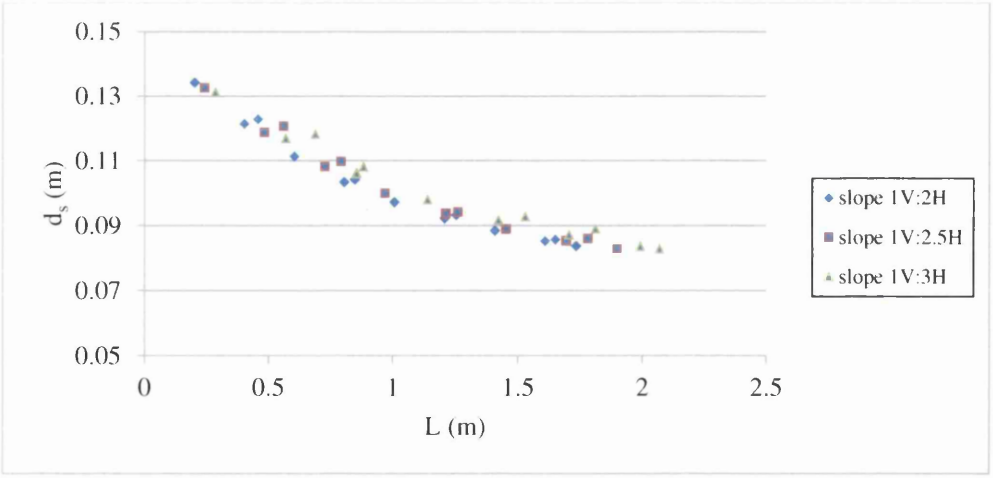

b

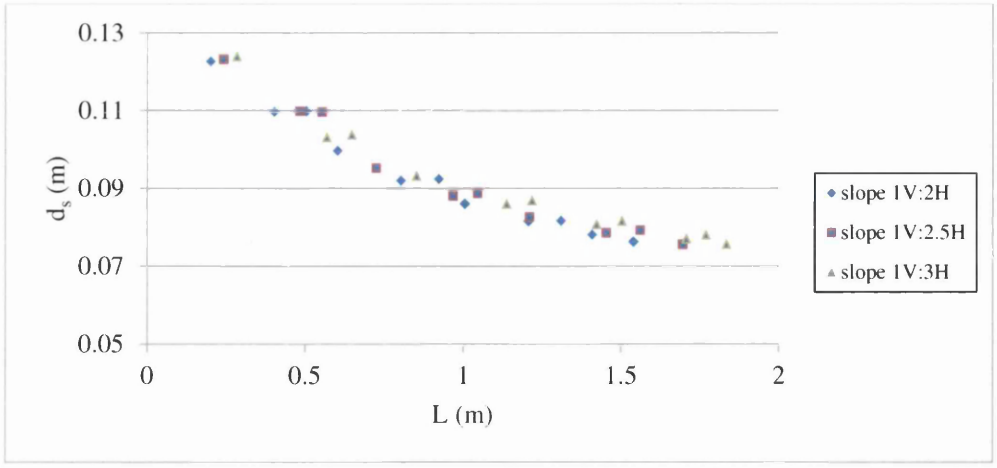

c

Figure 5.6. Free surface profile along the stepped spillway of bottom slopes 1V:2H, 1V:2.5H and 1V:3H over horizontal steps having the height of 0.09m, for unit discharges: a) q_w=0.250m^2/s, b) q_w=0.210m^2/s and c) q_w=0.182m^2/s.

Now, let's have a look at the free surface profile over upward inclined steps. To do so, the free water surface profiles along the steeped spillway over the inclined steps having an identical step height of 0.09m, and three step inclinations of 1V:3H, 1V:4H and 1V:6H are plotted in Figure 5.7. The water surface profiles shown in this figure are due to the chute slope of 1V:2H and three unit discharges of q_w= *0.250, 0.210* and *0.182m^2/s*. As is clear from this figure, the characteristics of the free surface profile over the upward inclined steps, which are represented by the wavy surface and drop down, for all step inclinations tested in the present study are approximately the same as those obtained with the horizontal steps discussed above. Also, from this figure one can observe that for a given unit discharge the inclined step of steeper adverse slope, 1V:3H, produces a higher free water surface profile than the other step inclinations tested in the current work. This is possibly due to the fact that an increase in the step inclination angle increases the obstruction area to the overflowing water, and consequently the flow velocity decreases accordingly.

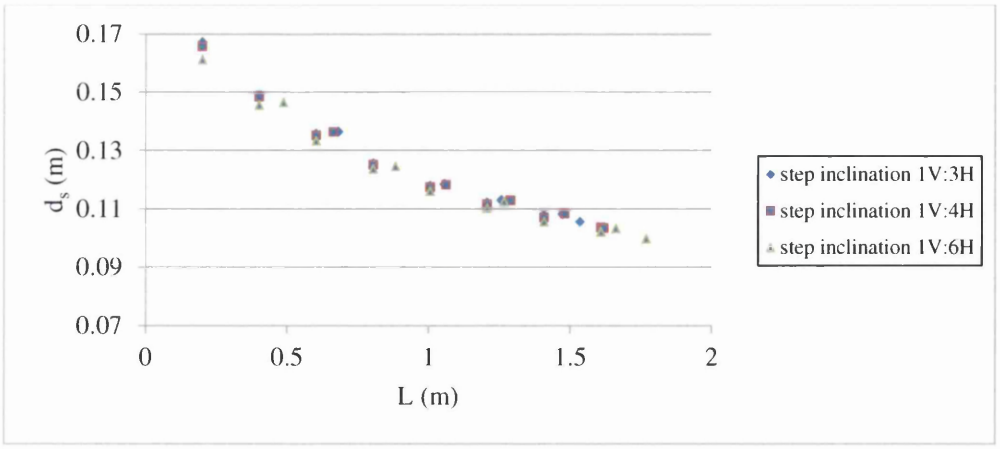

a

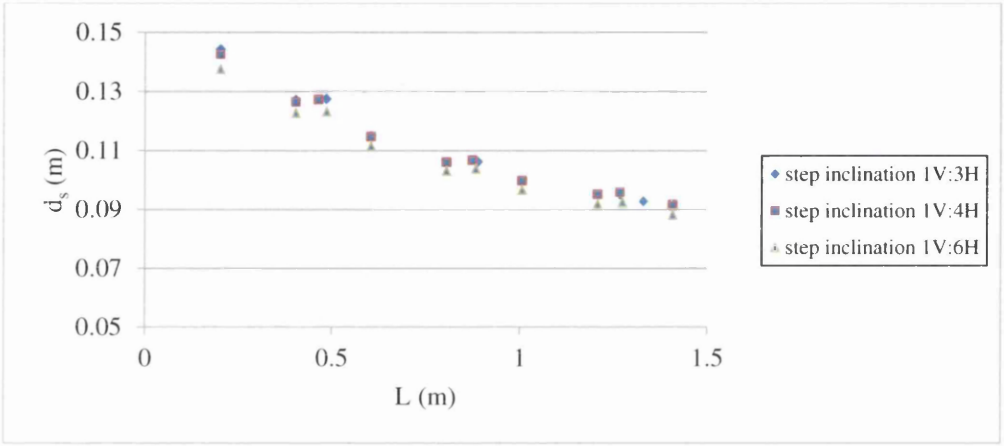

b

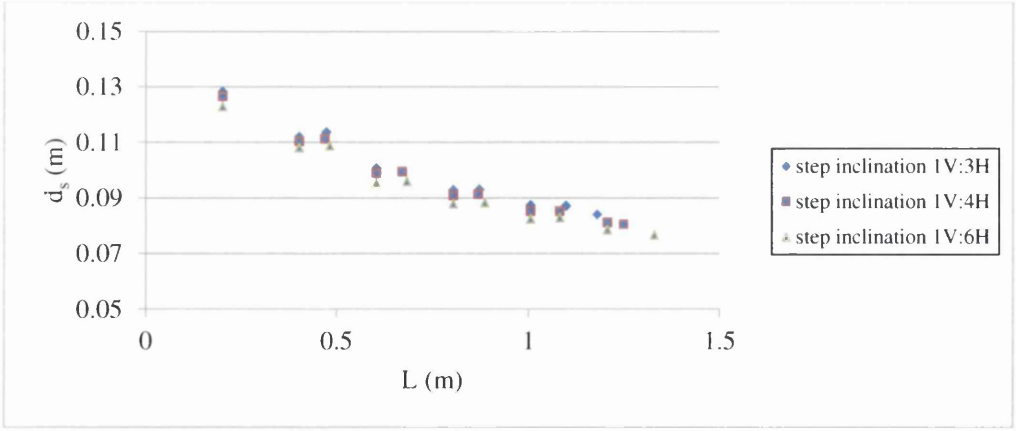

c

Figure 5.7. Free surface profile along the stepped spillway of bottom slope 1V:2H over upward inclined steps having the step height of 0.09m and inclinations of 1V:3H, 1V:4H and 1V:6H, for unit discharges of: a) q_w=0.250m^2/s, b) q_w= 0.210m^2/s and c) q_w=0.182m^2/s.

To compare the free surface profile over horizontal and inclined steps, Figures 5.8, 5.9 and 5.10 are plotted to show the free surface profile along the non-aerated flow region on both step configurations, over chute slopes of 1V:2H, 1V:2.5H and 1V:3H respectively. It is worth mentioning that the numerical results for both step shapes shown in each of these figures are obtained with step height of 0.09m and unit discharges of q_w= *0.25, 0.21* and *0.182*m^2/s. From these figures it can be observed that higher free surface profiles are associated with upward inclined steps. These figures also show that with the step inclinations of 1V:3H, the position of the free water surface moves upwards by about 6% compared with the horizontal steps. This is an indication that the upward inclined steps perform better than the horizontal steps in terms of slowing down the velocity of the rapid flow. This feature of inclined steps agrees well Essery & Horner (1978), Chinnarasri & Wongwises (2004) and Barani et al. (2005) regarding the performance of upward inclined steps in terms of slowing down flow velocity over steeply sloping stepped spillways.

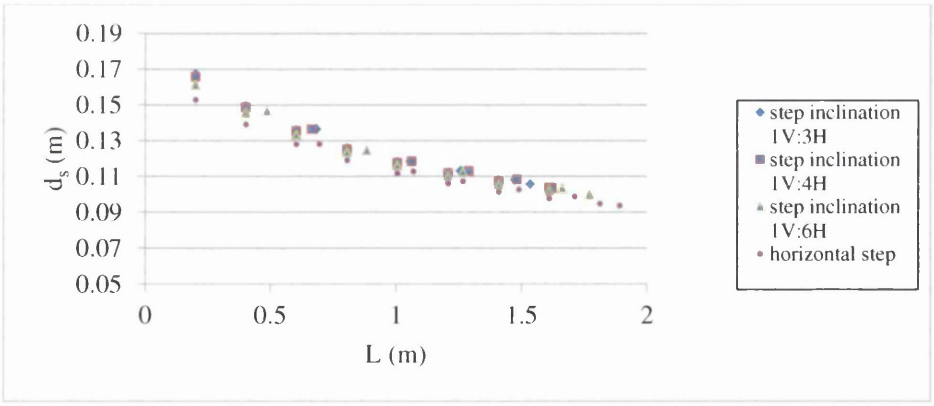

a

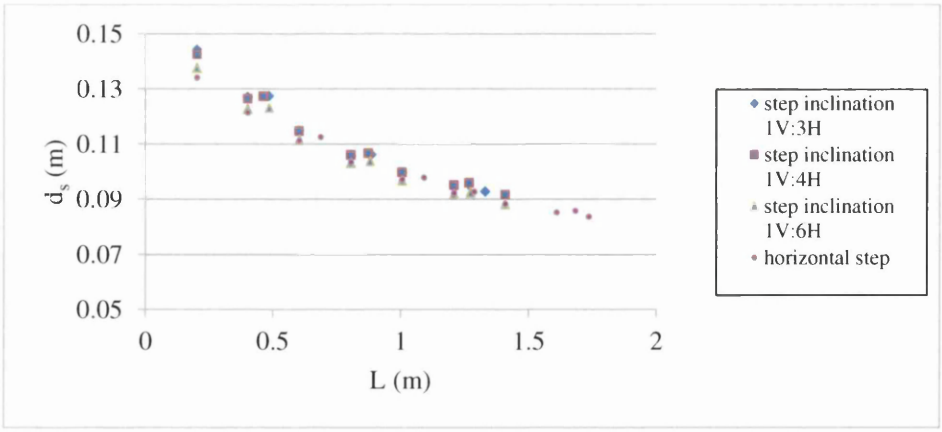

b

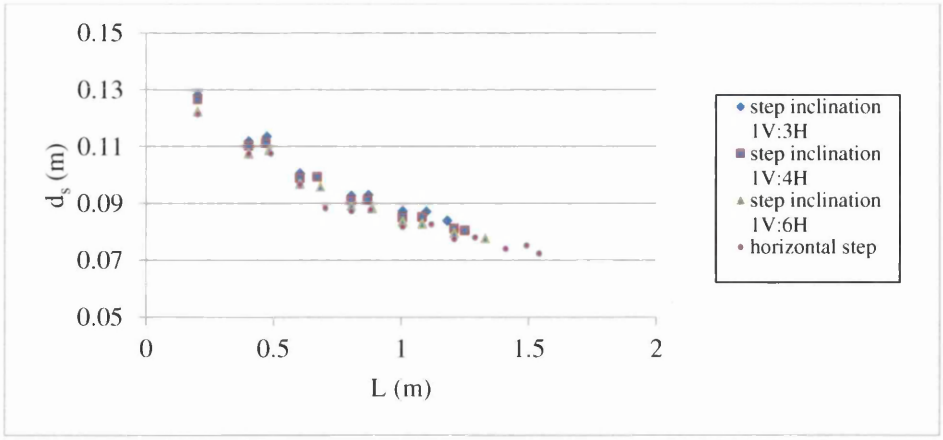

c

Figure 5.8. Free surface profile along the stepped spillway of bottom slope 1V:2H over horizontal and upward inclined steps having the step height of 0.09m and inclinations of 1V:3H, 1V:4H and 1V:6H, for unit discharges of: a) q_w=0.250m^2/s, b) q_w=0.210m^2/s and c) q_w=0.182m^2/s.

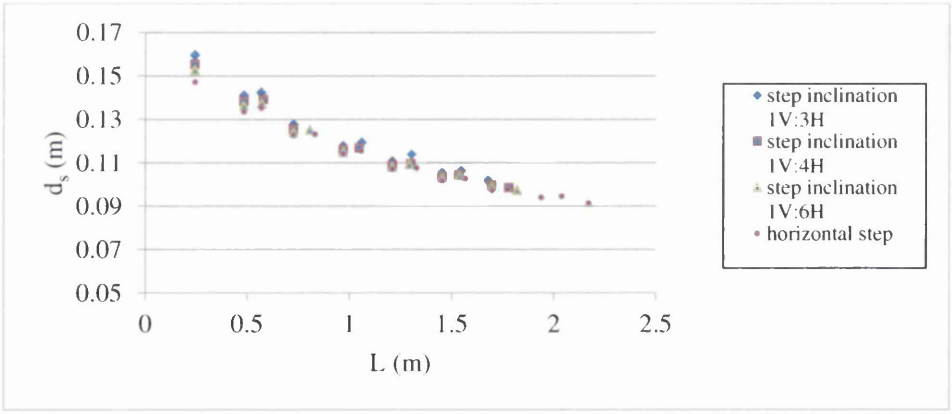

a

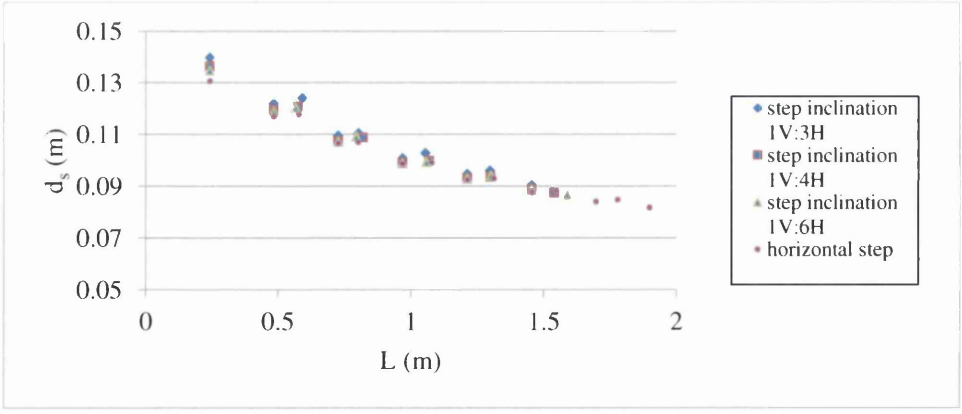

b

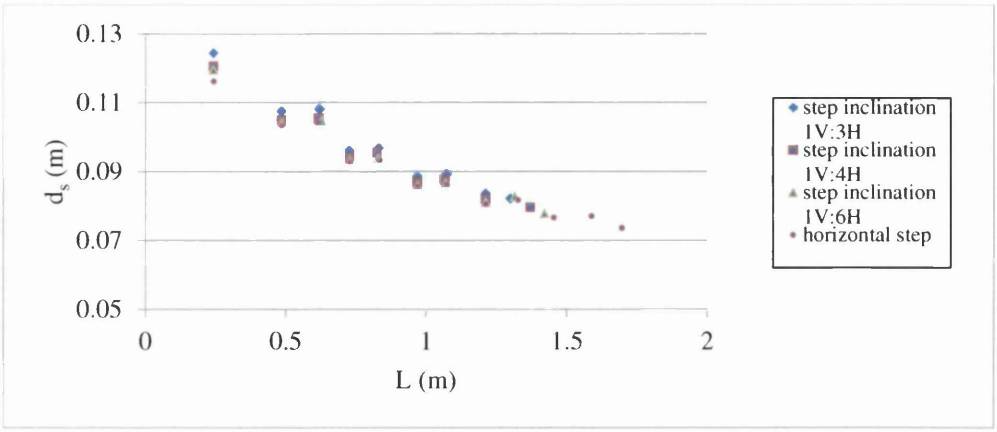

c

Figure 5.9. Free surface profile along the stepped spillway of bottom slope 1V:2.5H over horizontal and upward inclined steps having the step height of 0.09m and inclinations of 1V:3H, 1V:4H and 1V:6H, for unit discharges of: a) q_w=0.250m^2/s, b) q_w=0.210m^2/s and c) q_w=0.182m^2/s.

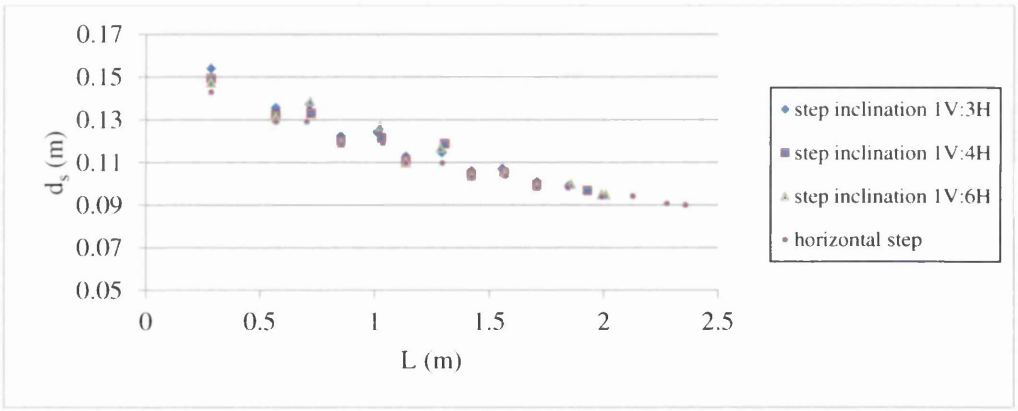

a

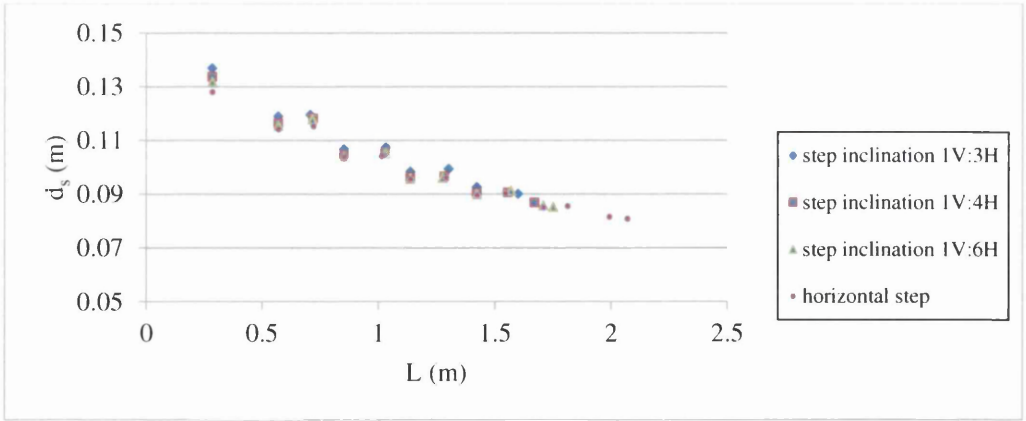

b

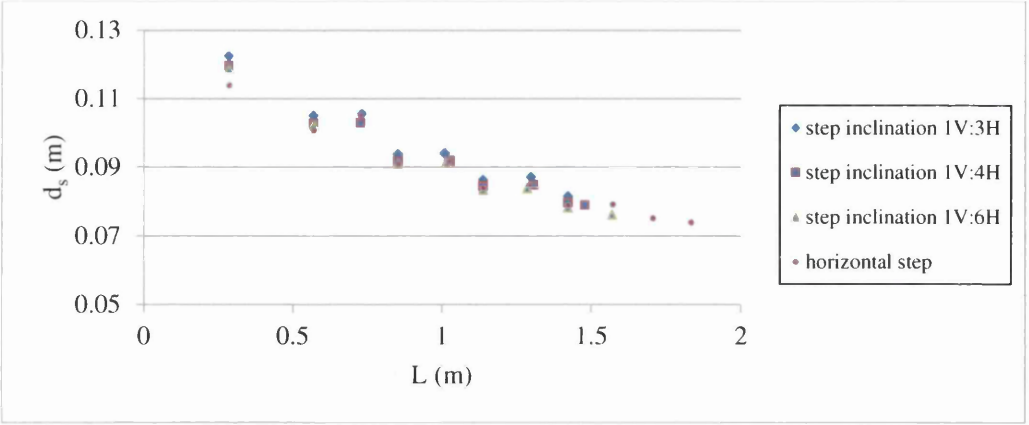

c

Figure 5.10. Free surface profile along the stepped spillway of bottom slope 1V:3H over horizontal and upward inclined steps having the step height of 0.09m and inclinations of 1V:3H, 1V:4H and 1V:6H, for unit discharges of: a) q_w=0.250m^2/s, b) q_w=0.210m^2/s and c) q_w=0.182m^2/s.

5.3.2. Inception point of air entrainment

Air has been considered a successful means of protecting hydraulic structures, which are usually designed to pass water with high velocities, against the damage caused by cavitation (Peterka, 1945; Falvey, 1991). This may be due to the low resistance of concrete, which is usually used to cover the surface of such structures, against the impact of the vaporized bubbles when they collapse. Determining the location of the point where self-aeration begins on stepped spillways is therefore essential for the designer, since the upstream part of this point is prone to cavitation damage (Boes & Minor, 2002; Amador et al. 2009). However, self-aeration on embankment dams during severe flood conditions may not take place, especially when the length of the downstream face is not long enough (Meireles and Matos, 2009) to allow the development of the boundary layer (Chanson, 2002).

A number of criteria are available in the literature, see Chapter 2 for more details, by which to define the location of the inception point of air entrainment. According to Chanson (2002), it is located where the turbulent boundary layer is fully developed and meets the free surface. This definition is in fact used in the present study to determine the length to the inception point of air entrainment. This can be justified on the basis that the single phase fluid is considered in the present work, as the

concern is to characterize the properties of the skimming flow conditions in the non-aerated flow region.

In addition, researchers have differed in identifying whether the step height, chute slope or both are also other significant factors, along with the discharge, that need to be considered in estimating the length to the inception point of air entrainment. In the present study three step heights and three slopes typical of embankment dams are used to assess their influence on the location of the inception point over the horizontal steps. Also, upward inclined steps with three different step inclinations are used to examine the effect of the step shape. These are tested with a range of flow rates typical of the skimming flow conditions.

Firstly, the effects of the step height and chute slope on the location of the inception point of air entrainment are investigated with the horizontal steps. Following Schlichting (1979), the boundary layer herein is defined as that layer of the flow depth above which the velocity is approximately 99% of the free stream velocity. This allows us to determine the thickness of the turbulent boundary layer from the velocity distribution over the outer edge of the steps located within the non-aerated flow region; see Chapter 6 for more detail on estimating the growth of the turbulent boundary layer in the present study.

Figures 5.11 and 5.12 illustrate the computed water surface level d and thickness of the boundary layer δ obtained in this study at the outer edge of the horizontal and upward inclined steps respectively. These steps are located at a distance L measured from the downstream face of the weir crest. Following Chanson (2002) the length of the non-aerated flow region in the current study is assumed to be located at the intersection point of the two curves shown in both figures. It should be noted that for each step height of the horizontal steps, step inclination of the upward inclined steps, and stepped spillway slope, this procedure is performed for 3-4 different values of the unit discharge.

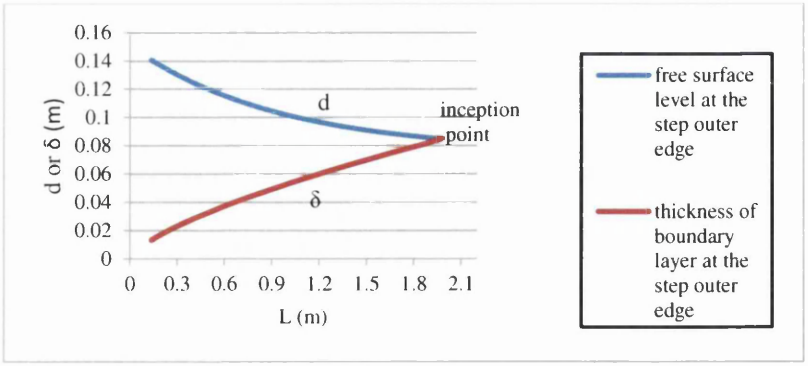

a

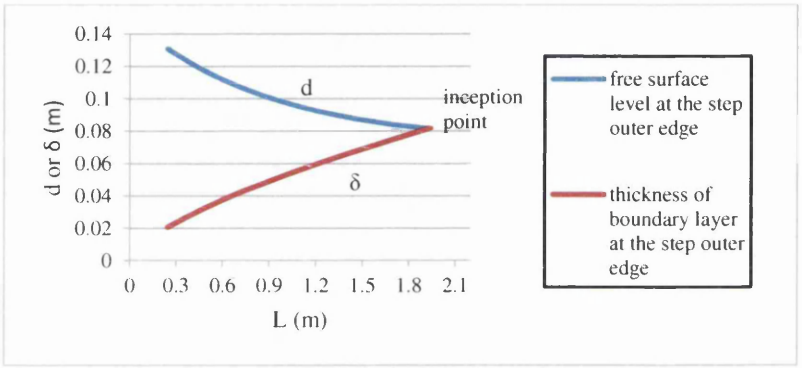

b

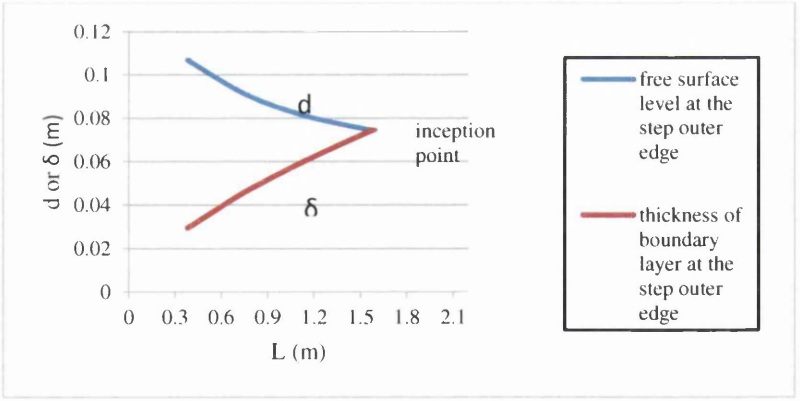

c

Figure 5.11. Estimation of the length to the inception point of air entrainment above the horizontal steps, based on the computed water flow depth and thickness of boundary layer: a) step height 0.06m, chute slope 1V:2H and unit discharge q_w=0.23 m^2/s, b) step height 0.09m, chute slope 1V:2.5H and unit discharge q_w=0.20 m^2/s, and c) step height 0.12m, chute slope 1V:3H and unit discharge q_w=0.173 m^2/s.

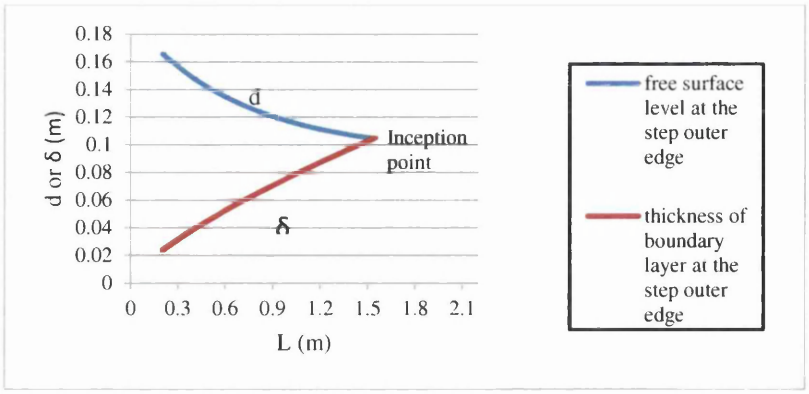

a

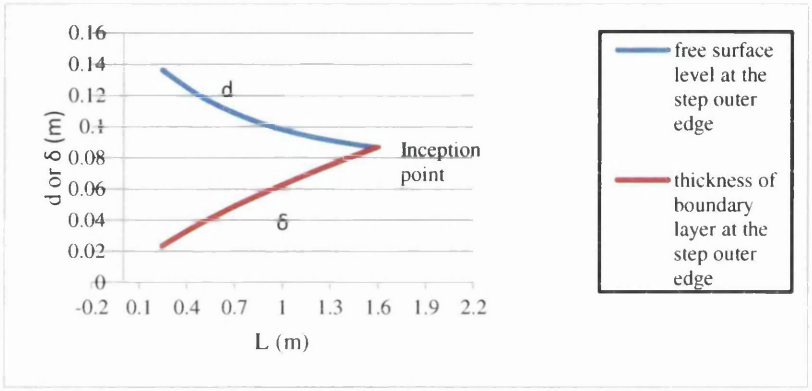

b

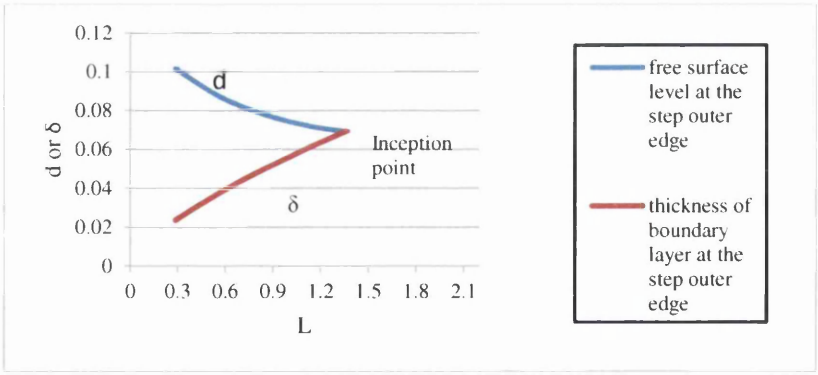

c

Figure 5.12. Estimation of the length to the inception point of air entrainment above upward inclined steps of step height 0.09m, based on the computed water flow depth and thickness of boundary layer: a) step inclination 1V:3H, chute slope 1V:2H and unit discharge q_w=0.25 m^2/s, b) step inclination 1V:4H, chute slope 1V:2.5H and unit discharge q_w=0.21 m^2/s, and c) step inclination 1V:6H, chute slope 1V:3H and unit discharge q_w=0.182 m^2/s.

As can be clearly seen from these figures, the thickness of the turbulent boundary layer close to the weir crest is small, as it has just developed. This can be explained

by the uniform velocity distribution along the flow depth, see Chapter 6, above the step outer edge. In other words, the flow velocity above the outer edge of these steps reaches the maximum value over a short distance. Then the turbulent boundary layer develops as the water flows down and its thickness increases until meets the free surface at a point called the inception point of air entrainment.

In order to investigate the effect of the step height on the length to the point of surface self-aeration with horizontal steps, the computational results of L_i/K_s obtained from various step heights used in the present work are plotted in Figure 5.13, against the corresponding values of the roughness Froude number F_*. The experimental data gathered in other stepped spillways with slopes typical of embankment dams, namely those by Chanson (1996), Chanson & Toombes (2002), Carosi & Chanson and (2008) and Meireles & Matos (2009), are also shown in this figure for the sake of comparison. In this figure L_i is the length to the inception point measured from the downstream edge of the weir, K_s is the roughness defined by $K_s=h_s cos\theta$, h_s as the step height and θ is the chute bottom slope. The roughness Froude number F_* is determined from $F_* = q_w/\sqrt{g \sin\theta K_s^3}$, in which q_w is the discharge per unit width and g is the gravitational acceleration.

As can be seen from this figure, the point of inception moves further downstream from the weir crest as the discharge is increased. This means that the increase in the length of the non-aerated flow region with the increase of the unit discharge. This can be attributed to the fact that the increase in the discharge increases both the flow depth and mean velocity in the flow direction. However, when the flow depth increases, the length required for the boundary layer to meet the free surface will be increased. This observation has been confirmed by most of the researchers on moderate and steep slope stepped spillways.

In Figure 5.13 it can be also observed that for a given chute slope and value of F_*, the inception point moves upstream towards the weir crest with the larger step height 0.12m used. This can be explained by the fact that large step sizes are more efficient than small step sizes in decelerating the velocity of the overflowing water when it passes from the outer step edge and hits the horizontal face. This was observed by Chamani (2000) from his experimental results on steeply sloping stepped spillways and the experimental results of Hunt et al. (2009) on flat slope stepped spillways. It should be mentioned here that the length to the section of self-aeration is decreased

only by 13%, when the step height of 0.06m is changed to 0.12m. This suggests that the length of the non-aerated flow region is slightly influenced by the step height. Furthermore, this figure shows that the numerical results obtained in this study agree well with the experimental data of other researchers. In addition, it is obvious that the results of the present study underestimate those obtained from applying Equation (2.3) proposed by Chanson (1996), see Chapter 2, especially when F_* is smaller than 8. However, as mentioned earlier, Equation (23) is derived from a wide range of model and prototype data of slopes steeper than those examined in this study. Also, Chanson (1996) revealed that Equation (2.3) may be applied on moderate slopes for F_* values greater than 10, whereas the numerical results obtained in this study are due to F_*values smaller than 10.

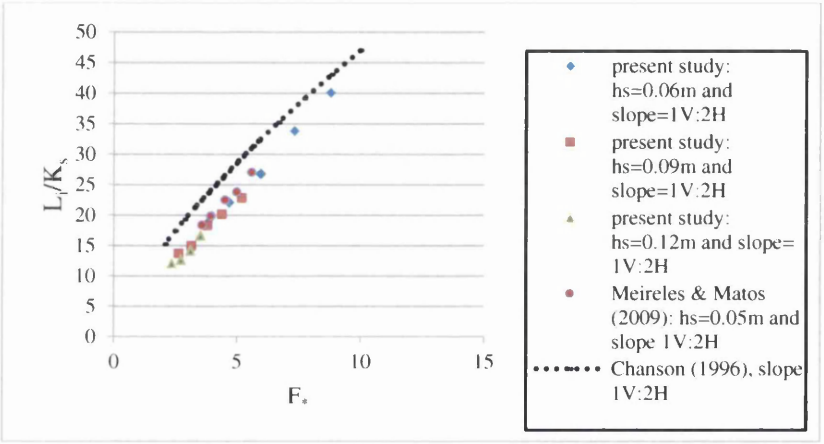

a

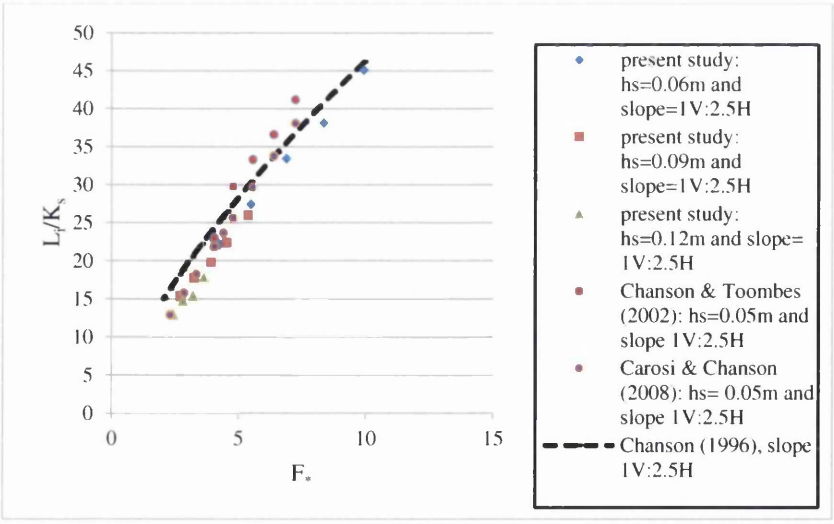

b

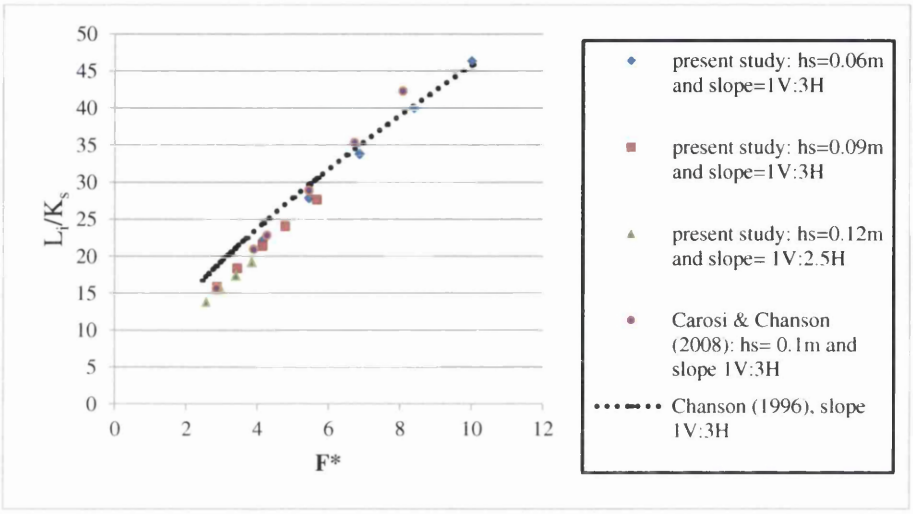

c

Figure 5.13. Numerical SPHysics predictions of the location of the free surface aeration on moderate slope stepped spillways and comparison with the experimental data for slopes: a) 1V:2H, b) 1V:2.5H and c) 1V:3H.

To see what effect the chute slope has on the length of the non-aerated flow region, Figure 5.14 presents the computational results of L_i/K_s obtained in this study versus the F_* values for the three slopes examined. This figure demonstrates that the slope inversely affects the length of the non-aerated flow region. In other words, for a given step height and F_* value the process of self-aeration over steep slopes may start earlier than on flat slopes. This may be due to the longitudinal velocity, which is much higher on steeper slopes compared to flatter slopes. Hence, the level of the free surface at any section on steep chutes is lower compared to flatter slopes. Therefore, the turbulent boundary layer meets the free surface in steep slopes over a shorter distance than the flatter slopes. This agrees with the experimental observation made by Boes and Matos (2002) and André (2004). It is worth mentioning here that the length to the inception point is decreased by about 27% when the chute slope is changed from 1V:3H to 1V:2H. This is an indication that the slope has a significant

effect on the location of the self-aeration mechanism on the moderate slope stepped spillways.

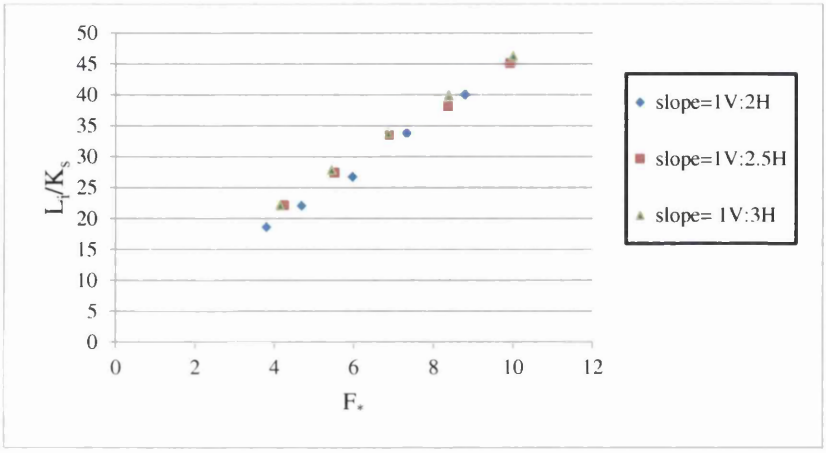

a

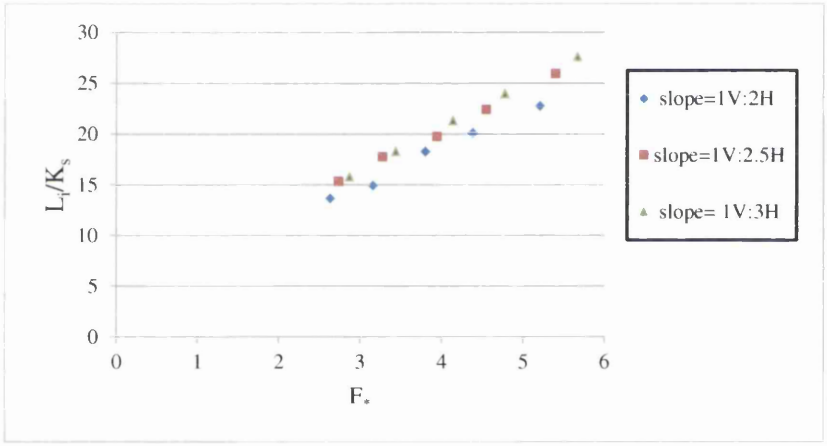

b

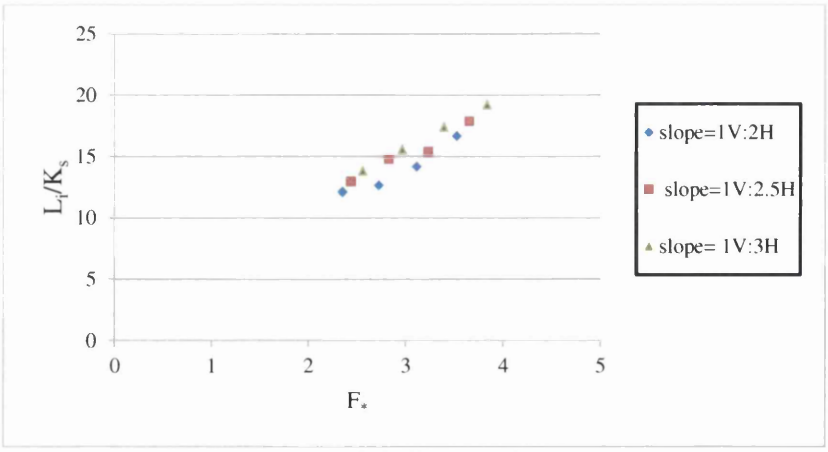

c

Figure 5.14. Numerical SPHysics predictions of the location of the free surface aeration on moderate slope stepped spillways using horizontal steps of heights: a) h_s=0.06m, b)h_s=0.09m and c) h_s=0.12m.

Following past studies, namely Chanson, (1996); Carosi & Chanson (2008); Meireles & Matos (2009) and Hunt et al. (2010) a power non-linear multiple regression is performed to develop an equation that fits the computational results obtained in the present study. For this purpose the values of L_i/K_s and the corresponding values of F_* collected from various step heights, chute slopes and discharges tested in this work are used to obtain the following relationship with r=0.993:

$$\frac{L_i}{K_s} = 4.495 \frac{(F_*)^{0.867}}{(sin\theta)^{0.283}} \tag{5.3}$$

The accuracy of Equation (5.3) is examined by comparing it with the empirical Equation (2.3) derived by Chanson (1996), experimental results of Chanson and Toombes (2002) obtained on 1V:2.5H stepped spillway with the step height of 0.1m, the experimental data set of Carosi and Chanson (2008) on a stepped spillway using the step height of 0.1m and chute slope of 1V:2.5H, and the experimental data of Meireles and Matos (2009) on a stepped spillway of bottom slope 1V:2H with the step height of 0.05m. These are all plotted together in Figure 5.15, which demonstrates that Equation (5.3) agrees well with the existing experimental data. This confirms that Equation (5.3) can be applied to predict the longitudinal distance between the downstream edge of an uncontrolled broad crested weir to the point where the self-aeration mechanism starts on horizontal slopes over moderate slope stepped spillways.

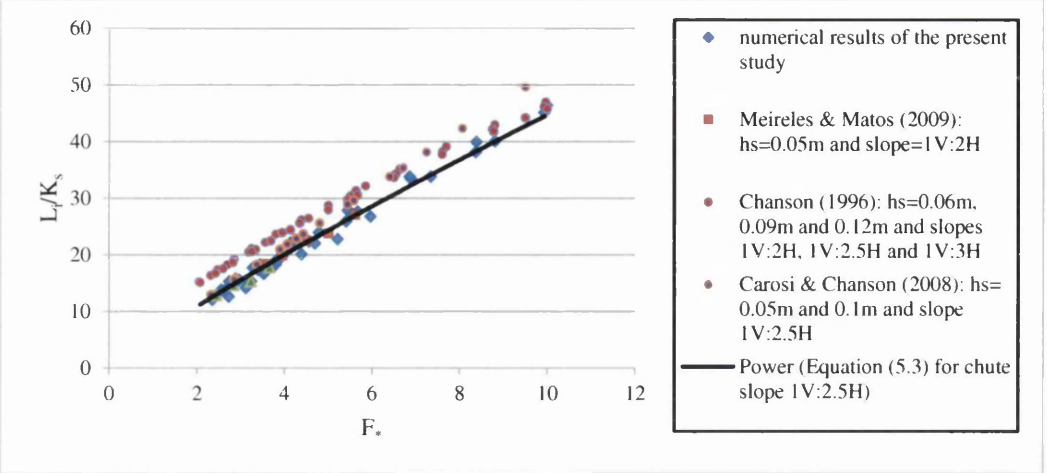

Figure 5.15 Regression for the numerical values of the normalized L_i versus $F_*$of the present study using horizontal steps with different step heights, and comparison with the existing experimental results for moderate slope stepped spillways.

The following section presents and discusses the effect of upward inclined steps on the length of the non-aerated flow region over three bottom slopes: 1V:2H, 1V:2.5H and 1V:3H. For this purpose the step height is fixed to 0.09m and three step inclinations, 1V:2H, 1V:2.5H and 1V:3H, are examined with unit discharges typical of the skimming flow conditions. Figure 5.16 plots the computational results of L_i/K_s against F_* obtained on both the horizontal and upward inclined steps with three step inclinations, to compare their influence on estimating the distance to the inception point of air entrainment with the step height of 0.09m. The comparison clearly shows that the length required for the free surface aeration to take place on upward inclined steps is shorter compared to the horizontal steps. The location of self-aeration is approximately 15% further downstream for the horizontal steps. Also, it is obvious that the steeper the slope of the inclined steps, the shorter the length of the non-aerated flow region will be. This can be explained by the efficiency of the upward inclined steps in terms of decelerating the flow velocity. In addition, it is clear that inclined steps become more efficient when the inclination angle of the horizontal face is increased. This is possibly because upward inclined steps act as an obstruction against the overflowing water and hence the flow velocity reduces more. These findings are consistent with the observations and made by Barani et al. (2005) and Chinnarasri and Wongwises (2006) during their experimental works on comparing the efficiency of different step shapes, such as endsills and upward inclined steps, with horizontal steps, in terms of the energy dissipation.

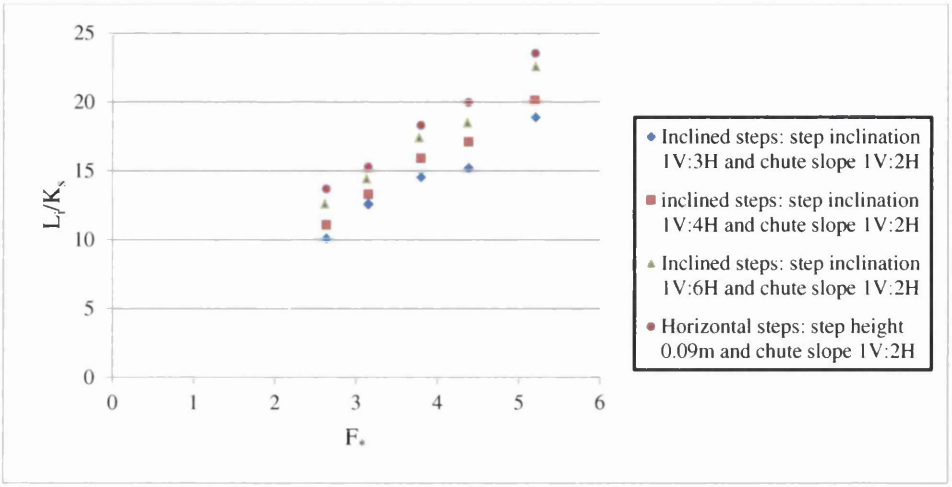
25
20
15
10
5
0
0
1
2
3
4
5
6
L_r/K_s
F_*
Inclined steps: step inclination 1V:3H and chute slope 1V:2H
inclined steps: step inclination 1V:4H and chute slope 1V:2H
Inclined steps: step inclination 1V:6H and chute slope 1V:2H
Horizontal steps: step height 0.09m and chute slope 1V:2H

a

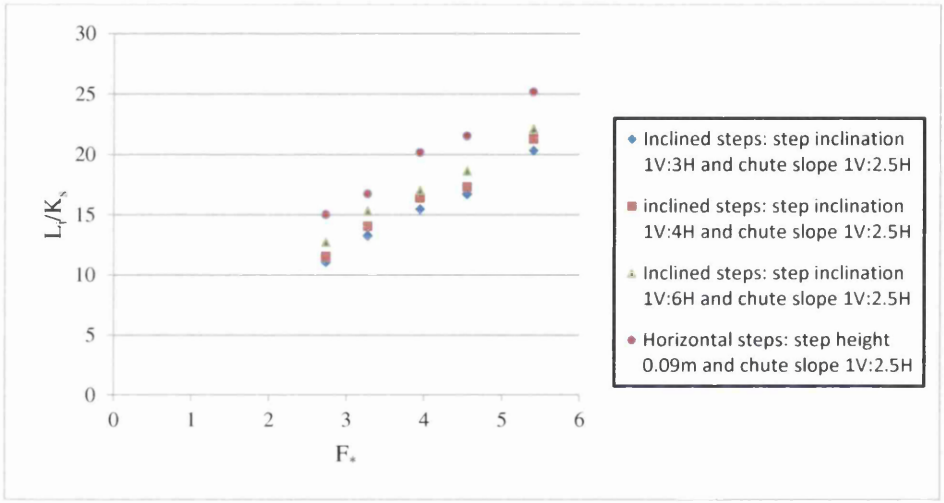
30
25
20
15
10
5
0
0
1
2
3
4
5
6
L_r/K_s
F_*
Inclined steps: step inclination 1V:3H and chute slope 1V:2.5H
inclined steps: step inclination 1V:4H and chute slope 1V:2.5H
Inclined steps: step inclination 1V:6H and chute slope 1V:2.5H
Horizontal steps: step height 0.09m and chute slope 1V:2.5H

b

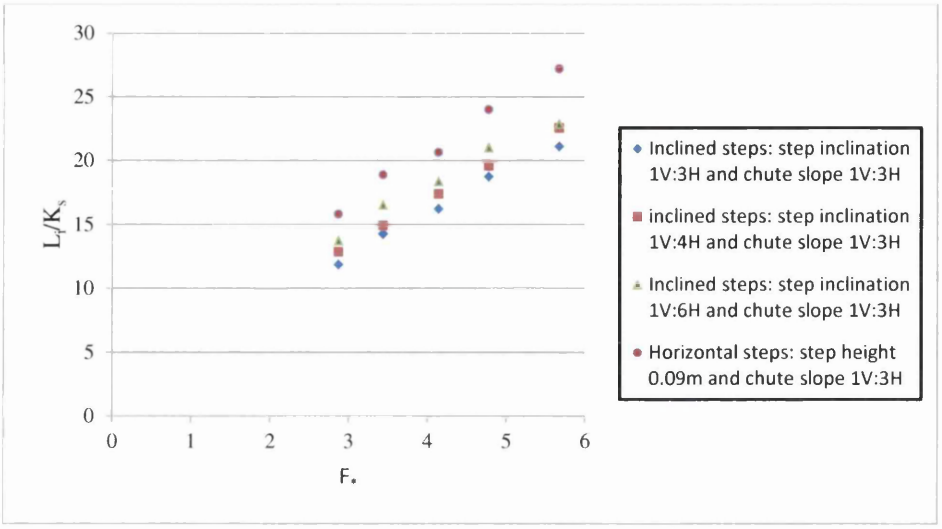

c

Figure 5.16. Numerical SPHysics predictions of the location of the free surface aeration using upward inclined steps and comparison with the horizontal steps of step height 0.09m on stepped spillways of slope: a) 1V:2H, b) 1V:2.5H, and c) 1V:3H.

Finally, similarly to the horizontal steps, a power law relation is used to fit the computed results obtained with different chute slopes, step inclinations and unit discharge tested in the present study using the upward inclined steps, and the following expression is obtained with r=0.906:

$$\frac{L_i}{K_s} = 3.79 \frac{(F_*)^{0.83}}{(sin\theta)^{0.1}(\sin\vartheta)^{0.16}} \tag{5.4}$$

The parameters appearing in Equation (5.4) are the same as those in Equation (5.3) except the parameter ϑ, which is added to Equation (5.4) to introduce the effect of the adverse slope of inclined steps with the horizontal face. However, it should be noted that Equation (5.4) is obtained with only one step height of 0.09m, therefore great care needs to be taken when it is applied to determine the location of self-aeration over upward inclined steps having heights different to those used in this study. Figure 5.17 presents the numerical values of L_i/K_s against F_* obtained in this study on upward inclined steps with three different step inclinations due to various unit discharges. Equation (5.4), which is derived from these numerical predictions is also shown. However, due to the lack of published data on the characteristics of the

inception point on stepped spillways, only the computational results of the current work are presented in Figure 5.17.

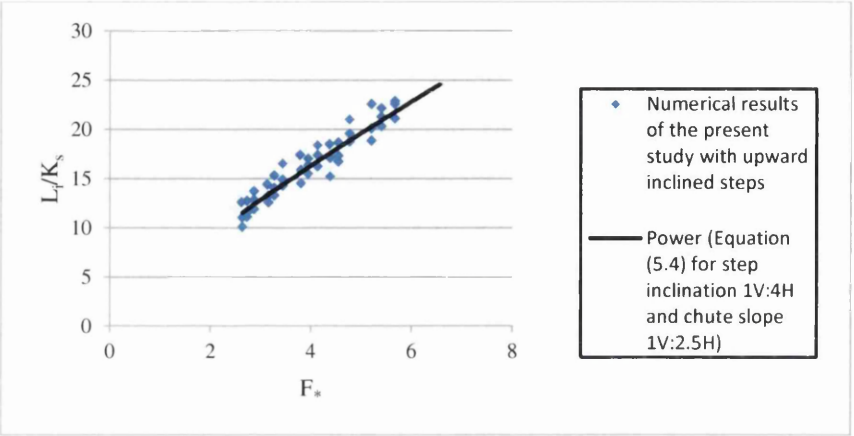

Figure 5.17. Regression for the numerical values of the normalized L_i versus F_* of the present study, using upward inclined steps with different step inclinations.

Based on the numerical results obtained in this study, the next chapter will focus on three main issues of skimming flow conditions in the non-aerated flow region over stepped spillways, namely longitudinal flow velocity profile, growth of the turbulent boundary layer and energy dissipation rate using horizontal and upward inclined steps.

CHAPTER SIX

RESULTS AND DISCUSSION:

VELOCITY DISTRIBUTION AND ENERGY DISSIPATION RATE

Chapter Six: Results and Discussion: Velocity Distribution and Energy Dissipation Rate

6.1. Introduction

The widespread interest in the design of stepped spillways is possibly due to their capability to dissipate a significant portion of the flow energy on the steps themselves during an overtopping event (Frizzell & Mefford, 1991; Chanson, 1994) without the need for a large basin at the end of the structure to dissipate the residual energy. Thus, estimating the energy dissipation rates on the steps is necessary in the design of stepped spillways. The energy dissipation rate in the non-aerated flow region is considered here since the present study concentrates on the features of skimming flow regime in that region. The parameters that need to be known in estimating the energy dissipation rate in the non-aerated flow region are the flow depth and mean flow depth at different sections (Meireles & Matos, 2009; Hunt et al. 2009).

This chapter is divided into two main sections: the first section sheds light on the behaviour of flow velocity in the non-aerated flow region. The second section focuses on evaluating the energy dissipation rate, based on the flow depth and mean flow velocity.

6.2. Velocity distribution

This section focuses on the features of the velocity flow field on both horizontal and upward inclined steps over moderate slope stepped spillways, due to various flow rates typical of the skimming flow regime. Figure 6.1 shows the velocity flow field obtained with horizontal steps of height 0.09m down 1V:2H, 1V:2.5H and 1V:3H bottom slopes, for the unit discharge of $q_w=0.25m^2/s$. The velocity pattern shown in Figure 6.2 is that of inclined steps with a step inclination of 1V:4H, height of 0.09m and unit discharge of $q_w=0.25m^2/s$ over the bottom stepped spillway slopes 1V:2H, 1V:2.5H and 1V:3H. In these figures the fluid particles are coloured according to the flow velocity they carry. As may be observed from these figures, although the velocity flow field is quantitatively different from the abovementioned step

configurations, the velocity trend is nearly identical for both. The following section presents and discusses the characteristics of the velocity profile on horizontal and upward inclined steps.

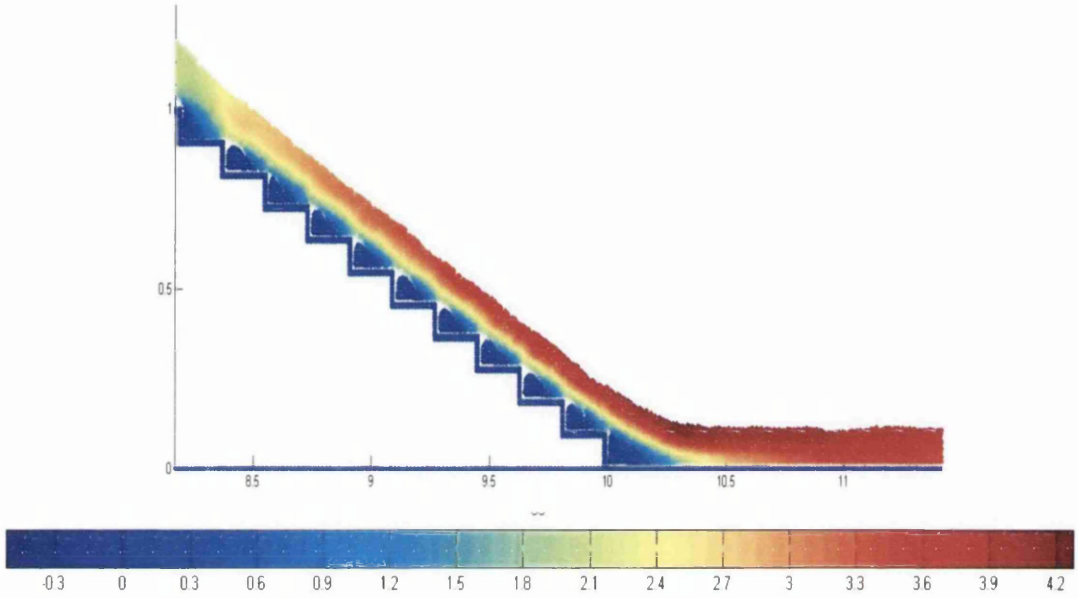

a

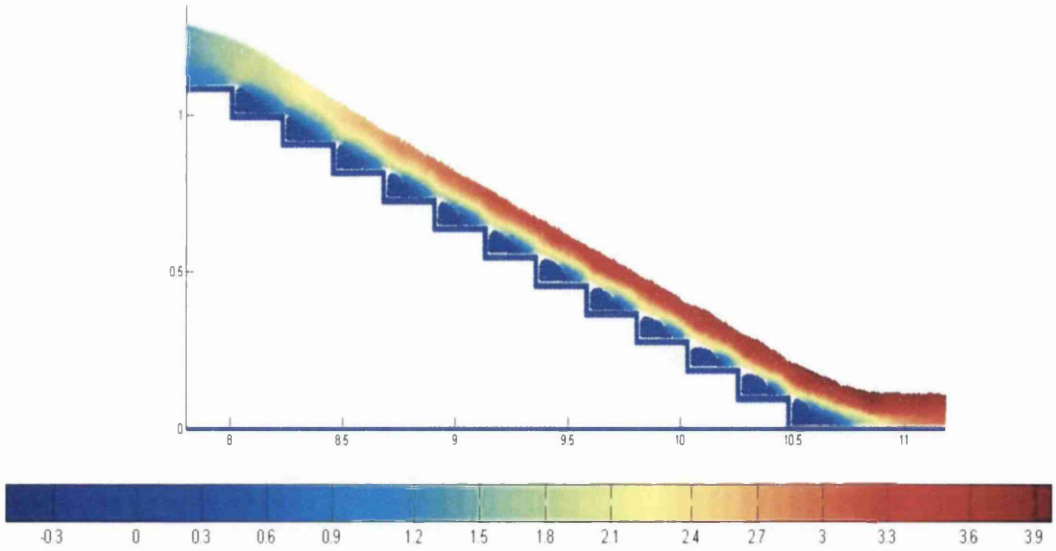

b

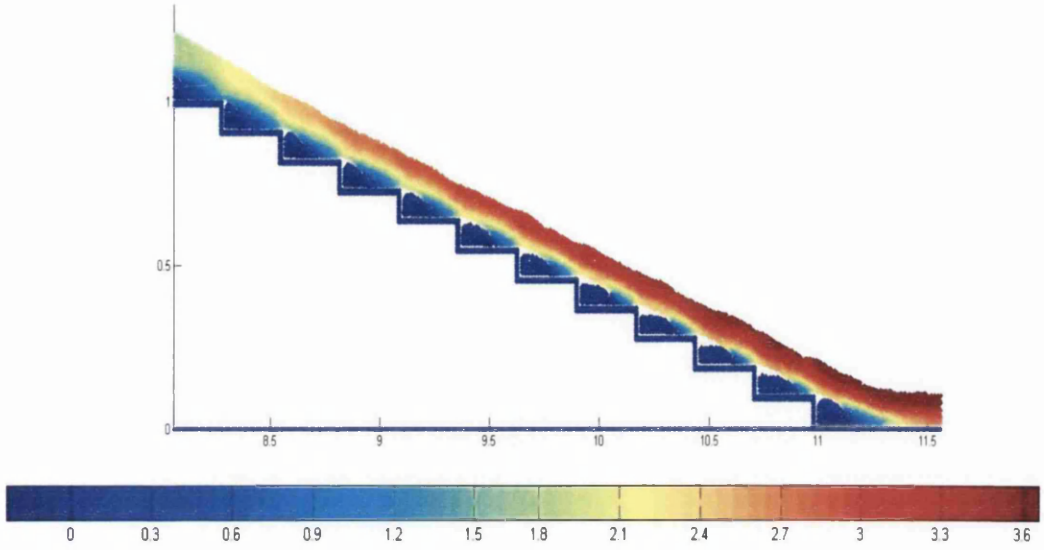

c

Figure 6.1. Velocity flow field for unit discharge of q_w=0.25m^2/s along stepped spillway over horizontal steps of height 0.09m and bottom slope: a) 1V:2H, b) 1V:2.5H and c) 1V:3H.

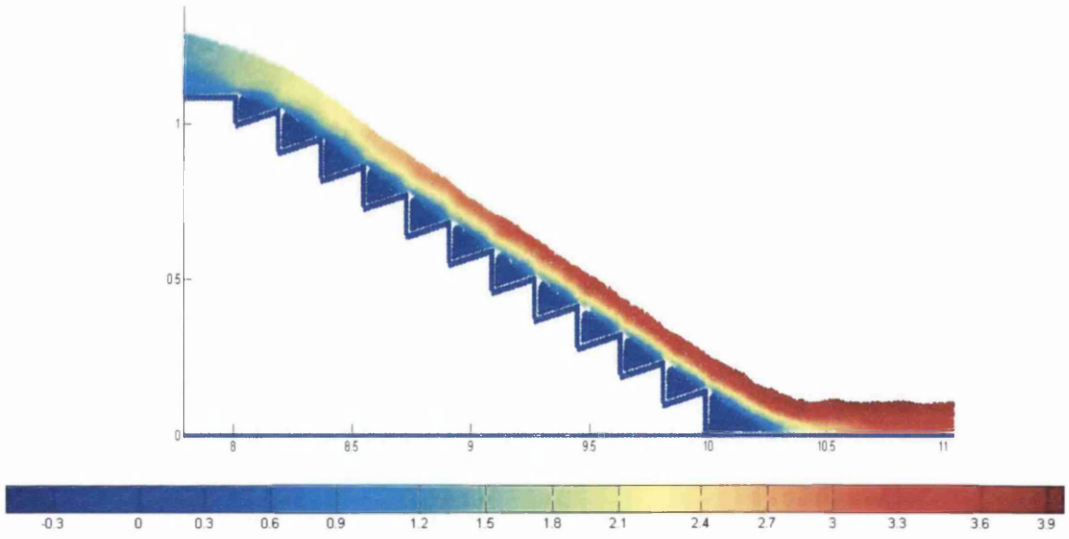

a

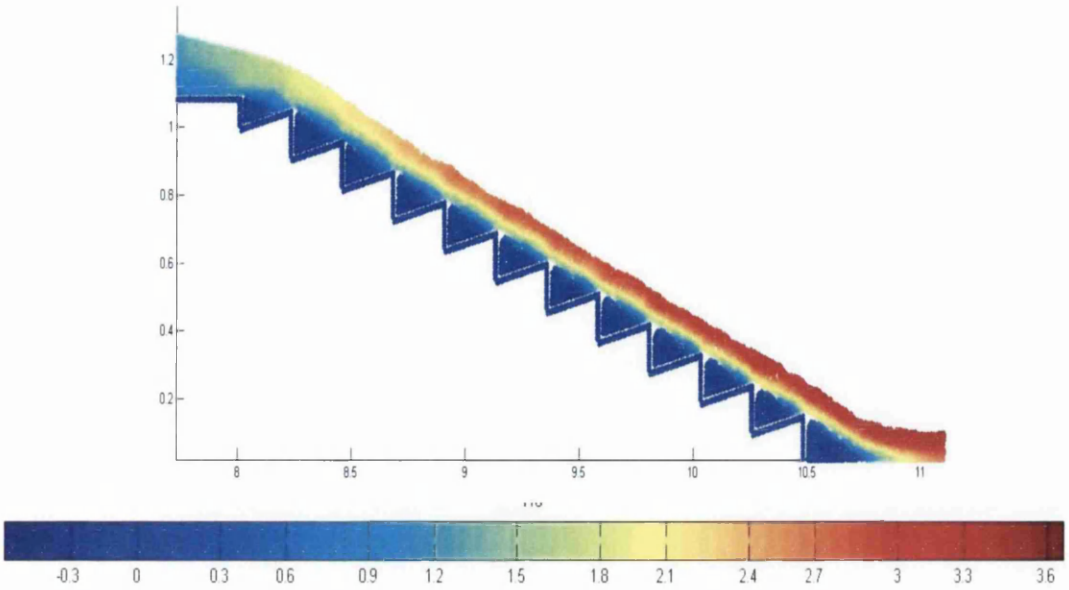

b

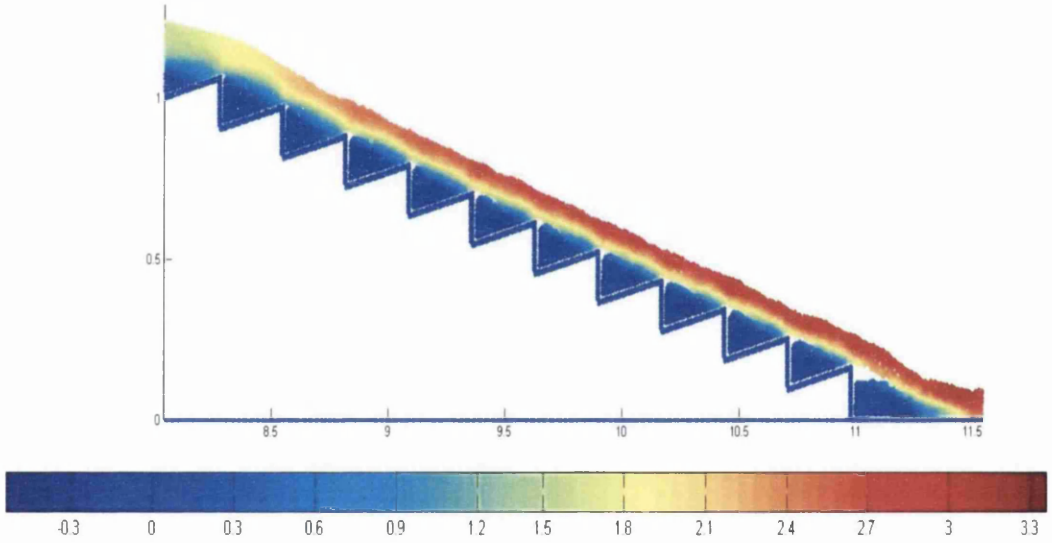

c

Figure 6.2. Velocity flow field for unit discharge of q_w=0.25m^2/s along stepped spillway over inclined steps of height 0.09m, step inclination 1V:4H and bottom slope: a) 1V:2H, b) 1V:2.5H and c) 1V:3H.

To shed light on the velocity behaviour in the non-aerated flow region over the horizontal and upward inclined steps, velocity distributions are computed in the present work at different sections along the non-aerated flow region. These sections are taken perpendicular to the pseudo bottom with an origin at the step's outer edge. In each section the flow depth is divided into a number of points and the flow velocity parallel to the chute slope is computed at each of these points. Figure 6.3 is

a 2D schematic view of a stepped spillway demonstrating how the velocity distribution is computed in the present study, on both the horizontal and upward inclined steps. In this figure, y denotes the distance between the step outer edge and the point where the streamwise velocity v is computed, δ is the thickness of the boundary layer, where the velocity is about $0.99V_{max}$, V_{max} represents the maximum flow velocity at the section where the velocity profile is taken, K_S is the roughness height and L is the distance between the downstream face of the weir and the outer edge of the step under consideration.

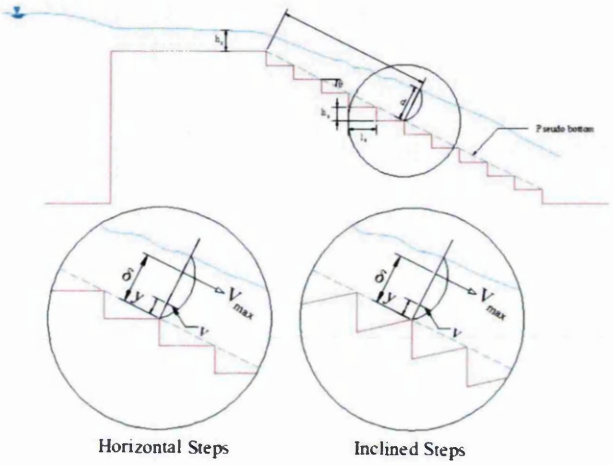

Figure 6.3. 2D schematic view of a stepped spillway which defines the parameters required to determine the velocity distribution along the chute slope at the outer edge of horizontal and inclined steps.

Figure 6.4 plots the velocity profiles relating to unit discharges of q_w= *0.23, 0.20* and *0.173*, computed at the outer edge of a number of horizontal steps within the non-aerated flow region, located at different distances, L, normalized by the step roughness, K_s. In this figure the horizontal steps with heights of 0.06, 0.09 and 0.12m and bottom chute slope of 1V:2H are considered.

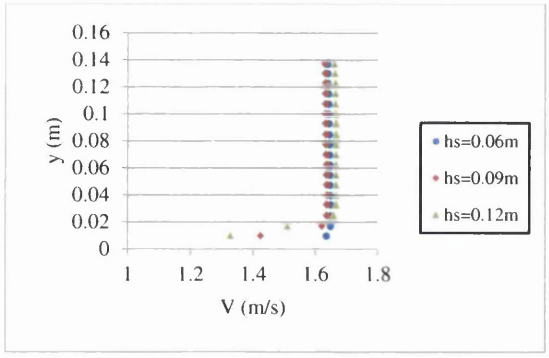

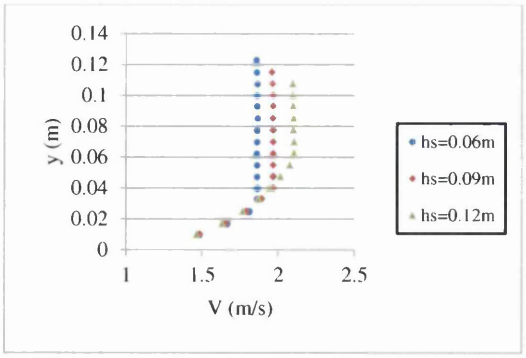

L/K$_s$= 2.5 *L/K$_s$= 7.5*

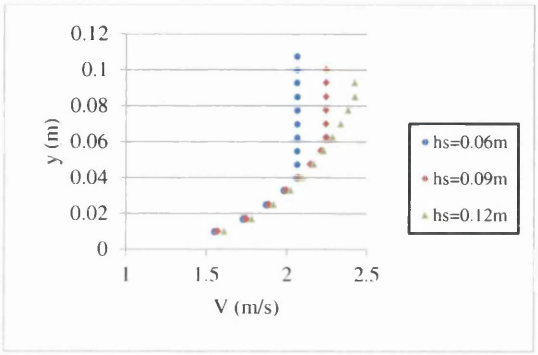

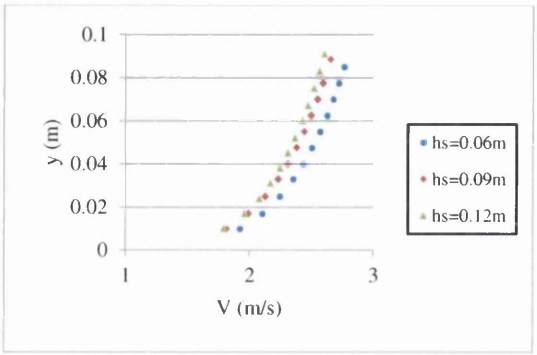

L/K$_s$= 12.5 *inception point*

a) q_w= 0.23m^2/s

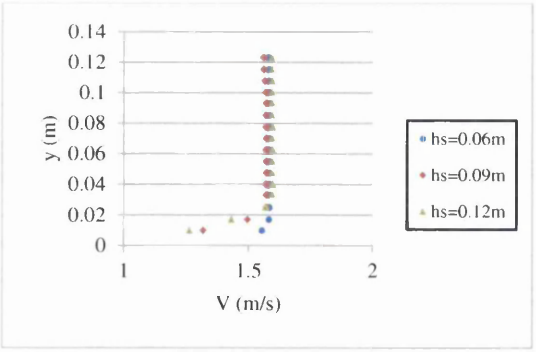

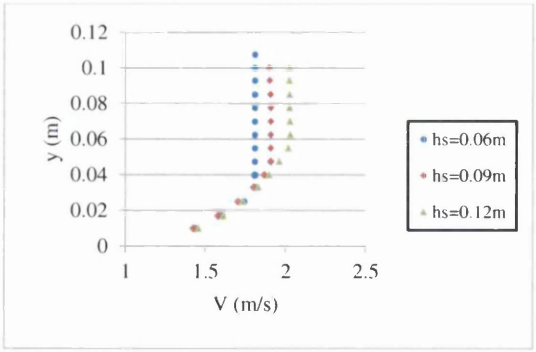

L/K$_s$= 2.5 *L/K$_s$= 7.5*

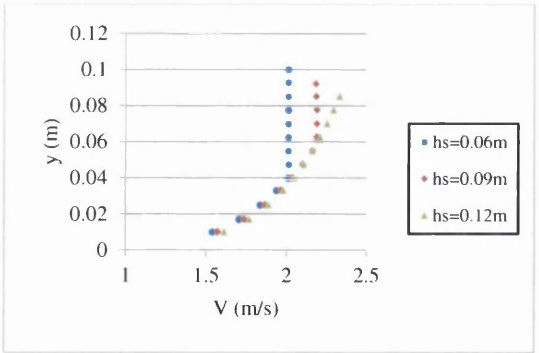

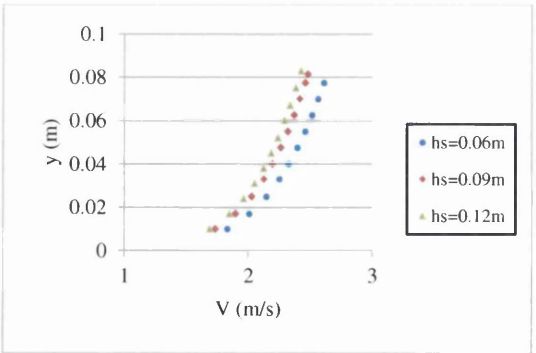

L/K$_s$= 12.5 *inception point*

b) q_w= 0.20m^2/s

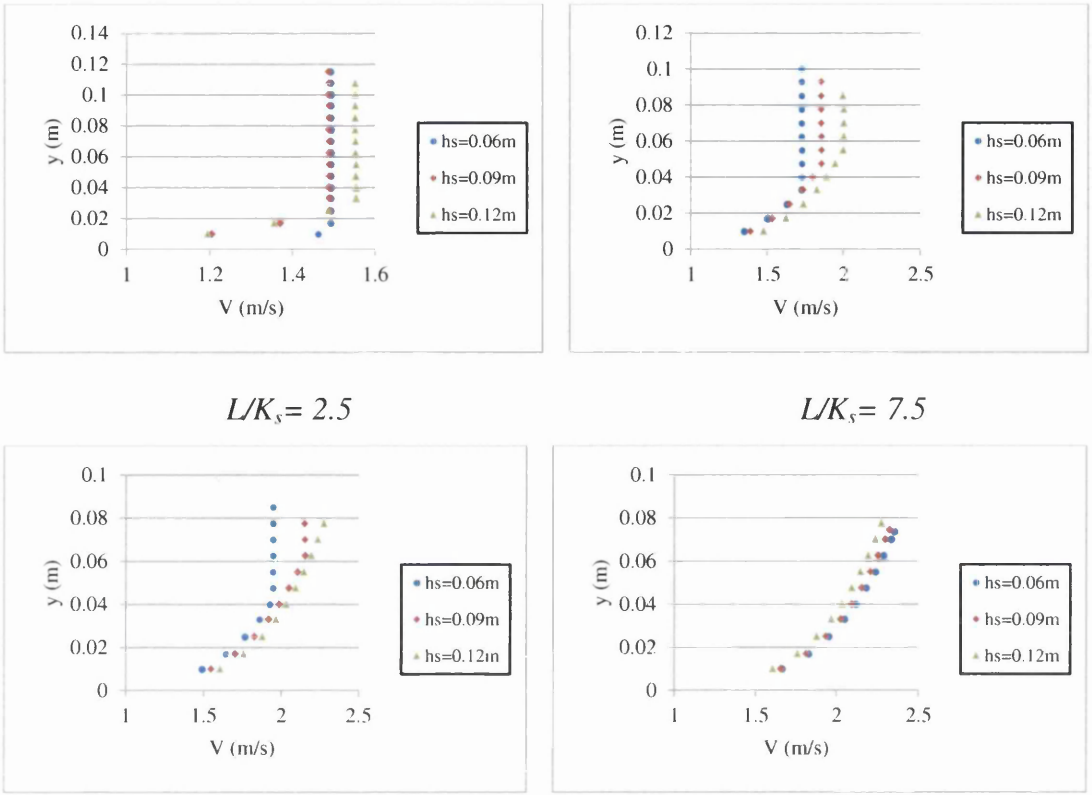

L/K_s= 2.5 *L/K_s= 7.5*

L/K_s= 12.5 *inception point*

c) $q_w = 0.173 m^2/s$

Figure 6.4. Velocity profile along the non-aerated flow region over the bottom stepped spillway slope of 1V:2H, using horizontal steps of heights 0.06m, 0.09m and 0.12m with unit discharges of: a) q_w=0.23m^2/s, b) q_w=0.20m^2/s and c) q_w=0.173m^2/s.

As can be observed, the skimming flow produces different velocity profile trends along the non-aerated flow region. This is because the velocity on the steps close to the crest is relatively small and uniformly distributed across the entire flow depth measured from the step outer edge. In addition, it is clear that the flow velocity close to the outer edge of these steps is high, which implies that the growth of the turbulent boundary layer in this region has just started and hence its thickness would be small. Then, due to gravitational acceleration, the velocity increases and the uniformity of the velocity profile vanishes gradually as the water flows further downward, reaching its peak value close to the inception point where the velocity varies over the whole flow depth. The same characteristics of the flow velocity are observed on the other chute slopes and unit discharges examined in the current work.

These figures also demonstrate that for the same spillway height, the mean flow velocity close to the inception point of air entrainment is reduced by about 4.0% and 6.2% when the step height of 0.06m is replaced by 0.09m and 0.12m respectively. This is possibly due to the increase of the recirculating area under the skimming layer inside the step cavity when the step height is increased. In fact, this area is significant for decelerating the velocity of the rapid flow because: 1) it acts as an obstacle against the overflowing water and 2) inside this area vortices continuously develop, rotate, eject back and mix with the skimming layer.

The characteristics of the velocity distribution mentioned above are nearly the same across the whole flow depth over the other stepped spillway slopes examined in the present work. Figures 6.5 and 6.6 show the velocity profiles obtained at different sections along the non-aerated flow region due to various unit water discharges flowing over the chute slopes of 1V:2.5H and 1V:3H respectively.

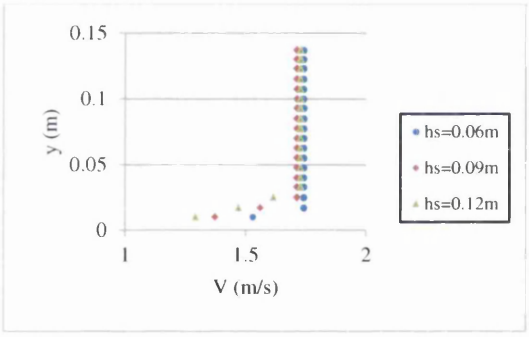

$L/K_s = 2.9$

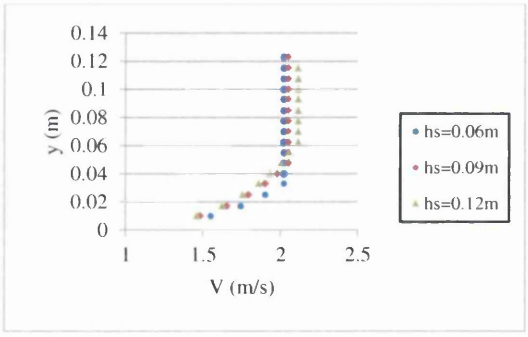

$L/K_s = 8.7$

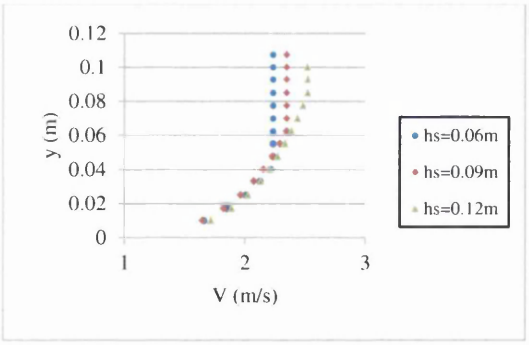

$L/K_s = 14.5$

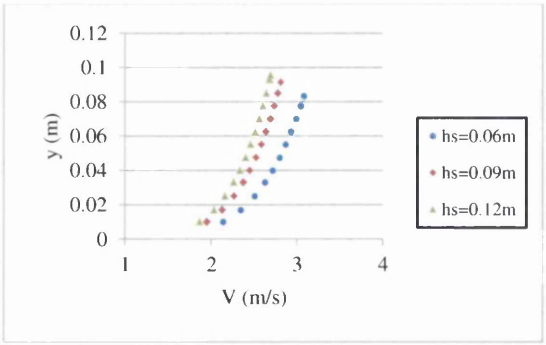

inception point

a) $q_w = 0.25 m^2/s$

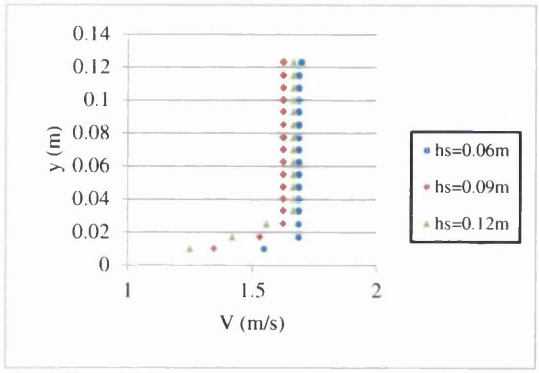

$L/K_s = 2.9$

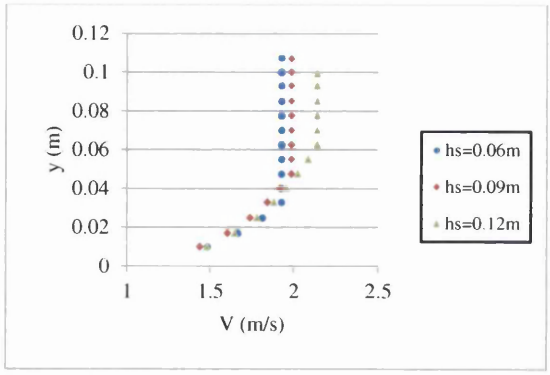

$L/K_s = 8.7$

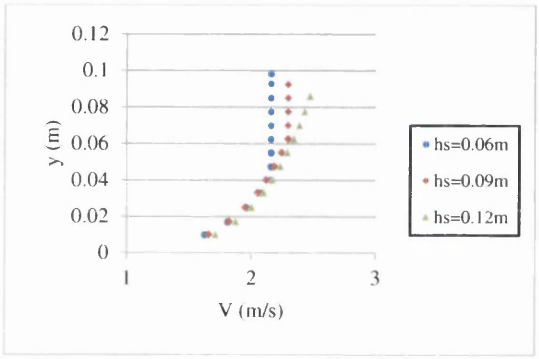

$L/K_s = 14.5$

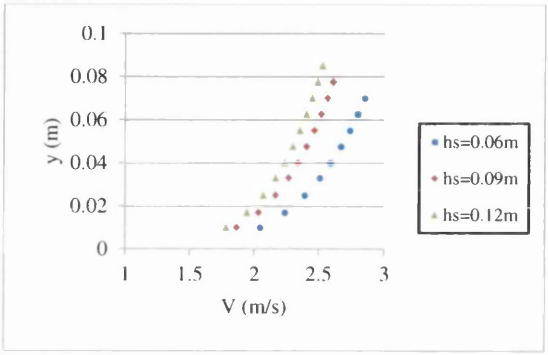

inception point

b) $q_w = 0.21 m^2/s$

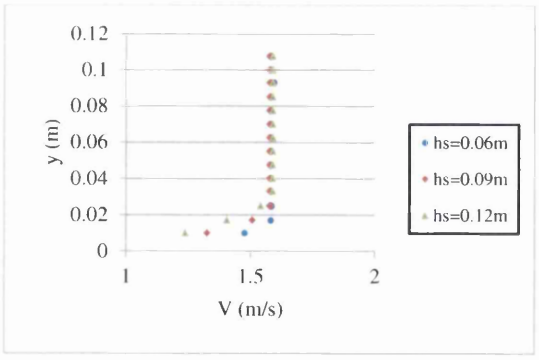

$L/K_s = 2.9$

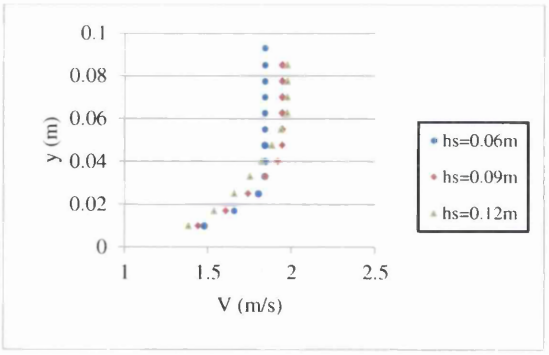

$L/K_s = 8.7$

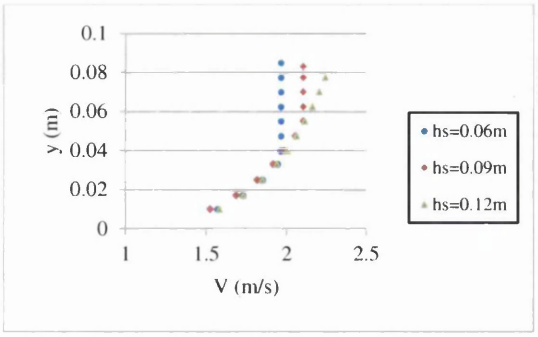

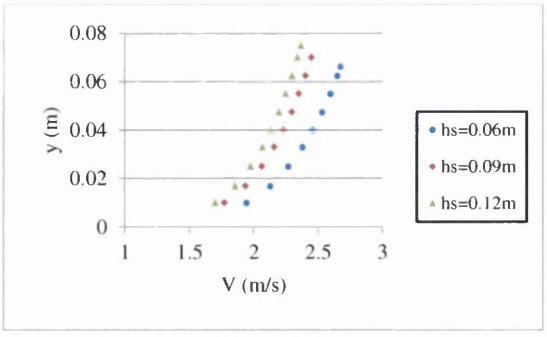

L/K_s= 11.6 *inception point*

c) $q_w = 0.173 m^2/s$

Figure 6.5. Velocity profile along the non-aerated flow region over the bottom stepped spillway slope of 1V:2.5H, using horizontal steps of heights 0.06m, 0.09m and 0.12m, for unit discharges of: a) q_w=0.25m^2/s, b) q_w=0.21m^2/s and c) q_w=0.173m^2/s.

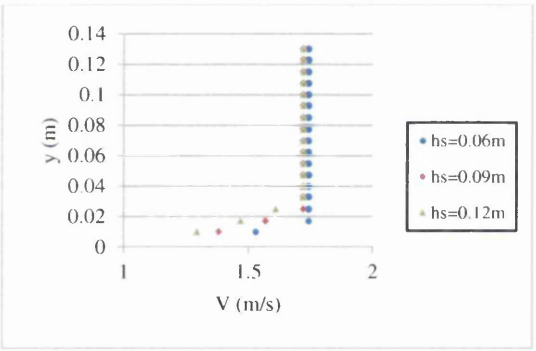

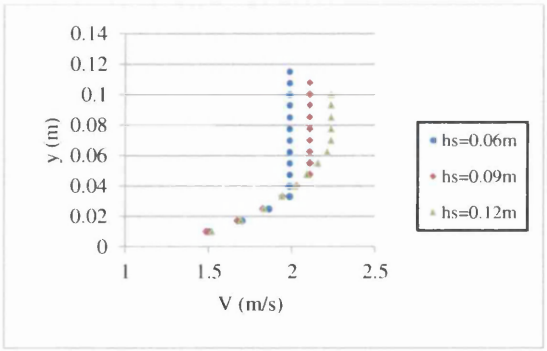

L/K_s= 3.33 *L/K_s= 10*

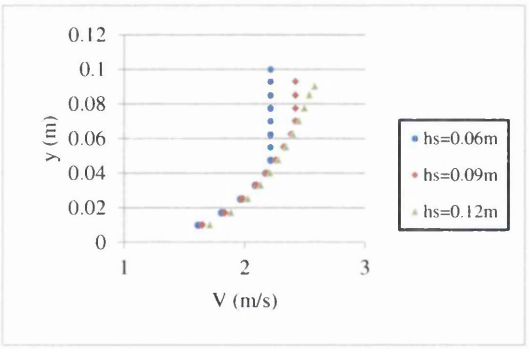

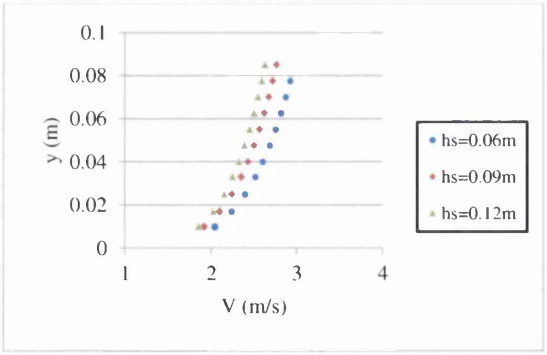

L/K_s= 14.5 *inception point*

a) $q_w = 0.23 m^2/s$

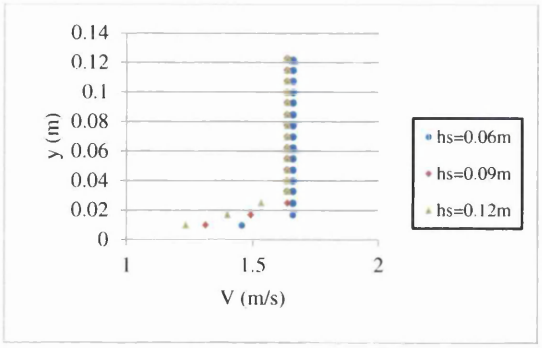

L/K_s= 3.33

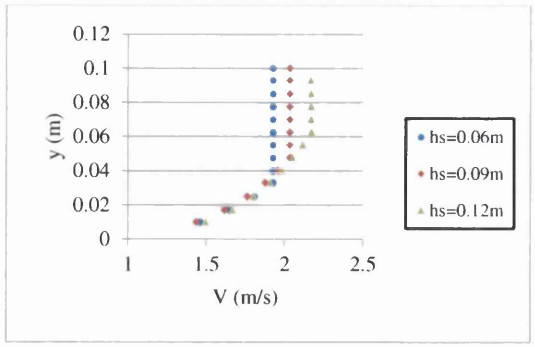

L/K_s= 10

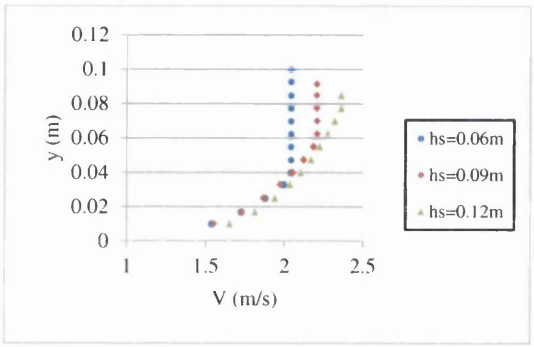

L/K_s= 13.33

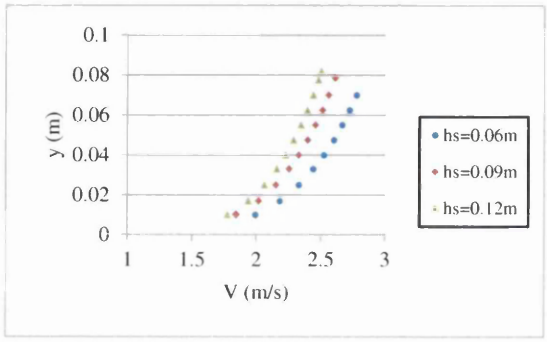

inception point

b) q_w= 0.20m^2/s

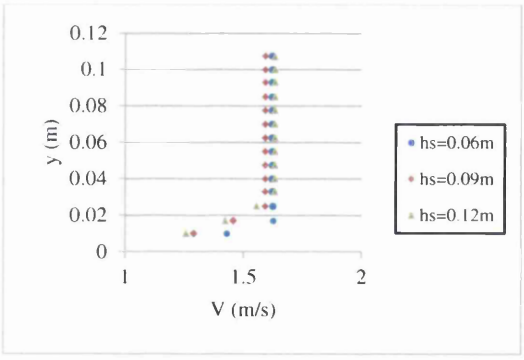

L/K_s= 3.33

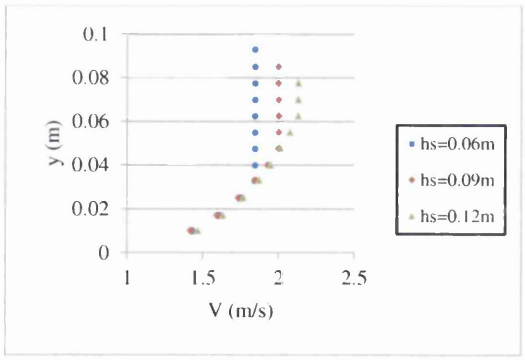

L/K_s= 10

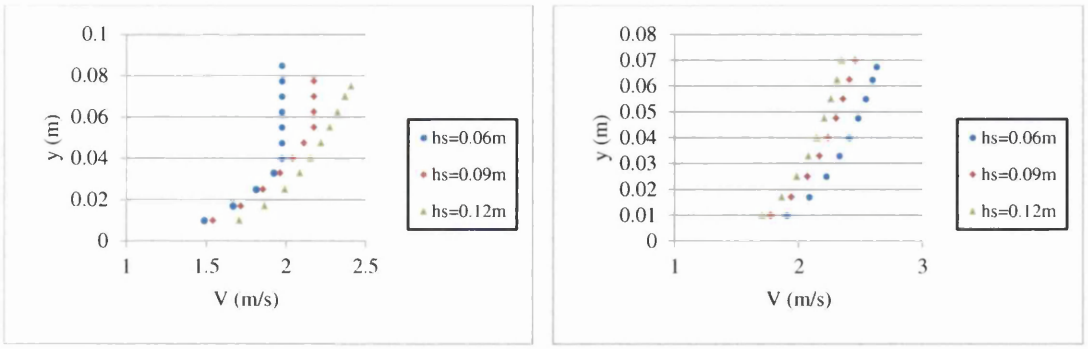

L/K_s= 13.33 *inception point*

c) $q_w = 0.173 m^2/s$

Figure 6.6. Velocity profile along the non-aerated flow region over the bottom stepped spillway slope of 1V:3H, using horizontal steps of heights 0.06m, 0.09m and 0.12m, for unit discharges of: a) q_w=0.23m^2/s, b) q_w=0.21m^2/s and c) q_w=0.173m^2/s.

This section concerns the velocity profile obtained with the upward inclined steps. Figure 6.7 illustrates the velocity profiles at the outer edge of upward inclined steps located at different distances measured from the downstream face of the weir crest, along the non-aerated flow region of 1V:2H bottom slope, for different unit discharges. This figure presents the velocity profiles of the upward inclined steps of height 0.09m obtained for the three step inclinations of 1V:2H, 1V:3H and 1V:6H. It also includes the velocity profile obtained with horizontal steps of the same height as that of the inclined steps, and with the chute slopes mentioned above. This figure clearly shows that the velocity profile along the non-aerated flow region on inclined steps possesses the same features mentioned above with the horizontal steps. Moreover, it demonstrates that for a given discharge and stepped spillway geometry, in terms of step height and chute slope, the velocity of the skimming flow on inclined steps is slower than that on the horizontal steps. The mean flow velocity close to the inception point of air entrainment is reduced by 10.5% and 6.9% when the horizontal steps are replaced by inclined steps of inclinations 1V:3H and 1V:6H respectively. This indicates that the inclined steps are more efficient in reducing the flow velocity than the horizontal steps, and this efficiency is increased when the slope of the inclined steps is increased. This can be due to the fact that the upward inclined steps act as a barrier against the overflowing water and its impact increases as the angle of the inclined steps is increased.

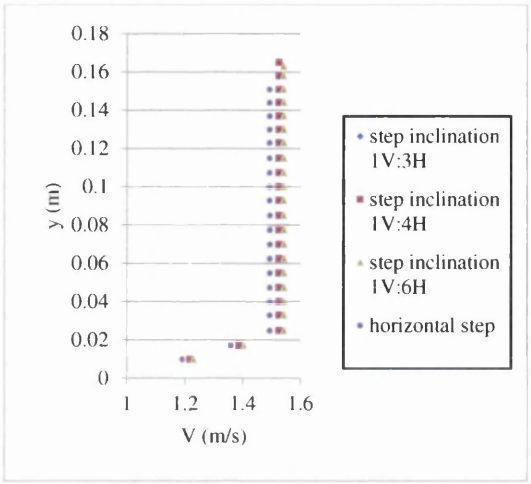

$L/K_s = 2.5$

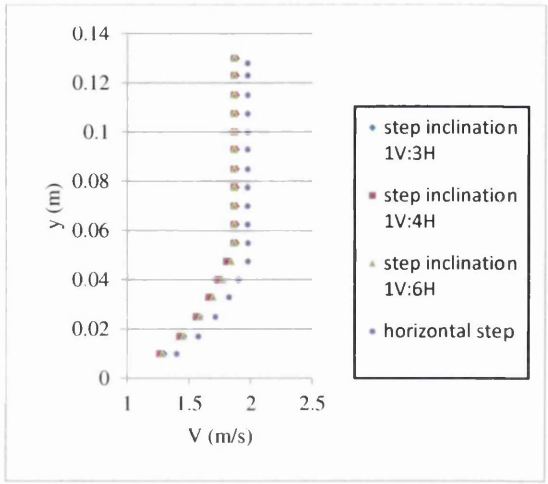

$L/K_s = 7.5$

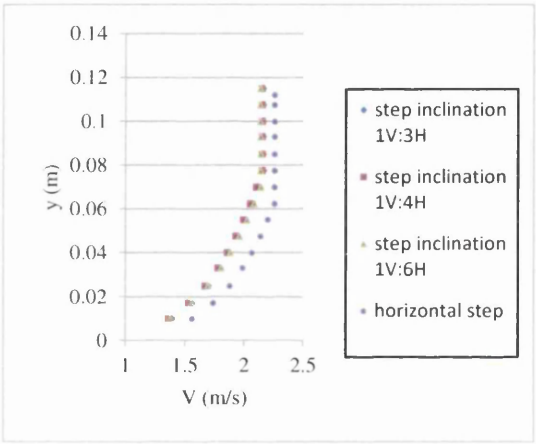

$L/Ks = 12.5$

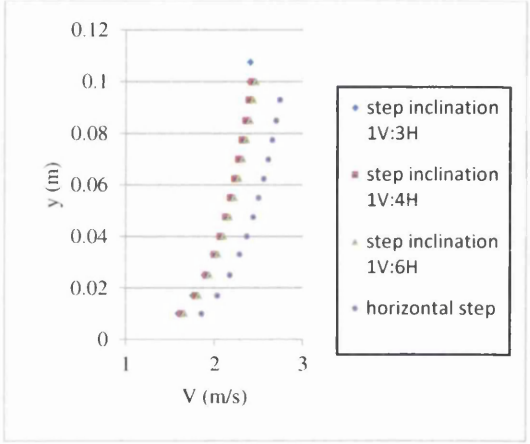

inception point

a) $q_w = 0.25 m^2/s$

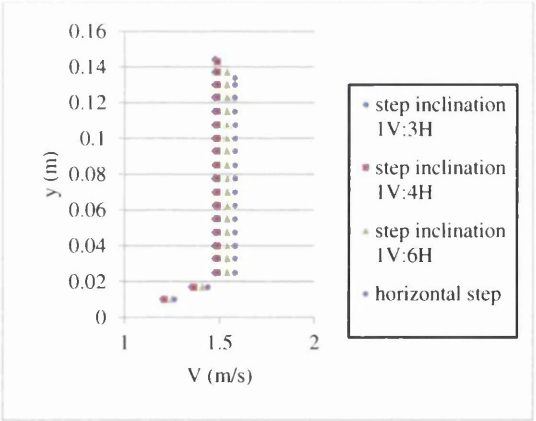

$L/K_s = 2.5$

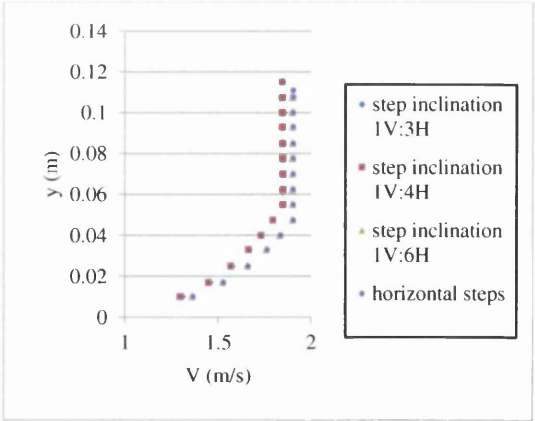

$L/K_s = 7.5$

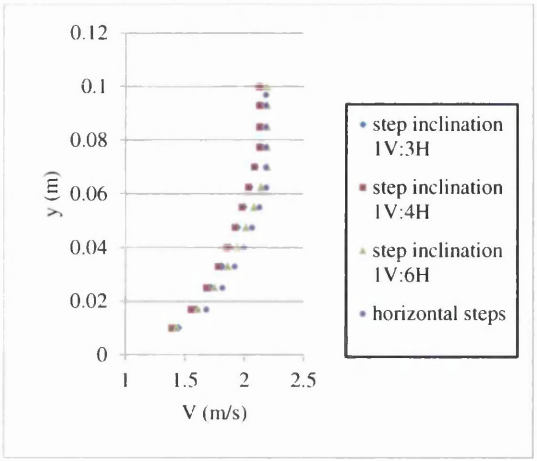

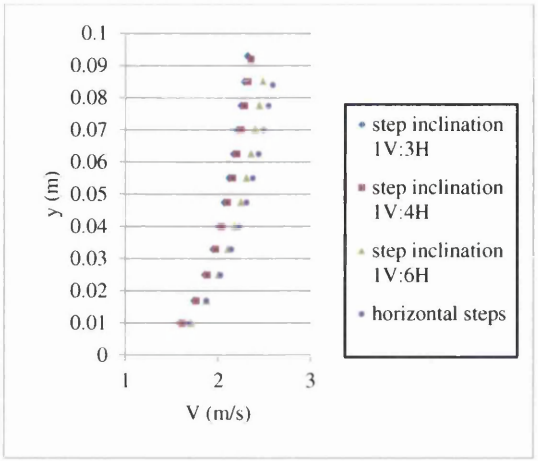

L/K_s= 12.5 *inception point*

b) q_w= 0.21m^2/s

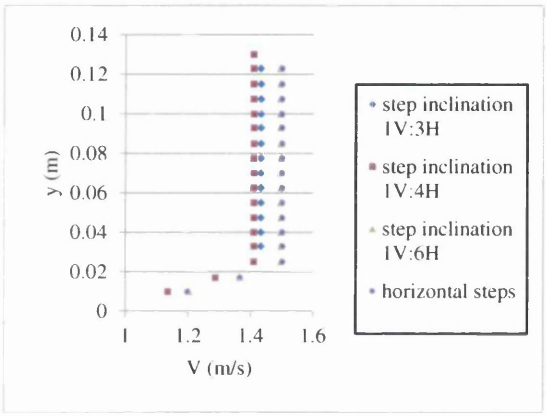

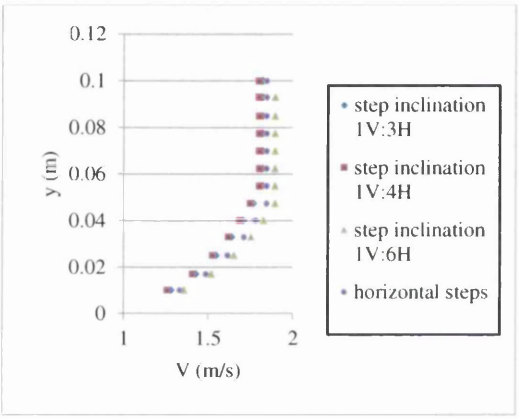

L/K_s= 2.5 *L/K_s= 7.5*

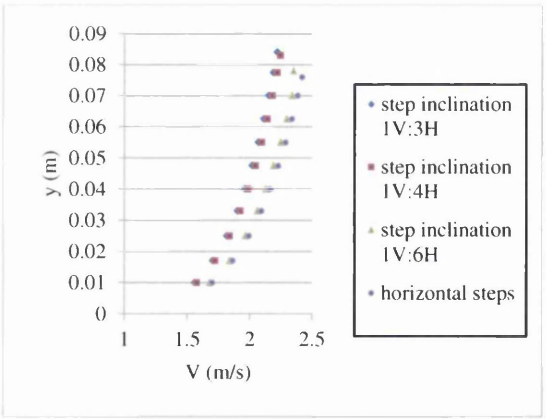

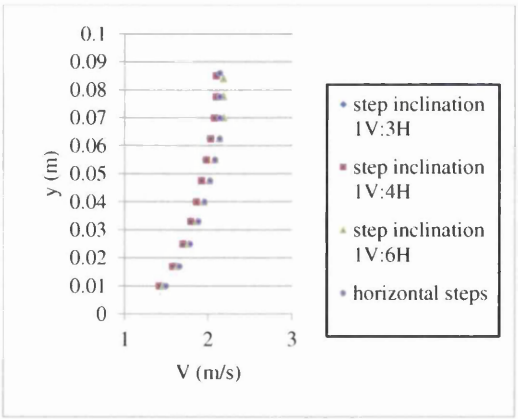

L/K_s= 12.5 *inception point*

c) q_w= 0.182m^2/s

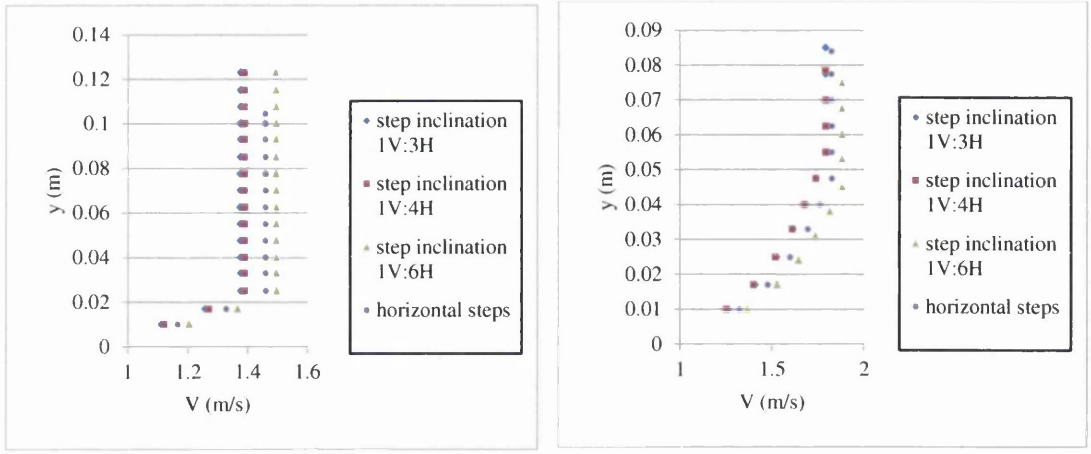

L/K$_s$= 2.5 *L/K$_s$= 7.5*

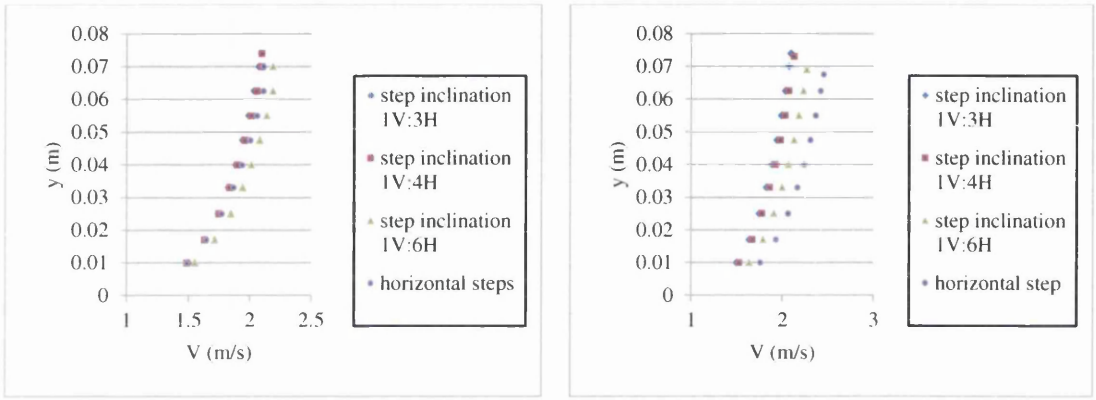

L/K$_s$= 12.5 *inception point*

d) $q_w = 0.151 m^2/s$

Figure 6.7. Velocity profile along the non-aerated flow region over the stepped spillway of bottom slope 1V:2H, using upward inclined steps of height 0.09m and three inclinations 1V:3H, 1V:4H and 1V:6H, with unit discharges of: a) q_w=0.25m^2/s, b) q_w=0.21m^2/s, c) q_w=0.182m^2/s and d) q_w=0.151m^2/s.

Chanson (2002) stated that the velocity profile at any section along the non-aerated flow region perpendicular to the pseudo bottom originating at the step outer edge can be defined by a power law as:

$$\frac{V}{V_{max}} = \left(\frac{y}{\delta}\right)^{1/N} \qquad (6.1)$$

where V is the time averaged flow velocity at distance y, measured perpendicular to the pseudo bottom originating at the outer edge of the steps, V_{max} is the maximum flow velocity, N is constant and δ is the whole thickness of the boundary layer, where the flow velocity is 0.99 V_{max}. Past experimental studies showed that the exponent N depends mainly on the chute slope and the section where the velocity distribution is measured. Meireles and Matos (2009), from their experimental study on 1V:2H stepped spillways, observed that the value of the exponent N varied between 4.4 and 6.3, with an average value of 5.1, for a wide range of unit discharges typical to the skimming flow regime. They obtained these values at different sections starting at about 40% length of the non-aerated flow region and extending to the inception point of air entrainment. Moreover, Chanson (2002) analysed the velocity measurements, which were taken with a laser Doppler anemometer by Ohtsu and Yasuda (1997), and found that the value of N was 5.0 for the single discharge test of 0.089 $m^3/s/m$ over a stepped spillway of slope 1V:2.9H. Furthermore, Hunt et al. (2009) measured the velocity profiles at the outer edge of a number of steps along the non-aerated region, of the skimming flow regime. They pointed out that the velocity profile follows the one-six power trend $N=6$ close to the inception point of air entrainment, with smaller values $N<6$ further upstream.

It is essential to investigate the growth of the turbulent boundary layer in the non-aerated flow region, in order to obtain the value of the exponent N appearing in Equation (6.1). The velocity profiles obtained for various discharges and step geometries examined in the present investigation reveal that they follow different trends along the non-aerated flow region. This is possibly because of the development of the turbulent boundary layer in this region. Chanson (2002) mentioned that although there is no precise analytical or mathematical expression to describe this development, it is highly influenced by both the chute slope and step height, and slightly affected by the discharge and crest shape. He proposed the following power equation:

$$\frac{\delta}{L} = 0.06106 * (sin\theta)^{0.133} * \left(\frac{L}{K_s}\right)^{-0.17} \quad (6.2)$$

where δ is the thickness of turbulent boundary layer, L is the length to the step outer edge measured from the downstream face of the weir corner and K_s is the roughness

height. The real numbers appearing in Equation (6.2) are obtained from the analysis of a wide range of model prototype data having slopes stepper than 30°.

The experimental results of André (2004) on different step configurations showed that the growth of the boundary layer on a particular arrangement of endsills and spaced blocks is faster compared with the horizontal steps. Moreover, Chamani et al. (2000) analysed their experimental data on steeply stepped spillway, and found that the development of the boundary layer is dependent on the step height.

In the present study the thickness of the turbulent boundary is deduced from the velocity profiles at the outer edges of steps located along the non-aerated flow region, for various discharges, step heights and shapes, and chute slopes. In order to develop an equation that expresses the growth of the turbulent boundary layer along the non-aerated flow region of moderate slope stepped spillways, Equation (6.2) is modified in this study so as to introduce the effects of the discharge, step height and chute slope. For this purpose, two dimensionless parameters h_c/h_s and $\sin\theta$ are added to Equation (6.2) to develop an expression for determining the thickness of the boundary layer on horizontal steps, taking into consideration the effect of discharge, step height and chute slope. The non-linear multiple regression is performed on these parameters and the following equation is obtained in the present work:

$$\frac{\delta}{L} = 0.218\left(\frac{L}{K_s}\right)^{-0.332}\left(\frac{h_c}{h_s}\right)^{-0.028}(sin\theta)^{0.557} \tag{6.3}$$

Equation (6.3) shows that the growth of the turbulent boundary layer along the non-aerated flow region on moderate stepped spillways is slightly influenced by the discharge and step height, and significantly affected by the chute slope.

Moreover, in addition to the above two parameters, $\sin\vartheta$ is also added to Equation (6.3) to introduce the influence of the step inclination on the growth of the turbulent boundary layer on upward inclined steps, yielding the following expression:

$$\frac{\delta}{L} = 0.269\left(\frac{L}{K_s}\right)^{-0.321}\left(\frac{h_c}{h_s}\right)^{-0.032}(sin\theta)^{0.464}(\sin\vartheta)^{0.161} \tag{6.4}$$

It is clear from Equation (6.4) that the steeper the step inclination, the faster the growth of the turbulent boundary layer will be. This can be attributed to the fact that

the increase of the adverse slope of the steps with the horizontal face may increase the area where the vortices, which have a significant role in the growth of the boundary layer, develop and rotate inside the step cavities. Furthermore, for the same discharge, step height and chute slope, Equation (6.4) provides higher values of the thickness of turbulent boundary layer compared with Equation (6.3). This indicates that the growth of the turbulent boundary layer on upward inclined steps is faster than that on horizontal steps.

Turning to the determination of the value of N in Equation (6.1), the velocity profiles obtained from both the horizontal and upward inclined steps are analysed for the skimming flow discharges tested in the current work. Figures 6.8 and 6.9 show the velocity profiles on the horizontal and upward inclined steps respectively. The computational results shown in these figures are obtained for the different step heights, step inclination angles, chute slopes and discharges tested in the present study. The numerical results presented in Figure 6.8 are gathered at the outer edge of steps located within the range of $0.0828 \leq L/L_i \leq 1$, whilst the numerical data shown in Figure 6.9 are velocity profiles obtained at the outer edge of the upward inclined steps located within $0.202 \leq L/L_i \leq 1$, where L is the distance between the downstream face of the weir and the outer edge of the step under investigation, and L_i is the length to the inception point of air entrainment. Also, these figures show the value of the exponent N for each slope tested in the present study. The value of the exponent N obtained in the current study for horizontal steps varies between 4.37 for steps close to the weir crest, and about 6.14 close to the inception point. These values are respectively 4.28 and 5.76 for the upward inclined steps. This agrees well with the N values obtained from the experimental work of Chanson (2002), Meireles and Matos (2009) and Hunt et al. (2009).

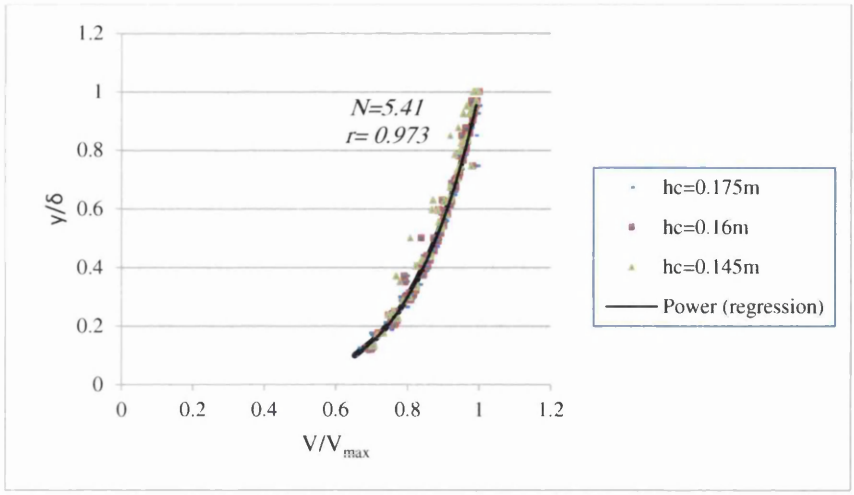
N=5.41
r= 0.973
y/δ
V/V max
hc=0.175m
hc=0.16m
hc=0.145m
Power (regression)

a

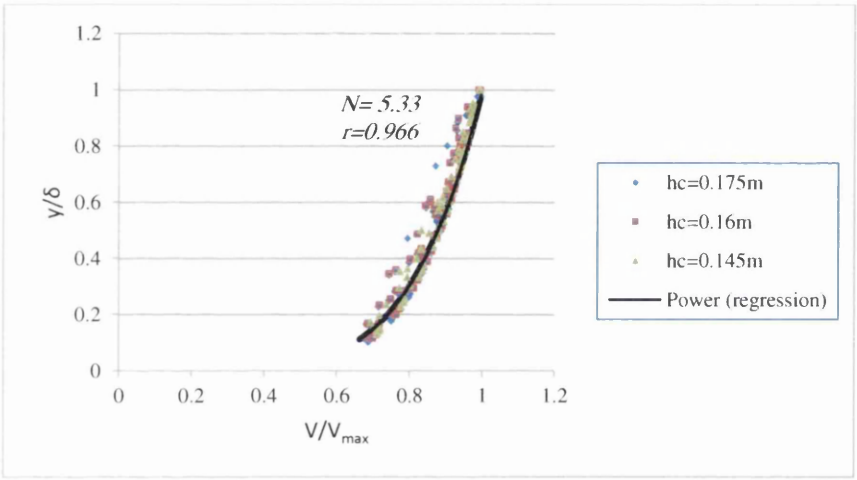
N= 5.33
r=0.966
y/δ
V/V max
hc=0.175m
hc=0.16m
hc=0.145m
Power (regression)

b

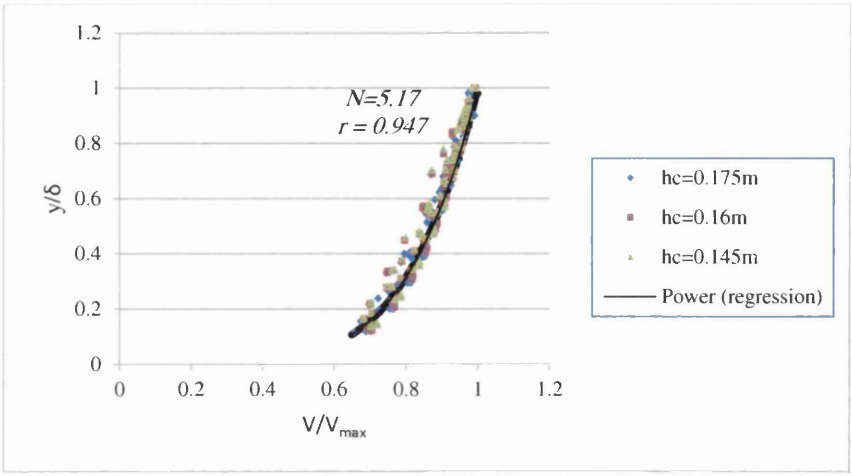

c

Figure 6.8. Velocity distribution in the non-aerated flow region over horizontal steps of 0.06, 0.09 and 0.12m step heights versus the power law regression for slopes: a) 1V:2H, b) 1V:2.5H and 1V:3H.

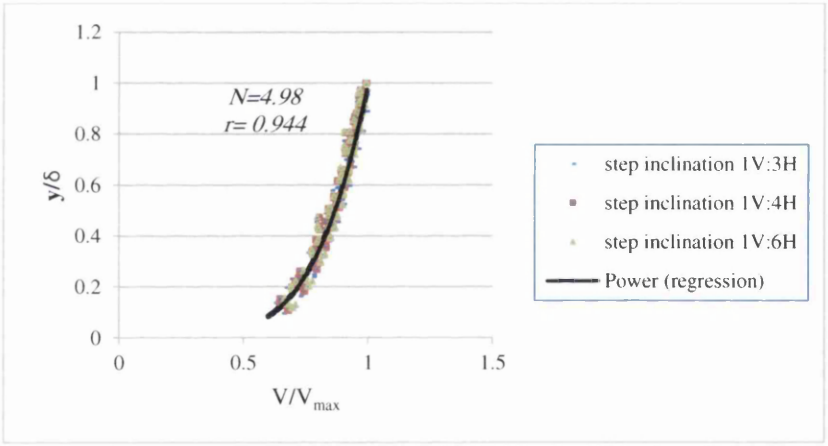

a

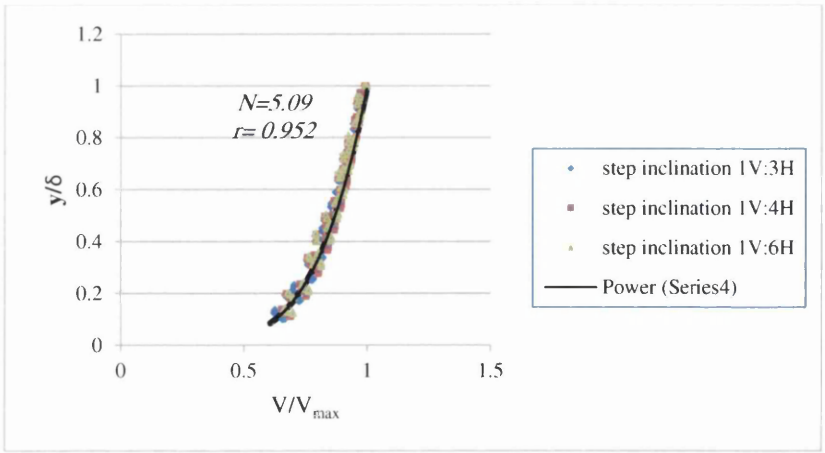

b

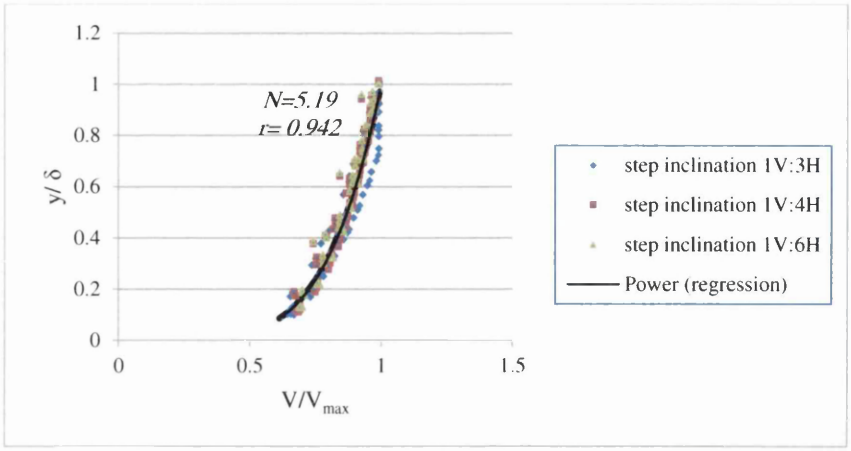

c

Figure 6.9. Velocity distribution in the non-aerated flow region over upward inclined steps of 0.09m step height versus the power law regression for slopes: a) 1V:2H, b) 1V:2.5H and 1V:3H.

6.3. Energy dissipation

One of the most important features that has attracted the attention of hydraulic engineers in the design of stepped spillways is their efficiency in dissipating a significant portion of the overflowing energy. As mentioned earlier, estimating the amount of the residual energy is necessary in the design of the stilling basin at the toe of the spillway. In fact, steps have the ability to generate high levels of turbulence when introduced into the downstream slope of smooth spillways. Indeed, the high level of turbulence is the main property of the flow over stepped spillways, which greatly enhances the energy dissipation mechanism (Chanson, 2002). The energy dissipation in the skimming flow regime over stepped spillways takes place on the steps, which is mainly due to the momentum transfer between the over-running flow and the recirculating fluid underneath (Rajaratnam, 1990; Rice & Kadavy, 1996; Chanson, 2002). The turbulence on stepped spillways includes the recirculating vortices that develop inside the cavity of each step and the internal transverse jet (Chanson, 1994; Boes & Hager, 2002; André, 2004).

In the present study, the steps located upstream of the inception point of air entrainment are considered, to estimate the residual energy on the stepped spillway. Figure 6.10 is a 2D schematic view of a moderate slope stepped spillway, where the

parameters required to estimate the residual energy on the horizontal and upward inclined steps are defined.

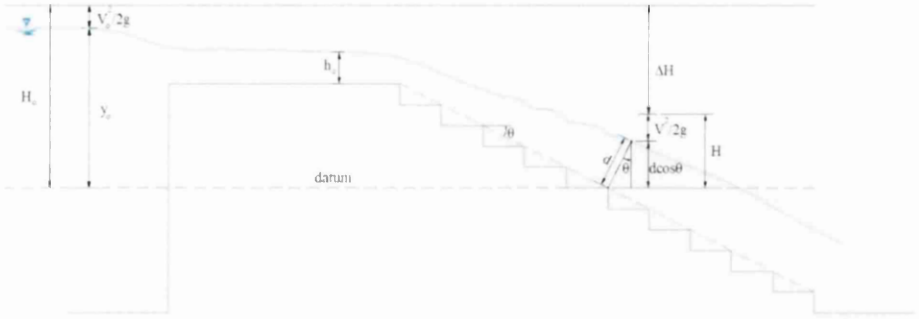

a

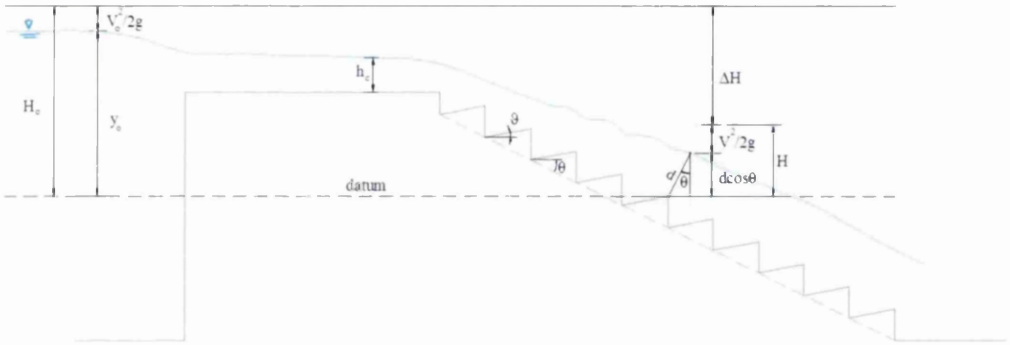

b

Figure 6.10. 2D schematic view of a stepped spillway showing the parameters required to estimate the residual energy at the outer edge of: a) horizontal steps and b) inclined steps.

Chanson (2002) stated that Bernoulli's equation can be applied to determine the total flow energy H at the outer edge of each step along the non-aerated flow region, as follows:

$$H = y\cos\theta + \alpha\frac{V_{mean}^2}{2g} \tag{6.5}$$

where y and V_{mean} are respectively the flow depth and mean flow velocity at the step under consideration, θ is the bottom chute slope, α is the energy coefficient and g is the gravitational acceleration. The energy coefficient α is introduced into Equation

(6.5) to account for non-uniform velocity distribution over stepped spillways (Chow, 1959) which can be estimated from the following expression:

$$\alpha \approx \frac{\sum v^3 \Delta A}{V^3 A} \tag{6.6}$$

where v is the flow velocity in the velocity distribution corresponding to the incremental area ΔA and A is the flow area. Assuming uniform flow across the channel width, then the area A can be replaced by the flow depth y. Similarly, the total flow energy H_o upstream of the weir can be determined in terms of the approach flow depth y_o above the horizontal surface of the step under consideration and approach flow velocity V_o as:

$$H_o = y_o + \frac{V_o^2}{2g} \tag{6.7}$$

Hence, the total dissipated energy ΔH with respect to the step under consideration is:

$$\Delta H = H_o - H \tag{6.8}$$

However, Equations (6.5) to (6.8) can be used to determine the parameters required for evaluating the energy dissipation rates. In the present study the value of the energy coefficient is found to vary between 1.03 and 1.08, which is in good agreement with results obtained by André (2004) and Meireles and Matos (2009). The energy dissipation rate on stepped spillways is commonly represented by either the residual energy relative to the total flow energy H/H_o or the total energy lost relative to the total energy flow $\Delta H/H_o$. In the present work the term $\Delta H/H_o$ is used to evaluate the energy dissipation rate along the non-aerated flow region. The rate of energy dissipation in the present study quantifies the total energy loss from the beginning of the non-aerated flow region to the step under consideration.

This section presents and discusses the computational results obtained in this study, in terms of the evolution of the flow energy along the non-aerated flow region on moderate slopes, with horizontal and upward inclined steps, over the tested chute slopes. Figures 6.11, 6.12 and 6.13 show the variation of the relative energy

dissipation rate $\Delta H/H_o$ versus the dimensionless term L/Li on the horizontal steps, with step heights of 0.06m, 0.09m and 0.12m over chute slopes of 1V:2H, 1V:2.5H and 1V:3H respectively, for different unit discharges. In these figures L is the length measured from the downstream edge of the weir to the step under scrutiny and L_i is the length to the inception point of air entrainment.

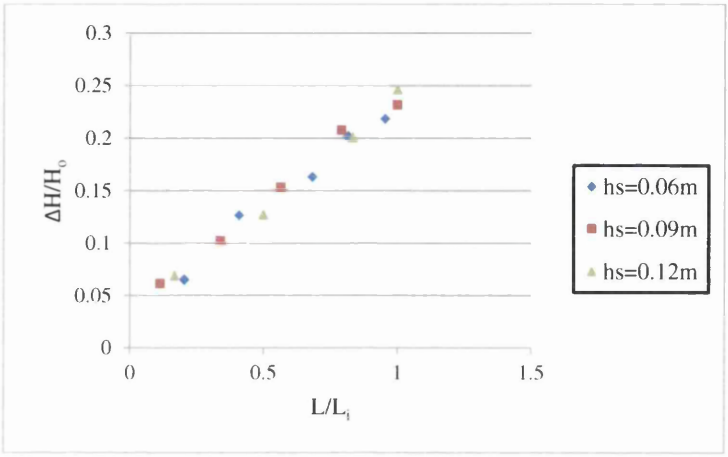

a

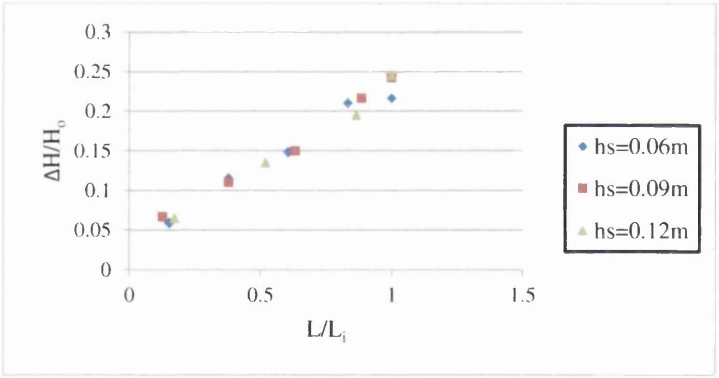

b

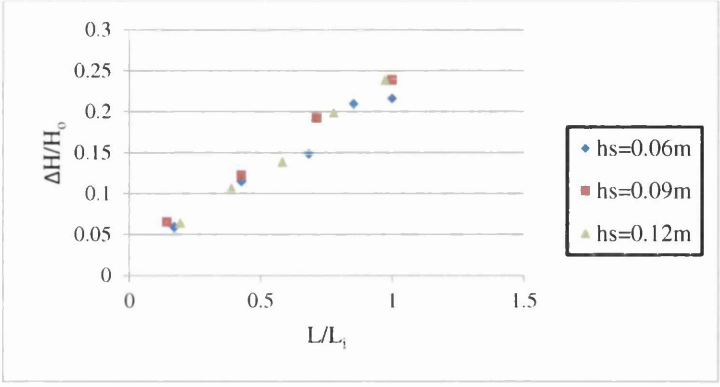

c

Figure 6.11. Variation of relative energy loss along the non-aerated flow region of a stepped spillway of bottom slope 1V:2H, using horizontal steps, for unit discharges of: a) q_w=0.23m^2/s, b) q_w=0.20m^2/s and c) q_w=0.173m^2/s.

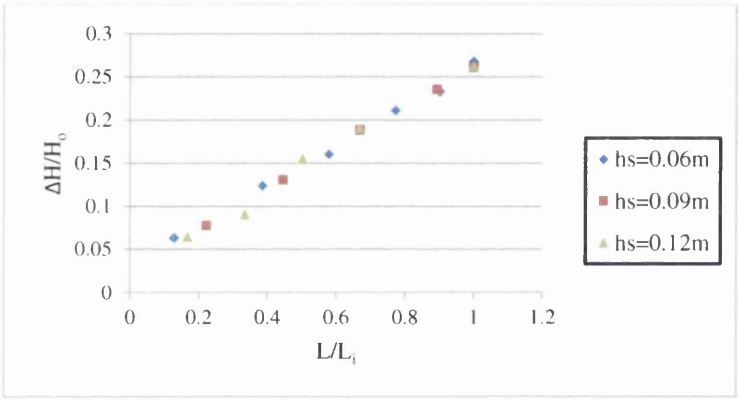

a

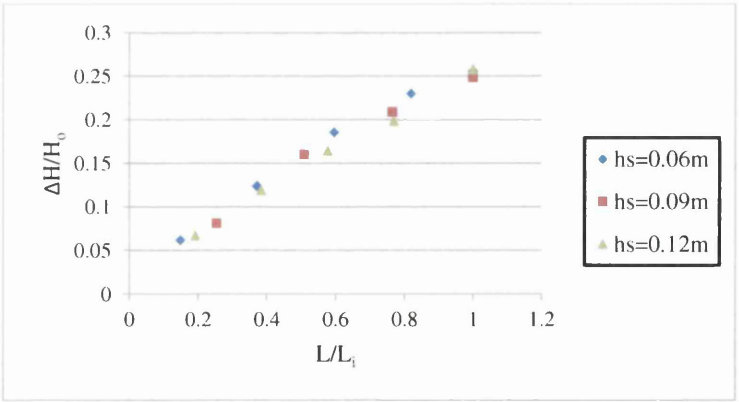

b

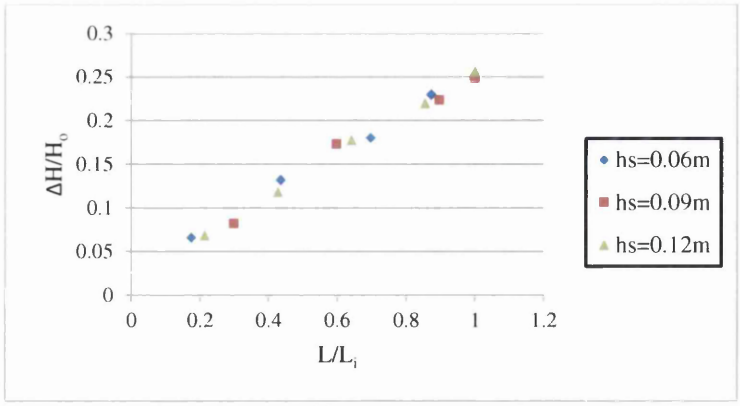

c

Figure 6.12. Variation of relative energy loss along the non-aerated flow region of a stepped spillway of bottom slope 1V:2.5H, using horizontal steps, for unit discharges of: a) q_w=0.23m^2/s, b) q_w=0.20m^2/s and c) q_w=0.173m^2/s.

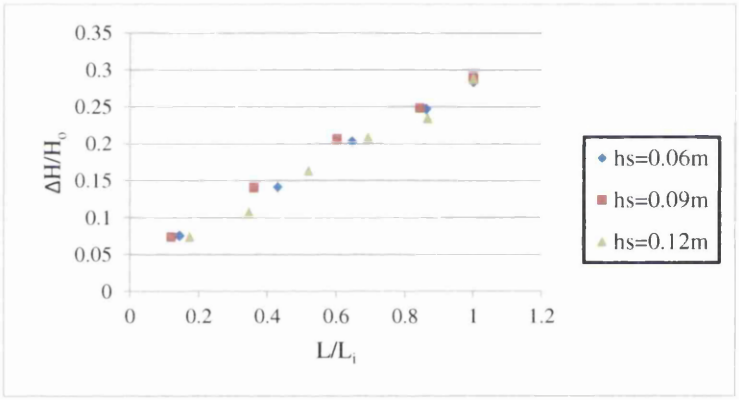

a

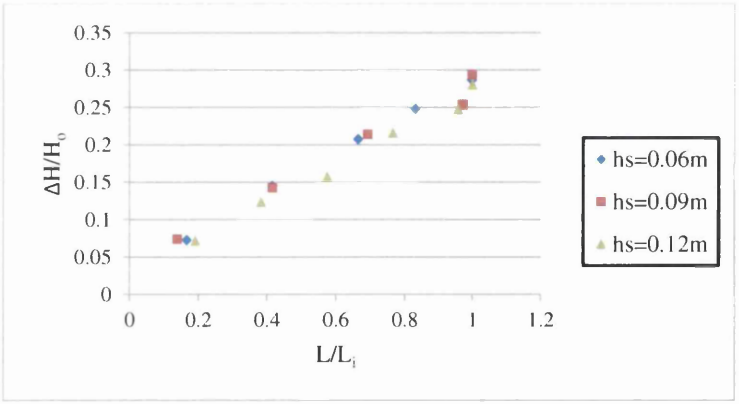

b

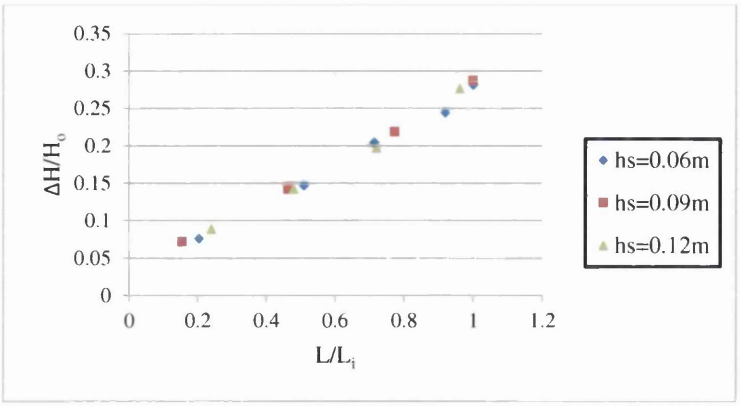

c

Figure 6.13. Variation of relative energy loss along the non-aerated flow region of a stepped spillway of bottom slope 1V:3H, using horizontal steps, for unit discharges of: a) q_w=0.23m^2/s, b) q_w=0.20m^2/s and c) q_w=0.173m^2/s.

It is obvious from these figures that for all discharges and chute slopes the rate of energy dissipation is small at the steps close to the weir crest and then progressively increases downward, reaching its peak value at the inception point. Further, it is clear that the energy dissipation rate with the horizontal steps is independent of the step height, as the relative energy loss at any section along the non-aerated flow region is approximately the same for all step heights 0.06m, 0.09m and 0.12m on the identical chute slope. Also, it can be observed that the relative energy loss at the inception point of air entrainment is increased from about 0.245 to 0.295 when the slope of 1V:2H is replaced by 1V:3H. This indicates that the flatter the bottom slope of the stepped spillway, the higher the energy dissipation rate at the surface self-aeration point. Following Meireles and Matos (2009) and Hunt et al. (2010) a linear regression is conducted to find out the relationship between the relative energy loss $\Delta H/H_o$ at the outer edge of steps situated in the non-aerated flow region, and the normalized distance between the downstream corner of the weir and the step under consideration, L/L_i, as follows:

$$\frac{\Delta H}{H_o} = A\frac{L}{L_i} \tag{6.9}$$

where A is a real number to be determined from the computational results. Figure 6.14 displays the relationship between the relative energy loss and the normalized length along the chute slopes. It should be noted that these data represent the numerical results gathered from all the chute slopes, step heights and unit discharges examined in the current work using the horizontal steps.

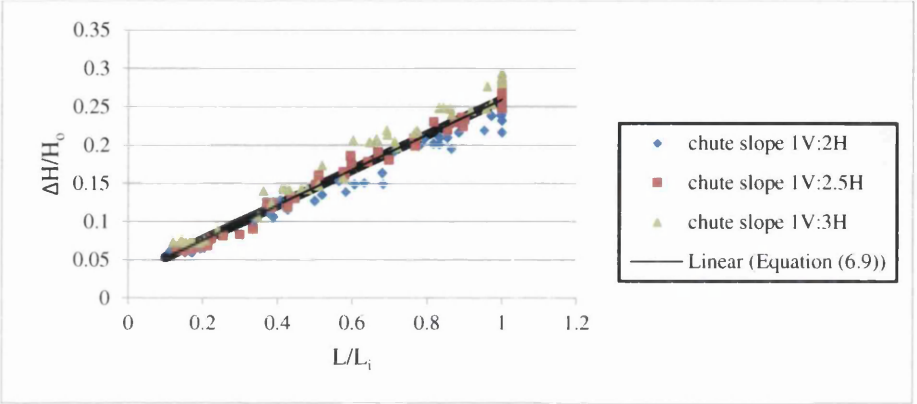

Figure 6.14. Linear relationship between the relative energy loss and the normalized length to the step outer edge of horizontal steps along the non-aerated flow region, on moderate slopes.

In the present study the value of A in Equation (6.9) is found to be 0.23, which is in close agreement to the values of 0.20 and 0.30 obtained in the experiments on two laboratory models conducted respectively by Meireles and Matos (2009) on a chute slope of 1V:2H and Hunt et al. (2009) on a bottom slope of 1V:4H.

In order to investigate the effect of upward inclined steps on the energy dissipation on moderate slope stepped spillways, Figures 6.15, 6.16 and 6.17 are plotted, to show the amount of the relative energy loss at the outer edge of a number of upward inclined steps of three different step inclinations, located in the non-aerated flow region, for various unit discharges, on chute slopes of 1:2H, 1V:2.5H and 1V:3H respectively. Also, these figures present the relative energy loss on the horizontal steps of height 0.09m, to compare their efficiencies with the inclined steps of the same step height.

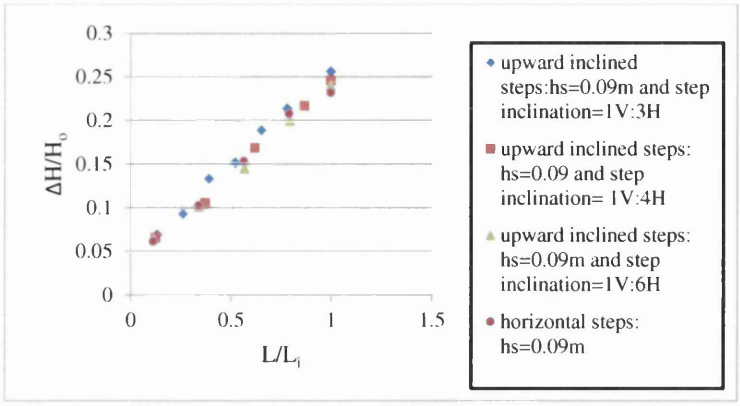

a

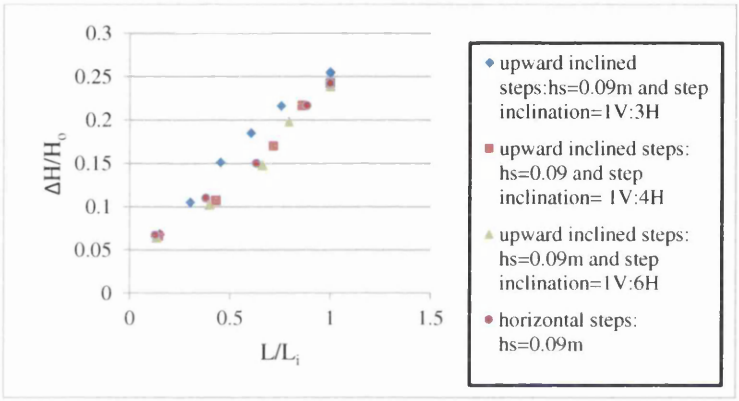

b

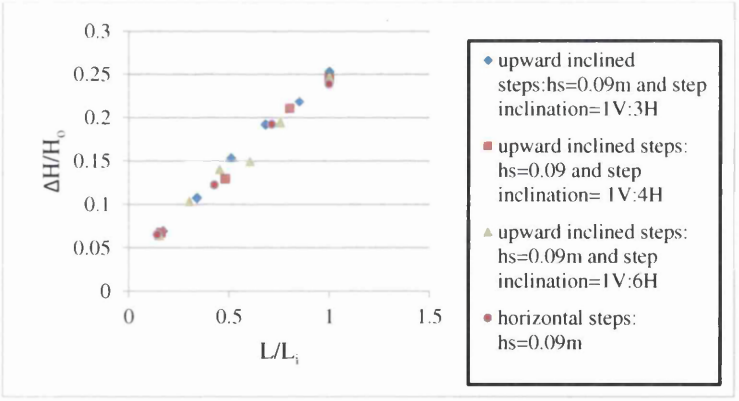

c

Figure 6.15. Variation of relative energy loss along the non-aerated flow region of a stepped spillway of bottom slope 1V:2H, using inclined steps, for unit discharges of: a) q_w= 0.23m^2/s, b) q_w= 0.20m^2/s and c) q_w=0.173m^2/s.

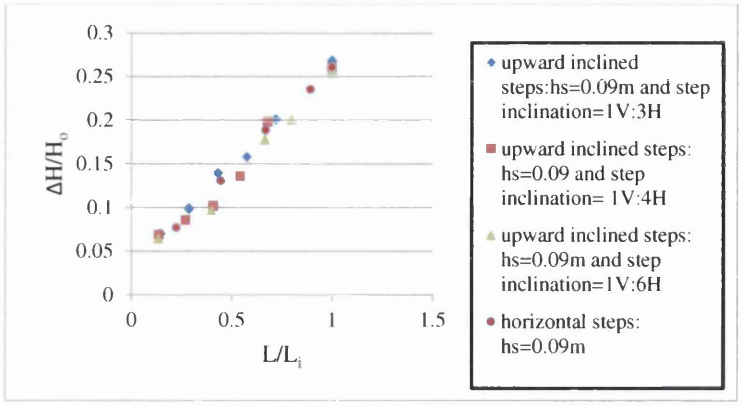

a

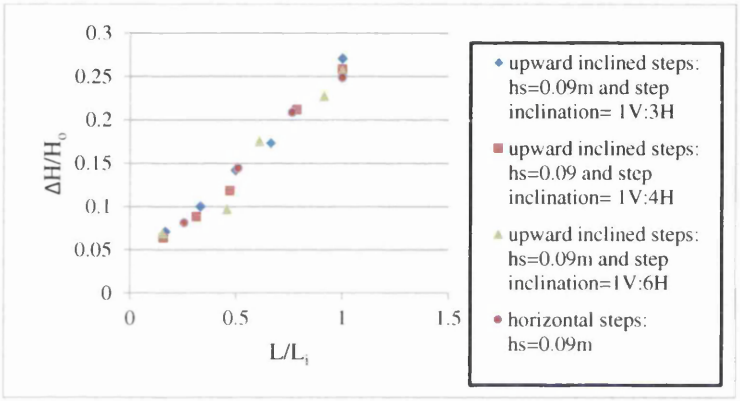

b

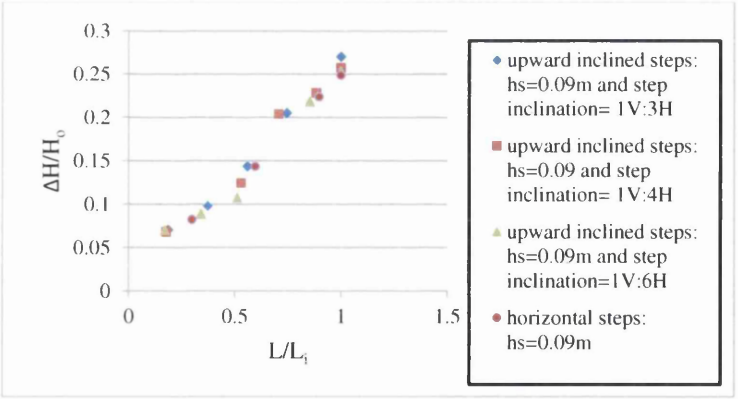

c

Figure 6.16. Variation of relative energy loss along the non-aerated flow region of a stepped spillway of bottom slope 1V:2.5H, using inclined steps, for unit discharges of: a) q_w= 0.23m^2/s, b) q_w= 0.20m^2/s and c) q_w=0.173m^2/s.

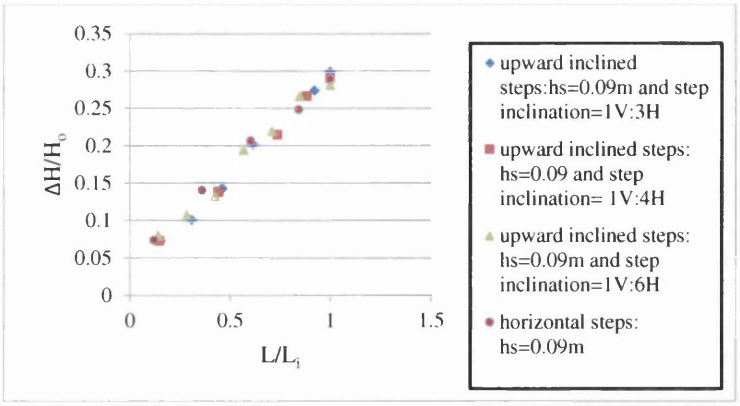

a

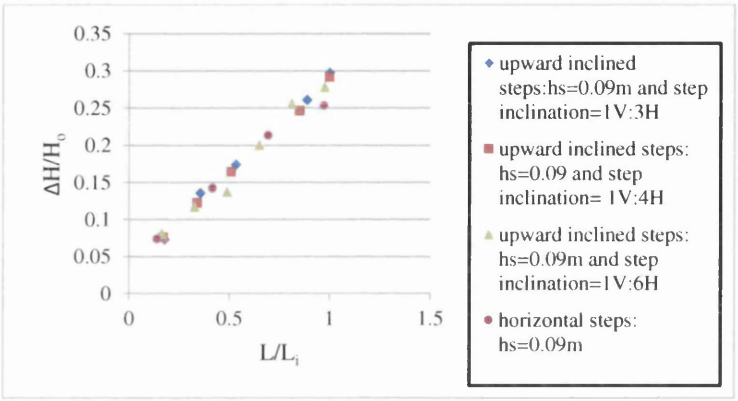

b

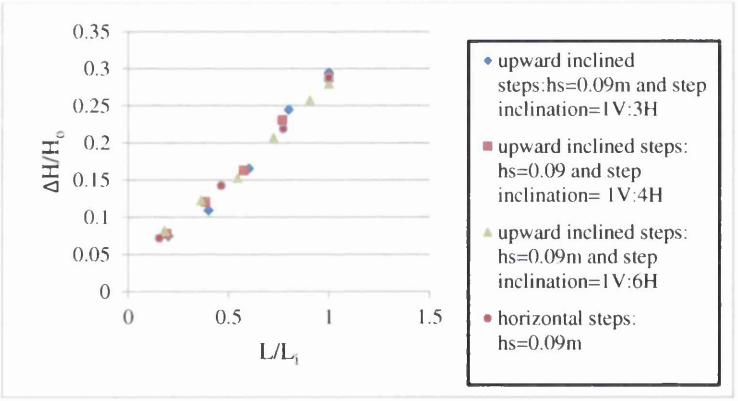

c

Figure 6.17. Variation of relative energy loss along the non-aerated flow region of a stepped spillway of bottom slope 1V:3H, using inclined steps, for unit discharges of: a) q_w= 0.23m^2/s, b) q_w= 0.20m^2/s and c) q_w=0.173m^2/s.

As can be seen, the relative energy loss on the horizontal step of height 0.09m is increased by about 6.6% when it is replaced by the upward inclined steps with the same step height, over the chute slope of 1V:2H. This demonstrates that the upward inclined steps are more efficient in dissipating the flow energy than the horizontal steps. It should also be mentioned that Chinnarasri and Wongwises (2006), based on their experimental data on steeply sloping stepped spillways, stated that the total residual energy at the toe of the structure was reduced by 6% when upward inclined steps were used instead of horizontal steps. In addition, Barani et al. (2005) analysed their experimental results on steep slopes, to compare the efficiency of horizontal steps with endsills and upward inclined steps, in terms of the energy dissipation at the toe of the spillway. They observed that the upward inclined steps increased the total energy dissipation rate by about 8% compared with the horizontal steps, for discharge values typical of the skimming flow condition.

Furthermore, as may be observed, the relative energy loss is also improved by the inclination angle of the upward inclined steps. Apparently, by changing the step inclination from 1V:6H to 1V:3H the relative energy loss is increased by 3.4% in the non-aerated flow region. This agrees reasonably well with what has been documented by Barani et al. (2005) and Chinnarasri and Wongwises (2006) in their evaluation of energy dissipation at the toe of the structure, based on their experimental results from various step inclinations tested with upward inclined steps.

Finally, the computational results obtained in the present work with the upward inclined steps are used to develop an equation for estimating the relative energy loss in the non-aerated flow region on moderate slope stepped spillways. For this purpose, a linear regression equation is performed on the relative energy loss, $\Delta H/H_o$, as a function of the normalized length, L/L_i, and the following equation is obtained with r=0.967:

$$\frac{\Delta H}{H_o} = 0.244\frac{L}{L_i} \tag{6.10}$$

As can be seen from Equation (6.10) the value of A appearing in Equation (6.9) is 0.244 for the upward inclined steps, which is higher than that obtained on the horizontal steps. This is an indication that the energy dissipation rate on the upward inclined steps is higher than the horizontal steps. Equation (6.10) is plotted in Figure

6.18 for various unit discharges and step inclinations examined in this work. It also displays Equation (6.10), which is obtained from the linear regression for the computational results of this study on upward inclined steps.

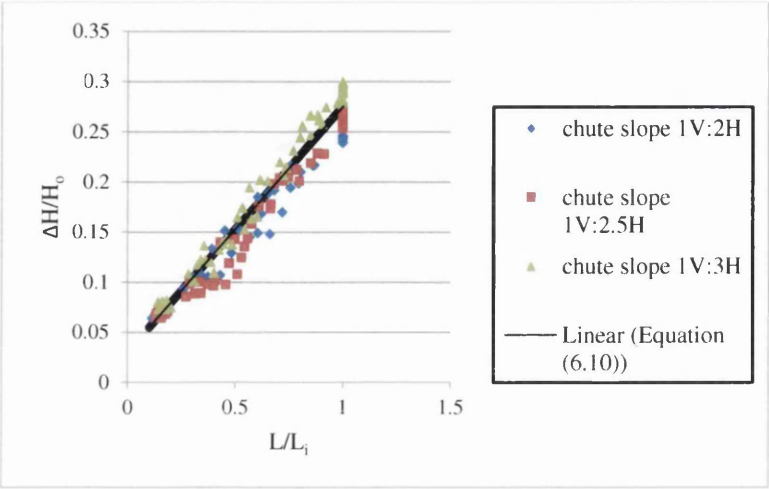

Figure 6.18. Linear relationship between the relative energy loss and the normalized length to the step outer edge of upward inclined steps along the non-aerated flow region on moderate slopes.

Chapter Seven concentrates on the pressure distributions on both faces of the horizontal and upward inclined steps, for various step geometries, chute slopes and unit discharges. Also, it looks at the issue of cavitation formation on moderate slope stepped spillways, in an attempt to determine maximum allowable discharges on both step configurations, which ensure the safety of steps against the damage caused by cavitation.

CHAPTER SEVEN

RESULTS AND DISCUSSION: PRESSURE DISTRIBUTION AND PREDICTION OF CAVITATION FORMATION

Chapter Seven: Results and Discussion: Pressure Distribution and Prediction of Cavitation Formation

7.1. Introduction

Investigating the pressure pattern is important in the design of open channels and hydraulic structures, especially when the velocity of the flowing water is high. This is because cavitation formation is the major concern for such kinds of flows, as the pressure may drop close to, and sometimes below, the vapour water pressure (Amador et al. 2006). As discussed earlier, the presence of air close to the spillway surface, in amounts of 5% to 8%, significantly reduces the risk of cavitation on stepped spillways (Peterka, 1953). In fact, air could enter the flow on stepped spillways naturally through the process of self-aeration. This process may take place once the boundary layer meets the free surface, at a point known as the inception point of air entrainment (Chanson, 2002), where the chute length will be divided into the non-aerated and aerated flow regions.

Past studies on steep slopes (e.g. Amador et al. 2009) showed that the non-aerated flow region is potentially more prone to cavitation damage than the aerated flow region. This may be because, on the one hand the flow velocity attains its peak value close to the inception point of air entrainment, and hence the pressure falls to its lowest values. On the other hand, air may be either entirely absent or insufficiently present in the non-aerated flow region to prevent such damage.

The computational results presented in Chapter 5 relating to the length to the inception point of air entrainment showed that the establishment of a surface self-aeration mechanism on moderate slope stepped spillways is mainly dependent on the discharge, chute slope and step geometry. However, during high flood events this mechanism may start at a significant distance from the crest, leaving behind a long flow reach without aeration. This increases the potential of cavitation formation on the downstream face, which may eventually cause entire failure of the structure (Amador et al. 2009). Understanding the pressure variation on both faces of steps located in the non-aerated flow region is therefore important to:

1- determine whether they are severe enough to form cavitation;

2- predict the maximum permissible discharge that can be passed by the spillway safely without cavitation;

This chapter presents and explains the main properties of the pressure flow field in the non-aerated flow region on horizontal and upward inclined steps, over moderate slope stepped spillways, due to various unit discharges typical of skimming flow conditions. It also focuses on estimating the safe water discharge that can flow over moderate slope stepped spillways without causing cavitation damage to the downstream face.

7.2. Pressure distribution

This section aims to provide detailed information on the characteristics of the pressure flow field due to the skimming flow conditions on moderate slope stepped spillways. It presents and discusses the pressure distribution on both faces of a number of horizontal and upward inclined steps situated in the non-aerated flow. In addition, it concentrates on the effects of the step geometry and chute slope on the pressure behaviour.

7.2.1. Pressure distribution on the horizontal and tilted faces

Figure 7.1 displays the pressure flow field on the horizontal steps of height 0.12m, over the three chute slopes examined in the present work, due to unit discharges of q_w=0.25m^2/s. Meanwhile, Figure 7.2 presents the pressure evolution along the chute of three different slopes over inclined steps of 0.09m height for unit discharges of q_w=0.25m^2/s. As can be seen in these figures, a smooth pressure flow field is obtained along the computational domain in both cases. Also, it is obvious that the pressure values downstream of the weir crest, along the chute slope over the horizontal and inclined steps, are low compared to the upstream part. This demonstrates that although the shape of the step is different, the pressure pattern is qualitatively similar.

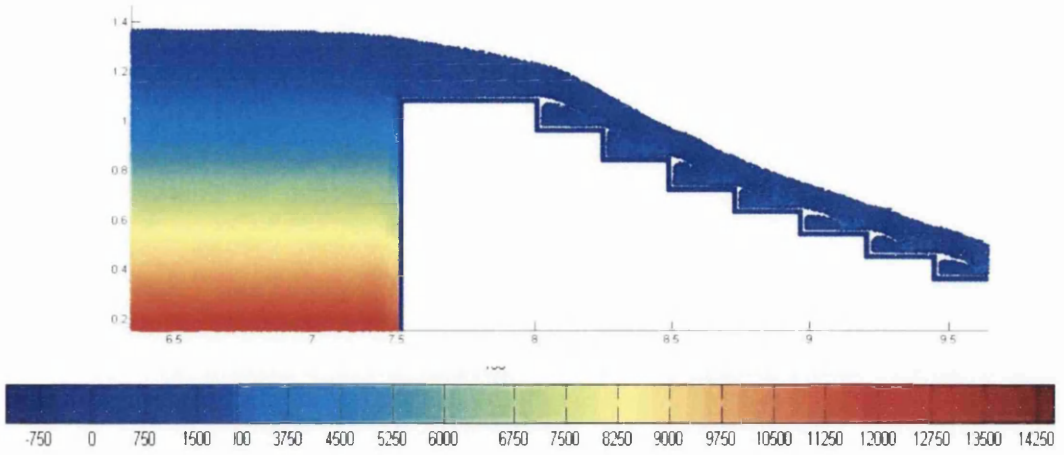

a

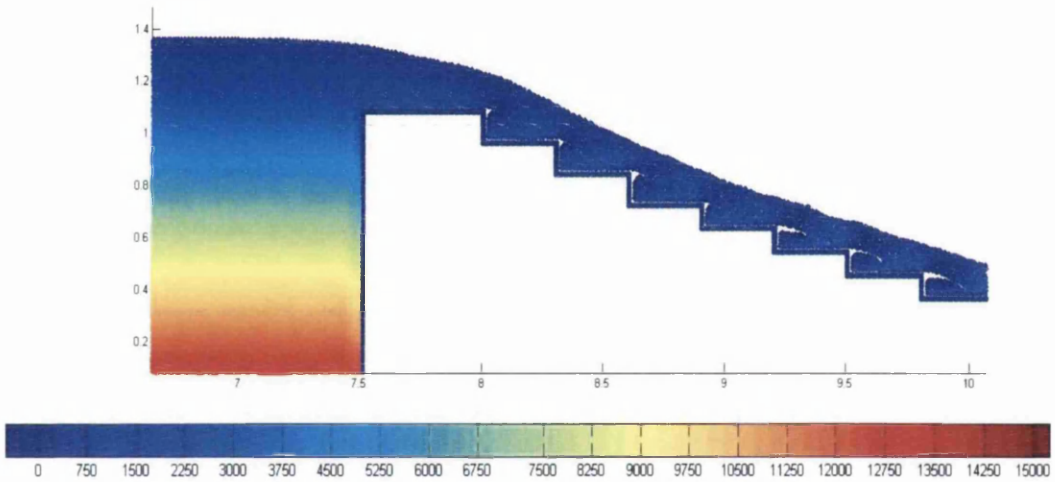

b

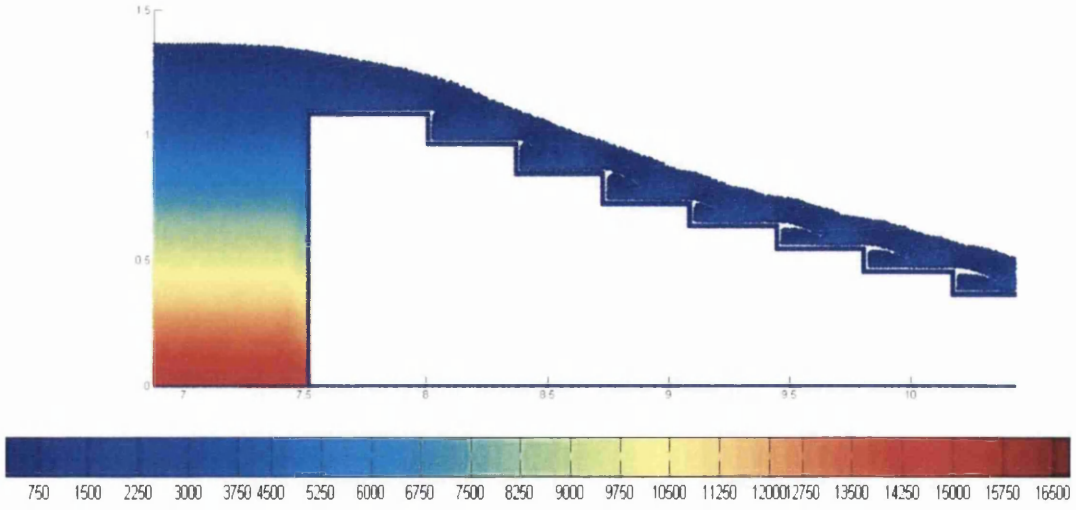

c

Figure 7.1. Pressure flow field along the non-aerated flow region for a unit discharge of q_w=0.25m^2/s, over a stepped spillway using horizontal steps with height 0.12m and slope: a) 1V:2H, b) 1V:2.5H and c) 1V:3H.

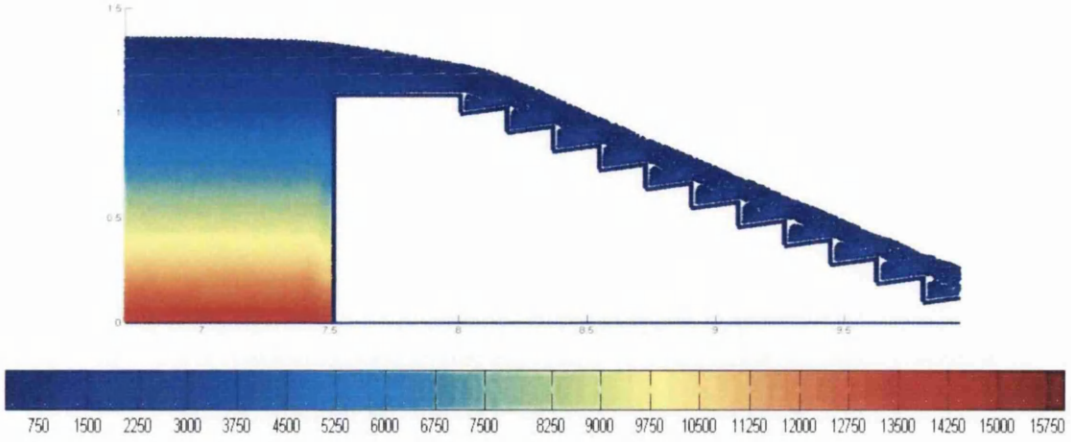

a

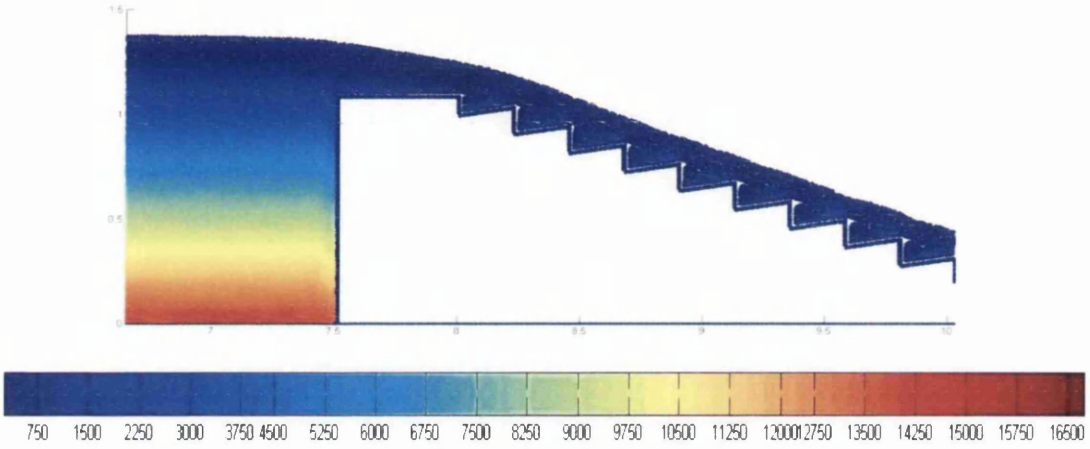

b

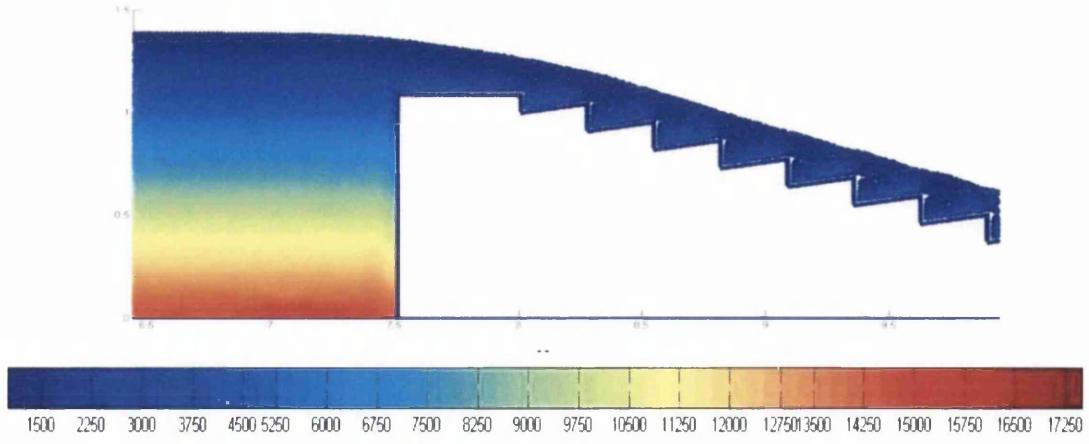

c

Figure 7.2. Pressure flow field along the non-aerated flow region for a unit discharge of q_w=0.25m^2/s, over a stepped spillway using inclined steps with height 0.09m and step inclination 1V:3H on the chute slope: a) 1V:2H, b) 1V:2.5H and c) 1V:3H.

The pressure distribution on the horizontal face of three steps of height 0.09m, located at different distances along the chute of bottom slope 1V:2H, is shown in Figure 7.3, where the normalized pressure values $P/\rho g h_c$ are plotted against the dimensionless term y_s/l_s for three different unit discharges. In this figure, P is the pressure, ρ is the fluid density, g is the gravitational acceleration, h_c is the critical flow depth on the weir crest, l_s is the step length, y_s is the distance measured from the step outer edge to the point under the consideration, L is the distance between the downstream face of the weir and the outer edge of the step under consideration, and K_s is the roughness height.

It is clear from this figure that for all discharges the pressure achieves its peak value at about 22% to 25% of the step length from its outer edge. Also, it shows that there will be a decrease in the pressure value inside the step cavity, reaching the minimum value close to the step corner. The highest pressure value on the horizontal face could be due to the impact of the skimming flow on the tread of the step, while the minimum pressure can be explained by the formation of eddies inside the step cavity. Nearly the same observations were made by Amador et al. (2009) in their experimental work, conducted mainly to characterize the pressure flow field on steeply sloping stepped spillways.

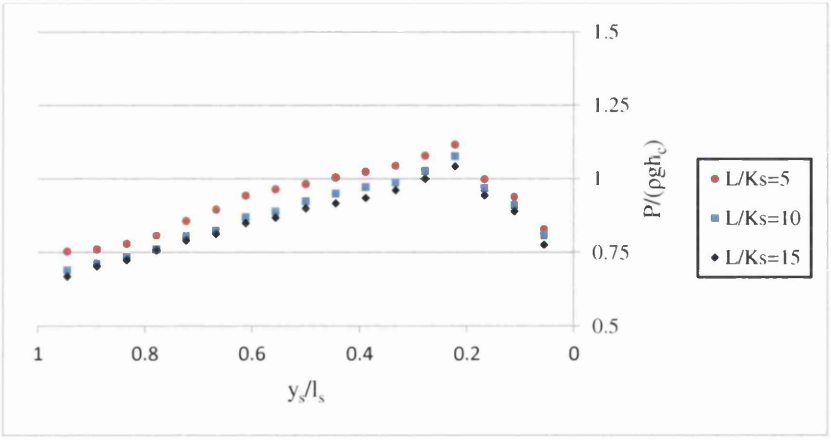

a

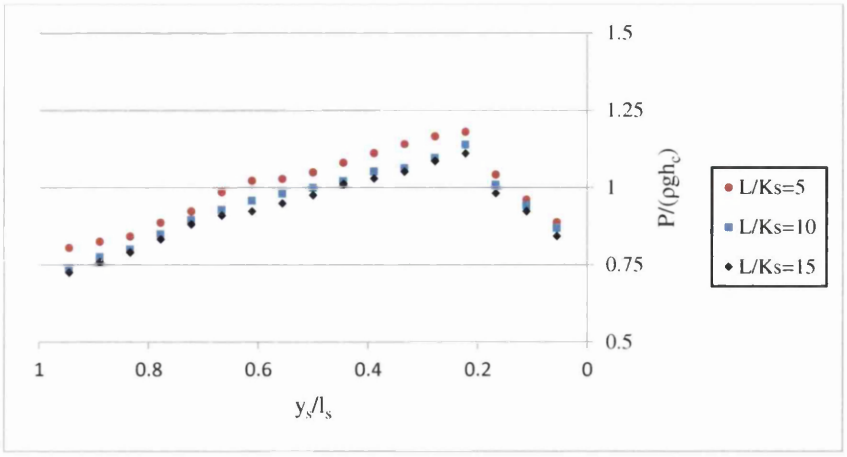

b

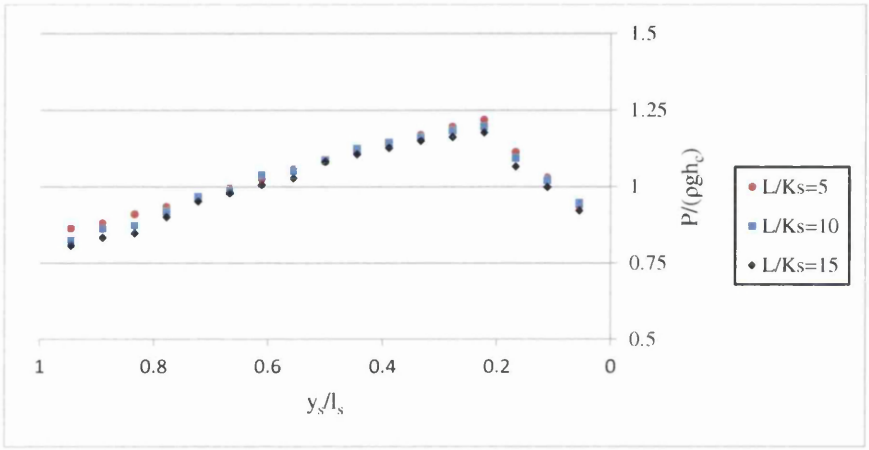

c

Figure 7.3. Pressure distribution along the horizontal face of step height 0.09m on a chute slope of 1V:2H for: a) q_w=0.25m^2/s, b) q_w=0.21m^2/s and c) q_w=0.182m^2/s.

The computational results of the pressure profile on the tilted face of upward inclined steps of height 0.09m and step inclination of 1V:4H are shown in Figure 7.4. It should be noted that the chute slope and location of the steps along the chute slope shown in this figure are the same as those used with the horizontal steps. As may be observed, this figure demonstrates that the pressure pattern on the inclined steps is approximately identical to that obtained on the horizontal steps. However, the main difference between them is that the maximum pressure on the upward inclined steps is obtained at about 25% to 27% of the step length, measured from the step's outer edge. This is because the tilted face of inclined steps is more exposed to the impact of the overflowing water than the straight face of the horizontal steps.

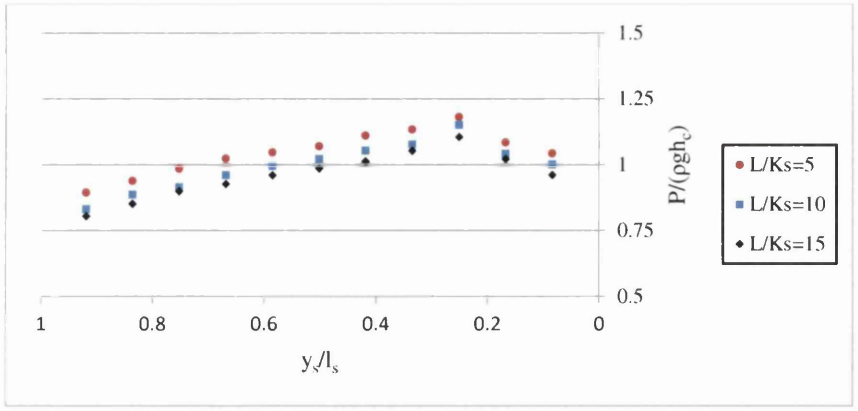

a

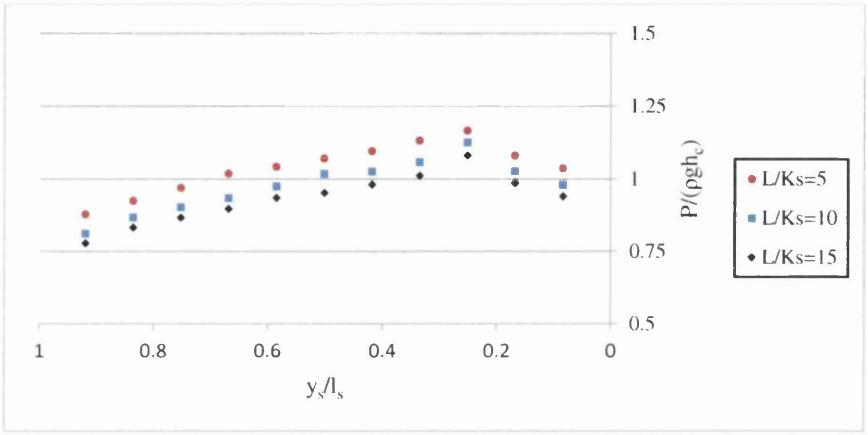

b

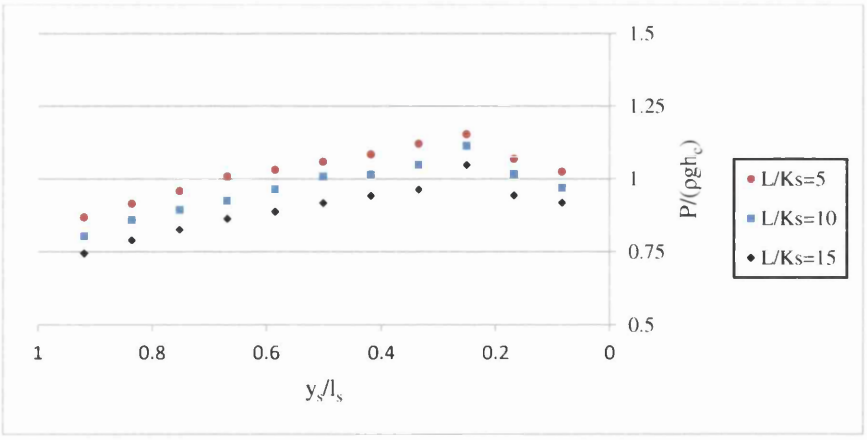

c

Figure 7.4. Pressure distribution along the tilted face of the upward inclined step with height 0.09m and step inclination 1V:4H, on a chute of bottom slope 1V:2H for: a) q_w=0.25m^2/s, b) q_w=0.21m^2/s and c) q_w=0.182m^2/s.

Figures 7.5 to 7.7 show the pressure distribution on the horizontal face of two steps having three different heights, due to various unit discharges flowing over the bottom chute slopes of 1V:2H, 1V:2.H and 1V:3H, respectively. One of these two steps is located at a distance from the weir crest along the non-aerated flow region, while the second step is located at the inception point of air entrainment.

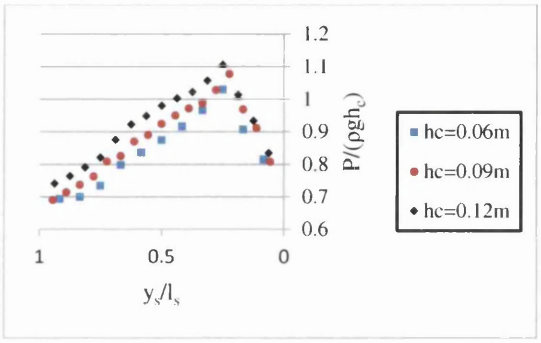

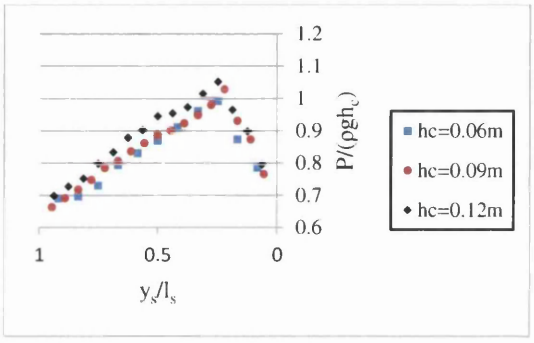

$L/K_s=10$ inception point

a) $q_w=0.23m^2/s$

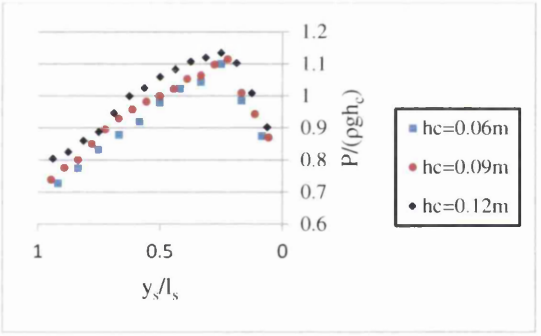

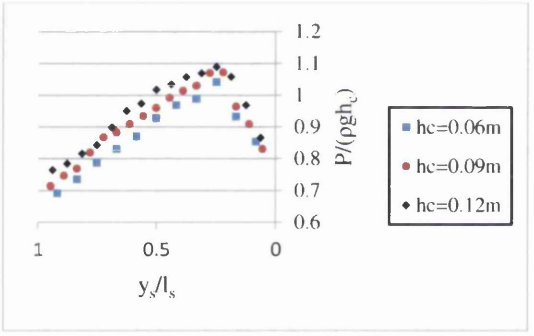

L/Ks=10 inception point

b) $q_w=0.20m^2/s$

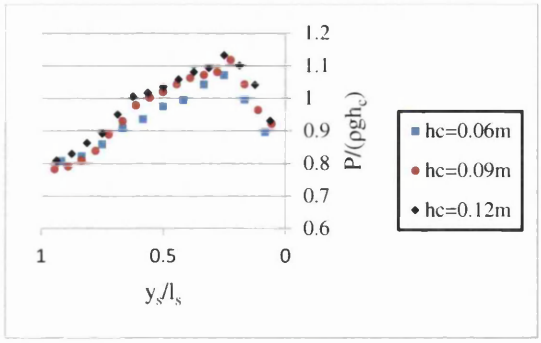

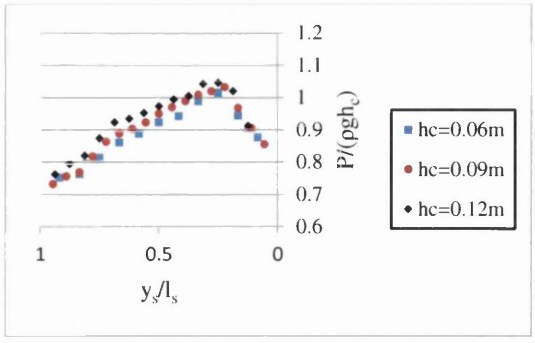

L/Ks=10 inception point

c) $q_w=0.173m^2/s$

Figure 7.5. Pressure distribution along the horizontal face of horizontal steps over the chute slope of 1V:2H for unit discharge: a) $q_w=0.23m^2/s$, b) $q_w=0.20m^2/s$ and c) $q_w=0.173m^2/s$.

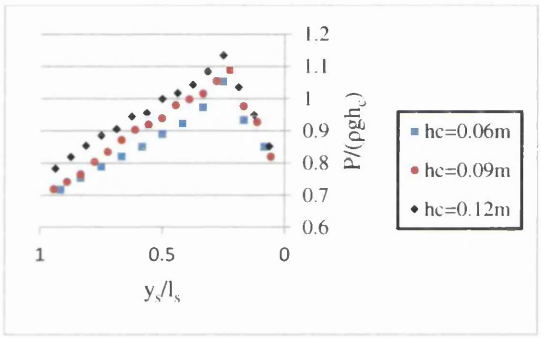

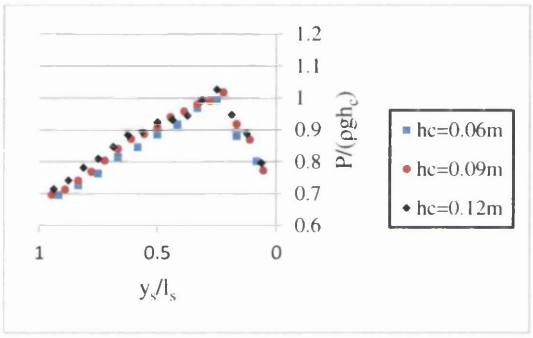

$L/K_s=11.6$ inception point

a) $q_w=0.23m^2/s$

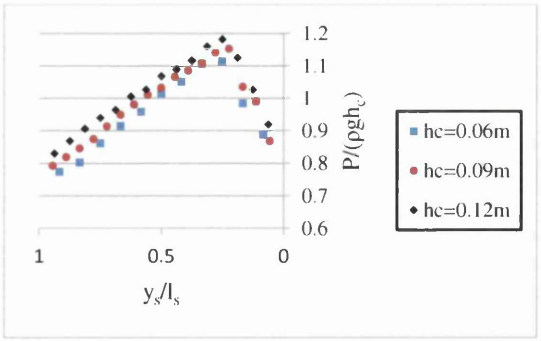

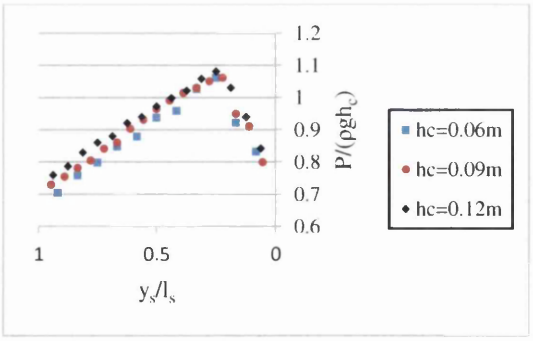

$L/K_s=11.6$ inception point

b) $q_w=0.20m^2/s$

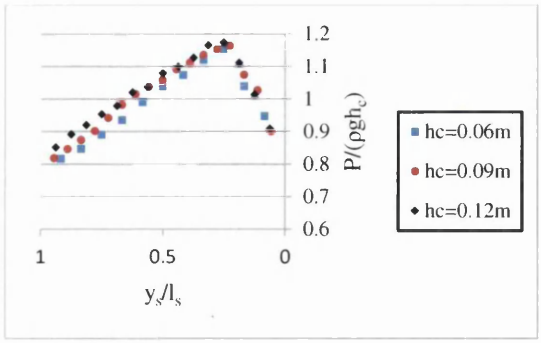

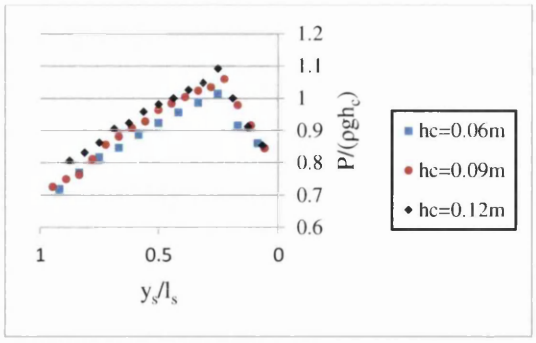

L/K_s=11.6 inception point

c) q_w=0.173m^2/s

Figure 7.6. Pressure distribution along the horizontal face of horizontal steps over the chute slope of 1V:2.5H for unit discharge: a) q_w=0.23m^2/s, b) q_w=0.20m^2/s and c) q_w=0.173m^2/s.

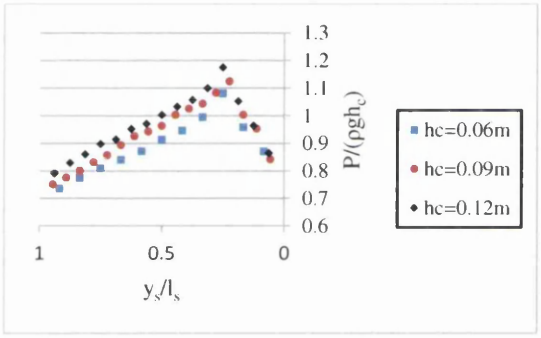

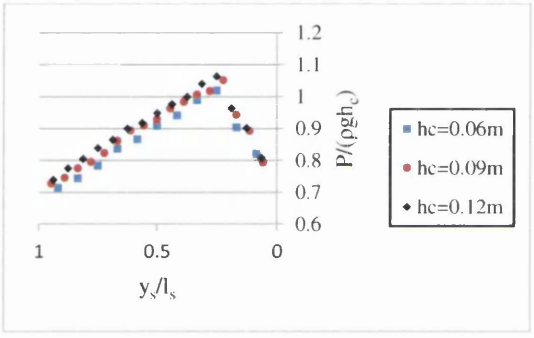

L/K_s=13.33 inception point

a) q_w=0.23m^2/s

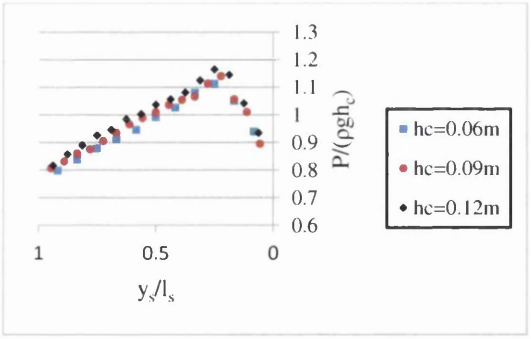

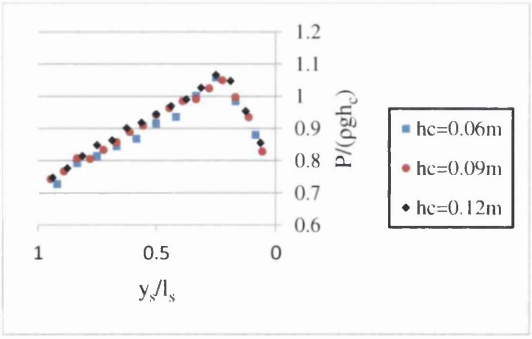

L/K_s=13.33 inception point

b) q_w=0.20m^2/s

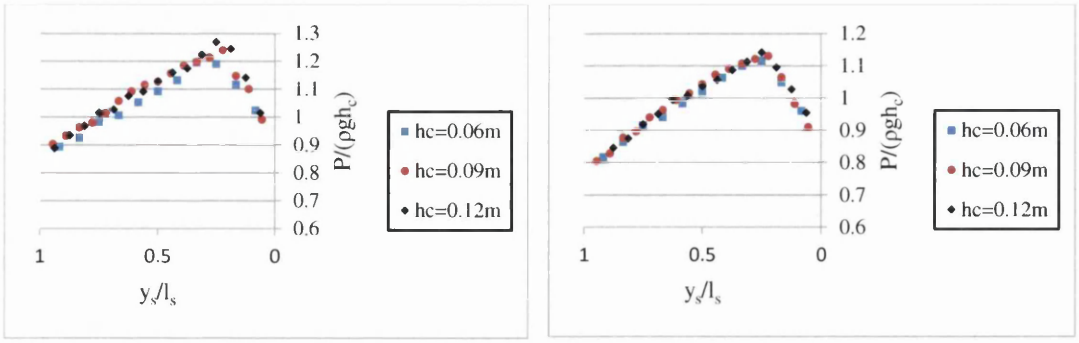

L/K_s=13.33 inception point

c) q_w=0.173m^2/s

Figure 7.7. Pressure distribution along the horizontal face of horizontal steps over the chute slope of 1V:3H, for unit discharge: a) q_w=0.25m^2/s, b) q_w=0.25m^2/s and c) q_w=0.25m^2/s.

In the event, no significant differences can be observed among these figures in terms of the characteristics of the pressure distribution along the horizontal face with the change of the step height and chute slope. However, it can be observed that the step height of 0.12m provides relatively higher pressure values than the other step heights tested in this study. Also, for a given discharge and step height it is clear that highest pressure values are obtained on the horizontal face of steps fitting the downstream face of the stepped spillway of 1V:3H bottom slope. This can be explained by the fact the mean flow velocity on both these configurations, as discussed in Section 6.2., is relatively lower than in the other configurations examined in this study. Furthermore, it is obvious that the pressure values acting on the horizontal faces of steps located close to the inception point are relatively lower compared to the steps located upstream to that point. This is because, as has been shown in Section 6.2., the mean flow velocity reaches its highest values at this point. Moreover, as can be seen for all unit discharges and step configurations tested in the current work, the pressure values acting on the horizontal face are positive, suggesting that cavitation is unlikely to form on the horizontal face.

To understand how the pressure distributes on the upward inclined steps, Figures 7.8 to 7.10 plot the pressure distribution on the tilted face of two upward inclined steps along the chute of bottom slopes 1V:2H, 1V:2.5H and 1V:3H respectively, due to different values of the discharge per unit width.

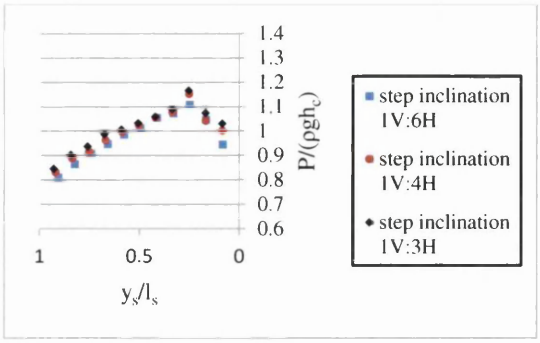

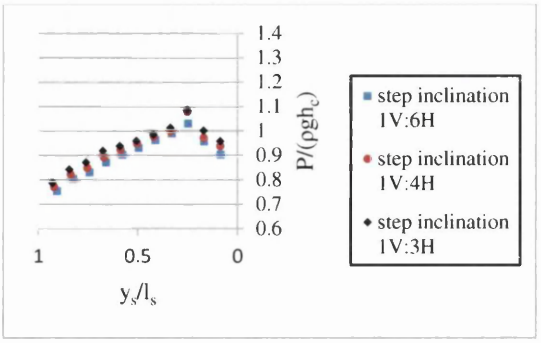

$L/K_s=10$ inception point

a) $q_w=0.25m^2/s$

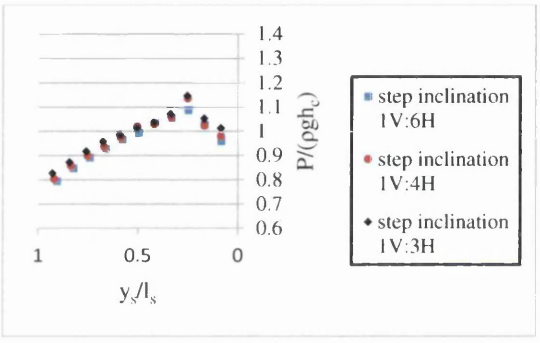

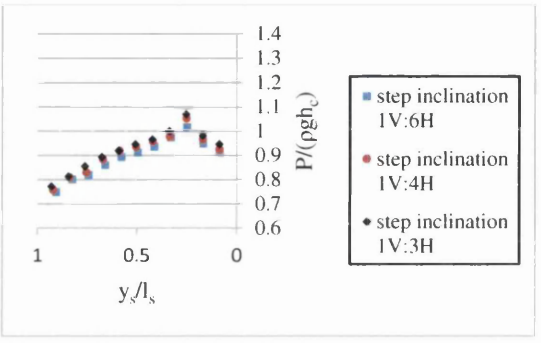

$L/K_s=10$ inception point

b) $q_w=0.21m^2/s$

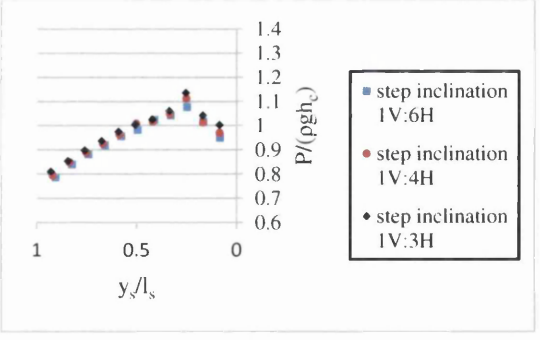

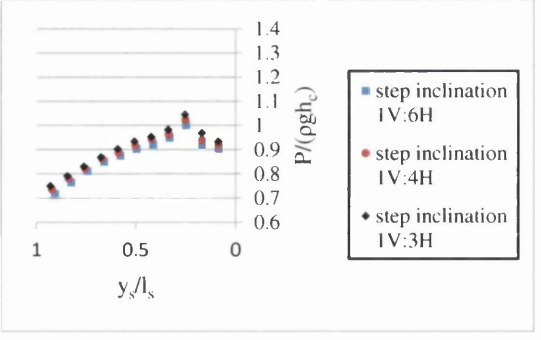

$L/K_s=10$ inception point

c) $q_w=0.182m^2/s$

Figure 7.8. Pressure distribution along the tilted face of upward inclined steps of height 0.09m over the chute slope 1V:2H, for unit discharge: a) $q_w=0.25m^2/s$, b) $q_w=0.21m^2/s$ and c) $q_w=0.183m^2/s$.

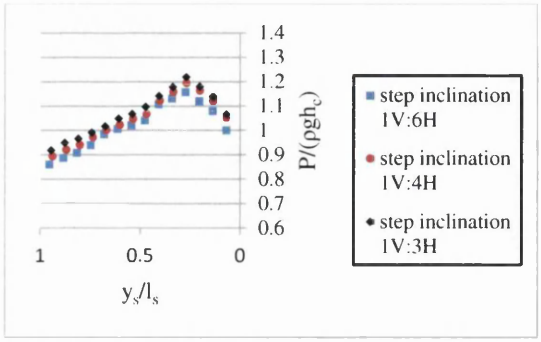

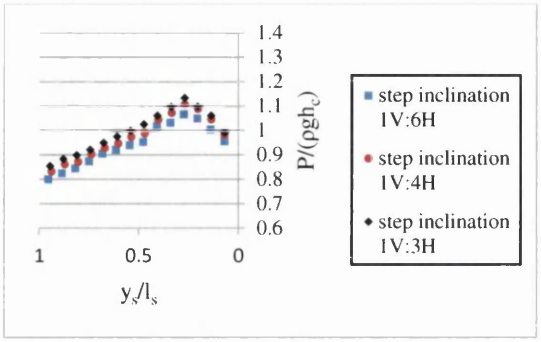

L/K_s=11.6 inception point

a) q_w=0.25m^2/s

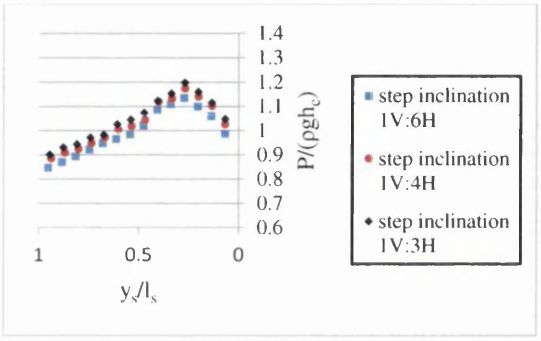

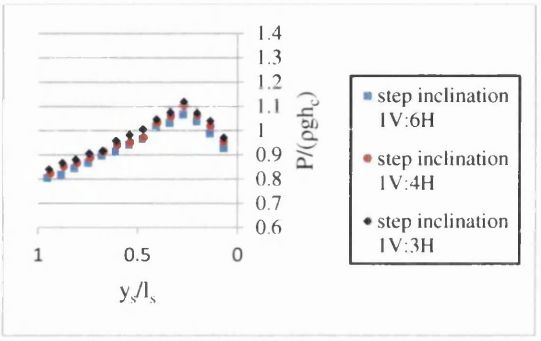

L/K_s=11.6 inception point

b) q_w=0.21m^2/s

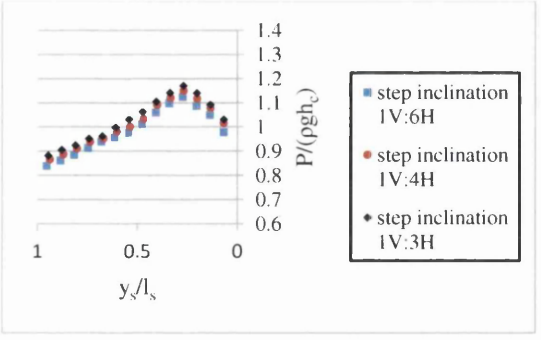

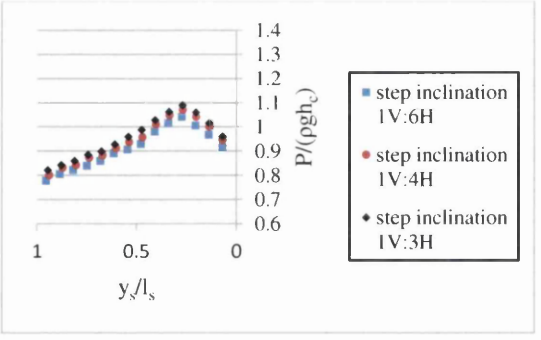

L/K_s=11.6 inception point

c) q_w=0.182m^2/s

Figure 7.9. Pressure distribution along the tilted face of upward inclined steps of height 0.09m over the chute slope 1V:2.5H, for unit discharge: a) q_w=0.25m^2/s, b) q_w=0.21m^2/s and c) q_w=0.182m^2/s.

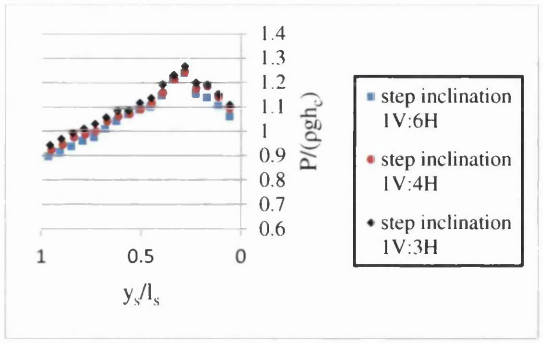

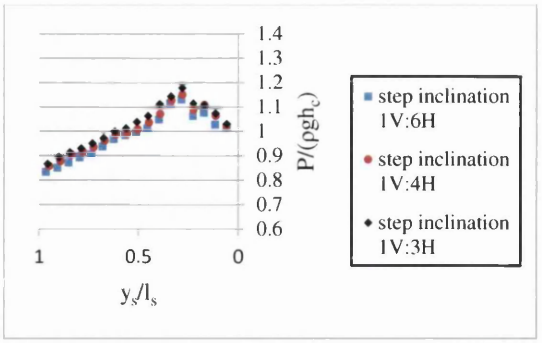

L/K_s=13.33 inception point

a) q_w=0.25m^2/s

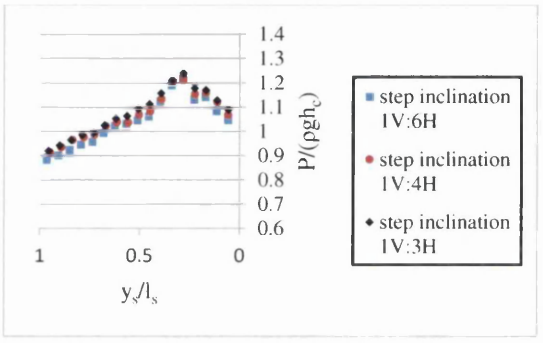

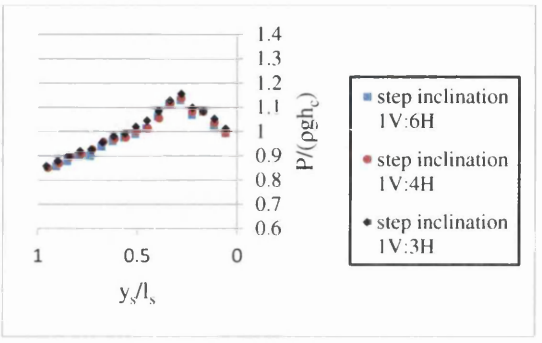

L/K_s=13.33 inception point

b) q_w=0.21m^2/s

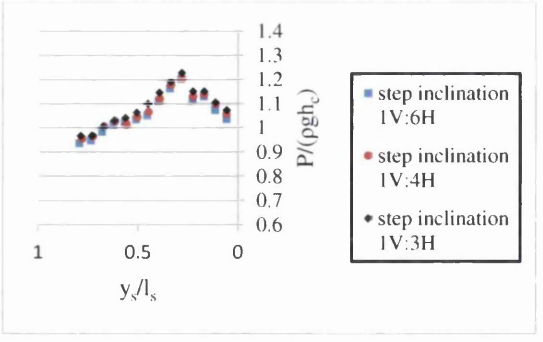

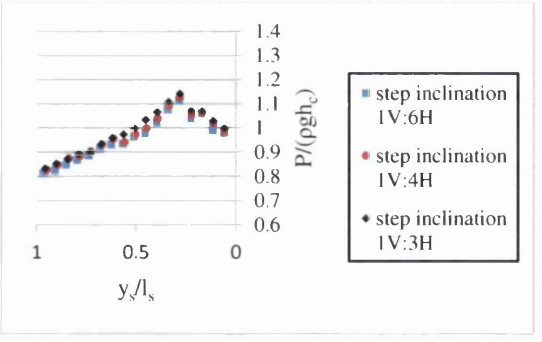

L/K_s=13.33 inception point

c) q_w=0.182m^2/s

Figure 7.10. Pressure distribution along the tilted face of upward inclined steps of height 0.09m over the chute slope 1V:3H, for unit discharge: a) q_w=0.25m^2/s, b) q_w=0.21m^2/s and c) q_w=0.182m^2/s.

These figures show that higher pressure values on the tilted face of upward inclined steps are obtained with the steepest step inclination used in this study. This can be

linked to the reduction of the flow velocity as the adverse slope of the tilted face is increased. Finally, for all flow conditions and stepped spillway geometries examined in this study with the upward inclined steps, the pressure distribution on the tilted face indicates that cavitation may not occur, as all the pressure values are above the atmospheric pressure.

7.2.2. Pressure distribution on the vertical face of the horizontal and upward inclined steps

The pressure distribution due to different unit discharge values, q_w, on the vertical face of the horizontal steps with height 0.09m, located at three different distances along the non-aerated flow region of the chute slope 1V:2H, is shown in Figure 7.11. In this figure the normalized pressure values $P/\rho g h_c$ are plotted against the values of the dimensionless term z_s/h_s for four different values of the unit discharge q_w, in which P refers to the pressure, ρ is the fluid density, g is the gravitational acceleration, h_s is the step height and z_s is the distance measured from the step outer edge to the point under scope along the vertical face. It should be noted that in this figure, for a given discharge the value of $L/K_s=15$ corresponds to the step which is very close to the inception point of air entrainment.

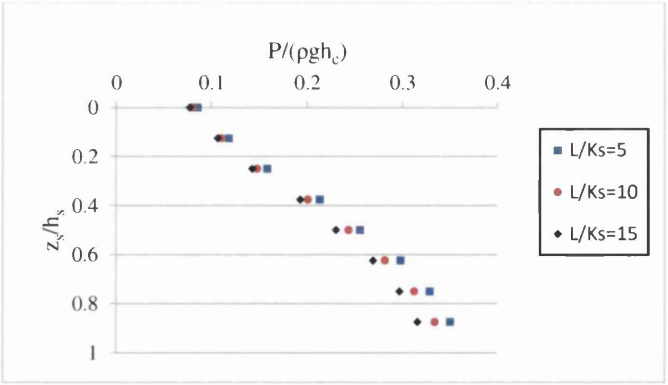

a

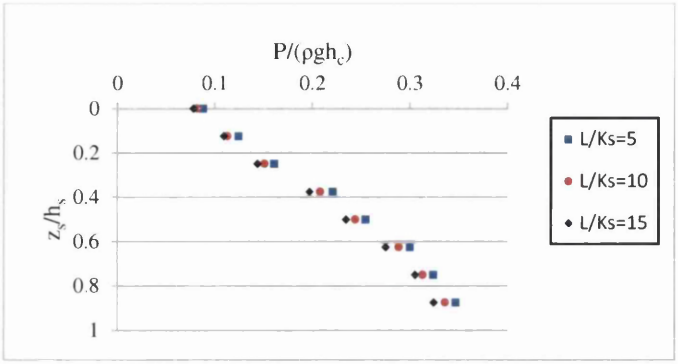

b

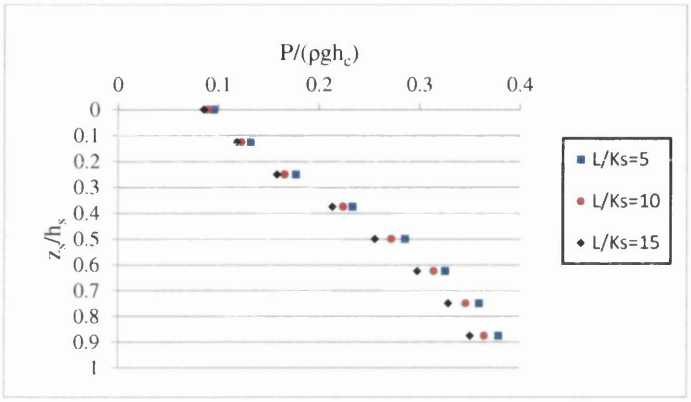

c

Figure 7.11. Pressure distribution on the vertical face of horizontal steps of height 0.09m and chute slope 1V:2H, for unit discharge: a) q_w=0.25m^2/s, b) q_w=0.21m^2/s and c) q_w=0.182m^2/s.

It can be seen that the pressure values acting on the vertical face are all positive, even with the maximum unit discharge examined here. In addition, one can observe that the pressure is at its minimum at the step outer edge, increasing towards the step corner. The minimum pressure value is due to the region where the streamlines of the skimming layer separate from the main flow when passing over the vertical face, whereas the increase of the pressure toward the corner may be due to the formation of the rotating vortices inside the step cavity. Also, it is clear that the increase of the discharge decreases the pressure on the step outer edge; the minimum pressures correspond to the maximum unit discharge tested in this study. This is because the flow velocity increases as the discharge is increased. In addition, for all discharges the minimum pressure values are obtained at the outer edge of steps located close to

the inception point. This can be attributed to the fact that the mean flow velocity close to the inception point of air entrainment achieves its peak value.

To investigate the effect of the step height on the pressure distribution of horizontal steps, Figures 7.12, 7.13 and 7.14 show the pressure distribution on the vertical face of a step close to the inception point of air entrainment, on chute slopes of 1V:2H, 1V:2.5H and 1V:3H respectively, with various unit discharges. It is obvious that for all chute slopes and discharge values the step height of 0.12 provides higher pressure values, especially at the step outer edge, which is more prone to cavitation damage, in comparison with the other step heights. As has been shown in Section 6.2., the step height of 0.12 is more efficient in decelerating the flow velocity compared with the step heights 0.06 and 0.09m. This may explain why the pressure on the vertical step face of height 0.12m is relatively higher than the step heights 0.09 and 0.06m. Moreover, with respect to the effect of the chute slope on the pressure on the vertical face, the results demonstrate that the flatter the chute slope the higher the pressure on the vertical step face, and hence the lower the possibility of cavitation formation at the step outer edge.

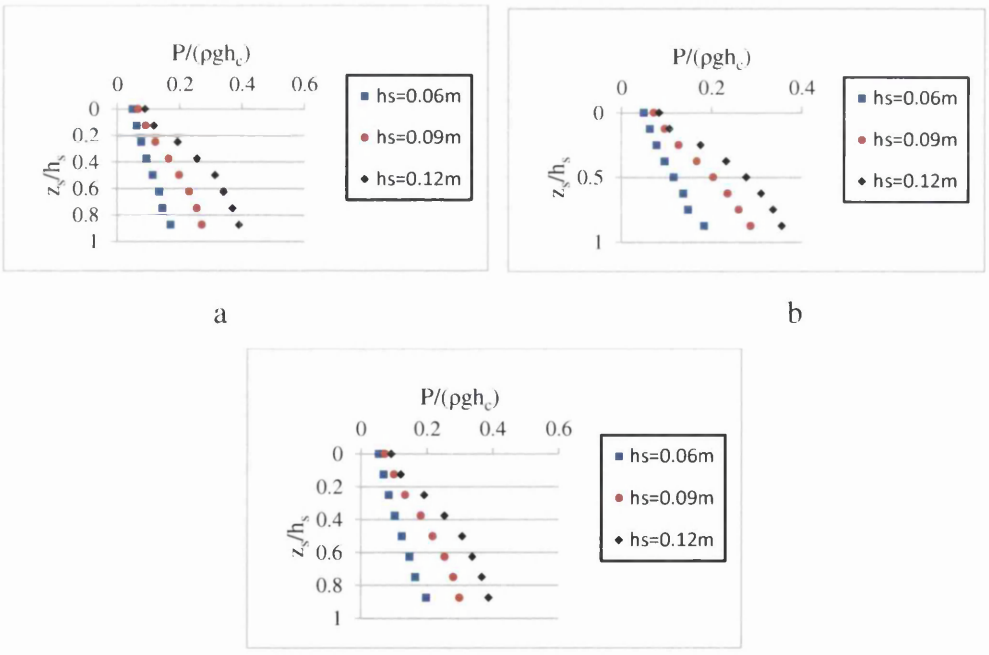

Figure 7.12. Pressure distribution on the vertical face of a step located at the inception point of air entrainment on the chute slope 1V:2H, for unit discharges: a) q_w= 0.23m$_2$/s, b) q_w=0.20m^2/s and c) q_w=0.173m^2/s.

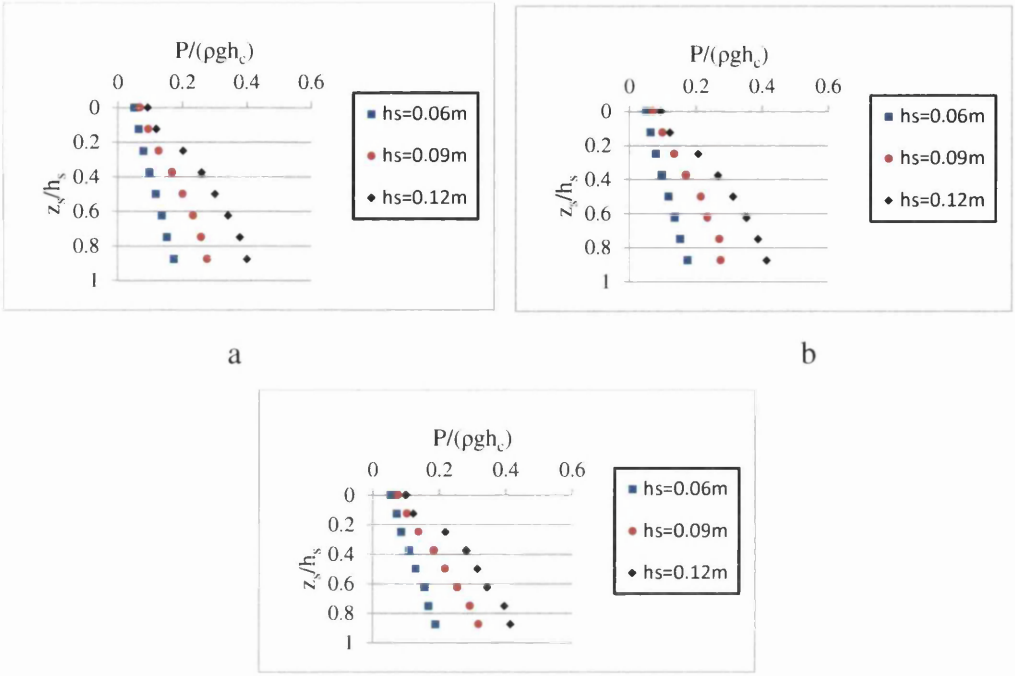

Figure 7.13. Pressure distribution on the vertical face of a step located at the inception point of air entrainment on the chute slope 1V:2.5H, for unit discharges: a) q_w= 0.23m_2/s, b) q_w=0.20m^2/s and c) q_w=0.173m^2/s.

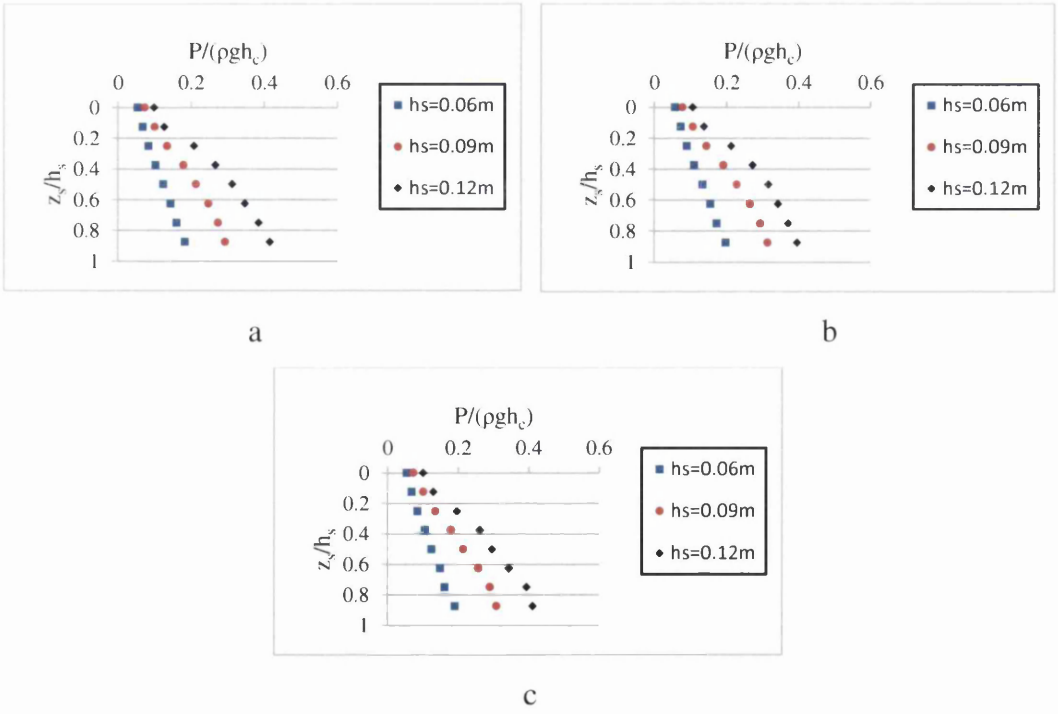

Figure 7.14. Pressure distribution on the vertical face of a step located at the inception point of air entrainment on the chute slope 1V:3H, for unit discharges: a) q_w= 0.23m_2/s, b) q_w=0.20m^2/s and c) q_w=0.173m^2/s.

The following section concentrates on the pressure distribution along the vertical face of the inclined steps. Figures 7.15 illustrates the pressure distribution due to various unit discharges typical of the skimming flow region on the vertical face of the inclined steps having an upward slope of 1V:4H. These steps are situated at different distances from the weir crest along the non-aerated flow region of the chute slope 1V:2H.

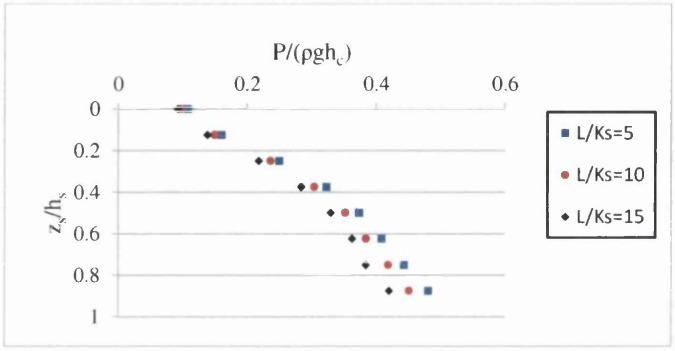

a

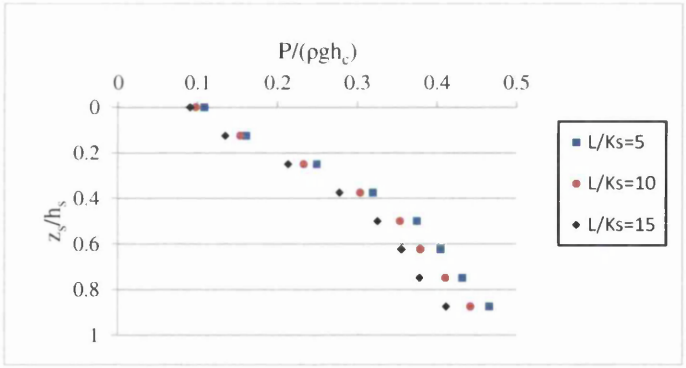

b

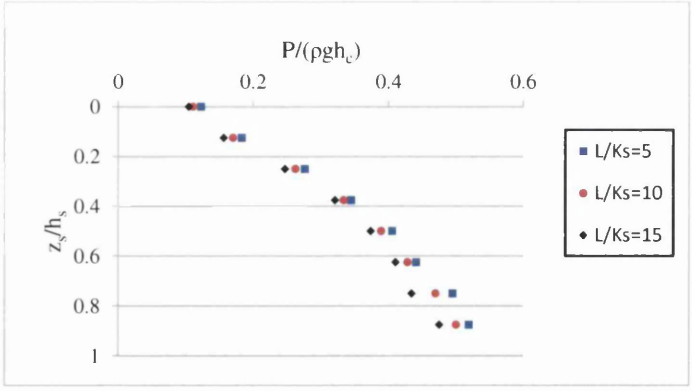

c

Figure 7.15. Pressure distribution on the vertical face of inclined steps of height 0.09m, step inclination 1V:4H and chute slope 1V:2H, for unit discharge: a) q_w=0.25m^2/s, b) q_w=0.22m^2/s and c) q_w=0.183m^2/s.

As may be observed, the characteristics of the pressure distribution on the vertical face of upward inclined steps are approximately identical, in terms of the maximum and minimum values, to those obtained on the vertical face of the horizontal steps. However, for the same unit discharge, upward inclined steps increase the pressure at the outer edge of the steps when compared with horizontal steps. This is because upward inclined steps are more efficient, as discussed in Section 6.2., in decelerating the flow velocity along the chute slope. Also, it can be seen that the pressure decreases on the vertical face of the step as its distance, L/K_s from the weir crest is increased.

Figures 7.16, 7.17 and 7.18 present the pressure distribution on the vertical face of upward inclined steps of different step inclinations due to various unit discharges, over the chute slopes 1V:2H, 1V:2.5H and 1V:3H, respectively.

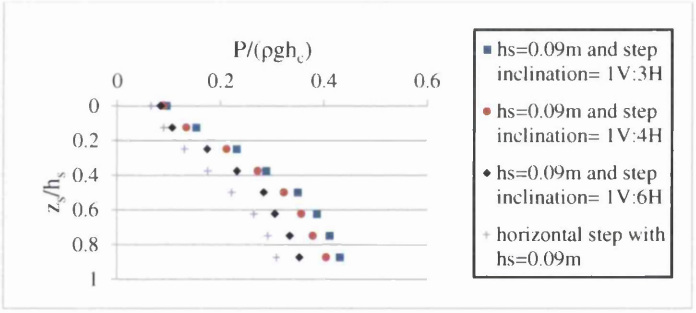

a

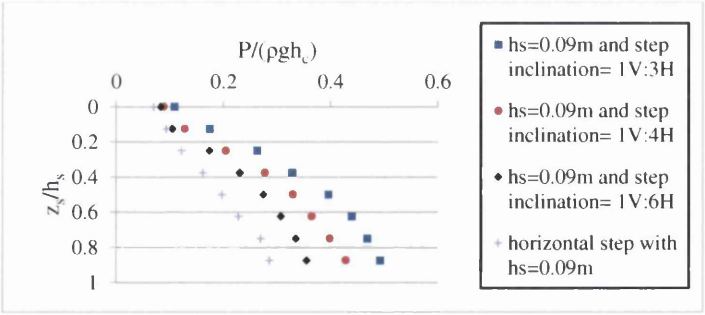

b

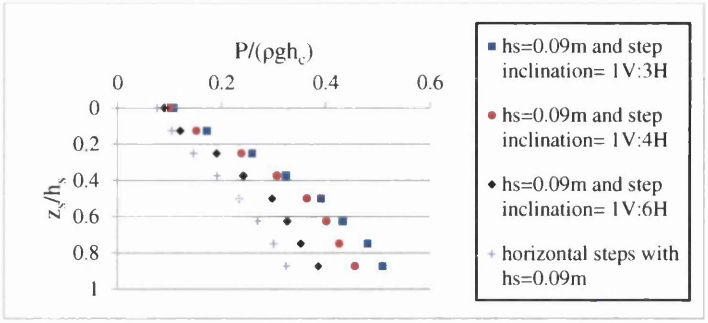

c

Figure 7.16. Pressure distribution on the vertical face of upward inclined steps of height 0.09m having different step inclinations, and horizontal steps over the chute slope 1V:2H, for unit discharge: a) q_w=0.25m^2/s, b) q_w=0.21m^2/s and c) q_w=0.183m^2/s.

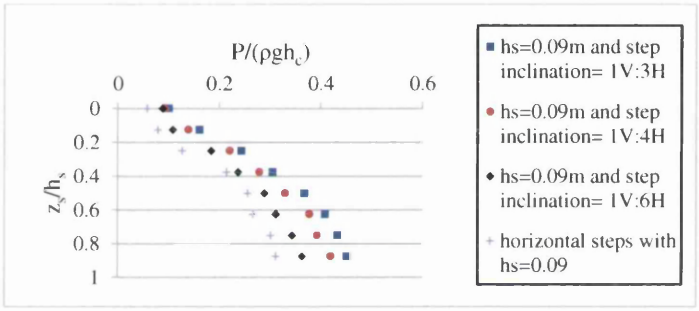

a

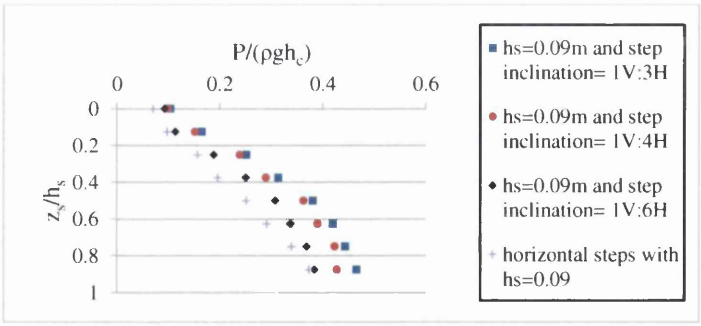

b

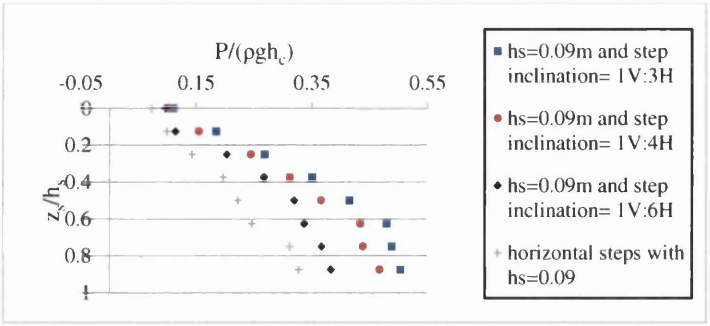

c

Figure 7.17. Pressure distribution on the vertical face of upward inclined steps of height 0.09m having different step inclinations, and horizontal steps over the chute slope 1V:2.5H, for unit discharge: a) q_w=0.25m^2/s, b) q_w=0.21m^2/s and c) q_w=0.183m^2/s.

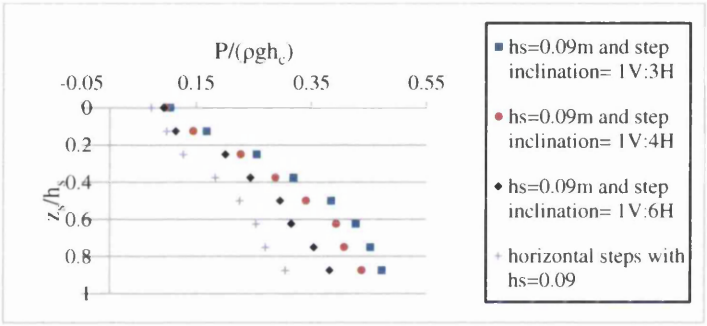

a

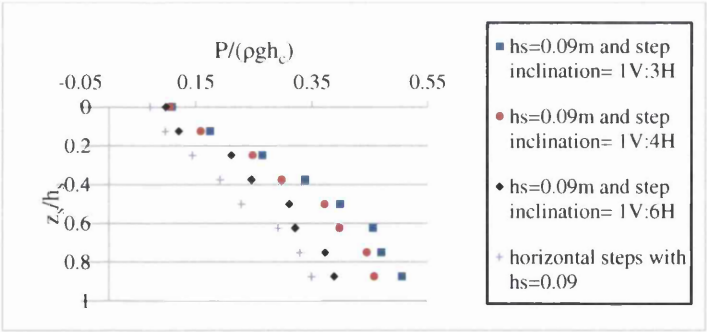

b

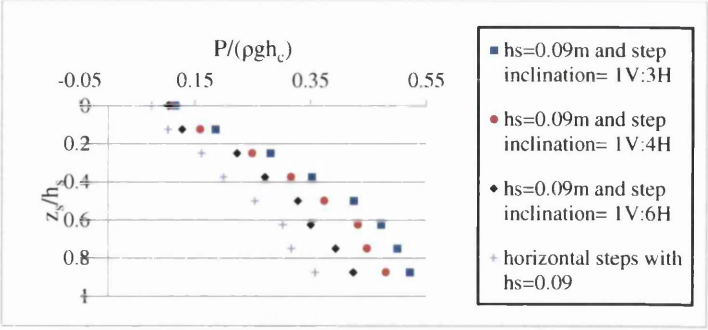

c

Figure 7.18. Pressure distribution on the vertical face of upward inclined steps of height 0.09m having different step inclinations, and horizontal steps over the chute slope 1V:3H, for unit discharge: a) q_w=0.25m^2/s, b) q_w=0.21m^2/s and c) q_w=0.183m^2/s.

In these figures, the pressure values obtained on the vertical face of horizontal steps of height 0.09m on the chute slope 1V:3H are also added, for the sake of comparison. It should be noted that for a given discharge and chute slope the pressure values shown in these figures are obtained on the vertical face of inclined steps located at the inception point of self-aeration. From these figures the following points can be observed:

1- the pressure values under all discharges and chute slopes are all positive;
2- there will be a decrease in the pressure at the upper half of the vertical step as the discharge is increased;
3- the pressures acting on the vertical face due to upward inclined steps are higher than those of the horizontal steps. This is because the upward inclined steps are more efficient in de-accelerating the velocity of the overflowing water, as discussed in Section 6.2.;
4- regarding the effect of the inclination of the upward inclined steps, the maximum pressure values close to the step outer edge are due to the steepest slope of the inclined steps examined in this work;
5- the flatter chute slope 1V:3H examined in this study provides higher pressure values than chute slopes of 1:2.5H and 1V:2H.

7.3. Assessment of cavitation potential

As mentioned earlier, cavitation is the major concern in high velocity channels (Chow, 1959; Henderson, 1966; Chanson, 2002 and Chanson, 2004). Following Frizzell and Renna (2011), the cavitation index number is used in this study, to see whether cavitation could occur on moderate slope stepped spillways. For this purpose the cavitation index equation used by Falvey (1990) is used, as follows:

$$\sigma = \frac{2(P_o - P_v)}{\rho V_o^2} \tag{7.1}$$

where σ is the cavitation index, P_o and P_v are respectively the boundary pressure and the vapour pressure of water at a given temperature, ρ is the density of water and V_o is the mean flow velocity. Equation (7.1) indicates that the lower the value of the cavitation index number, the greater the possibility of cavitation formation. Also, according to Equation (7.1) the cavitation index number is low where the pressure is low and flow velocity is high.

The cavitation index number of 0.6 is considered in the present work as the minimum cavitation index number below which cavitation could occur. This is justified on the grounds that Frizzell and Renna (2011), in their experimental work on moderate slope stepped spillways observed that cavitated bubbles were developed when the cavitation index number was between 0.6 and 0.7.

The computational results of the current work in terms of the flow velocity (see Section 6.2.) and pressure on the vertical face, demonstrate that the velocity and pressure reach their respective highest and lowest values close to the inception point of air entrainment.

To apply Equation (7.1) to prototype structures it is necessary to consider the following points:

1- Froude similitude is applied in this study, as both the gravity and inertia forces are dominant factors governing the free surface flow;
2- Following the hypothesis of Boes and Hager (2002) regarding the scale ratios of stepped spillways, the stepped spillways examined in this section are modelled using the scale ratio of 1:12, to avoid scale effects. Therefore, the

cavitation index number determined in this study is applicable to stepped spillways of step height 0.90m and chute slope of 1V:2H;

3- Vapour water pressure is assumed to be 2.00 KN/m^2, based on the water temperature of 17°C.

Having established the velocity and minimum pressure value on the vertical face of the step of height 0.06m, close to the inception point of air entrainment due to the maximum unit discharge of $q_w = 0.23m^2/s$ over the chute slope of 1V:2H, the minimum cavitation index number would be 1.83. This is an indication that cavitation is unlikely to occur with the aforementioned flow condition. It should be noted that the critical flow depth associated with the abovementioned discharge, which ensures the occurrence of the critical flow condition above the weir crest of length 0.5m, is 0.19m. Therefore, in order to predict the maximum permissible discharge above which cavitation can develop on moderate slope stepped spillways, a broad crested weir with relatively bigger dimensions needs to be examined.

In the present work eight numerical models are set up with the following properties:

1- the total height of the stepped spillway is fixed to 1.2m.
2- the crest length is set to 1.2m.
3- two chute slopes of 1V:2H and 1V:3H are considered.
4- Two step heights of 0.05 and 0.075m are used to represent the prototype stepped spillways of step heights 0.6 and 0.9m respectively, with scale ratio of 1:12.
5- Two step inclinations, 1V:2H and 1V:6H, are tested with the upward inclined step.

Figures 7.19 and 7.20 present the velocity flow field over the horizontal and upward inclined steps respectively, with two step heights 0.05 and 0.075m. In both step configurations various unit discharges typical of the skimming flow condition are examined over two chute slopes, 1V:2H and 1V:3H. It is worth mentioning that the inclination angle of the upward inclined steps is kept here the same as the chute slope. These figures demonstrate that the flow velocity over steps located at the downstream steps varies from about 4.9 for horizontal steps over the steep slopes, to nearly 6.0m/s for inclined steps.

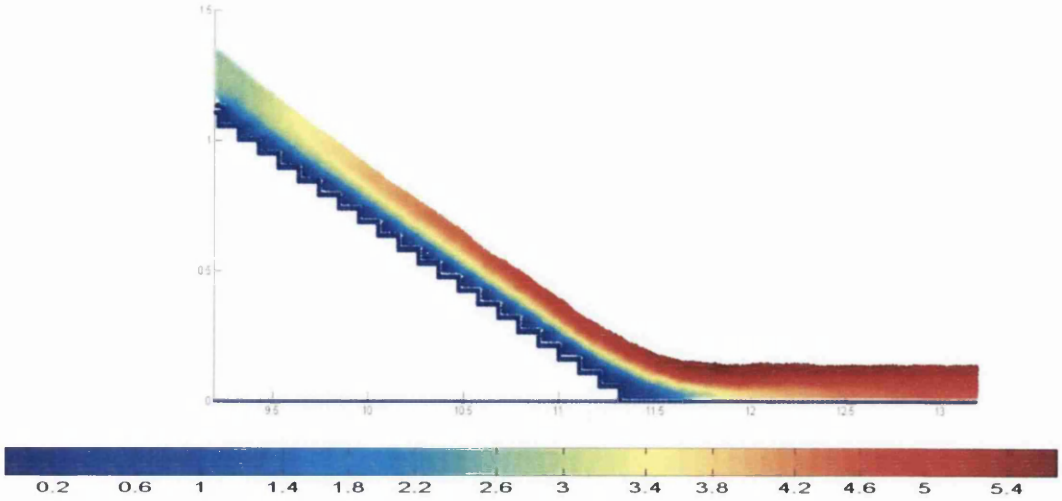

a) q_w=0.607m^2/s over the chute slope 1V:2H

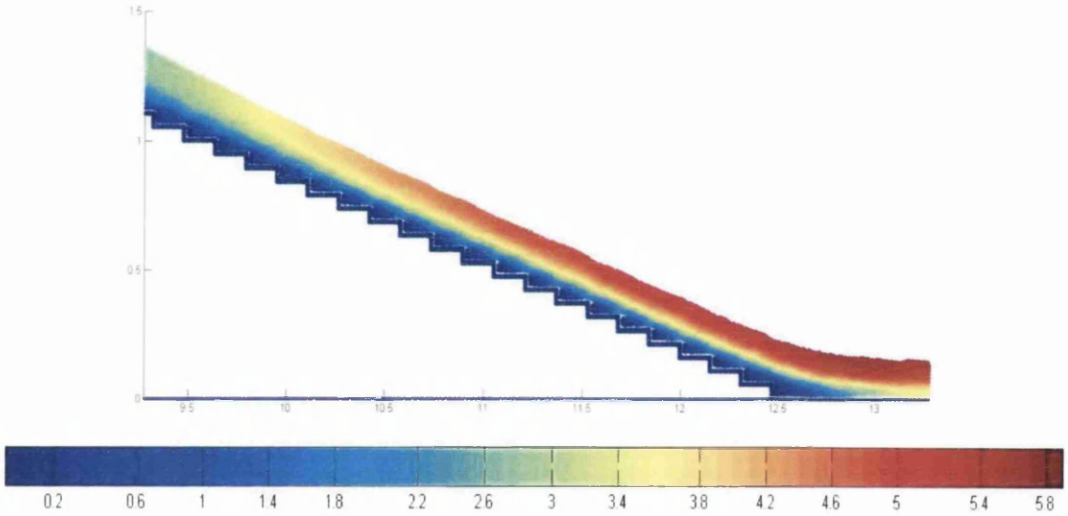

b) q_w=0.705m^2/s over the chute slope 1V:3H

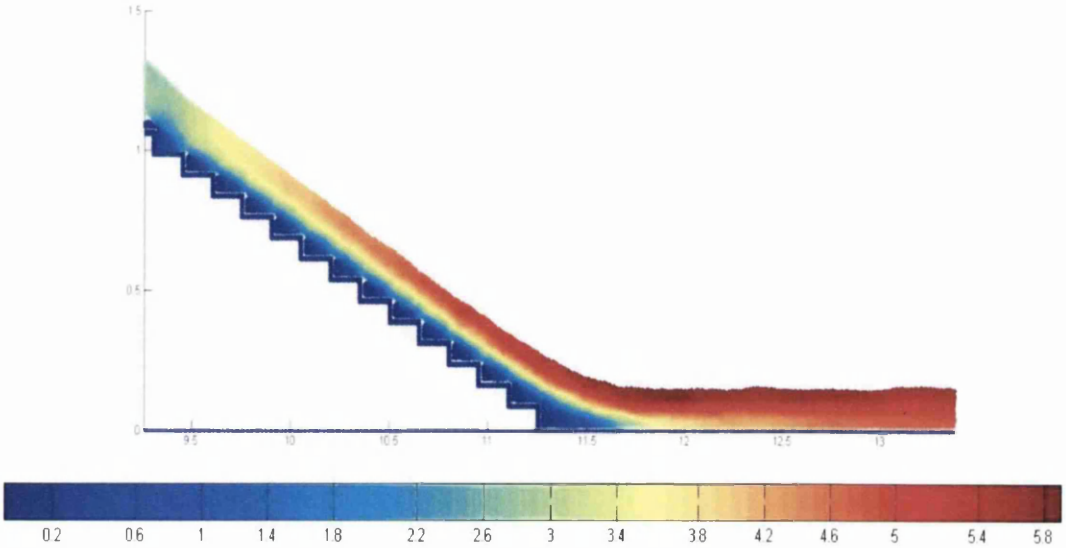

c) q_w=0.746m^2/s over the chute slope 1V:2H

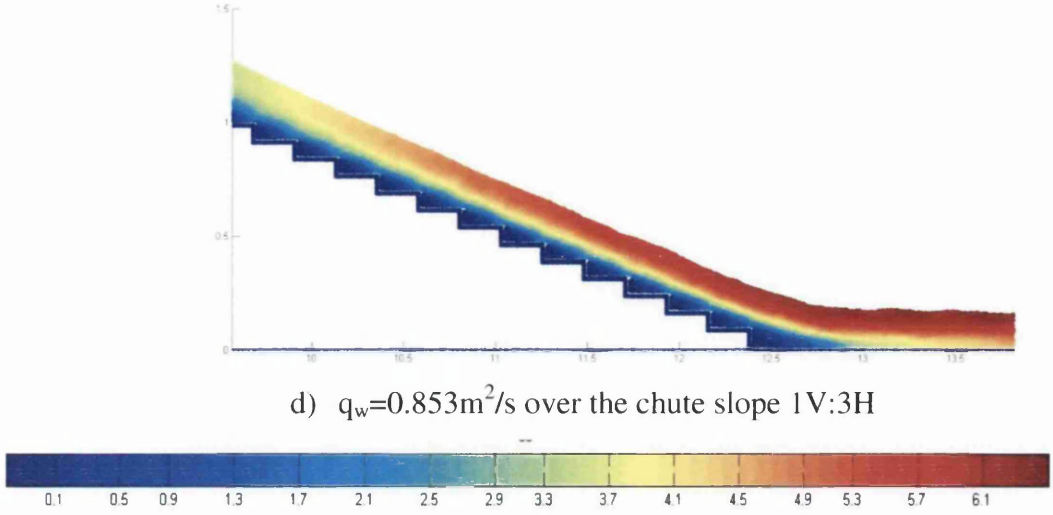

d) q_w=0.853m^2/s over the chute slope 1V:3H

Figure 7.19. Velocity flow field along the chute slope over horizontal steps of height 0.05m (a and b) and 0.075m (c and d).

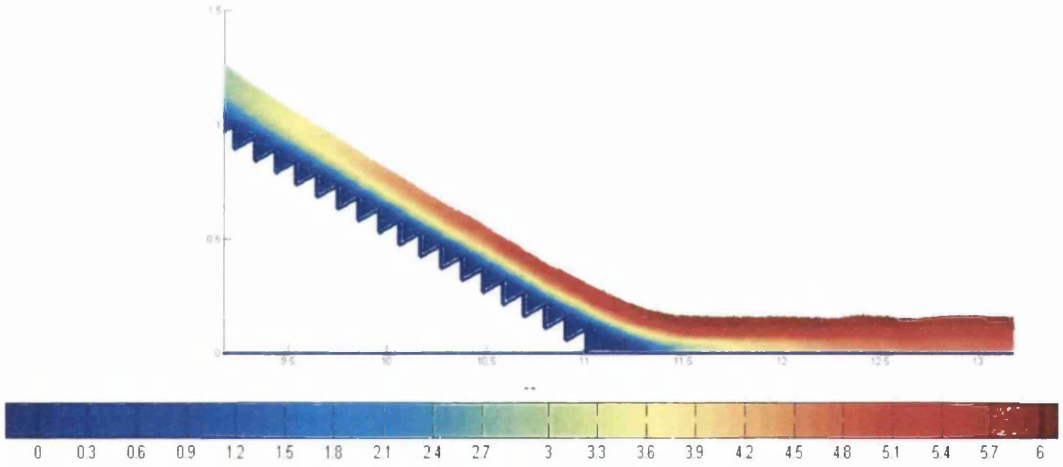

a) q_w=0.72m^2/s over the chute slope 1V:2H

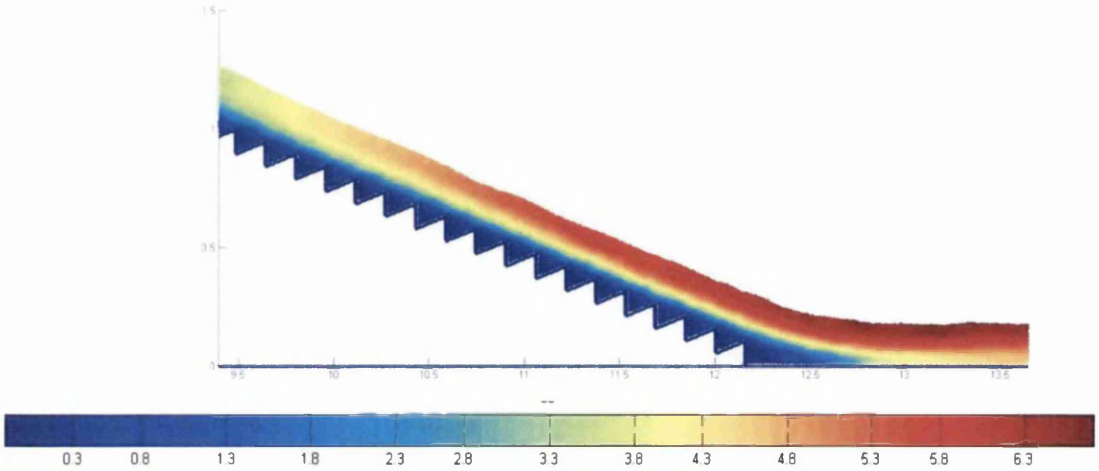

b) q_w=0.807m^2/s over the chute slope 1V:3H

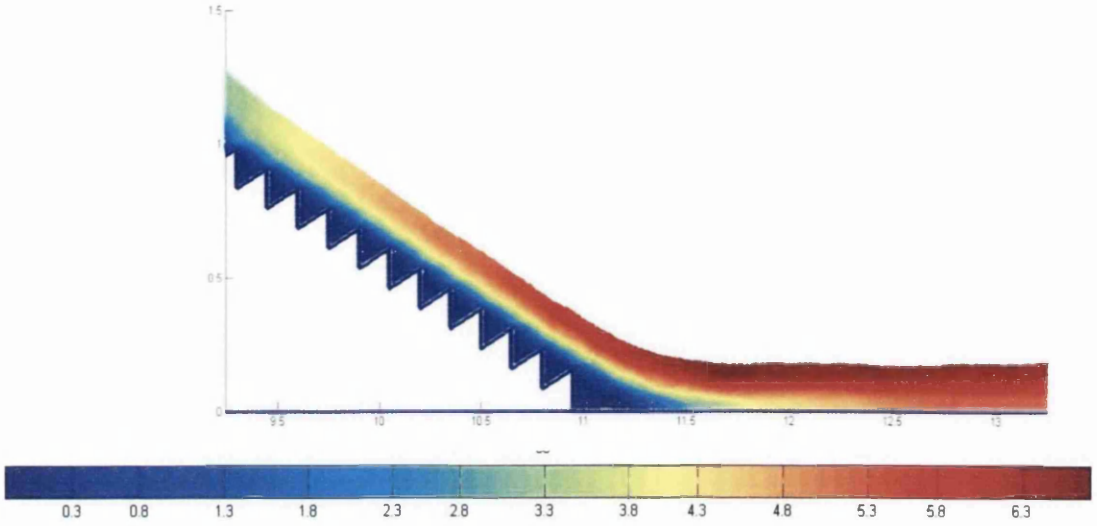

c) q_w=0.868m^2/s over the chute slope 1V:2H

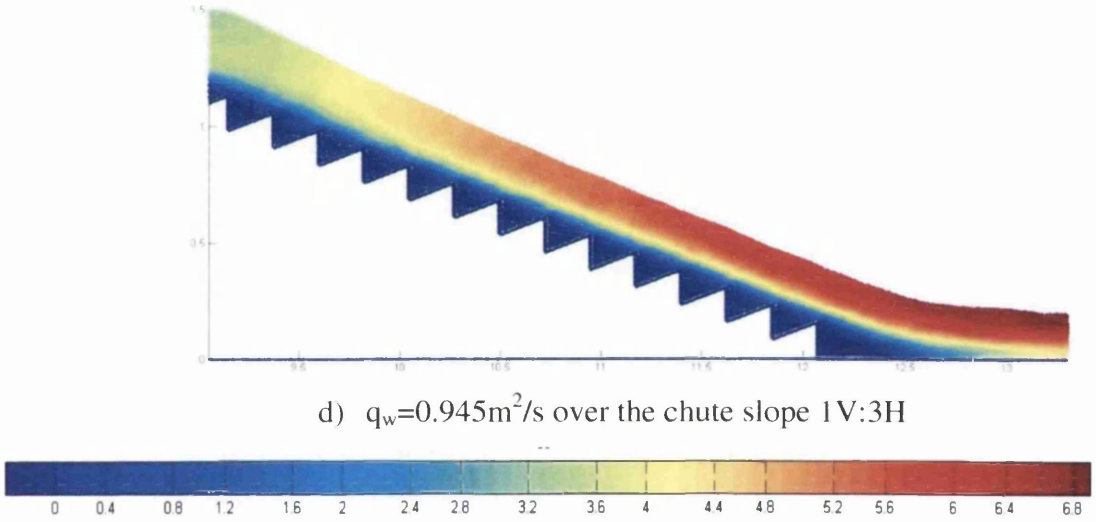

d) q_w=0.945m^2/s over the chute slope 1V:3H

Figure 7.20. Velocity flow field along the chute slope over upward inclined steps of height 0.05m (a and b) and 0.075m (c and d).

Further, the pressure flow field over the horizontal and upward inclined steps predicted in the present work are illustrated in Figures 7.21 and 7.22 respectively. It should be noted here that the step geometry, chute slope and flow condition examined to obtain the pressure flow field are identical to those mentioned above in the velocity flow field.

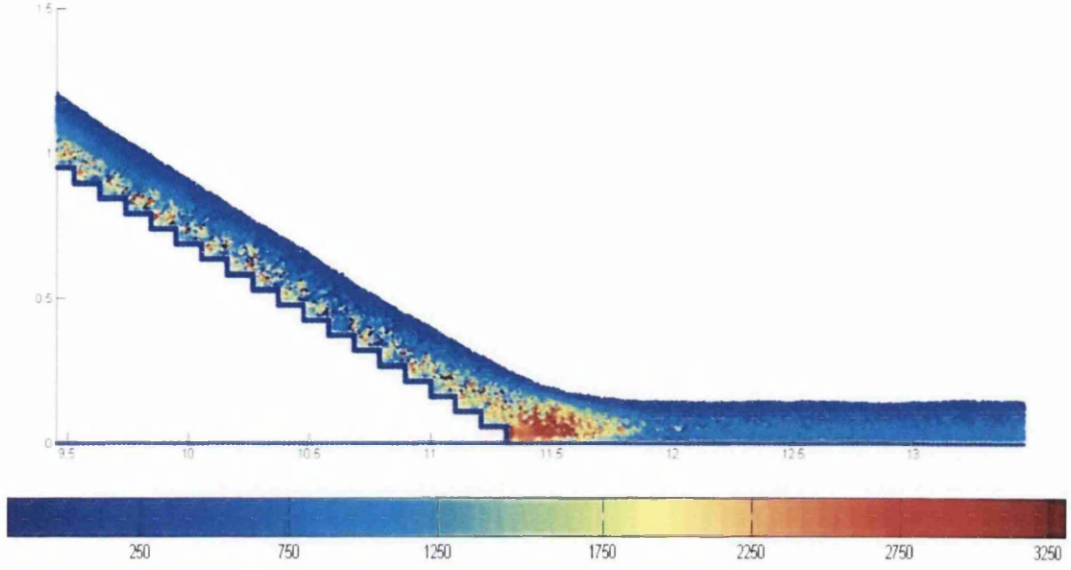
250
750
1250
1750
2250
2750
3250

a

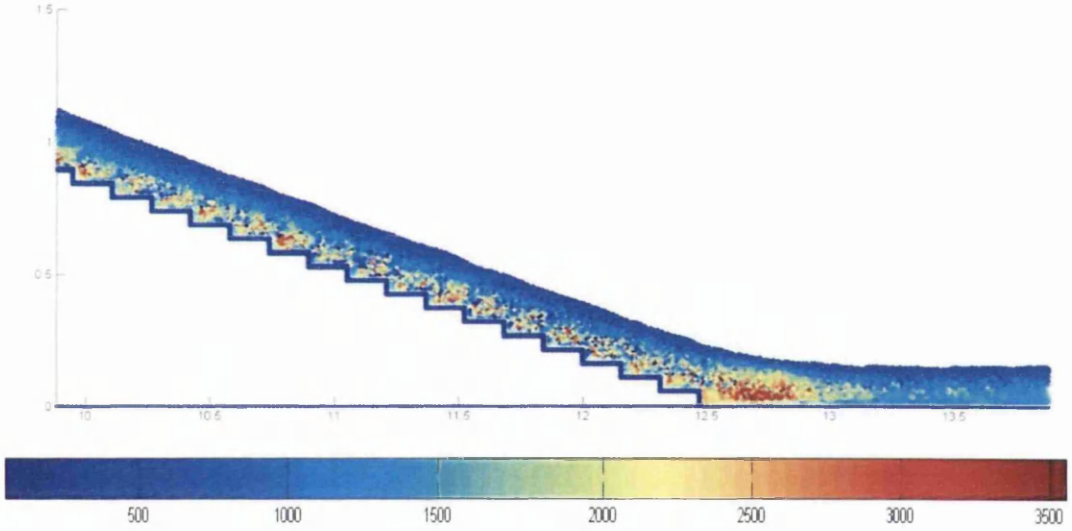
500
1000
1500
2000
2500
3000
3500

b

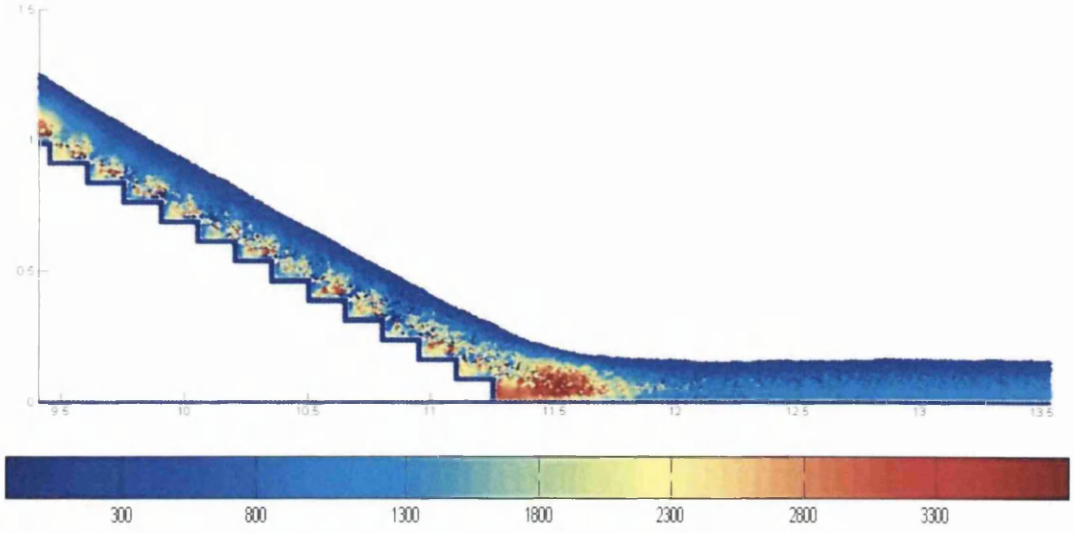
300
800
1300
1800
2300
2800
3300

c

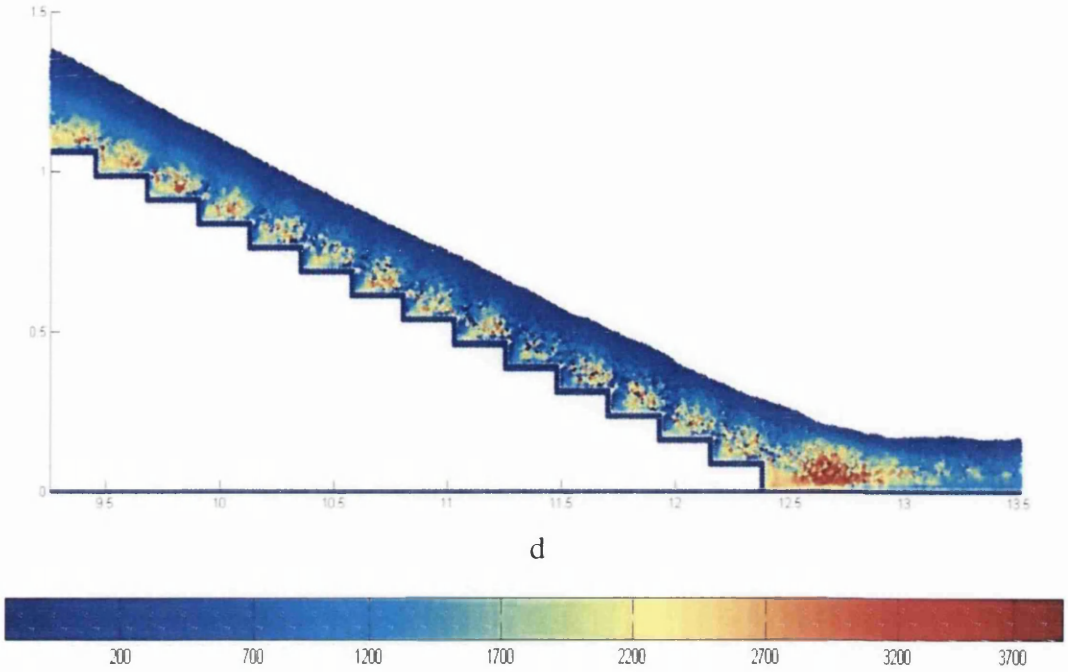

d

Figure 7.21. Pressure flow field along the chute slope over horizontal steps of height 0.05m (a and b) and 0.075m (c and d).

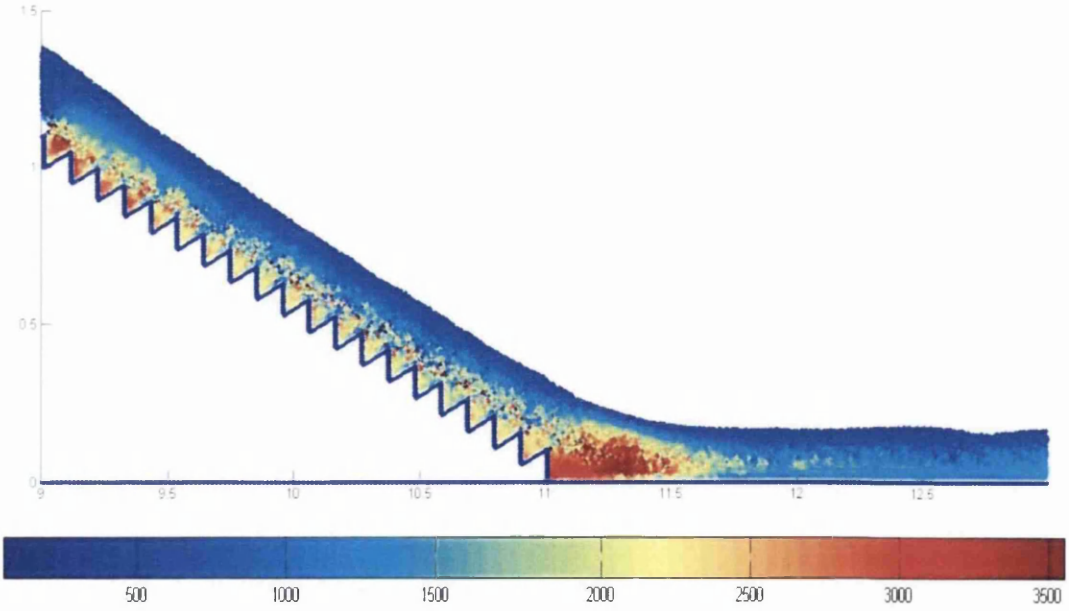

a

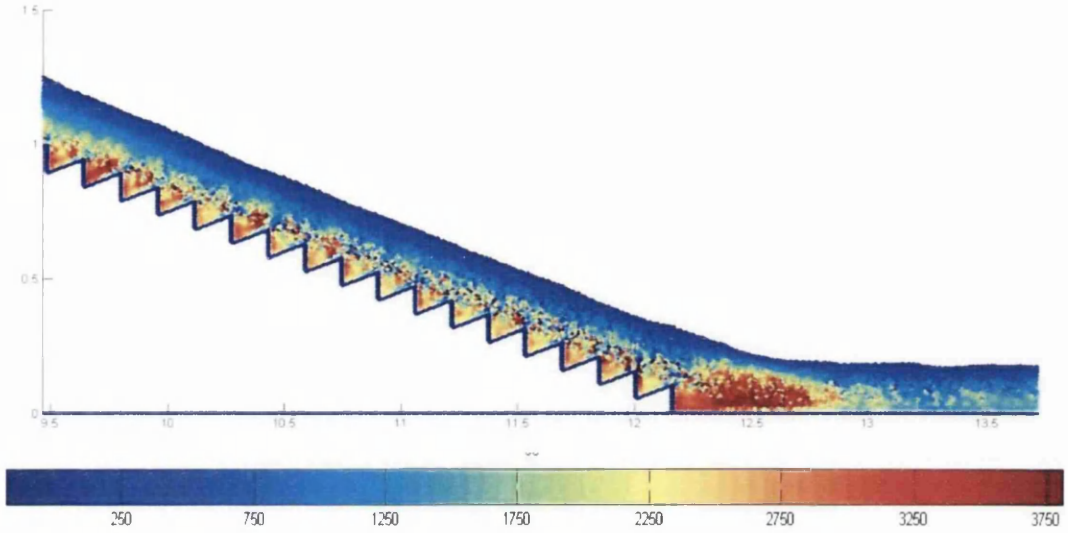

b

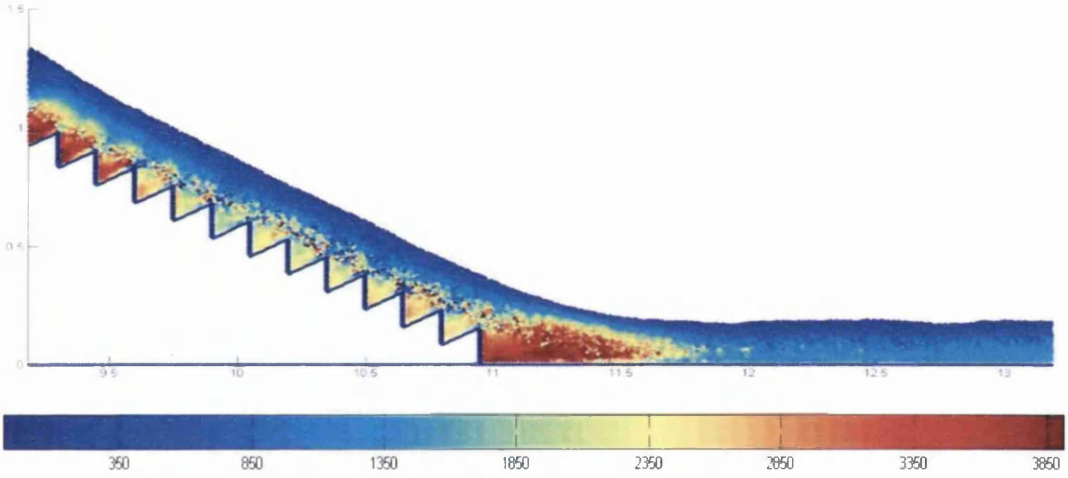

c

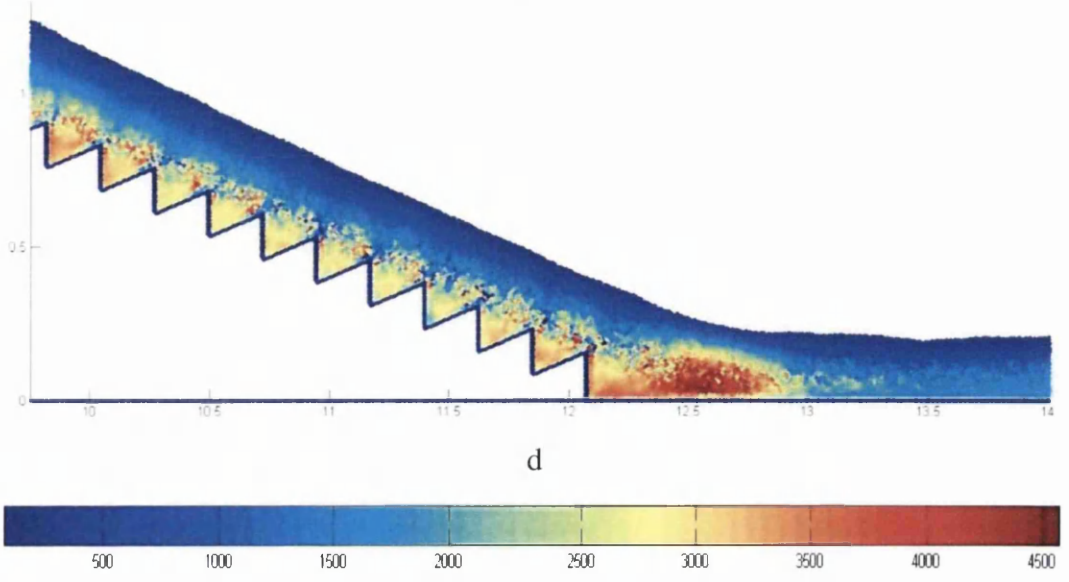

d

Figure 7.22. Pressure flow field along the chute slope over upward inclined steps of height 0.05m (a and b) and 0.075m (c and d).

These figures show that the pressure carried by fluid particles close to the outer edge of steps is relatively low, especially on those located at the downstream reach, and drops below the atmospheric pressure value, in particular with the steepest slope 1V:2H, and smallest step height 0.05m, examined here. This may be due to the separation of the overlying flow from the step tip. Both the velocity and pressure flow fields discussed above affirm that the upper half of the vertical face of steps located at the downstream part of the chutes is potentially prone to cavitation formation. This is consistent with the experimental observations made by Amador et al. (2009) regarding pressure variation on the vertical face of steps located far from the ogee type weir over steeply sloping stepped spillways.

The following section sheds light on the velocity and pressure distributions on steps located at a distance far from the weir crest along the chute slopes. In fact, these profiles can be used to deduce the mean flow velocity and low pressure values that should be considered in assessing the potential of cavitation formation based on the cavitation index number. Figures 7.23 and 7.24 show the velocity profile on the horizontal and upward inclined steps respectively, at various unit discharges.

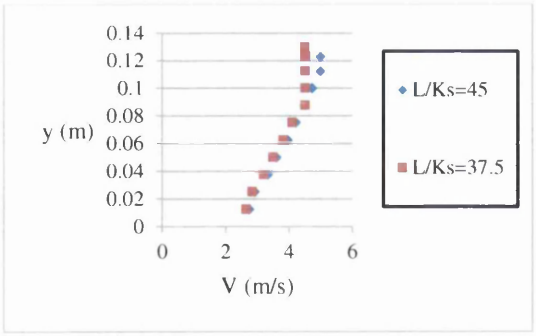

q_w=0.607m^2/s and chute slope 1V:2H

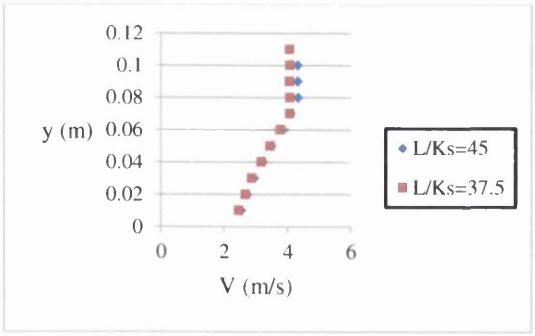

q_w=0.452m^2/s and chute slope 1V:2H

a)

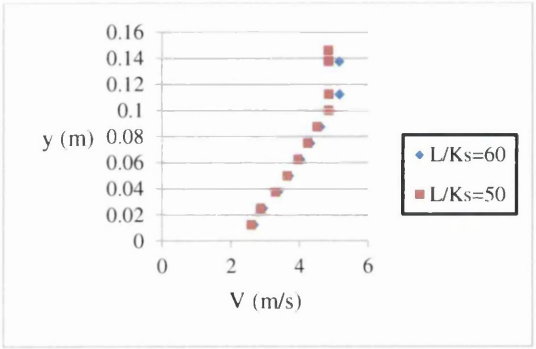

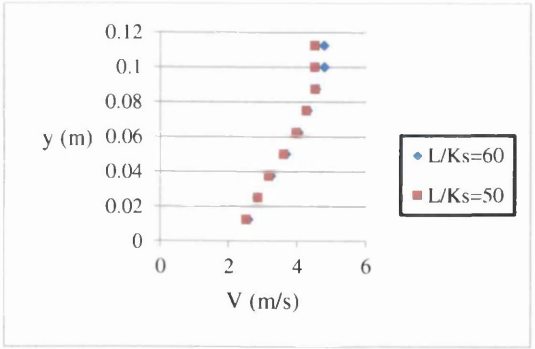

q_w=0.705m^2/s and chute slope 1V:3H q_w=0.515m^2/s and chute slope 1V:3H

b)

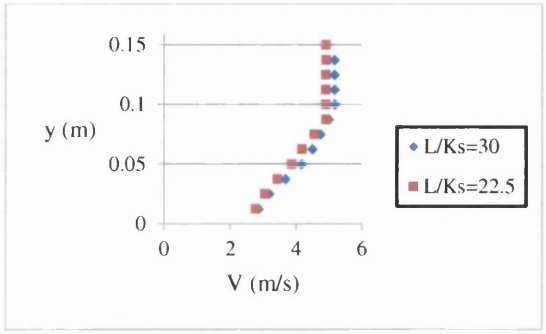

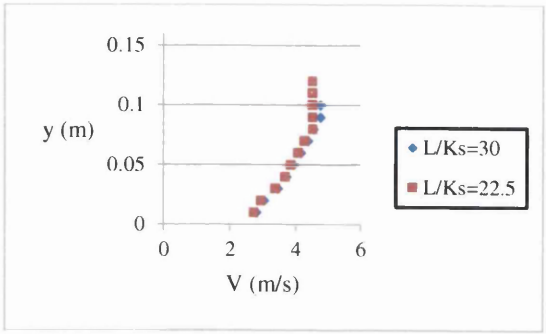

q_w=0.748m^2/s and chute slope 1V:2H q_w=0.541m^2/s and chute slope 1V:2H

c)

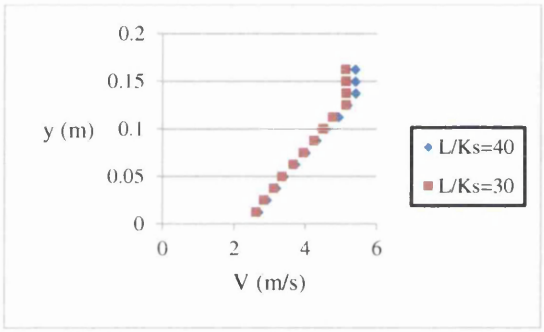

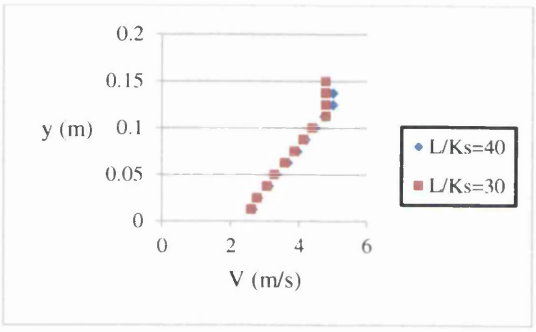

q_w=0.853m^2/s and chute slope 1V:3H q_w=0.676m^2/s and chute slope 1V:3H

d

Figure 7.23. Velocity profiles along the water flow depth over the outer edge of horizontal steps of height 0.05m (a and b) and 0.075m (c and d).

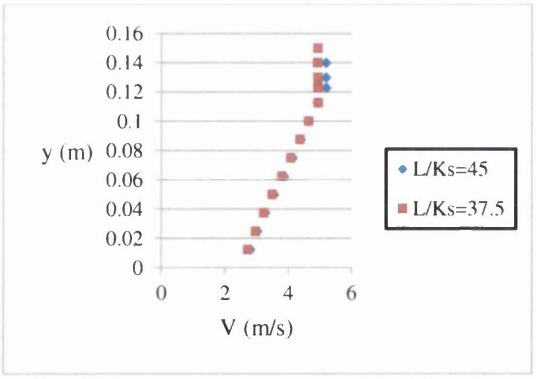

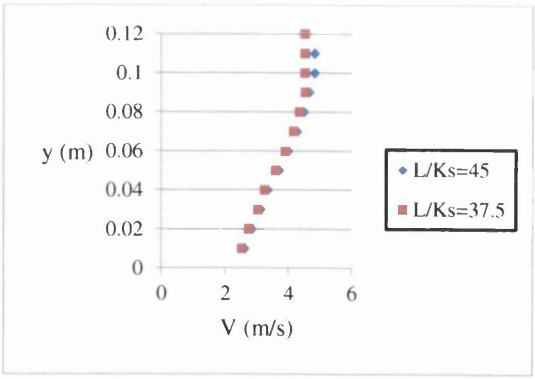

q_w=0.719m^2/s and chute slope 1V:2H q_w=0.554m^2/s and chute slope 1V:2H

a

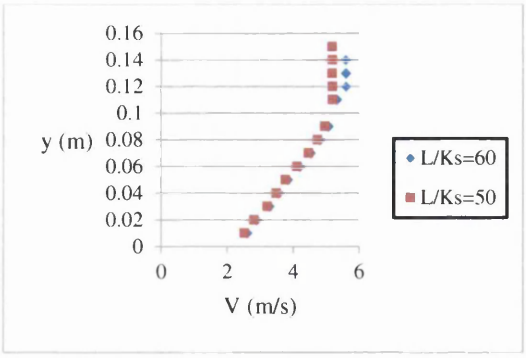

$q_w=0.807m^2/s$ and chute slope 1V:3H

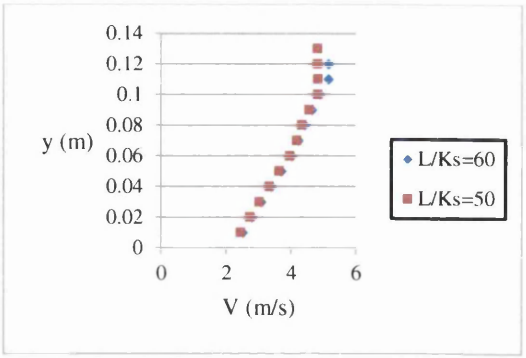

$q_w=0.621m^2/s$ and chute slope 1V:3H

b

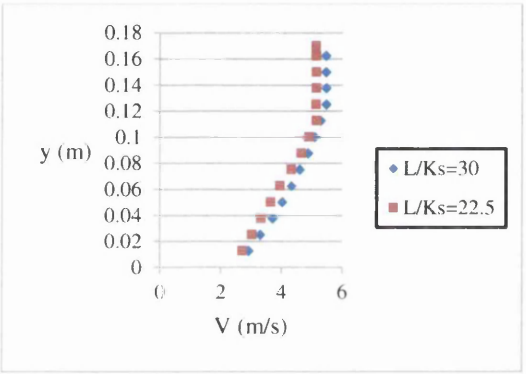

$q_w=0.867m^2/s$ and chute slope 1V:2H

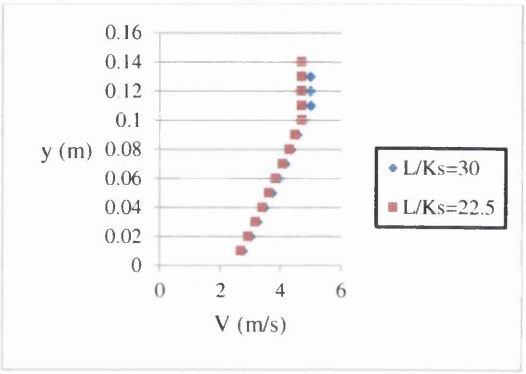

$q_w=0.663m^2/s$ and chute slope 1V:2H

c

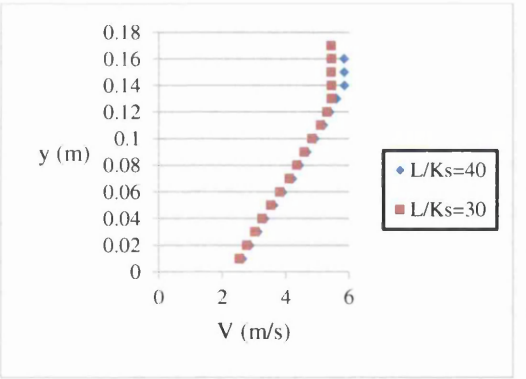

$q_w=0.945m^2/s$ and chute slope 1V:3H

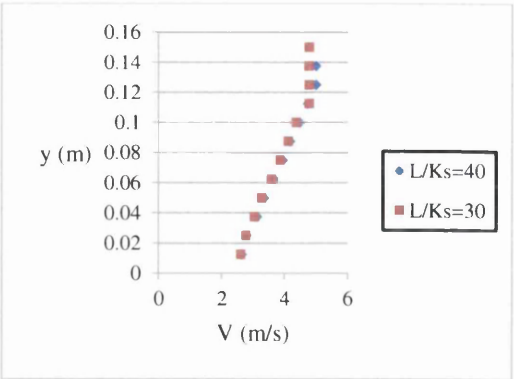

$q_w=0.705m^2/s$ and chute slope 1V:3H

d

Figure 7.24. Velocity profiles along the water flow depth over the outer edge of upward inclined steps of height 0.05m (a and b) and 0.075m (c and d).

As can be seen for all discharges and step geometries, the velocity profile indicates that the boundary layer has not been fully developed, as the velocity varies only

along a certain height of the flow depth until reaching maximum value above which the velocity keeps constant. This is possibly because in this part of the study high discharge values are used to attain high flow velocities, and low pressure values to predict the discharge above which cavitation may occur. Also, it can be observed that the velocity profiles are quantitatively different, which can be explained by the differences in the discharge values, chute slopes, step heights and step configurations tested in this study. However, the value of the mean velocity obtained in each of the above velocity profiles is used in Equation (7.1) as a reference velocity to predict the cavitation index number.

Figures 7.25 and 7.26 represent the pressure distribution acting on the vertical face of two steps located in the non-aerated flow region of the horizontal and upward inclined steps respectively. The computational results of the present investigation shown in both of these figures are obtained using the same discharge values and step geometries mentioned above in the velocity profile.

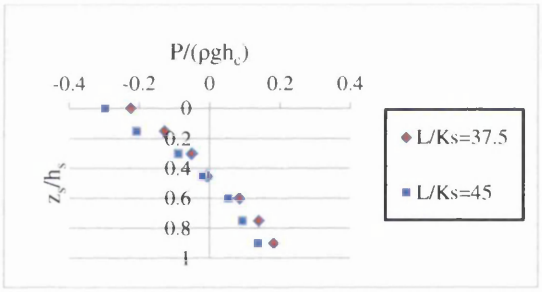

q_w=0.607m^2/s and chute slope 1V:2H

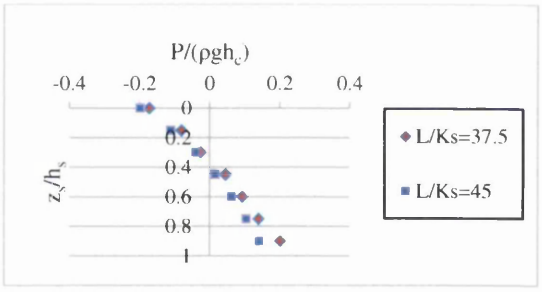

q_w=0.452m^2/s and chute slope 1V:2H

a

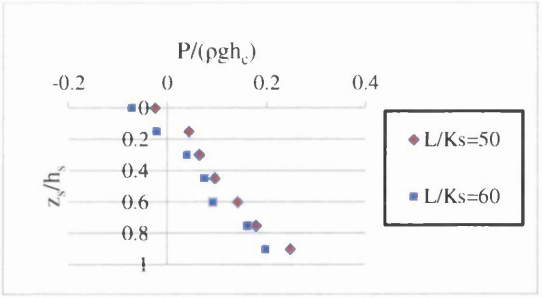

q_w=0.705m^2/s and chute slope 1V:3H

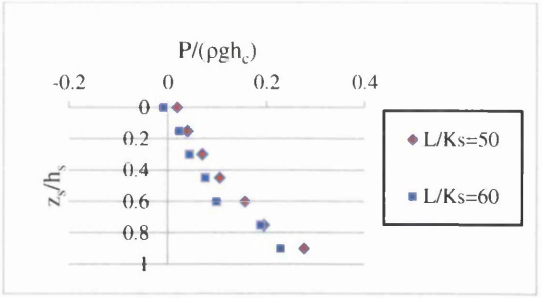

q_w=0.515m^2/s and chute slope 1V:3H

b

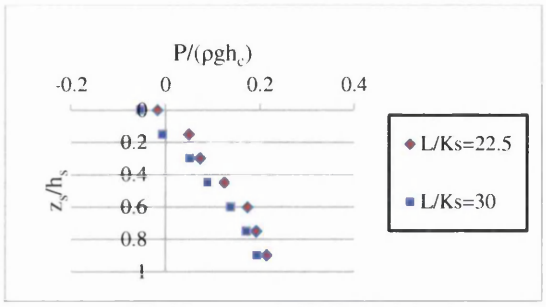

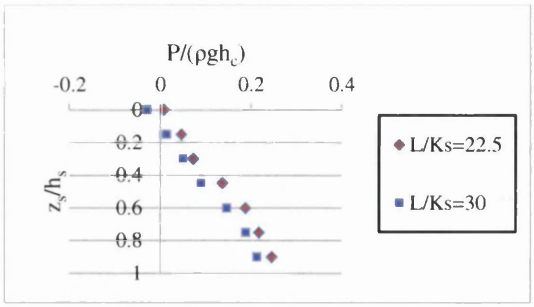

q_w=0.748m^2/s and chute slope 1V:2H

q_w=0.541m^2/s and chute slope 1V:2H

c

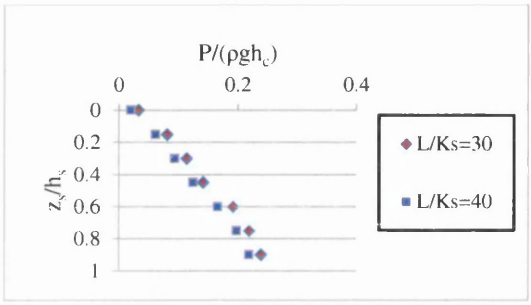

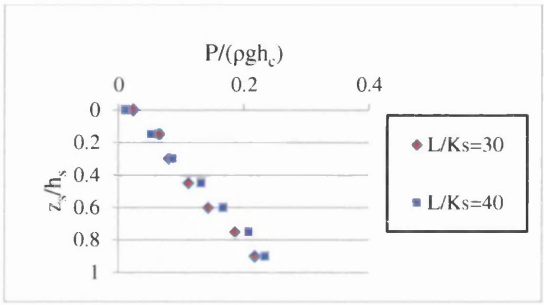

q_w=0.853m^2/s and chute slope 1V:3H

q_w=0.676m^2/s and chute slope 1V:3H

d

Figure 7.25. Pressure distribution on the vertical face of horizontal steps of height 0.05m (a and b) and 0.075m (c and d).

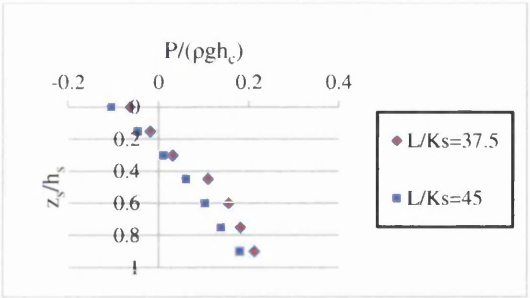

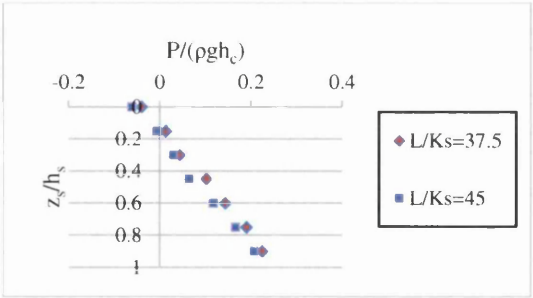

q_w=0.719m^2/s and chute slope 1V:2H

q_w=0.554m^2/s and chute slope 1V:2H

a

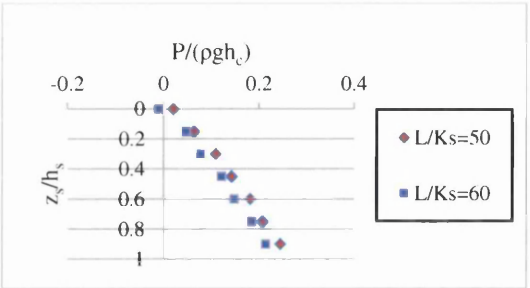

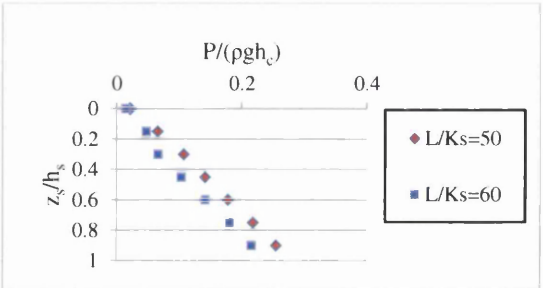

q_w=0.807m^2/s and chute slope 1V:3H

q_w=0.621m^2/s and chute slope 1V:3H

b

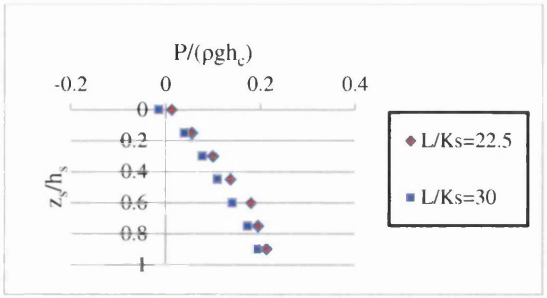

q_w=0.867m^2/s and chute slope 1V:2H

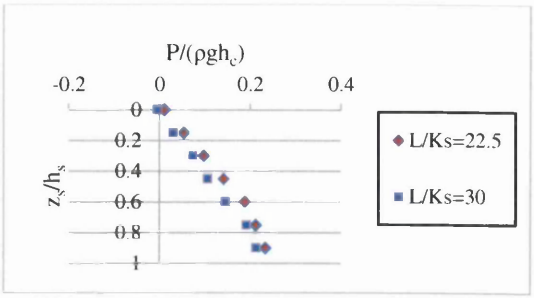

q_w=0.663m^2/s and chute slope 1V:2H

c

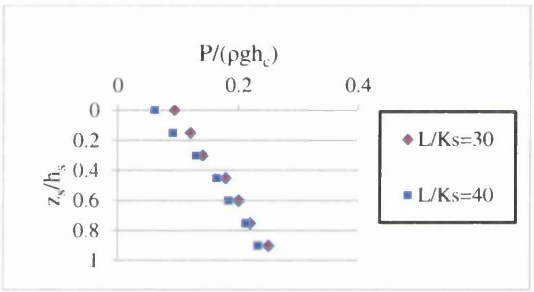

q_w=0.945m^2/s and chute slope 1V:2H

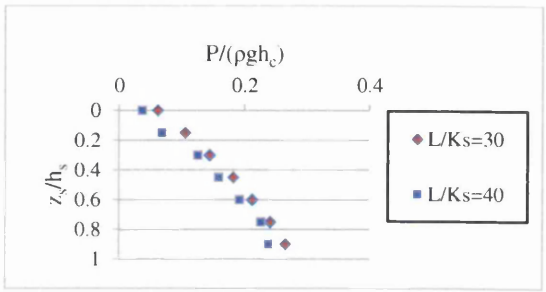

q_w=0.705m^2/s and chute slope 1V:2H

d

Figure 7.26. Pressure distribution on the vertical face of upward inclined steps of height 0.05m (a and b) and 0.075m (c and d).

The computational results of the pressure distribution on the vertical face of the steps examined in this study, shown in the two figures above, demonstrate that there is a drop in the pressure at the outer edge, to either below atmospheric pressure value or close to the water vapour pressure values, which in turn may cause cavitation to develop especially when the mean flow velocity in the tested section is relatively high. However, the minimum pressure value obtained on the vertical face is used in this study to determine the cavitation index number.

Figure 7.27 plots the cavitation index number obtained in this study versus the unit discharge for different step heights, step inclination angles and chute slopes. The critical cavitation index number of 0.6, which was found experimentally by Frizzell and Renna (2011), is also drawn. It is worth mentioning that the computational

results obtained in this study in terms of the cavitation index number and unit discharge are applied on prototype stepped spillways using the scale ratio of 1:12.

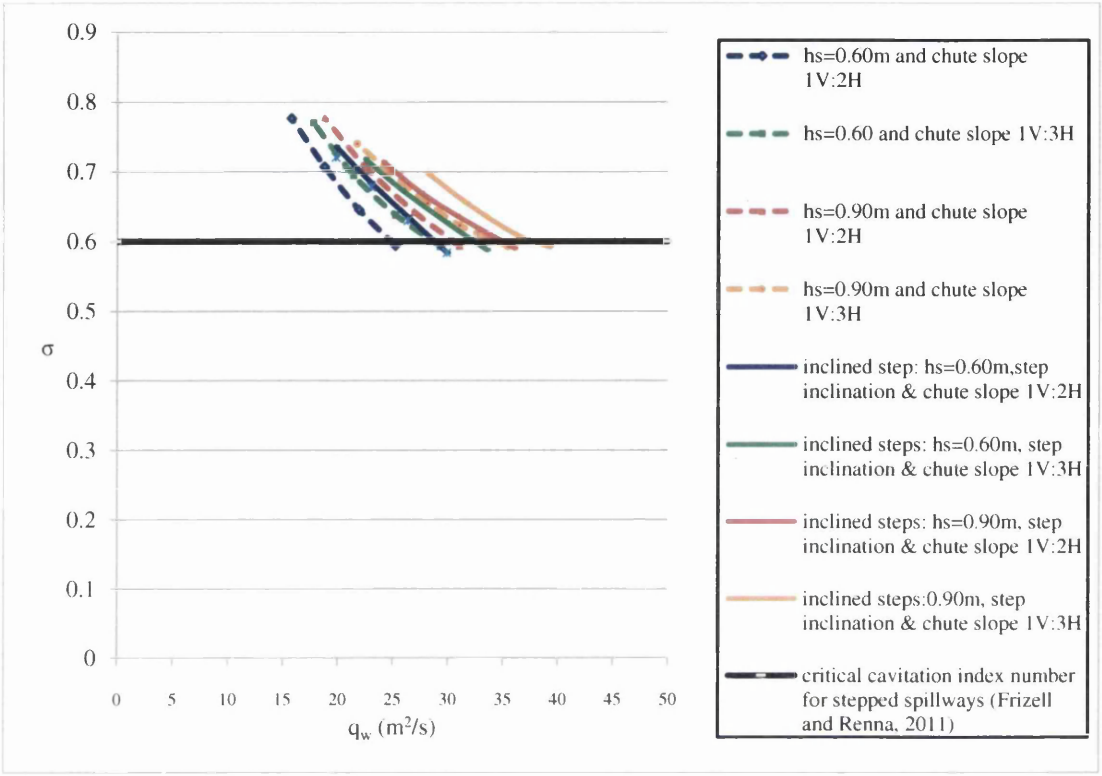

Figure 7.27. Cavitation index number versus unit discharges for various step configurations and geometries over moderate slope stepped spillways.

Figure 7.27 demonstrates that at the critical cavitation index number of 0.6:

1- the unit discharge increases with the increase of the step height for a certain chute slope;
2- the unit discharge increases with the decrease of the chute slope for a certain step height;
3- the unit discharge provided by upward inclined steps is approximately 9% more than that provided by the horizontal steps for the same step height and chute slope;
4- For all conditions, the unit discharge that may cause cavitation to form on moderate slope stepped spillways of step heights 0.60m and 0.90m is between 25 and 42m^2/s.

Table 7.1 presents the maximum allowable discharge above which cavitation can commence, for different step geometries and chute slopes typical of embankment

dams. This table has direct implications for the design of moderate slope stepped spillways, as it presents the maximum discharge that can flow over the downstream face without the damage of cavitation. It is worth mentioning here that the stepped spillway needs to be equipped with one or more aerators when the design requires the passing of unit discharges higher than those presented in Table 7.1.

step shape	step height (m)	chute slope	unit discharge (m^2/s)
horizontal	0.60	1V:2H	25.00
horizontal	0.60	1V:3H	29.50
horizontal	0.90	1V:2H	31.00
horizontal	0.90	1V:3H	35.50
inclined 1V:2H	0.60	1V:2H	29.90
inclined 1V:3H	0.60	1V:3H	35.50
inclined 1V:2H	0.90	1V:2H	36.00
inclined 1V:3H	0.90	1V:3H	39.00

Table 7.1. The maximum allowable unit discharge to avoid cavitation formation on moderate slope stepped spillways, for various step configurations and geometries.

CHAPTER EIGHT

CONCLUSIONS AND RECOMMENDATIONS FOR FUTURE WORK

Chapter Eight: Conclusions and Recommendations for Future Work

8.1. Introduction

This study was carried out to numerically characterize skimming flow conditions over moderate slope stepped spillways. The focus was on the properties of the skimming flow over a reach of the structure known as the non-aerated flow region. Aside from the techniques of the conventional numerical grid-based method, such as finite difference, finite element and finite volume, the technique of smoothed particle hydrodynamics, as one of the most efficient techniques for the numerical particle-based method has been used in this study to examine its efficiency and accuracy in predicting the flow field variables of free surface flow over stepped spillways. For this purpose, the numerical 2D SPHysics model, as an implementation of the computational smoothed particle hydrodynamics method, was applied. The study set out to explore the effects of step height and chute slope on the characteristics of the skimming flow regime. It has also sought to study the behaviour of the skimming flow regime over upward inclined steps. Further, the project investigated the potential for cavitation formation on moderate slope stepped spillways. Understanding the characteristics of the skimming flow regime in the non-aerated flow region is important for improving the design of moderate slope stepped spillways, and the downstream slope of small embankment dams.

This study sought to answer the following key research questions:

1- Is the weakly compressible smoothed particle hydrodynamics method capable of simulating free surface flow over stepped spillways? If yes, which numerical particle-based method technique should be applied to accurately simulate and predict flow properties over this kind of hydraulic structure?

2- What effects do the step height, chute slope and step shape have on a number of key elements of the design of this type of hydraulic structure? These elements include the length of the non-aerated flow region, growth of the boundary layer, the energy dissipation rate and pressure on both step faces.

3- How does the skimming flow condition behave in the non-aerated flow region when conventional horizontal steps are replaced by upward inclined steps?
4- Is it possible for cavitation to occur on moderate slope stepped spillways? If yes, what is the maximum discharge that can be passed safely without damage being caused by cavitation.

This chapter initially synthesizes the main findings obtained in this study, then highlights the main implications and limitations of the current study. Finally, it makes some suggestions for directions and areas of future works.

8.2. Synthesis of research findings

This section will synthesize the main findings obtained, to answer the research questions raised in this study. The first research question was about the efficiency and accuracy of the particle-based method in simulating and predicting flow properties over stepped spillways. For this purpose, the numerical 2D SPHysics code, as an implementation of the computational smoothed particle hydrodynamics particle-based method, was applied. The numerical code was calibrated against the experimental data gathered from experiments conducted previously on two laboratory models, namely the flow over broad crested weirs and skimming flow over moderate slope stepped spillways. The differences between the computational and experimental results, in terms of the unit discharge on the weir crest for various values of the total upstream head, were high when the Navier-Stokes governing equations were solved on the basis of classical formulations of the smoothed particle hydrodynamics method. This affirms that the numerical model may not produce accurate results unless the recently developed numerical particle-based techniques are applied.

This motivated us to apply all the numerical techniques provided by the 2D SPHysics model, through a sensitivity analysis, to determine the most efficient ones in order to optimize the accuracy of the numerical results and computational time.

The computational results of the sensitivity analysis showed that:

1- as well as the technique of corrected kernel function for handling the numerical instabilities associated with the truncation of kernel function near the domain boundaries, the Riemann solver density filter technique is also needed, in order to remove the fluctuations appearing in the density and pressure flow fields. This is because the numerical code applied in this study uses an equation of state to determine the pressure acting on the particles, as the partial differential equations governing the fluid flow are solved considering the fluid as weakly compressible;
2- the accuracy of the computational results can be increased with the use of the repulsive boundary condition technique, instead of the dynamic boundary condition method. This could be due to the behaviour of a number of fluid particles, which were observed penetrating the boundary walls of the computational domain generated by the latter method.

Qualitative and quantitative comparisons between the computational and experimental results were also made, to verify the efficiency and accuracy of the numerical model applied in this study. Agreement between the computed results and measured data for both test cases was fairly good. This demonstrates that the numerical SPH model, which solves the weakly compressible Navier-Stokes equations, could be a useful tool for simulating free surface flow over stepped spillways, attaining fairly good accuracy when the corrected kernel function and Riemann solver density filter are applied.

The validated code was then applied to twenty-six numerical stepped spillway cases, designed to achieve the main objectives set out in the present work. These cases were divided into two groups; the first was represented by eighteen cases, to study the effects of step geometry aspects, such as step height, step shape and chute slope, on the characteristics of the skimming flow conditions. The rest of the cases were categorized under the second group, which were designed with larger dimensions and examined under higher unit discharges than the cases of the first group, to assess the potential for cavitation formation on moderate slope stepped spillways.

The second research question addressed in this study was about the effects of step geometry on the characteristics of the skimming flow conditions in the non-aerated

flow region over moderate slope stepped spillways. The length of the non-aerated flow region was the first parameter investigated. This was determined according to the definition which states that it corresponds to the distance between the weir crest and the section along the chute slope at which the boundary layer is fully developed. Based on the computational results of free surface and velocity profiles at different sections along the non-aerated flow region, obtained for different step heights, chute slopes and unit discharges typical of skimming flow conditions, an equation was developed to estimate the location of the inception point for horizontal steps. This equation affirms that the unit discharge is not the only factor that may affect the location of the inception point of air entrainment on moderate slope stepped spillways; the step height and chute slope are two important factors that must also be considered in determining the longitudinal distance between the weir crest and the inception point of air entrainment.

The accuracy of this equation was examined by comparing the computed results with the measurement data of a number of experimental works previously conducted on moderate slope stepped spillways. Some discrepancies were observed between the computational results obtained in this study and those recorded in past experimental works for the same flow and geometry conditions. This can be explained by the fact that the experimental data of these studies were gathered considering either the step height or the chute slope as the main factor affecting the location of the inception point, whereas the computational results obtained in this investigation are due to various step heights and chute slopes.

This investigation has also shed light on the effects of the step geometry and chute slope on the growth of the boundary layer. The numerical results obtained in this study showed that greater boundary layer growth is associated with larger step height. The computational results further demonstrated that the growth of the boundary layer is accelerated when the chute slope is increased. The findings obtained in this study, in terms of the effects of the flow and geometry conditions on the growth of the boundary layer, were consistent with what has been observed by other researchers in experimental work on stepped spillways. However, as claimed by most of the researchers, there is no a definite equation to estimate the growth of the boundary layer on stepped spillways.

Based on the computational results obtained in this study from various step heights, chute slopes and discharges, an equation was proposed to determine the thickness of

the turbulent boundary layer along the non-aerated flow region, for horizontal steps on moderate slope stepped spillways. The main difference between this equation and those proposed by other investigators is that along with the roughness height it takes into account the effects of the discharge and chute slope as well.

The effects of the discharge and step geometry on the energy dissipation rate in the non-aerated flow region over moderate slope stepped spillways was another research point investigated in the present work. The computational results gathered from various step heights, chute slopes and unit discharges showed that the energy dissipation rate in this region is slightly influenced by the unit discharge and step height, and highly affected by the chute slope. This agrees well with the experimental observations made by other researchers who conducted their experiments on moderate slope stepped spillways. The computational results obtained in this study were used to obtain an equation for estimating the energy dissipation rate at any section along the non-aerated flow region.

The effect of step geometry on features of the velocity distribution for various unit discharges was addressed in this research. For this purpose, the velocity profiles for various unit discharges at the outer edge of a number of steps, located along the non-aerated flow region at different distances from the weir crest, were computed. The velocity profiles obtained in this study followed the power law, agreeing well with past research. The computational results showed that for the same chute slope the use of large step height can result in a significant decrease in the mean flow velocity, especially close to the point of free surface aeration. It was also observed that for the same step height the minimum mean flow velocity near the inception point of self-aeration is associated with the flatter chute slope.

Moreover, in the present work the influence of step geometry and unit discharge on the pressure flow field in the non-aerated flow region was studied. For this purpose, the pressure acting on the vertical and horizontal faces of a number of steps was considered. These steps were located at different distances from the downstream face of the weir crest. This allowed us to see whether the pressure carried by fluid particles close to these faces is severe enough to cause cavitation to develop on the steps. From the pressure distributions obtained with various step heights and chute slopes it was observed that:

1- For a given chute slope and unit discharge the pressure values along both step faces increase as the step height is increased.

2- For a given step height and unit discharge the pressure values acting on both step faces increase as the chute slope is decreased.

These demonstrate that if cavitation can occur on stepped spillways, then small step heights and steep chute slopes are potentially more subject to such damage than larger step heights and flatter chute slopes. However, it was observed that the pressure values acting on both step faces at all sections examined in this study were positive. This affirms that cavitation is unlikely to occur for the range of unit discharges tested in the present work, with the numerical stepped spillway cases of the first group.

The third research question addressed how upward inclined steps affect the behaviour of skimming flow conditions in the non-aerated flow region over stepped spillways having slopes typical of embankment dams. Upward inclined steps have been proven to be one of the most efficient step configurations in terms of the energy dissipation rate. However, no detailed information is available regarding the hydraulics of skimming flow conditions over this kind of step configuration in the non-aerated flow regime. This is because past experimental studies with such step types were, on the one hand conducted on steep slopes, and on the other hand focused on two major points:

1- their performance in dissipating the flow energy;
2- their influence on the occurrence of flow regimes over stepped spillways.

The computational results obtained in this study with the upward inclined steps showed that in comparison with conventional horizontal steps, this kind of steps not only improves the energy dissipation rates, but also:

1- accelerates the growth of the boundary layer, which may cause the inception point, where the self-aeration process begins, to move further upstream toward the weir crest. Hence, the length of the non-aerated flow region over stepped spillways, which may be prone to cavitation damage, will be reduced;
2- lowers the mean flow velocity and increases the pressure acting on the vertical and tilted faces. Hence, the maximum safe discharge in terms of cavitation damage can be increased.

These findings make it possible to state that this kind of steps can present more efficient designs for stepped spillways than the conventional horizontal steps.

The last research question addressed in the present investigation was about whether cavitation is able to occur on moderate slope stepped spillways, and what the maximum discharge that can be passed by this kind of hydraulic structure safely is. This is because up to now the potential for cavitation formation on moderate slope stepped spillways has received little attention, and the maximum discharge above which such damage can occur has not yet been established. For this purpose, the critical cavitation index number determined from experiments previously conducted on moderate slope stepped spillways is used in this study, to evaluate this issue. To do so, the mean flow velocity and minimum pressure at different sections along the non-aerated flow region for different step heights, step configurations, and chute slopes were considered in estimating the maximum safe discharge. The computational results of this study showed that at the critical cavitation index number, the maximum safe discharge can be increased when:

1- the step height is increased for the same chute slope;
2- the chute slope is decreased for the same step height;
3- Upward inclined steps are used instead of horizontal steps for the same step height and chute slope;
4- the adverse slope of the upward inclined steps is increased for the same step height and chute slope.

The computational results further demonstrated that for all conditions, the unit discharge that may cause cavitation to form on moderate slope stepped spillways of step heights 0.60m and 0.90m is between 25 and 42m^2/s.

8.3. Implications and limitations of this study

The present work provides more insight into the properties of the skimming flow regime over moderate slope stepped spillways. It contributes in extending current knowledge of the non-aerated flow region, by developing a number of equations which may be of significant use in establishing key design parameters for the downstream slope of embankment dams subject to overtopping during times of peak flow.

These parameters include:

1- the length to the inception point of air entrainment. This parameter is important in the design, as it indicates whether the self-aeration mechanism will take place on the structure or not. Two separate equations were developed in the current work to predict the location of the self-aeration mechanism for horizontal and upward inclined steps, respectively, over moderate slope stepped spillways, as a function of the discharge and step geometry. These equations can be used for stepped spillways having slopes not steeper than 1V:2H and not flatter than 1V:3H. The equation proposed for horizontal steps is valid only with step heights between 0.30m and 0.90m, while the other equation can be applied to upward inclined steps of heights between 0.30m and 1.2m, with step inclinations ranging between 1V:3H and 1V:6H. For all conditions, the application of these equations is only valuable for roughness Froude numbers not greater than 10.

2- energy dissipation rate. This parameter has direct implications for the design of the stilling basin located at the end of the structure, where the residual energy of the flow will be dissipated, especially when the downstream length of the moderate slope stepped spillway and embankment dam is relatively small, so that the self-aeration mechanism may not take place.

3- safe design discharge, which assures the safety of the steps against cavitation damage. This parameter provides the designer with information about the maximum amount of unit discharge that can be passed by a stepped spillway safely, without the need for aerators, to prevent the formation of cavitation. The present study presents the maximum design unit discharge for various step heights and chute slopes typical of embankment dams, for both horizontal and upward inclined steps. However, the structure needs to be equipped with one or more aerators in case it is required to pass unit discharges higher than those presented in this project.

4- step configuration. Upward inclined steps can be considered as an optimal alternative step configuration that could lead to more efficient designs of stepped spillways.

8.4. Suggestions for future research

This section presents a number of additional investigations which need to be carried out to understand more fully the properties of the flow over stepped spillways, and to find how the computational SPH particle based method performs in simulating more complex aspects of the free surface flow over said structures:

1- In this study a single phase flow, water, is implemented to characterize the skimming flow regime over a reach of stepped spillways, known as the non-aerated flow region, where air content is assumed to be entirely absent. Detailed information regarding the skimming flow properties over the aerated flow region is still lacking, especially for structures with upward inclined steps. Therefore, it would be of interest to apply a two phase flow, water and air, to estimate the global energy dissipation rate. This also can be used to investigate the performance of the computation SPH particle-based method, in simulating air-water flow over stepped spillways.

2- The present work provides new insights into the skimming flow condition over moderate slope stepped, using horizontal and upward inclined steps. The behaviour of the upward inclined steps with the nappe and transition flow regimes has not yet been investigated. It would therefore be interesting to conduct further research in order to provide more definitions for the hydraulics of flow over upward inclined steps.

3- The current work shows that the upward inclined steps perform better than the conventional steps, in terms of decelerating the flow velocity, dissipating the energy of the overflowing water and increasing the maximum unit discharge that can be passed safely by moderate slope stepped spillways without cavitation damage. Additional work needs to be performed with pooled steps, in order to compare their performance with upward inclined steps, since both can be used in the design of fish ladder structures. To do so, 3D SPHysics code needs to be applied, and run with high performance computers.

4- The current research indicates that the length to the inception point of air entrainment depends on the unit discharge, step height, chute slope and step shape. However, in this study, with the upward inclined steps, only one step height is used, with three different step inclinations and chute slopes to

determine the location of the inception point of self-aeration. Hence, further study is needed to address this issue, by using different step heights to obtain a relationship to define the location of this point in a more accurate manner.

Bibliography

Amador, A., Sanchez-Juny, M., and Dolz, J. (2006). "Characterization of the non-aerated flow region in a stepped spillway by PIV", Journal of Fluids Engineering, Transactions of the ASME, 138(6): pp.1266-1273.

Amador, A., Sanchez-Juny, M. and Dolz, J. (2009). "Developing flow region and pressure fluctuations on steeply sloping stepped spillways" Journal of Hydraulic Engineering, 135(12): pp.1092-1100.

André, S. (2004). "High velocity aerated flows on stepped-chutes with macro-roughness elements" Communication 20, Laboratorie de Constructions Hydrauliques Ecole Polytechnique Federale de Lausanne: Lausanne, Switzerland. ISSN 1661-1179.

André, S., and A. J. Schleiss (2008). "Pressures on a stepped spillway." Journal of Hydraulic Research 46: 574-576.

Barani G.A., Rahmani, M. B., and Sohrabipoor, N. (2005). "Investigation of flow energy dissipation over different stepped spillways." American Journal of Applied Sciences 2(6): 1101-1105.

Batchelor, G., K. (1974). "Introduction to fluid mechanics" Cambridge University press, UK.

Beitz, E., and Lawless, M. (1992). "Hydraulic model study for dam on GHFL 3791 Isaac River at Burton Gorge." Water Resources Commission, Brisbane, Australia.

Benz, W. (1990). Smoothed particle hydrodynamics: a review. In The numerical modelling of nonlinear stellar pulsations, Springer Netherlands. pp.: 269-288.

Bindo, M., J. Gautier, et al. (1993). "Stepped spillway of M'Bali dam" International Water Power and Dam Construction , 45 (1): 35-36.

Boes, R. M. and Hager, W. H. (2003). "Hydraulic design of stepped spillways." Journal of Hydraulic Engineering, 129(9): pp.671-679.

Boes, R. and Minor, H. E. (2002). "Hydraulic design of stepped spillways for RCC dams" International Journal on Hydropower and Dams, 9(3): pp.87-91.

Bonet, J. and Lok, T. S. (1999). "Variational and momentum preservation aspects of Smooth Particle Hydrodynamics." Journal of Computer Methods in Applied Mechanics and Engineering, 180 (1): pp.97-115.

Calagrossi, A. and Landrini, M. (2003) "Numerical simulation of interfacial flows by smoothed particle hydrodynamics" Journal of Computational Physics, 191(2):448-475.

Capone, T., Panizzo, A., Cecioni, C., and Dalrymple, R. A. (2007). Accuracy and stability of numerical schemes in SPH. SPHERIC second international workshop, Madrid, Spain.

Carosi, G., and H. Chanson (2008). "Turbulence characteristics in skimming flows on stepped spillways." Canadian Journal of Civil Engineering 35(9): 865-880.

Carosi, G., and H. Chanson (2009). "Reply to discussion by G. Carosi and H. Chanson on "Turbulence characteristics in skimming flows on stepped spillways"." Canadian Journal of Civil Engineering 36: 678-679.

Carvalho, R. F. and Martins, R. (2009). Stepped spillway with hydraulic jumps: application of a numerical model to a scale model of a conceptual prototype.Journal of hydraulic engineering, 135(7), 615-619.

Cha, S.-H., and Whitworth, A. P. (2003). Implementations and tests of Godunov-particle hydrodynamics, Mon. Not. R. Astro. Soc., 340, pp.73-90.

Chamani, M. R. and Rajaratnam, N. (1999). "Characteristics of skimming flow over stepped spillways" Journal of Hydraulic Engineering , 125(4): pp.361-368.

Chamani, M. R., and N. Rajaratnam (2000). "Onset of skimming flow on stepped spillways." Journal of Hydraulic Engineering 125: 969-971.

Chanson, H. (1993). "Stepped spillway flows and air entrainment." Canadian Journal of Civil Engineering 20: 422-435.

Chanson, H. (1994). "Hydraulics of skimming flows over stepped channels and spillways" Journal of Hydraulic Research , 32(3): pp.445-460.

Chanson, H. (1995). "History of stepped channels and spillways: a rediscovery of the 'wheel' " Canadian Journal of Civil Engineering , 22(2): pp.247-259.

Chanson, H. (1996). "Prediction of the transition nappe/skimming flow on a stepped channel." Journal of Hydraulic Research, IAHR , 34(3): pp.421-429.

Chanson, H. (1997). Air bubble entrainment in free-surface turbulent shear flows. Academic press, London.

Chanson, H. (2000a). "Characteristics of Skimming Flow over Stepped Spillways" Journal of Hydraulic Engineering , 126(11): pp.862-865.

Chanson, H. (2000b). Embankment overflow stepped spillways & Earth dam spillways with precast concrete blocks. Internet Resource, 1-1.

Chanson, H. (2002). The hydraulics of stepped chutes and spillways. Lisse, A.A. Balkema publishers.

Chanson, H. (2004). The hydraulics of open channel flow: an introduction, 2nd edition. Butterworth-Heinemann, Oxford, UK.

Chanson, H. (2005). "Discussion of "hydraulic design of stepped spillways" by Robert M. Boes and Willi H. Hager." Journal of Hydraulic Engineering 131: 521-524.

Chanson, H. (2006). "Hydraulics of skimming flows on stepped chutes: The effects of inflow conditions?" Journal of Hydraulic Research 44: 51-60.

Chanson, H. (2007). "Embankment overflow protection systems and earth dam spillways" "In: dams: Impacts, stability and design", Nova Science Publishers, Hauppauge NY, USA, Ed. W.P. Hayes and M.C. Barnes, Chapter 4, pp. 101-132.

Chanson, H., and C. Gonzalez (2005). "Physical modelling and scale effects of air-water flows on stepped spillways." Journal of Zhejiang University-Science A 6(3): 243-250.

Chanson, H., and L. Toombes (1997). Flow aeration at stepped cascades. Brisbane, Australia, Univ. of Queensland.

Chanson, H., and L. Toombes (2002). "Experimental study of gas-liquid interfacial properties in a stepped cascade flow." Environmental Fluid Mechanics 2(3): 241-263.

Chanson, H., and L. Toombes (2003). "Strong interactions between free-surface aeration and turbulence in an open channel flow." Experimental Thermal and Fluid Science 27(5): 525-535.

Chanson, H., and L. Toombes (2004). "Hydraulics of stepped chutes: The transition flow/ L'hydraulique des chutes en marches d'escalier: L'ecoulement de transition." Journal of Hydraulic Research 42: 43-54.

Chanson, H., Yasuda, Y., and Othsu, I. (2002). "Flow resistance in skimming flows in stepped spillways and its modelling." Canadian Journal of Civil Engineering 29(6): 809-819.

Chatila, J., and Tabbara, M. (2004). "Computational modelling of flow over an ogee spillway." Computers & Structures 82(22): 1805-1812.

Chatila, J. G., and Jurdi, B. R. (1999). On the hydraulics of flow over stepped spillways. Canadian Society for Civil Engineering - 1999 Annual Conference, June 2, 1999 - June 5, 1999, Regina Saskatchewan, Canada, Canadian Society for Civil Engineering.

Chatila, J. G., and Jurdi, B. R. (2004). "Stepped spillway as an energy dissipater." Canadian Water Resources Journal 29: 147-158.

Chen, Q., Dai, G., and Liu, H. (2002). "Volume of fluid model for turbulence numerical simulation of stepped spillway overflow." Journal of Hydraulic Engineering 128(Compendex): 683-688.

Chen, Q., Dai, G., and Liu, H. (2004). "Three-dimensional turbulence numerical simulation of a stepped spillway overflow." Journal of Hydrodynamics 16: 74-79.

Chen, Q., Dai, G., and Liu, H. (2005). "Influencing factors for the energy dissipation ratio of stepped spillways." Journal of Hydrodynamics 17: 50-57.

Cheng, X., Luo, L., Zhao,W., and Li, R. (2004). "Two-phase flow simulation of aeration on stepped spillway." Progress in Natural Science 14: 626-630.

Cheng, X., Chen, Y. and Luo, L. (2006). "Numerical simulation of air-water two-phase flow over stepped spillways." Science in China, Series E: Technological Sciences 49: 674-684.

Chinnarasri, C., and Wongwises, S. (2004). "Flow regimes and energy loss on chutes with upward inclined steps." Canadian Journal of Civil Engineering, 31(5), 870-879.

Chinnarasri, C., and Wongwises, S. (2006). "Flow patterns and energy dissipation over various stepped chutes." Journal of irrigation and drainage engineering,132(1), 70-76.

Chou, H.T. (1993). Energy dissipation in stepped spillway. International Conference on Hydropower, Rotterdam, Neth, Publ by A.A. Balkema.

Chow, V., T. (1959). Open channel hydraulics , McGraw-Hill, New York, USA.

Christodoulou, G. C. (1993). "Energy dissipation on stepped spillways." Journal of Hydraulic Engineering 119(5): 644-650.

Christodoulou, G., C. (1999). "Design of stepped spillways for optimal energy dissipation." International Journal on Hydropower and Dams 6: 90-93.

Craft, T. J., Launder, B. E., and Suga, K. (1996). "Development and application of a cubic eddy-viscosity model of turbulence." International Journal of Heat and Fluid Flow, 17, 108–111.

Crespo, A. J .C., Gómez-Gesteira, M and Dalrymple, R. A. (2007). "Boundary conditions generated by dynamic particles in SPH methods" Journal of Computers, Materials and Continua, 5(3): pp.173-184.

Crespo, A. J. C. (2008). "Application of the smoothed particle hydrodynamics model SPHysics to free-surface hydrodynamics" PhD thesis, University of Vigo. Galicia, Spain.

Dalrymple, R. A. and Kino, O. (2000). "SPH modelling of water waves" Proc. Coastal Dynamics, Lund.

Dalrymple, R. A. and Rogers, B. D. (2006). "Numerical modelling of water waves with SPH method" Journal of Coastal Engineering , 53(2-3): pp.141-147.

Diez-Cascon, J., J. L. Blanco, et al. (1991). "Studies on the hydraulic behaviour of stepped spillways." International Water Power and Dam Construction 43: 22-26.

Dilts, G. A. (1999). "Moving-Least-Squares-Particle Hydrodynamics - I. Consistency and Stability" International Journal for Numerical Methods in Engineering, 44(8): pp.1115-1155.

Ditchey, E. and Campbell, D. (2000). "Roller Compacted Concrete and Stepped Spillway.", Proceeding of the International workshop on Hydraulics of Stepped Spillways, IHAR, A. A., Balkema/ Rotterdam/Brookfield, Zurich, Switzerland, Minor, H. E. and Hager, W., H. (edts): PP. 171-178.

Dong, Z. Y., and Lee, J. H. (2006). "Numerical simulation of skimming flow over mild stepped channel*." Journal of Hydrodynamics 18(3): 367-371.

Dumbser, A. (2011). "A Simple Two-Phase Method for the Simulation of Complex Free Surface Flows" Journal of Computer Methods in Applied Mechanics and Engineering, 200: pp.1204-1219.

El-Kamash, M. K., Lowen, M. R., and Rajaratnam, M. (2005) "An experimental investigation of jet flow on a stepped chute." Journal of Hydraulic Research, IAHR 43(1): 31-43.

Elviro, V., and Mateos, C. (1995). "Spanish research into stepped spillways." International Journal on Hydropower & Dams 2: 61-61.

Essery, I. T. S., and Horner, M.W., (1978) "The hydraulic design of stepped spillway". Report no. 33, CIRIA, London, United Kingdom.

Fabian, A., Ines, M., Matos, J. (2010). "Laboratory measurements and multi-block numerical simulations of the mean flow and turbulence in the non-aerated skimming flow region of steep stepped spillways." Journal of Environmental Fluid Mechanics: in press 26/8/2010: DOI 10.1007/s10652-010-9188-6.

Falvey, H. T. (1990). "Cavitation in chutes and spillways" Engineering Monograph 42, Bureau of Reclamation, Denver.

Federico, I., Marrone, S., Colagrossi, A., Aristodemo, F. and Veltri, P. (2010). Simulating free-surface channel flows through SPH. In Proc. 5th International SPHERIC Workshop, Manchester.

Felder, S. and Chanson, H. (2009). "energy dissipation and residual energy on embankment dam stepped spillways" 33 rd IHAR congress: Water Engineering for Sustainable Environment.

Ferrari, A., Dumbser, M., Toro, E. F. and Armanini, A., (2008). "A New 3D Parallel SPH scheme for Free Surface Flows" in Computers & Fluids, 38(6): pp.1203-1217.

Ferrari, A. (2010). "SPH simulation of free surface flow over a sharp crested weir " Journal of Advances in Water Resources, 33 (3): pp.270-276.

Frizzell, K. H., and Mefford, B. W. (1991). "Designing Spillways to Prevent Dam cavitation" Concrete International, 13(5), pp.58-64.

Frizzell, K. and Renna, F. M. (2011). Laboratory Studies on the Cavitation Potential of Stepped Spillways [online]. In: Valentine, EM (Editor); Apelt, CJ (Editor); Ball, J (Editor); Chanson, H (Editor); Cox, R (Editor); Ettema, R (Editor); Kuczera, G (Editor); Lambert, M (Editor); Melville, BW (Editor); Sargison, JE (Editor). Proceedings of the 34th World Congress of the International Association for Hydro-Environment Research and Engineering: 33rd Hydrology and Water Resources Symposium and 10th Conference on Hydraulics in Water Engineering. Barton, A.C.T.: Engineers Australia, 2011: 2420-2427. Availability:<http://search.informit.com.au/documentSummary;dn=353984483387170;res=IELENG> ISBN: 9780858258686.

Gatti , D., Maffio, A., Zuccala, D. and Di Monaco, A., (2007). "SPH Simulation of Hydrodynamics Problems Related To Dam Safety" (2007). 32nd Congress of IAHR,. CD-ROM. Paper 2, SS09. Venice. Italy.

Gingold, R. A., and Monaghan, J. J. (1977). "Smoothed particle hydrodynamics, theory and application to non-spherical stars" Mon. Not. Roy. Astr. Soc., 181, pp.375-389.

Gómez-Gesteira, M., Cerqueiro. D., Crespo, C., and Dalrymple, R. A. (2005). "Green water overtopping analysed with a SPH model." Journal of Ocean Engineering, 32, pp.223-238.

Gómez-Gesteira, M. and Dalrymple, R. A. (2004). " Using a 3D SPH method for wave impact on a tall structure." Journal of Waterway, Port, Coastal, and Ocean engineering. 130(2):63-69.

Gómez-Gesteira, M., Rogers B.D., Crespo A.J.C., Dalrymple R.A, Narayanaswamy M. and Dominguez J.M., (2012) "SPHysics - development of a free-surface fluid solver- Part 1: Theory and Formulations". Computers & Geosciences, DOI:10.1016/j. cageo.2012.02.029, 2012.

Gómez-Gesteira, M., Rogers, B., Dalrymple, R. A. and Crespo, A. J. C. (2010). "State-of-the-art of classical SPH for free-surface flows" Journal of Hydraulic Research, 48, Extra issue: pp.6-27.

Gómez-Gesteira, M., Rogers, B., Dalrymple, R. A., Crespo, A. J. C., and Narayanaswamy, M., (2012). User Guide for the SPHysics Code v2.0, http://www.sphysics.org.

Gonzalez, C. A. (2005) "An Experimental Study of Free-surface Aeration on Embankment Stepped Chutes." PhD thesis. Faculty of Engineering, Physical Sciences and Architecture. University of Queensland, Brisbane, Australia.

Gonzalez, C. A. and Chanson, H. (2007), "Experiment Measurements of Velocity and Pressure Distributions on a Large Broad-Crester Weir", Flow Measurement and Instrumentation, Vol.18, pp.107-113.

Gotoh, H., Shao, S. And Memita, T. (2004). "SPH-LES model for numerical investigation of wave interaction with partially immersed breakwater" Journal of Coastal Engineering, 46(1):p39-63.

Hager, W. H, Schwalt, M, (1994). "Broad crested weir" Journal of Irrigation and Drainage Engineering 120(1): pp.13-26.

Hargreaves, D.M., Morvan, H.P., Wright, N.G. (2007). "Validation of the volume of fluid method for free surface calculation: the broad crested weir" Journal of Engineering Applications of Computational Fluid Mechanics, 1(2): pp.136-146.

Henderson, F. M. (1966). Open channel flow. MacMillan. New York, USA.

Horner, M. W., (1969) "An analysis of flow on cascades of steps." PhD thesis, University of Birmingham, Birmingham, United Kingdom.

Hunt, S. L. and Kadavy, K. C. (2010). "Energy dissipation on flat sloped-stepped spillway: I. Upstream of the inception point" Transactions of the American Society of Agricultural and Biological Engineers, ASABE, 53(1):103-109.

ICOLD(1997). Dams less than thirty metres high-cost savings and safety improvements, Bulletin, 109. ICOLD.

Johnson, G. R., Stryk, S. R. and Beissel, S. R. (1996). " SPH for high velocity impact computations" Journal of Computer methods in Applied Mechanics and Engineering, 139 (1- 4): 347-373.

Karim, K.J., Mariam, K.L (2009). "Study of Conveniences of Using Stepped Spillway in Roller Compacted Concrete Dams (RCCD)." Engineering and Technology Journal 27(16): 1-13.

Khatsuria, R. M. (2005). Hydraulics of spillways and energy dissipators. CRC Press.

Lee, E. S., Violeau, D., Issa, R. and Ploix, S. (2010). "Application of weakly compressible and truly compressible SPH to 3-D water collapse in waterworks" Journal of Hydraulic Research, 48(extra issue): pp.50-60.

Leimkuhler, B. J., Reich, S. and Skeel, RD. (1997). "Integration methods for molecular dynamics" IMA Volumes in Mathematics and its application. Springer Verlag, 82:161-186.

Leveque, R. J. (2002). Finite volume methods for hyperbolic problems. Vol. 31. Cambridge university press.

Liu, G. R. (2010). Mesh free methods: Moving beyond the finite element method. CRC press.

Liu, M. B. and Liu, G. R. (2003). "Smoothed Particle Hydrodynamics-A Mesh free Particle Method." Singapore, World scientific.

Liu, W. K., Li, S., and Belytschko, T. (1997). "Moving least-square reproducing kernel methods (I) methodology and convergence." Journal of computer methods in applied mechanics and engineering, 143(1), 113-154.

Liu, G. R., & Quek, S. S. (203). The finite element method: a practical course.

Lo, Y. E. M. and Shao, S. (2002). "Simulation of near-shore solitary wave mechanics by an incompressible SPH method", Journal of Applied Ocean Research, 24(5):275-286.

Lopez, D., Marivela, R. (2009a). "Applications of the SPH model to the design of fishways." 33rd Congress of IAHR. Water Engineering for a Sustainable Environment (Vancouvert 9-14 de agosto de 2009). ISBN: 978- 90-78046-08-0.

Lopez, D., Marivela, R. and Garrote, L. (2009b). "Calibration of SPH using prototype pressure data from the stilling basin of the Villar del Rey dam, Spain". 33rd Congress of IAHR. Water Engineering for a Sustainable Environment (Vancouvert 9-14 de agosto de 2009). ISBN: 978- 90-78046-08-0.

Lopez, D., Marivela, R. and Garrote, L. (2010). "Smooth particle hydrodynamics model applied to hydraulic structures: A hydraulic jump test case" Journal of Hydraulic Research. Vol 48. , Extra Issue (2010), pp. 142-158. ISSN: 0022-1686.

Lucy, L. B. (1977). "A numerical approach to testing the fission hypothesis" The Astronomical Journal, 82(12): pp.1013–1924.

Lv, X., Zou, Q., & Reeve, D. (2011). "Numerical simulation of overflow at vertical weirs using a hybrid level set/VOF method" Journal of Advances in Water Resources, 34(10): pp.1320-1334.

Manso de Almeida, P. and Schleiss, A. J. (2000). "Stability of concrete macro-roughness linings for overflow protection of earth embankment dams", Canadian Journal of Civil Engineering, 29(5): 762-776.

Matos, J. (2000). "Characteristics of Skimming Flow over Stepped Spillways" Discussion by Chamani, M. R. and Rajaratnam, N., Journal of Hydraulic Engineering, ASCE, 126(11):865-868.

Matos, J. (2001). "Onset of Skimming Flow on Stepped Spillways." Discussion by Chamani, M. R. and Rajaratnam, N., Journal of Hydraulic Engineering, ASCE, 127(7):519-521.

Mehdi, A. (1997) "The hydraulics of flow on stepped ogee-profile spillways." PhD thesis. Faculty of Engineering, University of Ottawa, Ottawa, Canada.

Monaghan, J. J. (1994). "Simulating free surface flows with SPH." Journ
computational physics, 110: pp.399-406.

Monaghan, J. J. (2000). "SPH without a tensile instability." Journal of computa
physics, 159(2), 290-311.

Monaghan, J. J. (2005). Smoothed particle hydrodynamics. Reports on Progr
Physics 68(8), pp.1703—1759.

Monaghan, J. J. and Kos, A. (1999). "Solitary waves on a Cretan beach" Jour
waterway, port, coastal, and ocean Engineering, 125(3): pp.145-154.

Monaghan, J. J., Kos, A., ad Issa, N. (2003). "Fluid motion generated by im
Journal of waterway, port, coastal, and ocean engineering, 129(6), 250-259.

Monaghan, J. J., and Lattanzio, J. C. (1985). "A refined particle metho
astrophysical problems" Journal of Astronomy and Astrophysics, 149 (1): pp
143.

Morris, J. P., Fox, P. J., and Zhu, Y. (1997). "Modeling low Reynolds nu
incompressible flows using SPH." Journal of computational physics, 136(1),
226.

Moulinec, C., Issa, R., Marongiu, J.C., Violeau, D. (2008). "Parallel 3-D
simulations" Journal of Computer Modelling in Engineering and Sciences,
pp.133–148.

Oger, G., Doring, M., Alessandrini, B. and Ferrant, P. (2006). "Two-dimens
SPH simulations of wedge water entries". Journal of Computational Physics,
pp.803–822.

Othsu, I. and Yasuda, Y. (1997). "Characteristics of flow conditions on st
channels" The 27th Congress of IAHR, Water Resources Eng. Div./ASCE, Aug
Francisco, USA, pp. 583-588.

the 5th IAHR/ASCE congress, Vol. Joint meeting paper, Minneapolis, USA, pp
518.

Peyras, L., Royet, P. and Degoutte, G. (1992). "Flow and energy dissipation
stepped gabion weirs" Journal of Hydraulic Engineering, ASCE, 118 (5):707-7

Pope, S. B. (1994). "Lagrangian PDF methods for turbulent flows" Annual R
Fluid Mechanics, 26: pp.23-63.

Qian, Z. D., Hu, X. Q., Huai, W. X. and Amador, A. (2009). "Numerical simu
and analysis of water flow over stepped spillways." Science in China ser
Technological Sciences, 52(7):1958-1965.

Rajaratnam, N. (1990). "Skimming flow in stepped spillways." Journal of Hyd
Engineering 116: 587-591.

Ramamurthy, A. S., Tim, U. S., and Rio, M. V. J. (1988)."Characteristics of S
Edged and Round- Nosed Broad-Crested Weirs ", Journal of Irrigation and Dra
Eng., ASCE, 99(2), pp.61-73.

Rogers, B., Dalrymple, R. A., Stansby, P. K., and Laurence D. R. P. (
Development of a parallel SPH code for free-surface wave hydrodynamics,
2nd SPHERIC International Workshop, Madrid (Spain), 23rd–25th May
pp.111–114.

Rogers, B. D., and Dalrymple, R. A. (2008), SPH Modeling of tsunami w
Advances in Coastal and Ocean Engineering, Vol. 10 Advanced Numerical M
for tsunami waves and runup, World Scientific.

Rogers, B. D., Dalrymple, R. A., and Stansby, P. K. (2010). "Simulation of c
breakwater movement using 2-D SPH" Journal of Hydraulic Research, 48
issue: pp.135-141.

Rouse, H. (1978), Elementary Mechanics of Fluids, John Wiley & Sons, New
1946 (republished by Dover Publications, Inc., New York, 1978), pp. 62, 84-8
235-238.

Scimemi E. Sulla (1930). "The form of the flow over weirs." L'Energia Ele Milano;7: 293–305.

Smagorinsky, J. (1963). "General circulation experiments with the pri equations. I. The basic experiment" Monthly Weather Review. 91(3):99-164.

Sorenson, R. (1985). "Stepped spillway hydraulic model investigation." Jour Hydraulic Engineering 111(12): 1461-1472.

Stephenson, D. (1991). "Energy dissipation down stepped spillways." Interna Water Power and Dam Construction, 43(11):27-30.

Tabbara, M., Chatila, J. and Awwad, R. (2005). "Computational simulation o over stepped spillways." Computers and Structures 83: 2215-2224.

Tatewar, S. P. and R. N. Ingle (1999). "Nappe flow on inclined stepped spill Journal of the Institution of Engineers (India): Civil Engineering Division, 79 178.

Tongkratoke, A., Chinnarasri, C., Pornprommin, A., Dechaumphai, P., & Junt V. (2009). Non-linear turbulence models for multiphase recirculating free-s flow over stepped spillways. International Journal of Computational Dynamics, 23(5), 401-409.

Toombes, A. (2002) "Experimental Study of Air-Water Flow Properties on Gradient Stepped Cascades. " PhD thesis. Faculty of Engineering, Physical Sc and Architecture. University of Queensland, Brisbane, Australia.

Toombes, L., and Chanson, H. (2008). "Flow patterns in nappe flow regime low gradient stepped chutes." Journal of Hydraulic Research 46: 4-14.

Toro, E. F., Spruce, M., and Speares, W. (1994). "Restoration of the contact s in the HLL-Riemann solver." Journal of shock waves, 4(1), 25-34.

Tozzi, M. J. (1994). "Residual energy in stepped spillways" International Power and Dam Construction, 74(2): 32-34.

flows with the SPH method: An overview. Int. J. Numer. Meth. Fluids pp.277–304.

Violeau, D., Issa, R., Benhamadouche, S., Saleh, K., Chorda, J. and Maubou M.-M. (2008). Modelling a fish passage with SPH and Eulerian codes: The inf of turbulent closure, Proc. 3rd SPHERIC International Workshop, 3rd–6th 2008, Lausanne, (Switzerland), pp85-91.

Wendland, H. (1995). "Piecewise polynomial, positive definite and com supported radial functions of minimal degree" Journal of Advanc Computational Mathematics. 4(1): 389-396

Yasuda, Y., and Chanson, H. (2003)."Micro and macro-scopic study of two flow on a stepped chute." Proc. 30th IAHR congress, Thessaloniki, Greece.

Yasuda, Y., and Othsu. I. (1999). "Flow resistance in skimming flow in st channels. " Proceedings, 28th IAHR congress, Graz, Australia.